Degradation Mechanisms of the Lanthanum Strontium Cobalt Ferrite Used as Oxygen Electrode in Solid Oxide Cells

Giuseppe Sassone

THÈSE

Pour obtenir le grade de

DOCTEUR DE L'UNIVERSITÉ GRENOBLE ALPES

École doctorale : I-MEP2 - Ingénierie - Matériaux, Mécanique, Environnement, Energétique, Procédés, Production
Spécialité : 2MGE - Matériaux, Mécanique, Génie civil, Electrochimie
Unité de recherche : CEA Grenoble / LITEN

Mécanismes de dégradation de l'électrode à oxygène en ferro-cobaltite de lanthane dopée au strontium pour cellules à oxydes solides

Degradation Mechanisms of the Lanthanum Strontium Cobalt Ferrite Used as Oxygen Electrode in Solid Oxide Cells

Présentée par :

Giuseppe SASSONE

Direction de thèse :

Jérôme LAURENCIN DIRECTEUR DE RECHERCHE, Université Grenoble Alpes	Directeur de thèse
Aline LEON Université Grenoble Alpes	Co-directrice de thèse
Bertrand MOREL INGENIEUR DE RECHERCHE, CEA	Co-encadrant de thèse

Rapporteurs :

Federico SMEACETTO
FULL PROFESSOR, Politecnico di Torino
Spiros ZAFEIRATOS
DIRECTEUR DE RECHERCHE, CNRS délégation Alsace

Thèse soutenue publiquement le **17 avril 2024**, devant le jury composé de :

Elisabeth DJURADO, PROFESSEURE DES UNIVERSITES, Grenoble INP	Présidente
Jérôme LAURENCIN, DIRECTEUR DE RECHERCHE, CEA centre de Grenoble	Directeur de thèse
Aline LEON, SENIOR SCIENTIST, Europäisches Institut für Energieforschung	Co-directrice de thèse
Federico SMEACETTO, FULL PROFESSOR, Politecnico di Torino	Rapporteur
Spiros ZAFEIRATOS, DIRECTEUR DE RECHERCHE, CNRS délégation Alsace	Rapporteur
Katherine DEVELOS-BAGARINAO, SENIOR SCIENTIST, National Institute of Advanced Industrial Science and Technology	Examinatrice

Invités :

Bertrand Morel
INGENIEUR DE RECHERCHE, CEA Grenoble
Maxime Hubert
INGENIEUR DE RECHERCHE, CEA Grenoble

Acknowledgements

This work was mostly carried out at the “Laboratoire essais et systèmes” (LES), which is part of the “Service technologies hydrogène” (STH2) in the “Department termique conversion and hydrogen” (DTCH) of the French Alternative Energies and Atomic Energy Commission (CEA) in Grenoble. For this reason, I would like to thank Ms. Julie Mougin, previous head of the Laboratory and subsequently of the Service, along with Cyril Bourasseau, current head of the Laboratory and Mathias Gerard, current head of the Service, for allowing me to be part of this amazing research team. I am deeply thankful for the opportunity to be part of this exceptional research team.

I am grateful to the members of the jury for my PhD defense. Special thanks to Prof. Federico Smeacetto from Politecnico di Torino (PoliTO) and Dr. Spiros Zafeiratos from the Institut de chimie et procédés pour l’énergie, l’environnement et la santé (ICPEES) for their invaluable contributions to the manuscript review. I extend my gratitude to Dr. Katherine Develos-Bagarinao from The National Institute of Advanced Industrial Science and Technology (AIST) in Japan and Prof. Elisabeth Djurado for their roles as examiners and for the stimulating discussions throughout the three years of the thesis. Thank you all for having dedicated your time to my work.

I would like to thank my thesis director, Jérôme Laurencin, for the privilege of working alongside him and witnessing his competence and rigor. Special thanks to my co-supervisors, Bertrand Morel from CEA and Aline Léon from the European Institute for Energy Research (EIFER), for their help and suggestions concerning the experimental testing and post-test characterizations. I extend my thanks to Maxime Hubert for his assistance throughout the thesis.

This work would not have been feasible without valuable external collaborations. I extend my appreciation to Julien Vulliet from CEA Le Ripault for providing pristine cells for testing and analysis. Special thanks to Katherine Develos-Bagarinao, Isabelle Martin, Laure Guetaz, Thomas David, and Anass Benayad for their contributions to the scientific production with various post-test analyses.

During these years, I had the opportunity to participate in two experimental campaigns at synchrotron facilities. My sincere thanks to Dario Ferreira-Sanchez from the microXAS beamline of the Swiss Light Source (SLS) at the Paul Scherrer Institute (PSI) and Julie Villanova from the ID16B beamline of the European Synchrotron Radiation Facility (ESRF) for their assistance in data acquisition.

I extend my thanks to all the people working at the LES, including Karine Couturier, Jérémy Merlin, Thibaut Disparti, Denis Reynaud, Julien Manzi, Lionel Tallobre, Jérôme Aicart, and the others (please excuse me if I forget anyone). It was a pleasure to meet the PhD students and Postdocs at the lab: Léa Rorato, Giuseppe Sdanghi, Elisa Effori, Eduardo Da Rosa Silva, Lydia Yefsah, Amira Abaza, Manon Prioux, Amandine Jay, Quentin Brillaut, Ozden Celikbilek, Cintia Hartmann, Karthikeyan Saravanabavan, Zaman Yazbeck, Michael Spann, Angel Trivino Pelaez, Davide Cademartori, Gaurav Mahadev Tambade, and Sana. I deeply appreciate the collaborative spirit. Sharing the work with you during these years was a pleasure and I really appreciate all of you.

Finally, I would like to thank all my friends here in Grenoble, in Italy and across the world. Last but not least, heartfelt thanks to my family, especially my parents, for their endless support.

Abstract

This thesis investigates solid oxide cell degradation through a threefold approach, comprising multiscale physics-based modeling, long-term tests, and advanced post-test analyses. The model, adapted to the studied cell (Ni-YSZ/YSZ/GDC/LSCF) and validated with experimental data, provides an understanding of cell-level processes under varied operating conditions. The model includes morphological and microscale electrochemical kinetic models for the hydrogen and oxygen electrodes, complemented by a macroscale model simulating the complete cell response. Durability tests are performed to assess the impact of various operating conditions, including 2000-hour long-term tests at temperatures of 750, 800, and 850 °C, using 10/90 vol.% H_2/H_2O and dry air at the hydrogen and oxygen electrodes, respectively, and 1000-hour ageing tests at 800 °C to explore the effect of air humidity (0%, 3%, and 8%) under both SOEC and SOFC modes. Advanced post-test analyses, including synchrotron- and laboratory-based techniques down to the atomic scales, are selected to investigate microstructural, chemical, and structural material degradation. The findings demonstrate the model capability to predict both stationary and dynamic electrochemical responses, including local responses along the cell radius. The model interpretation of electrochemical impedance spectra (EIS), for the cells operated in SOEC mode under dry air, identified the hydrogen electrode as the primary source of performance loss. Conversely, the oxygen electrode-related performance remains relatively stable after ageing, indicating limited degradation. Post-test analyses confirmed a substantial microstructural evolution of the hydrogen electrode, including Ni migration and coarsening. In contrast, the oxygen electrode experienced slight Sr segregation. Elemental inter-diffusion across cell layers is identified in all samples, while the commonly observed $SrZrO_3$ phase is not detected. Exploring the impact of operating temperature in SOEC mode revealed an accelerated cell degradation at higher temperatures, particularly for Ni migration in the hydrogen electrode and, in a minor way, for Sr segregation in the oxygen electrode. Ageing under humid air introduced an additional degradation phenomenon at the oxygen electrode in both SOEC and SOFC modes. This consisted of an aggravated LSCF decomposition and the formation of a Sr oxide-based insulating phase on top of the current collector, especially in SOEC mode. The presence of this phase at the cell inlet impacted the current distribution along the cell radius, resulting in a non-uniform hydrogen electrode degradation. The main results are discussed, opening research questions to be investigated in future works as reported in the conclusions and perspectives of this thesis.

Résumé

Cette thèse étudie la dégradation des cellules à oxyde solide en utilisant une triple approche, comprenant une modélisation physique multi-échelle, des tests de longues durées et des analyses post-test avancées. Le modèle adapté à la cellule étudiée (Ni-YSZ/YSZ/GDC/LSCF) et validé grâce aux données expérimentales, permet de comprendre les processus à l'échelle de la cellule dans des conditions de fonctionnement variées. Le modèle prend en compte les paramètres microstructuraux et les cinétiques électrochimiques pour les électrodes à hydrogène et à oxygène (échelle microscopique), complétés par un modèle simulant la réponse de la cellule complète (échelle macroscopique). Des essais de durabilité sont réalisés pour évaluer l'impact de diverses conditions de fonctionnement, notamment des essais de longues durées à des températures de 750, 800 et 850 °C pendant 2000 heures, en utilisant 10/90 vol.% H_2/H_2O et de l'air sec aux électrodes à hydrogène et à oxygène, respectivement, et des essais de vieillissement de 1000 heures à 800 °C pour explorer l'effet de l'humidité de l'air (0 %, 3 % et 8 %) à la fois en mode SOEC et en mode SOFC. Des analyses avancées après les essais, y compris des techniques synchrotron et de laboratoire jusqu'à l'échelle atomique, sont sélectionnées pour étudier la dégradation microstructurale, chimique et structurelle des matériaux. Les résultats démontrent la capacité du modèle à prédire les réponses électrochimiques stationnaires et dynamiques, y compris les réponses locales le long du rayon de la cellule. L'interprétation par le modèle des spectres d'impédance électrochimique (EIS), pour les cellules fonctionnant en mode SOEC sous air sec, a permis d'identifier l'électrode à hydrogène comme la principale source de perte de performance. À l'inverse, les performances liées à l'électrode à oxygène restent relativement stables après le vieillissement, ce qui indique une dégradation limitée. Les analyses post-test ont confirmé une évolution substantielle de la microstructure de l'électrode à hydrogène, y compris la migration et le grossissement du Ni. En revanche, l'électrode à oxygène a connu une légère ségrégation du Sr. L'inter-diffusion des éléments entre les couches de la cellule est identifiée dans tous les échantillons, alors que la phase $SrZrO_3$ couramment observée dans la littérature n'est pas détectée. L'étude de l'impact de la température de fonctionnement en mode SOEC a révélé une dégradation accélérée de la cellule aux températures de fonctionnement les plus élevées, en particulier pour la migration du Ni dans l'électrode à hydrogène et, dans une moindre mesure, la ségrégation du Sr dans l'électrode à oxygène. Le vieillissement avec un air humidifié a introduit un phénomène de dégradation supplémentaire à l'électrode à oxygène, tant en mode SOEC qu'en mode SOFC. Il s'agit d'une aggravation de la décomposition du LSCF et de la formation d'une phase isolante à base d'oxyde de Sr au sommet de la couche collectrice de l'électrode, en particulier et plus fortement en mode SOEC. La présence de cette phase à l'entrée de la cellule a eu un impact sur la distribution du courant le long du rayon de la cellule, ce qui a entraîné une dégradation non uniforme de l'électrode à hydrogène. Les principaux résultats sont discutés et ouvrent la voie à des questions de recherche qui seront étudiées dans des travaux futurs, comme indiqué dans les conclusions et les perspectives de cette thèse.

Contents

List of Figures

List of Tables

List of Symbols

Abbreviations

AC	Alternating Current
ALD	Atomic Layer Deposition
APT	Atom Probe Tomography
ASC	Anode-Supported Cell
ASR	Area Specific Resistance
AST	Accelerated Stress Test
BL	Barrier Layer
BoP	Balance of Plant
CCL	Current Collecting Layer
CFD	Computational Fluid Dynamics
CHP	Combined Heat and Power
COP21	21st Conference Of Parties
CPE	Constant Phase Element
CSC	Cathode-Supported Cell
CSTR	Continuous Stirred Tank Reactor
DC	Direct Current
DFT	Density Functional Theory
DGM	Dusty Gas Model
DR	Degradation Rate
DRT	Distribution of Relaxation Times
EDS	Energy Dispersive X-ray Spectroscopy
EECM	Equivalent Electric Circuit Model
EIS	Electrochemical Impedance Spectroscopy
ESC	Electrolyte-Supported Cell
ESRF	European Synchrotron Radiation Facility
FEM	Finite Element Method
FIB-SEM	Focused Ion Beam-Scanning Electron Microscopy
FL	Functional Layer
FRA	Frequency Response Analyser
FU	Fuel Utilisation
FVM	Finite Volume Method
FWHM	Full Width at Half Maximum
G2P	Gas-to-Power
GDC (or CGO)	Gadolinium-doped Ceria
GHG	Greenhouse Gas
HF	High Frequency
HT	High Temperature
ICP-MS	Inductively Coupled Plasma Mass Spectroscopy
IDL	Inter-diffusion Layer
IEA	International Energy Agency
IT	Intermediate Temperature
IPCC	International Panel on Climate Change
KB	Kirkpatrick-Baez
KMC	Kinetic Monte Carlo
LF	Low Frequency

LSC	Lanthanum Strontium Cobaltite
LSCF	Lanthanum Strontium Cobaltite Ferrite
LSF	Lanthanum Strontium Ferrite
LSGM	Lanthanum Strontium Gallate Magnesite
LSM	Lanthanum Strontium Manganite
LT	Low Temperature
LZO	Lanthanum Zirconate
MF	Mid Frequency
MIEC	Mixed Ionic and Electronic Conductor
OCV	Open Circuit Voltage
P2G	Power-to-Gas
P2P	Power-to-Power
PDE	Partial Differential Equation
PEM	Proton Exchange Membrane
pFIB	Plasma-Focused Ion Beam
PLD	Pulsed Laser Deposition
PSI	Paul Scherrer Institute
PVD	Physical Vapour Deposition
RDS	Rate Determining Step
RES	Renewable Energy Sources
ROI	Region of interest
rSOC	Reversible Solid Oxide Cell
SC	Steam Conversion
ScSZ	Scandia Stabilized Zirconia
SEM	Scanning Electron Microscopy
SIMS	Secondary Ion Mass Spectroscopy
SLS	Swiss Light Source
SoA	State of the Art
SOC	Solid Oxide Cell
SOEC	Solid Oxide Electrolysis Cell
SOFC	Solid Oxide Fuel Cell
SRU	Single Uepeating Unit
STEM	Scanning Transmission Electron Microscopy
SZO	Strontium Zirconate
TEC	Thermal Expansion Coefficient
TEM	Transmission Electron Microscopy
TPBl	Triple Phase Boundaries length
UCV	Unit Cell Volume
XPS	X-ray Photoelectron Spectroscopy
XRD	X-ray Diffraction
XRF	X-ray Fluorescence
YSZ (or 8YSZ)	Yttria Stabilized Zirconia with 8 mol.% of Yttria
3YSZ	Yttria Stabilized Zirconia with 3 mol.% of Yttria

Chemical species

$H_2(g)$	Gaseous hydrogen
$H_2O(g)$	"Gaseous" water (steam)
H_{Ni}	H attached on Ni surface
H_2O_{Ni}	H_2O attached on Ni surface
H_2O_{YSZ}	H_2O attached on YSZ surface
$h^{\bullet}$	Hole defect in the LSCF

$O_2(g)$	Gaseous oxygen	
O_{YSZ}^{2-}	O^{2-} attached on YSZ surface	
O_o^x	Oxygen in the lattice	
$O_O^x(YSZ)$	Oxygen in the YSZ lattice	
OH_{YSZ}^-	OH^- attached on YSZ surface	
$O_O^x(GDC)$	Oxygen in GDC lattice	
$O_O^x(LSCF)$	Oxygen in LSCF lattice	
O_{LSCF}^-	Oxygen ad-ion on the LSCF surface	
O_{LSCF}	Oxygen ad-atom on the LSCF surface	
$O_{2_{LSCF}}$	Oxygen ad-molecule on the LSCF surface	
$V_o^{\bullet\bullet}$	Oxygen vacancy	
$V_O^{\bullet\bullet}(YSZ)$	Oxygen vacancies in the YSZ lattice	
$V_O^{\bullet\bullet}(LSCF)$	Oxygen vacancy in the LSCF lattice	
$V_O^{\bullet\bullet}(GDC)$	Oxygen vacancy in the GDC lattice	
Roman symbols		
a_j	Chemical activity	-
A	Exchange density pre-exponential factor in the hydrogen electrode	$A \cdot cm^{-2}$
B	Exchange density pre-exponential factor in the oxygen electrode	$A \cdot cm^{-2}$
$C_{O_O^x}^{max}$	Maximum concentration of oxygen incorporated in LSCF	$mol \cdot m^{-3}$
E_a^i	Activation energy of the exchange current density for the i-th electrode	$J \cdot mol^{-1}$
$E_{i=0}$	Open circuit voltage	V
e^-	Electron	-
f	Frequency	Hz
F	Faraday's constant	$C \cdot mol^{-1}$
i	Current density	$A \cdot cm^{-2}$
i_{AC}	AC current density	$A \cdot cm^{-2}$
i_{DC}	DC current density	$A \cdot cm^{-2}$
i_0	Exchange current density	$A \cdot cm^{-2}$
i_{io}	Local ionic current density	$A \cdot cm^{-2}$
i_{el}	Local electronic current density	$A \cdot cm^{-2}$
k	Kinetic constant of the reaction	
m	Exchange density exponent for the hydrogen partial pressure	-
n	Exchange density exponent for the steam partial pressure	-
p	Exchange density exponent for the oxygen partial pressure	-
p_i	Partial pressure of the i-th species	atm
R	Universal gas constant	$J \cdot mol^{-1} \cdot K^{-1}$
R_c	Contact resistance	$\Omega \cdot cm^2$
$\overline{r_i}$	Radius of the i-th phase	µm
R_{ohm}	Ohmic resistance	$\Omega \cdot cm^2$
R_p	Polarisation resistance	$\Omega \cdot cm^2$
R_s	Series resistance	$\Omega \cdot cm^2$
R_{tot}	Total resistance	$\Omega \cdot cm^2$

s_i	Free site on the surface for the i-th phase	-
T	Absolute temperature	K
U	Cell Voltage	V
U^0	Voltage in standard conditions	V
U_{AC}	AC voltage	V
U_{DC}	DC voltage	V
U_{OCV}	Open circuit voltage	V
Z	Impedance	Ω·cm^2
Z_{Im}	Imaginary part of the impedance	Ω·cm^2
Z_{Re}	Real part of the impedance	Ω·cm^2
Greek symbols		
ε_i	Volume fraction of the i-th phase	-
φ	Phase shift	°
η_{act}	Activation overpotential	V
η_{conc}	Concentration overpotential	V
η_{conv}	Conversion overpotential	V
η_{diff}	Diffusion overpotential	V
η_{ohm}	Ohmic overpotential	V
$\theta_{i\,j}$	Local coverage of the i-th species on the surface of the j-th phase	-
τ_i	Tortuosity factor of the i-th phase	-

General introduction

1.Context

Nowadays, the impact of human activities on climate change is evidenced by extreme natural events and catastrophic disasters. For example, adverse weather conditions and phenomena (e.g. wildfires, floods, droughts, cyclones and tornados, heat and cold waves, etc.) damage the landscape and the built environment, as well as causing many difficulties in growing various crops with a huge impact on the economies of the countries. In the last decade, the recorded increase in the global surface temperature is ca. 1.1 °C compared to 1850–1900 (1). The 21st Conference of Parties (COP21) established the Paris Agreement in 2015 as a global energy initiative with the goal of keeping the global temperature increase below 2 °C, ideally 1.5 °C, relative to pre-industrial levels (2). However, the current projections suggest that the COP21 target will not be achieved and the most likely scenario would lead to a global warming of 1.5°C by 2030-2052 (2) and 2.7 °C by 2100 (3) (see Figure 0-1).

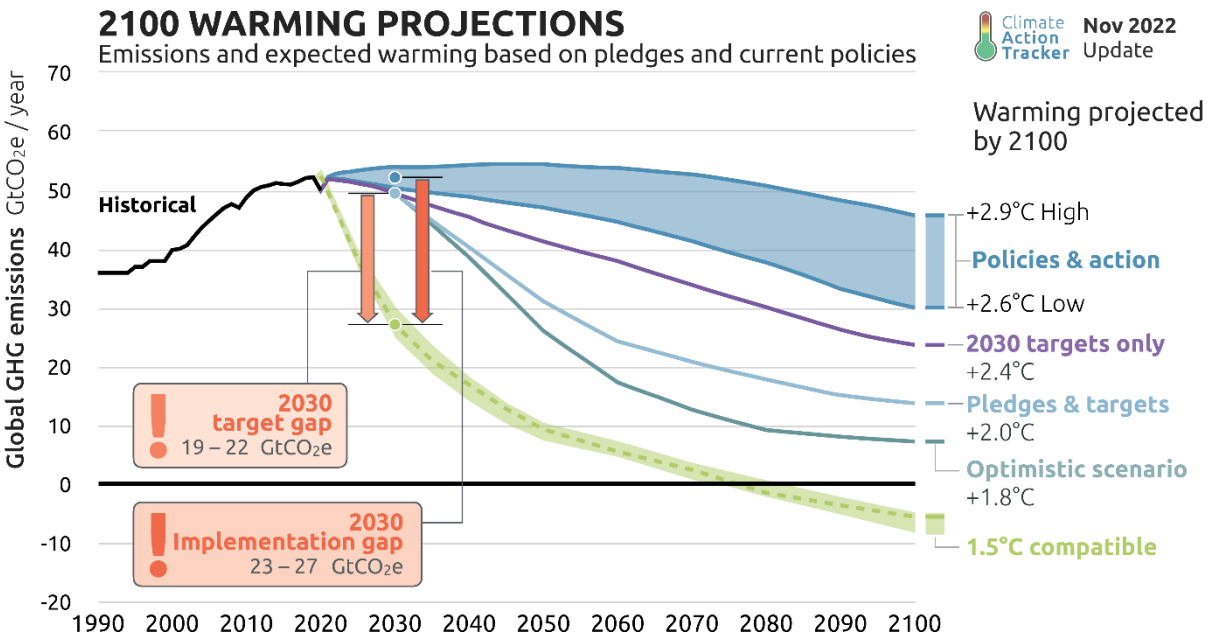

Figure 0-1. Global warming projections from 1990 to 2100 (3). Climate Action Tracker (2022). 2100 Warming Projections: Emissions and expected warming based on pledges and current policies. November 2022. Available at: https://climateactiontracker.org/global/temperatures/. Copyright ©2022 by Climate Analytics and NewClimate Institute. All rights reserved.

Therefore, there is still an urgent need to take action to limit the global temperature increase. According to the International Panel on Climate Change (IPCC), the global warming is associated to the greenhouse gas (GHG) emissions, mostly CO_2 and CH_4 emissions, from both natural and human sources (1). Figure 0-2 displays an analysis of the GHG emissions and their origins, as well as their effect on the surface temperature. As can be seen, the human activity contributes significantly to the climate change.

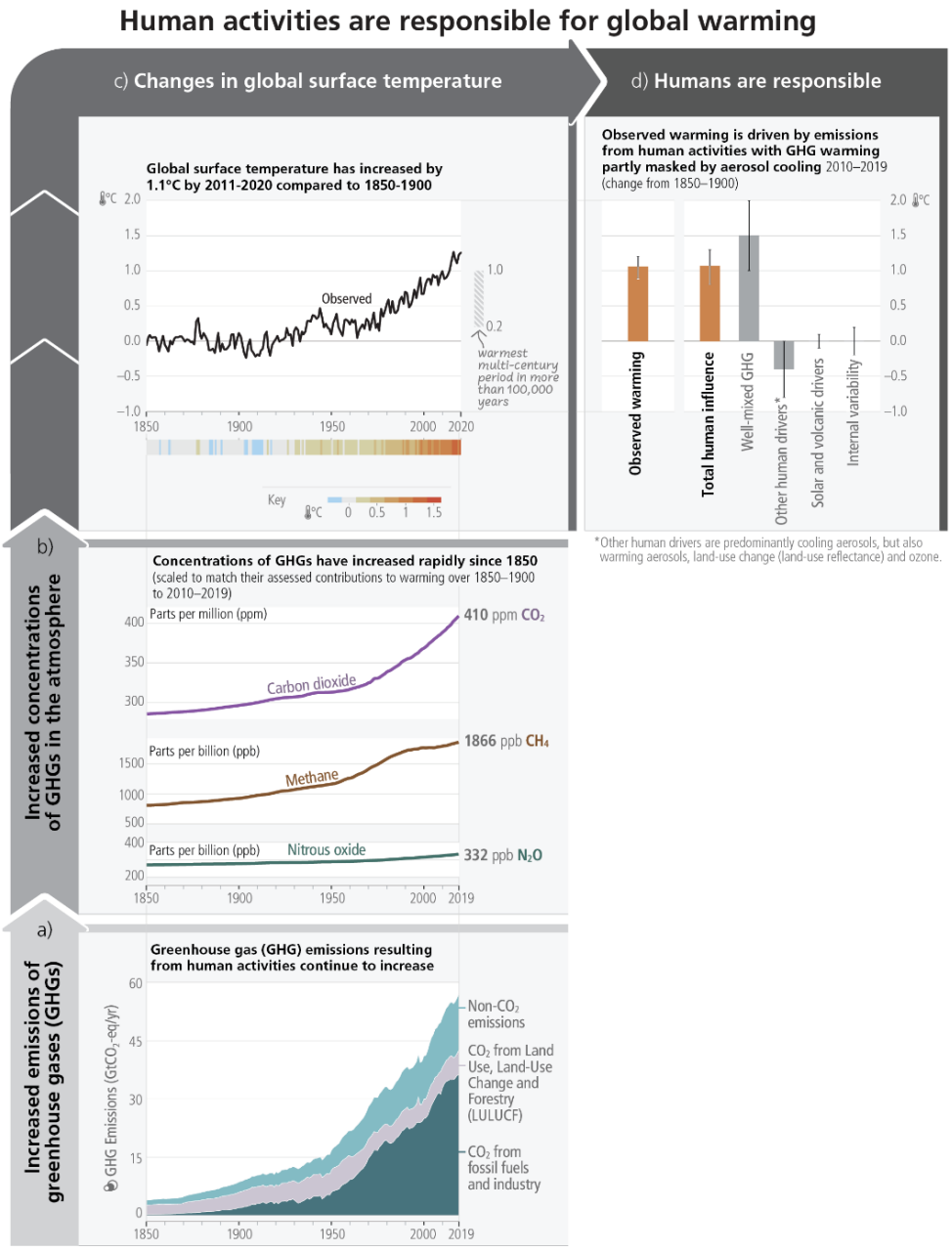

Figure 0-2. IPCC evolution GHG emissions and global surface temperature since 1850 (1)

The GHG emissions evolution in the time follows the same trend as the increase in fossil fuels consumption over time, as depicted in Figure 0-3. Thus, as a first step to limit the GHG emissions, a decrease of the fossil fuels consumption is mandatory.

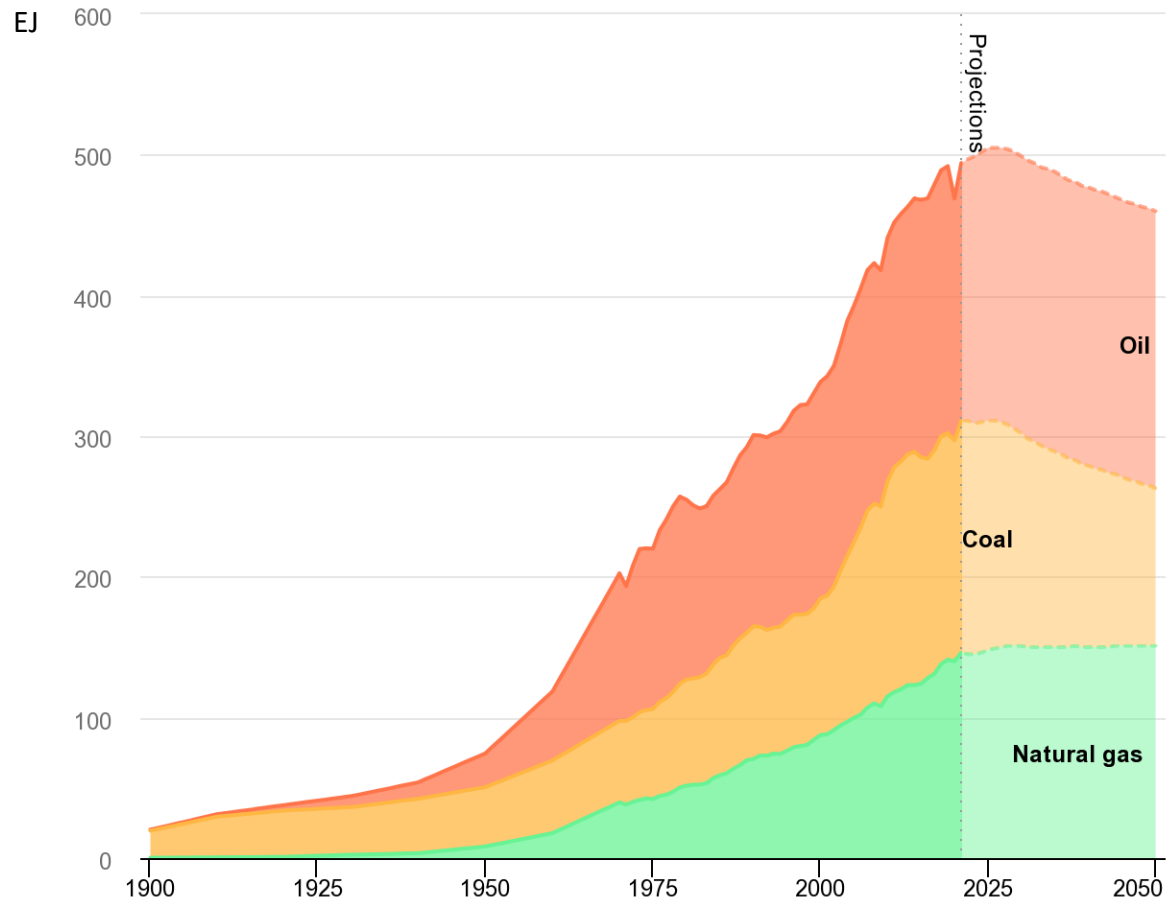

Figure 0-3. IEA, Fossil fuel demand in the Stated Policies Scenario, 1900-2050, IEA, Paris https://www.iea.org/data-and-statistics/charts/fossil-fuel-demand-in-the-stated-policies-scenario-1900-2050, IEA. Licence: CC BY 4.0

Now, more than ever, the transition towards a more sustainable energy system is imperative. Worldwide strategies have led policy makers to invest in the development of technologies based on renewable energy sources (RES).

The International Energy Agency (IEA) highlights the need for electrification and decarbonisation in the published report “Global Energy and Climate Model” (4). This report shows as well the importance of increasing the share of RES in the energy production and improving energy efficiency in both energy production and final consumption. Figure 0-4 displays the predicted share of electricity generation from various sources, indicating a significant increase in the RES share between 2021 and 2030 (4). For comparison, the actual share of the different energy sources are also shown.

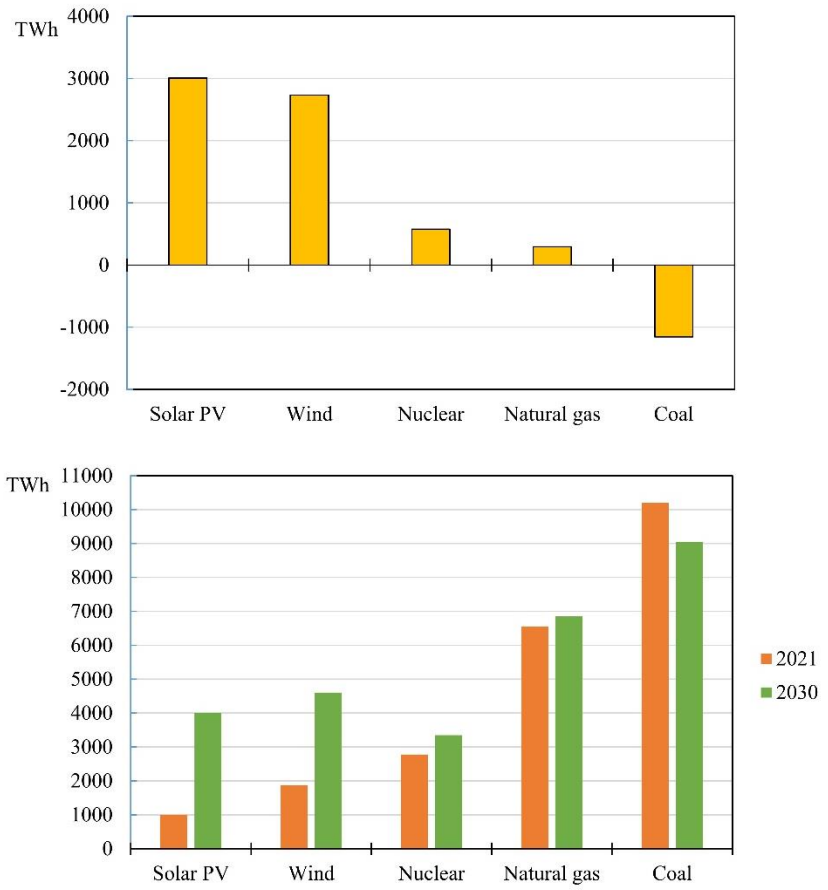

Figure 0-4. IEA, Change in electricity generation in the Stated Policies Scenario between 2021 and 2030, IEA, Paris https://www.iea.org/data-and-statistics/charts/change-in-electricity-generation-in-the-stated-policies-scenario-between-2021-and-2030, IEA. Licence: CC BY 4.0

Large-scale deployment and implementation of RES such as hydro, solar, wind, tidal, geothermal and biomass can help to limit GHG emissions in accordance with the aforementioned targets. Nevertheless, the intermittent nature of solar and wind energy raises some issues related to the mismatch between the energy production and the energy demand. For instance, a backup energy system is needed when RES production alone cannot meet the energy demand. Additionally, curtailment of excess RES power can occur when RES production is higher than the energy demand. Therefore, the development of energy conversion technologies aims to optimize the energy system while maintaining grid stability.

Among several alternatives, one possible solution is to convert electrical energy to chemical energy in the form of hydrogen. Hydrogen is an energy vector that possesses the highest specific energy (i.e. 120 MJ/kg) among all fuels. Various methods are used to obtain hydrogen, including steam-methane reforming, electrolysis, pyrolysis, thermolysis, as well as photoelectrochemical, thermochemical and photobiological water splitting. Depending on the primary energy source and on the production process, the hydrogen may have a different carbon footprint (or carbon intensity). For a better definition of the hydrogen origins, various classification have been established. The most common is a colour-based classification (5). In order to solve some ambiguities on the colour-based classification, new categories have been defined ranging from fossil-based, low-carbon to clean or renewable hydrogen (6, 7). The latter is obtained by the electrolysis of water using the electricity from RES. Electrolysis and fuel cell technologies enable the production and consumption of hydrogen and electricity without CO_2 emissions. Hydrogen and electricity energy carrier have the potential to be used in a circular

economy across all sectors, including energy, transport, and industry. Indeed, it is possible to store the surplus electrical energy coming from RES in the form of chemical energy as hydrogen by power-to-gas (P2G) processes using electrolysers (8, 9). Hydrogen can be then stored (in gaseous phase, liquid phase, or solid-matrices) and, finally, used for different purposes to enable the decarbonisation of industrial processes, such as the production of chemicals, synthetic fuels, concrete and steel. Alternatively, it can be converted again to electricity by gas-to-power (G2P) processes using fuel cells (9, 10). Figure 0-5 displays a scheme of the P2G and G2P concepts. Finally, the combination of P2G, storage and G2P constitutes the power-to-power (P2P) concept to decarbonize and electrify isolated micro-grids or remote off-grid areas to be self-sufficient.

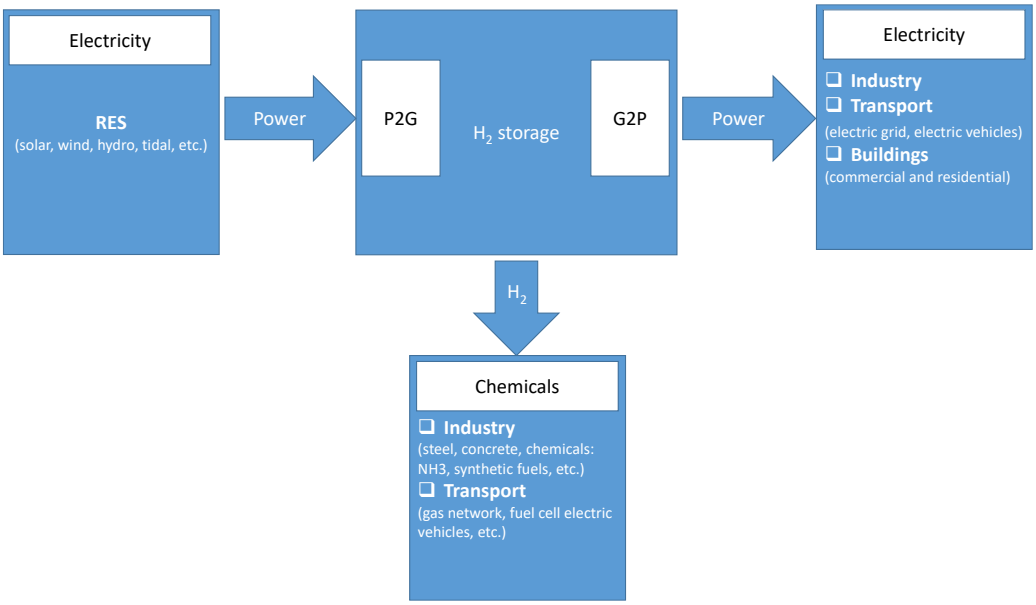

Figure 0-5. Scheme of P2G and G2P concepts

In this context of energy transition, the development and industrialisation of electrolysers and fuel cells are essential to achieve their deployment for the large-scale production of hydrogen and to ensure their continuous operation over 5 years. Several types of electrolyser and fuel cell technologies have been developed, differing mainly in terms of operating conditions and electrolyte materials. In terms of operating conditions, they are divided into low temperature (LT), intermediate temperature (IT) and high temperature (HT). According to the electrolyte material, they are distinguished as alkaline cells, proton exchange membrane (PEM) cells, phosphoric acid cells, proton conducting cells, molten carbonate cells, and solid oxide cells (SOCs).

Among them, SOCs are promising P2G and G2P electrochemical conversion devices working at high temperature in the range of 700-850 °C. Such high operating temperatures allow achieving very high efficiency due to favourable thermodynamics (reduced electrical energy demand and heat supply) and kinetics (accelerated electrochemical reaction). Furthermore, the same SOC can be operated reversibly in electrolysis (SOEC) mode and fuel cell (SOFC) mode using the same catalyst. Compared to LT technologies, SOCs exhibit higher tolerance to carbon monoxide and fuel impurities, as well as hydrocarbon fuels flexibility that avoids the need for an external fuel reformer (11). The electro-catalytic reaction is favoured at high temperatures, so that less expensive catalyst (e.g. Ni) can be employed, as compared to LT devices (e.g. Pt for PEM cells). In addition, they can be used in hybrid energy systems, where the high-quality

heat from the HT SOC system is recovered and used to drive other processes. For example, SOCs can work in combined heat and power (CHP) systems. These multiple advantages are currently valuable in the transition to a fossil-free sustainable energy market, particularly in business cases where waste heat can be used to power the electrolyser.

Extensive research and development has enabled the technology to progress to current demonstration systems at the MW scale. Nevertheless, the lifetime of SOCs remains insufficient for their large-scale commercialization (12). The degradation phenomena occurring in SOCs are activated during operation at high temperature and high polarization. Microstructural evolution, chemical decomposition, active site poisoning, inter-diffusion and reactivity between the different active layers are observed in the cell. Such phenomena have an impact on the materials electro-catalytic activity and on the ionic and electronic conductivities, which cause a deterioration of the cell performance. Further, moving to the stack level, diffusion of elements occurs from the interconnect to the cell and, moving to the system level, the balance of plant operation is currently an issue (13, 14). Thus, it is essential to advance the understanding of the degradation processes at the cell level, which is the core of the electrochemical system, in order to enhance the performance and durability of the cell, as well as to meet the EU commission targets (see Table 0-1). Table 0-1 shows that the current degradation rate in SOEC mode is significantly higher than in SOFC mode. Therefore, special efforts must be made to extend the lifetime of the high temperature electrolyser. The targeted lifetime for both SOFC and SOEC systems are 80’000 – 90’000 hours (15–17).

Table 0-1. SoA and targets of the EU commission for SOFC and SOEC stacks degradation (18).

	2020 SoA	2024 targets	2030 targets
SOFC	0.6 %·kh^{-1}	0.2 %·kh^{-1}	0.2 %·kh^{-1}
SOEC	1.9 %·kh^{-1}, -0.6 A·cm^{-2}	1.0 %·kh^{-1}, -0.85 A·cm^{-2}	0.5 %·kh^{-1}, -1.5 A·cm^{-2}

In this frame, the Ph.D. thesis aims to deepen the knowledge on the SOC degradation phenomena, with a focus on the SOEC mode, whilst also encompassing the SOFC mode. For this purpose, a multimodal approach based on long-term tests along with electrochemical characterizations, post-test imaging and modelling has been applied. This methodology allows information to be obtained at different length scales, ranging from the macro-scale down to the atomic-scale. The evolution of the electrochemical response over time provides information about the cell performance degradation in relevant operating conditions, as well as the experimental degradation rate. Advanced post-test characterizations with large field of view and high-spatial resolution have been used to investigate the degradation processes occurring in the cell materials after ageing. The comparison between the non-operated reference cell and the operated cells will highlight the detrimental processes under different ageing conditions. Finally, the modelling will be used to analyse the processes involved in the cell operation at different length scales. The model will be used to interpret the electrochemical response of the cell and to investigate the impact of operating conditions on the electrodes reaction mechanisms and cell performance degradation.

2.Main objectives of the thesis

The thesis aims to attain a comprehensive understanding of the SOC degradation in both SOEC and SOFC operating mode, with particular emphasis on the former. The main objectives of the thesis are set as follows:

1) Quantitative characterizations of the electrochemical response of the cell before and after ageing in SOEC and SOFC operating modes, in terms of polarization curves and electrochemical impedance spectra (EIS). The electrochemical characterizations are carried out in reference conditions, before and after the operation, to potentially compare the performance degradation as a function of the different operating conditions.
2) Assessment of the degradation phenomena after operation using several post-test characterization techniques performed in the various layers of the cell. Particular attention is given to the understanding of the long-term degradation phenomena in the oxygen electrode, for which high spatial resolution is required. Chemical, structural and microstructural information will be collected using laboratory- and synchrotron-based techniques.
3) Interpretation of the electrochemical response using a multiscale physics-based model available at the laboratory. The model will be adapted to the studied cell and extended to the simulation of the impedance spectra at the cell level. Thereafter, the model will be used to simulate the cell response in terms of i-V curves and EIS, as well as to identify the different contributions in the EIS diagrams, in terms of rate determining steps (RDSs) in the reaction mechanism. The purpose is to assess the evolution of the different contributions in the EIS after ageing, as well as to identify the most critical component for the cell degradation from the model interpretation of the complete cell experimental EIS.

3.Manuscript Layout

Based on the above objectives, this thesis is organized in six chapters as follows: The first chapter is dedicated to the technology fundamentals and the state of the art on the degradation phenomena. The second chapter is related to the materials and methods used in the work. The third chapter is devoted to the multiscale physics-based model used to simulate the stationary and dynamic response of the cell. The fourth chapter comprises the study of the cell degradation under dry air in SOEC mode, with a focus on the impact of the operating temperature on the cell layers degradation. The fifth chapter is dedicated to the study of the impact of humid air and operating mode on the cell degradation. The sixth chapter is devoted to the general discussion, main conclusions and perspectives.

References

1. IPCC, (2023) https://www.ipcc.ch/report/ar6/syr/.
2. IPCC, (2018) https://www.ipcc.ch/sr15/.
3. Climate Action Tracker, (2022) https://climateactiontracker.org/global/temperatures/.
4. IEA, (2022).
5. NanoScent Labs, *NanoScent Labs* (2023) https://www.nanoscentlabs.com/post/guide-to-the-types-of-hydrogen-colors.
6. E. Gregor, (2023) https://policycommons.net/artifacts/3531696/eu-rules-for-renewable-hydrogen/4332709/.
7. R. Savickas, *Copenhagen Centre on Energy Efficiency* (2023) https://c2e2.unepccc.org/kms_object/how-green-is-green-hydrogen-the-differences-between-green-low-carbon-and-renewable-hydrogen-webinar-27-04-2023/.
8. M. Sterner and M. Specht, *Energies*, **14**, 6594 (2021).
9. N. Cihangir Martin, F. Van Lith, and A. van der Molen, in *27th International Conference on Electricity Distribution (CIRED 2023)*, vol. 2023, p. 2150–2154 (2023) https://ieeexplore.ieee.org/abstract/document/10267251.
10. M. Patel, S. Kim, T. T. Nguyen, J. Kim, and C.-P. Wong, *Nano Energy*, **90**, 106496 (2021).
11. R. Mark Ormerod, *Chemical Society Reviews*, **32**, 17–28 (2003).
12. G. Chasta, Himanshu, and M. S. Dhaka, *International Journal of Energy Research*, **46**, 14627–14658 (2022).
13. M. J. Reddy, J.-E. Svensson, and J. Froitzheim, *Corrosion Science*, **190**, 109671 (2021).
14. L. Zhou, Z. Zeng, M. P. Brady, D. N. Leonard, H. M. Meyer, Y. Yamamoto, W. Li, G. Collins, and X. Liu, *International Journal of Hydrogen Energy*, **46**, 21619–21633 (2021).
15. A. Hagen, in *Fuel Cells : Data, Facts and Figures*,, p. 304–320, John Wiley & Sons, Ltd (2016) https://onlinelibrary.wiley.com/doi/abs/10.1002/9783527693924.ch31.
16. Department of Energy, *Energy.gov* (2023) https://www.energy.gov/eere/fuelcells/technical-targets-high-temperature-electrolysis.
17. D. Vladikova, B. Burdin, A. Sheikh, P. Piccardo, M. Krapchanska, D. Montinaro, and R. Spotorno, *Energies*, **15**, 3287 (2022).
18. European Commision, (2022) https://www.clean-hydrogen.europa.eu/knowledge-management/strategy-map-and-key-performance-indicators/clean-hydrogen-ju-sria-key-performance-indicators-kpis_en.

1. State of the art on solid oxide cell (SOC) technology

This chapter is devoted to define the state of the art of the technology and the related degradation phenomena. Based on this bibliographic review, the research lines of the thesis are derived, along with the main objectives and methodology to address the remaining questions related to the degradation of hydrogen electrode supported SOCs, with a particular focus on the oxygen electrode degradation.

1.1 Basics of SOCs

The solid oxide cells (SOCs) are high temperature electrochemical energy-conversion devices, which are considered as a promising solution in the transition towards a more sustainable energy system. The cell is typically made of a dense ceramic electrolyte sandwiched between two porous electrodes. The reason behind the operation at high temperature is the employment of ceramic materials for the electrolyte, which are ionic conductors at high temperatures (e.g. 650-900 °C for the YSZ). High temperature operation provides the following beneficial features: (i) high efficiency, (ii) promoted reversibility that enables operating in both SOEC and SOFC modes with the same cell, (iii) fuel flexibility thanks to the enhanced tolerance to hydrocarbons (iv) inexpensive catalyst, (v) possibility to recover high quality heat in cogeneration mode that can be used to drive other processes in a hybridized energy system. Figure 1-1 displays the scheme of the operation of a SOC in both SOEC and SOFC modes, considering the most standard reactants/products (i.e. hydrogen, oxygen and steam) for the main reactions occurring at the two electrodes.

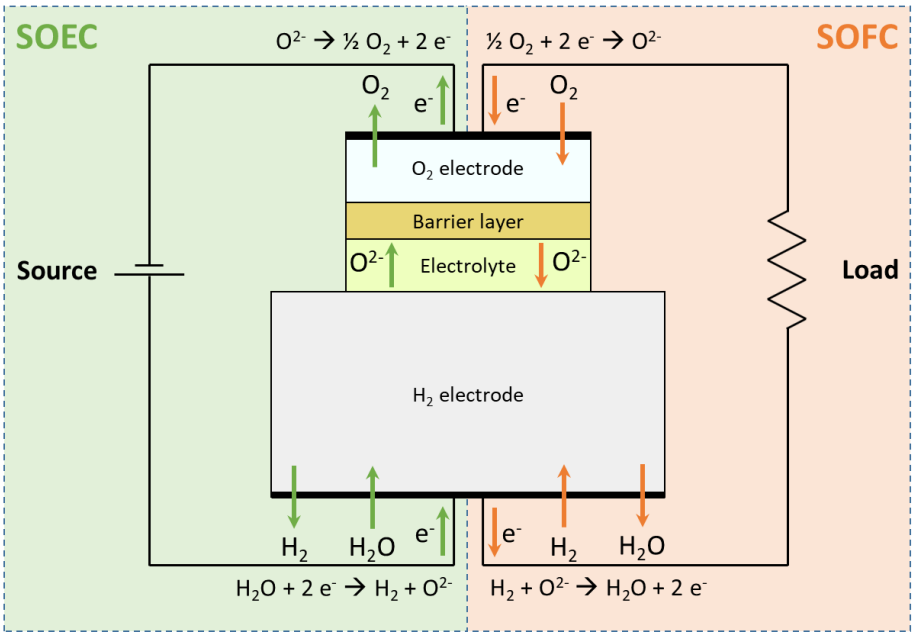

Figure 1-1. Scheme of a single solid oxide cell in both fuel cell and electrolysis operation for a fuel electrode supported cell

The transfer of oxygen ions from one electrode to the other occur in the ceramic electrolyte. The hydrogen oxidation (in SOFC) and steam reduction (in SOEC) reactions occurs in the hydrogen electrode, while the oxygen consumption (in SOFC) and formation (in SOEC) occur at the oxygen electrode according to the following equations:

$$H_2(g) + O_o^x(YSZ) \underset{SOEC}{\overset{SOFC}{\rightleftarrows}} H_2O(g) + V_o^{\bullet\bullet}(YSZ) + 2e^- \quad [1]$$

$$\frac{1}{2}O_2(g) + V_o^{\bullet\bullet}(YSZ) + 2e^- \underset{SOEC}{\overset{SOFC}{\rightleftarrows}} O_o^x(YSZ) \quad [2]$$

Where e^-, $V_o^{\bullet\bullet}$ and O_o^x represent the electron, the oxygen vacancy and the oxygen in the lattice of YSZ, respectively. $H_2(g)$, $O_2(g)$ and $H_2O(g)$ are the hydrogen, oxygen and water molecules in the gas phase, respectively.

1.2 Designs and architectures

The SOC designs that can be found in terms of geometry are planar, tubular, monolithic and segmented-cell-in-series (1–3). The planar and the tubular (4, 5) designs are the most common configurations employed today (see Figure 1-2). The tubular geometry presents high mechanical robustness and simple sealing process whereas the performance are lower due to the high ohmic losses (4, 6, 7). On the other hand, the planar configuration offers better performance and it has the advantages of simple fabrication process, lower ohmic losses at low temperature operation (i.e. 500-800 °C). However, the complexity lies in the sealing of the cells to achieve appropriate gas tightness (4, 5, 8).

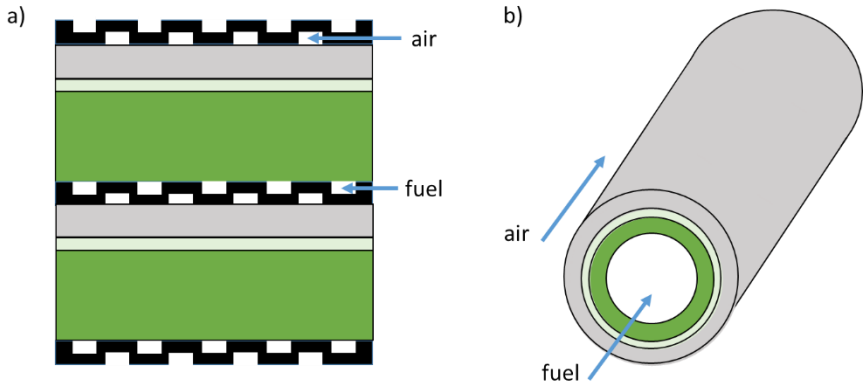

Figure 1-2. Scheme of a) planar and b) tubular designs.

For the planar configuration, the cells are connected in series using metallic interconnects to increase the power capacity and they are further sealed to prevent gas leakages. The metallic interconnect has multiple functions: it enables distributing the gases to the electrodes in different flow configurations (co-flow, counter-flow, cross-flow), it carries the sealing, and it connects the cell current collecting layers (at the top of the electrodes) to the external electric circuit. The assembly of the cell and interconnects is called the single repeating unit (SRU). The scale up to high power capacities is achieved with the planar design cells, by connecting several SRU (few W) in series to form a stack (up to tenth of kW). Then, a set of multiple stacks connected together defines a SOC module (hundred kW range). At this stage, a balance of plant (BoP) is necessary to handle the flow of gases and the current flow. Finally, a set of modules, together with the BoP, constitutes the MW system. Some MW-scale SOC systems under construction or planned are reported in (9–13).

Figure 1-3. Schematic of the current world's largest SOEC system within the MultiPLHY hydrogen project by Sunfire (14).

For planar cells, the mechanical robustness is ensured by a supporting layer. The cell can be self-supported when the support layer is one of the two electrodes or the electrolyte, or external supported (interconnect/metal support, porous substrate), as depicted in Figure 1-4. According to the type of supporting layer, SOCs can be divided into various architectures: electrode supported cells (i.e. cathode or anode supported cells), electrolyte supported cells (ESC), interconnect/metal supported cells, and porous substrate supported cells (1, 15, 16). The main drawback of the electrode supported cell architecture is the difficulty for the reactants to reach the active sites due to the longer path through the thicker electrode. On the other hand, the thin electrolyte results in lower ohmic losses. ESC benefits from easier sealing at the cell periphery

(17), while its performance are lower due to the higher ohmic losses related to the ionic transport through the electrolyte depending on its thickness. To overcome this drawback, the ESC are commonly operated at higher temperature compared to the electrode supported cell (18). Nevertheless, the ESC architecture is under development to improve performance and durability. A 30'000 hours test was proven for ESC in electrolysis mode (19). Moving to the external supported cells, their support layer is a metallic porous substrate or the interconnect (1), rather than a brittle ceramic material as for the self-supported cells. The support layer material (e.g. ferritic stainless steel) possesses high mechanical robustness, improved thermal and electrical conduction, as well as a good thermal compatibility with the other cell materials in terms of thermal expansion coefficient (TEC), which lowers the thermal stresses (15, 20). Today, the most conventional architectures are the hydrogen electrode and the electrolyte supported configurations.

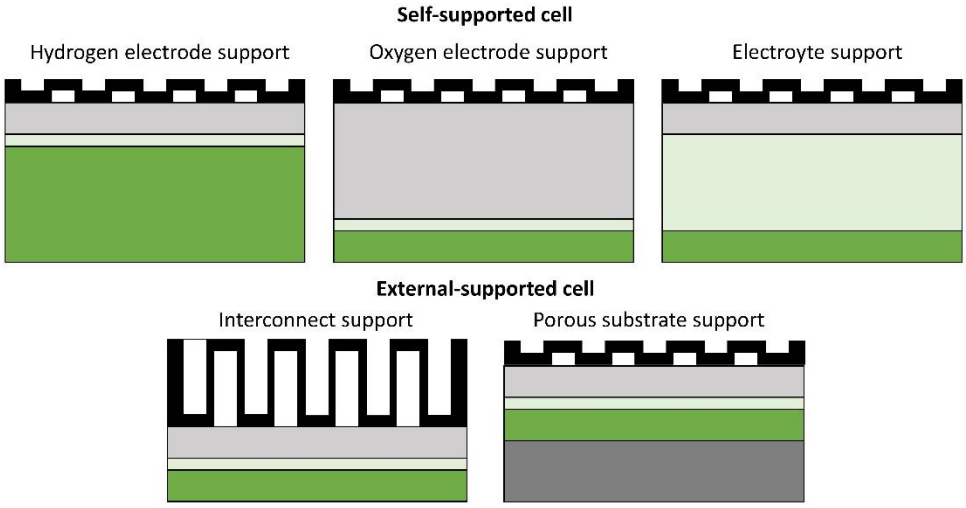

Figure 1-4. Schematics of planar cell architectures (1).

1.3 Cell materials and requirements

The material selection is driven by several requirements: (i) chemical stability in reducing/oxidizing environment, (ii) compatibility with the other layers materials in terms of thermal expansion coefficients (TEC) and chemical reactivity, (iii) good mechanical properties, (iv) high electro-catalytic activity for the electrodes, and (v) high ionic conductivity while near zero electronic conductivity for the electrolyte. Additionally, one should pay attention to the sustainability of the selected materials, including their cost and environmental impact.

1.3.1 Electrolyte

The dense electrolyte is typically made of fluorite-type ceramic materials stabilized in the cubic crystalline structure by doping/substitution of di- or tri-valent cations (21) to promote the formation of oxygen vacancies and, consequently, to increase the ionic conductivity of the material. The selection of the electrolyte is done on the basis of the targeted operating temperature, mechanical-chemical-thermal behaviour and compatibility with the cell materials. The most classical electrolyte material used for hydrogen electrode supported cells is the 8

mol.% yttria stabilized zirconia (8YSZ). This ceramic material possesses high ionic conductivity in the temperature range of 700-900 °C, e.g. 0.054 $S \cdot cm^{-1}$ at 800 °C (22, 23), and good mechanical properties. A lower yttria doping (e.g. 3YSZ) improves its mechanical properties and decreases its ionic conductivity, i.e. from 0.044 $S \cdot cm^{-1}$ in 8YSZ to 0.018 $S \cdot cm^{-1}$ 3YSZ at 800 °C (24–26). Other materials have been studied in order to decrease the operating temperature down to 500°C, such as Gd-doped ceria (GDC), scandia stabilized zirconia (ScSZ), lanthanum strontium gallate magnesite (LSGM), because of their higher ionic conductivity at lower temperatures compared to YSZ (27–30).

1.3.2 Oxygen electrode

The oxygen electrode is commonly made of perovskite oxide materials, with the typical structure ABO_3. In the past, the lanthanum strontium manganite (LSM) was used as one of the most common oxygen electrode material in SOCs due to its good compatibility in terms of chemical and thermal properties with common electrolytes. However, LSM is mostly an electronic conductor with low ionic conductivity causing the electrochemical reaction zone to be limited at the interface with the electrolyte (the only ionic conducting phase). Indeed, the reaction can only occurs at the so-called three-phase boundary (TPB) lines where the gas-electrolyte–electrode phases meet (31). In addition, LSM suffers from a delamination leading to the detachment of the electrode from the electrolyte especially observed in electrolysis mode (32). Thus, nowadays the oxygen electrode is typically made of a mixed ionic electronic conductor (MIEC) materials, which allow extending the electrochemical reaction to the whole gas-electrode contact surface (see Figure 1-5). The most commonly employed MIEC oxygen electrodes are made of under stoichiometric oxygen material such as $La_{1-x}Sr_xCo_yFe_{1-y}O_{3-\delta}$ (LSCF), $La_{1-x}Sr_xFeO_{3-\delta}$ (LSF) or $La_{1-x}Sr_xCoO_{3-\delta}$ (LSC) (33). Considering the LSCF, the A-site and B-site of the ABO_3 perovskite are composed by $(La_{1-x}Sr_x)$ and (Co_yFe_{1-y}), respectively. In general, such perovskite materials can have a cubic or a rhombohedral phase. For example, $La_{1-x}Sr_xCoO_{3-\delta}$ crystalline structure can vary from cubic ($0 < x < 0.5$, at room temperature) to rhombohedral ($0.55 < x < 0.7$, at room temperature) depending on the Sr content (34, 35). LSCF typically shows phase transition between cubic and rhombohedral phases, and it is also defined as a pseudo-cubic structure when the difference is not evident (36). In addition to cubic and rhombohedral structures, orthorhombic structure was found at room temperature (37), also depending on the Co/Fe ratio (38). An additional improvement in terms of performance was achieved with the use of the LSCF-GDC composite (33, 39). Despite the improved performance compared to the LSM, LSCF-based oxygen electrode materials are prone to decompose during operation (40–44). More recently, nanostructured materials and high entropy oxides are under investigations because of their enhanced performance and stability (45, 46). For the oxygen electrode material selection, it should be considered that cobalt-based materials are critical for several reasons, such as mining, scarcity, uneven distribution, high price, etc. (47–49). In addition, Co-based perovskites have a low thermal compatibility with other layers materials due to their high thermal expansion coefficient (TEC) (i.e. 16.3 LSCF vs 11.9 for GDC and 10.8 for 8YSZ) (50, 51). Much more attention should be paid on this aspect and move towards cobalt-free materials.

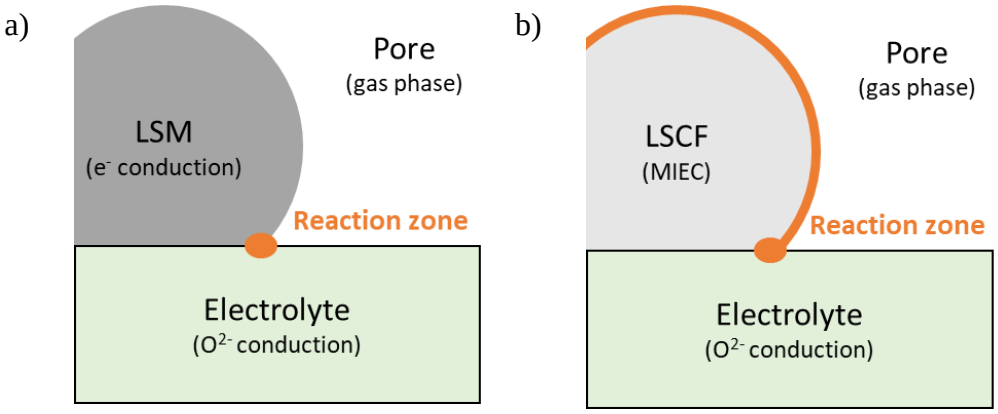

Figure 1-5. Schematics of the reaction zone in a) LSM and b) LSCF materials.

1.3.3 Hydrogen electrode

The porous hydrogen electrode is commonly made of Ni-YSZ cermet material, where Ni is the electronic conducting phase and the catalyst and the YSZ is the ionic conducting phase (52). As for the oxygen electrode, the presence of both electronic and ionic conducting phases in the cermet allows extending the active zone in terms of TPB. In the following section, it will be explained in more details that this material serves as functional and support layers for the cell. In this case, two different layers with different microstructures and compositions are considered for the hydrogen electrode: a thin (around tenths of µm) active functional layer near the electrolyte and a thick support layer (around hundreds of µm) near the interconnector. The active layer has a finer microstructure and it is usually made of a Ni-8YSZ cermet material that possesses a higher ionic conductivity. The support layer has a coarser microstructure and it is made of a Ni-3YSZ cermet that has improved mechanical robustness (25). Other materials are continuously being studied to achieve an improved microstructural stability during operation, such as Ni-GDC, perovskite materials, etc. (53–56).

1.3.4 Barrier layer

In order to limit the LSC or LSCF reactivity with the YSZ and the consequent formation of secondary phases as observed by many authors (57–60), a barrier layer made of $Gd_xCe_{1-x}O_{2-\delta}$ (GDC) is added between the oxygen electrode and the electrolyte. The method selected for the preparation of the GDC layer has been shown to be a key factor in preventing the reactivity of the oxygen electrode with the electrolyte. Typically, 10-20% Gd-doping is employed to prepare a porous GDC layer with standard screen-printing method, or dense GDC layer with physical vapour deposition (PVD) and pulsed laser deposition (PLD) methods (61–66). The comparison of the different methods shows that an improved performance and phase stability without reactivity is possible with a dense GDC layer (61, 62, 66–68). This can be explained by the fact that Sr preferentially diffuses through the pores in the gas phase as $Sr(OH)_2$ to react with cations from the electrolyte (69, 70). A dense GDC layer can also prevent or limit the elemental inter-

diffusion and reactivity at the GDC/YSZ interface during manufacturing (64, 65). Accordingly, the formation of secondary phases at the SDC/YSZ interface can be completely eliminated by employing a dense and pore-free SDC interlayer to block gas species diffusion (70).

1.4 Modelling of SOCs

The modelling is generally recognised as an effective tool to unravel the complex set of processes occurring in real systems. As depicted in Figure 1-6, there are several categories of models, which can be subdivided as follows (71–73): phenomenological, semi-empirical or empirical, physics-based or statistics-based; zero to three dimensional; stationary (steady-state) or dynamic (transient state); atomic- to macro-scale, up to the system-level.

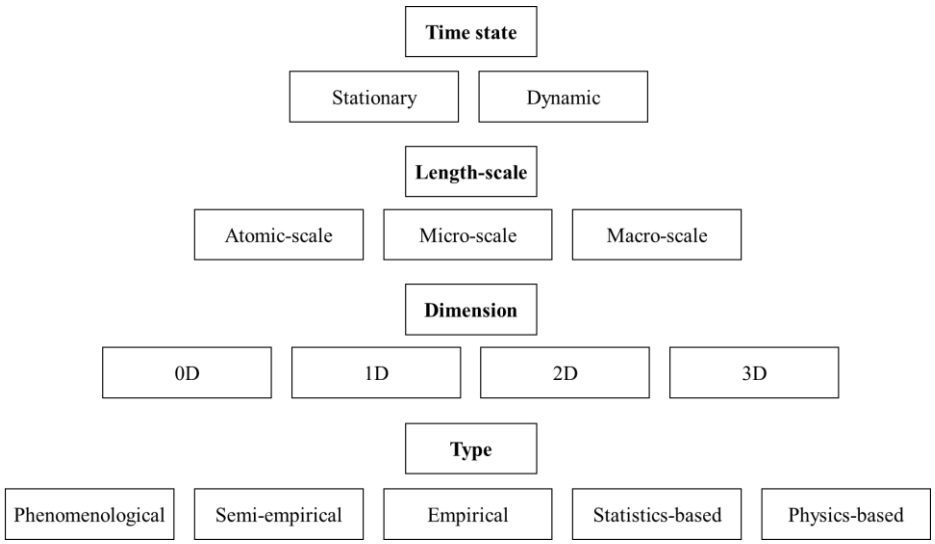

Figure 1-6. General model categories (71).

Modelling is generally used to simulate the real response of the cell according to various parameters. The modelling of SOCs provides guidelines in terms of cell design and materials selection (74), as well as materials optimization (75–77). Additionally, modelling is used to assess the optimal operating conditions (78), as well as to investigate the factors that play a role on the cell performance (79) and cell durability (80–82).In order to consider the phenomena occurring in the cell at different length scales, multiscale modelling is required. In the next sections, a brief summary of the state of the art on the various modelling methods for SOCs is reported for the different length scales. Additionally, the multiscale physics-based model used in this thesis is briefly described.

1.4.1 Atomic-scale modelling methods

The most employed methods at the atomic scale are the density functional theory (DFT) (83, 84) and molecular dynamics (85). Kinetic Monte Carlo (KMC)-based codes can be used to link atomic-scale models to the meso- or macro-scale models (86). For instance, DFT atomic-scale models can be coupled with electrode level kinetic model (87).

1.4.2 Meso-scale modelling methods

At the meso-scale, the elementary steps in the reaction mechanism can be described using elementary kinetics approaches (88). Additionally, the 3D microstructure and morphology of the electrodes can be modelled at this length scale, using discrete element methods (89) or stochastic-based models (90).

1.4.3 Macro-scale modelling methods

Approaching the macro-scale modelling, the model usually considers the mass, momentum, energy conservation equations, as well as charge transfer, chemical and electrochemical reactions (91–93). The most commonly employed methods are the computational fluid dynamics (CFD) models are used to solve the Navier-Stokes equations (94–97) with finite volume (FVM) or finite element (FEM) discretisation methods (98–101). The continuum approach is also extensively used to treat the heterogeneous material as a continuum mean with homogenized microstructural and physical properties (102–104). Finally, the response of the complete system, along with the BoP, can be modelled with process simulation methods (105).

1.4.4 Multiscale physics-based model

Despite the extensive literature devoted to modelling, there is still a lack of fundamental understanding of the governing degradation mechanisms in the cell components. The identification of the rate determining steps (RDSs) in the reaction pathway has not yet been extensively addressed with a physics-based impedance model at the cell level, which considers an elementary description of the reaction mechanisms at the two electrodes. Indeed, the simulation of the dynamic electrochemical response and the identification of the contributions in the EIS at the complete cell level have to be studied in the detail. Only few works considered elementary steps in physics-based model to simulate the impedance spectra at the cell level (106, 107). Despite the proved effectiveness of the physics-based approach, there are still uncertainties on the contributions identifications and further investigations are required. Finally, the governing degradation mechanisms have not been clearly understood yet.

The multiscale physics-based model available in the research group takes into account (i) atomic scale DFT simulations, (ii) a 3D representation of the electrodes microstructure (76), (iii) a description of the reaction mechanisms in full elementary steps for the two electrodes (108, 109), as well as (iv) the SOC geometry together and the gas flow configuration at the cell level (110, 111) (see Figure 1-7).

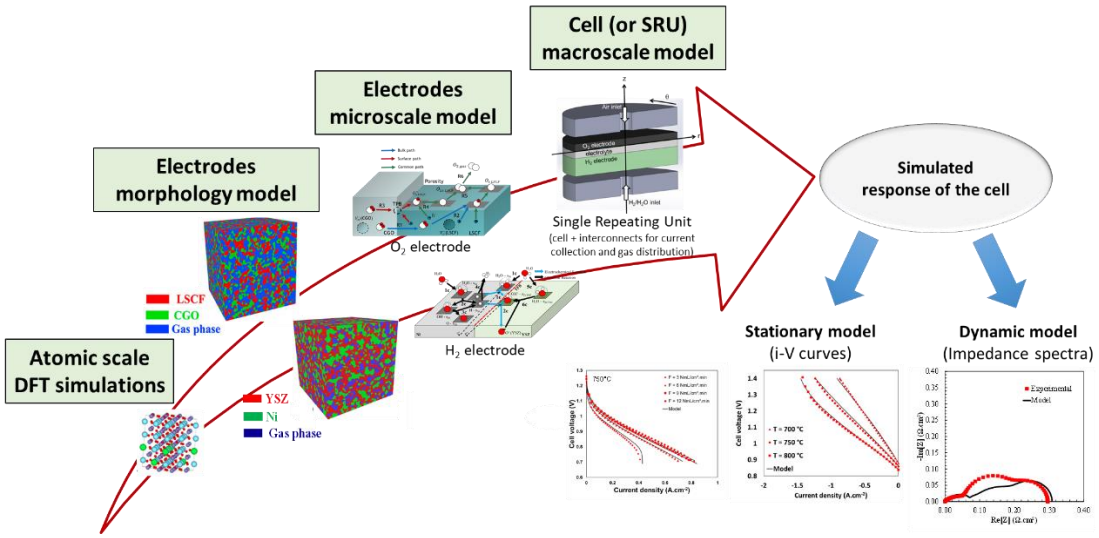

Figure 1-7. Scheme of the multiscale physics-based model available in the research laboratory.

The electrode morphology model is a mathematical model used to compute the synthetic microstructure of the electrodes, which are the digital twins of the real microstructure (76). Hence, it has the potential to reproduce the electrode microstructures and it can be used to retrieve the microstructural properties. As an alternative to the electrode morphology model, 3D FIB-SEM reconstructions of the electrodes can be used. After image segmentation post treatments, it is possible to retrieve the microstructural properties related to the two electrodes.

The electrode-level microscale model is an electrochemical kinetic model that considers the microstructural properties from the synthetic microstructure (or 3D reconstructions) and the most important processes. The electrode activation overpotential is computed from this microscale model. The reaction mechanism is described in elementary steps for the two electrodes. The mass and charge transport conservation equations for charged and non-charged species are solved at the steady state and in the time domain, considering the transient terms in a non-linear system of partial differential equations (PDEs). Thus, stationary and dynamic simulations can be performed. Indeed, the electrodes microscale models were used in previous works to predict the stationary and dynamic response of the oxygen electrode (108) and the hydrogen electrode (109).

The cell level macroscale model is a physics-based 2D model able to evaluate the local parameters (e.g. partial pressure, current density, activation overpotentials, etc.) along the cell radius and, thus, it considers the design of the studied system along with the cell geometry, the flow configuration and the gas distribution (58, 112). The functional layers are described in the microscale model and introduced as electrode/electrolyte interface in this macroscale model. All the kinetics and the electrochemistry are computed with the Butler-Volmer equation for the activation overpotentials (111, 113), considering the apparent exchange current densities calculated all along the cell length from the microscale model. The parameters used to calculate the exchange current densities are extracted under the condition that the cell local activation overpotential in the macroscale model matches the electrode overpotential in the microscale model. Finally, the partial pressures at the electrode/electrolyte interface resulting from the cell level model are used as boundary condition in the microscale model. The gas transport is modelled using the dusty gas model, considering both molecular diffusion and Knudsen diffusion in the pores of the electrodes. The microstructural parameters (e.g. volume fraction, tortuosity) from synthetic microstructures (or 3D reconstructions) are included in the calculation of the diffusion coefficients.

In the frame of this thesis, the electrodes morphology was obtained from 3D reconstructions (i.e. 3D FIB-SEM images after segmentation) of the two electrodes, the stationary model was used to reproduce the experimental polarization curves at the cell level, and the dynamic model has been extended to the simulation of the EIS at the cell level.

The multiscale physics-based model will be thoroughly described in the **Chapter III**. The following section describes the basics of the electrochemical modelling based on the Nernst equation and overpotentials.

1.5 Nernst equation and overpotentials

Considering a single complete cell with hydrogen and oxygen as reactants and steam as product, the open circuit voltage (OCV) can be expressed according to the Nernst equation (18), as follows:

$$U_{\mathrm{OCV}} = U^0 + \frac{\mathrm{R}\cdot T}{2\cdot \mathrm{F}} \ln\left(\frac{a_{\mathrm{H_2}}\cdot a_{\mathrm{O_2}}^{0.5}}{a_{\mathrm{H_2O}}}\right) \quad [3]$$

Where U^0 is the voltage of the cell assessed in the standard conditions, R is the universal gas constant (8.314 J·mol^{-1}·K^{-1}), T is the absolute temperature (K), F is the Faraday's constant (96485 C·mol^{-1}), and a_{j} is the chemical activity of the j-th species (i.e. hydrogen, oxygen or steam) evaluated at the electroactive sites under zero current.

When the cell is under polarization, various phenomena occurs causing voltage losses (i.e. overpotentials or overvoltages). The three main types of losses are distinguished as activation, ohmic and concentration overpotentials and they are briefly described in this section.

Close to OCV, the activation overpotential causes a first cell voltage loss at low current densities. This term is derived from the Butler-Volmer equation (114, 115) considering the symmetry factor (or charge transfer coefficient) equal to 0.5 (113, 116–121):

$$\eta_{\mathrm{act}}^{\mathrm{H_2\ electrode}} = \frac{\mathrm{R}\cdot T}{\mathrm{F}} \sinh^{-1}\left(\frac{i}{2\cdot i_0^{\mathrm{H_2\ electrode}}}\right) \quad [4]$$

$$\eta_{\mathrm{act}}^{\mathrm{O_2\ electrode}} = \frac{\mathrm{R}\cdot T}{\mathrm{F}} \sinh^{-1}\left(\frac{i}{2\cdot i_0^{\mathrm{H_2\ electrode}}}\right) \quad [5]$$

Where i_0 is the exchange current density associated to the given electrode (hydrogen or oxygen electrode).

Approaching the linear region of the i-V curve at higher current densities, the ohmic overpotential prevails. The ohmic losses are caused by the resistance associated to the electrons flow in the electrodes and ions flow across the electrolyte, as well as by the contact resistance in between the electrodes and the current collectors. This ohmic overpotential is expressed considering the term $\mathrm{R_{ohm}}$ as global resistance in the classic Ohm's law as follow:

$$\eta_{\mathrm{ohm}} = \mathrm{R_{ohm}}\cdot i \quad [6]$$

Finally, the concentration overpotential are related to the gas conversion (122) and gas diffusion losses (123) and it becomes predominant at high current density:

$$\eta_{\text{conc}} = \eta_{\text{conv}} + \eta_{\text{diff}} \quad [7]$$

As for the activation overpotential, both conversion and diffusion overpotentials have different expression according to the electrode. The conversion overpotential is a reversible loss related to the change in composition with the current according to the Faraday's law. It is derived from the Nernst equation and expressed as follows (115):

$$\eta_{\text{conv}}^{\text{H}_2\text{ electrode}} = \frac{\text{R} \cdot T}{2 \cdot \text{F}} \ln\left(\frac{a_{\text{H}_2}^{\text{ch},i=0} \cdot a_{\text{H}_2\text{O}}^{\text{ch},i\neq 0}}{a_{\text{H}_2}^{\text{ch},i\neq 0} \cdot a_{\text{H}_2\text{O}}^{\text{ch},i=0}}\right) \quad [8]$$

$$\eta_{\text{conv}}^{\text{O}_2\text{ electrode}} = \frac{\text{R} \cdot T}{4 \cdot \text{F}} \ln\left(\frac{a_{\text{O}_2}^{\text{ch},i\neq 0}}{a_{\text{O}_2}^{\text{ch},i=0}}\right) \quad [9]$$

Where $a_{\text{j}}^{\text{ch},i=0}$ and $a_{\text{j}}^{\text{ch},i\neq 0}$ are the chemical activities of the j-th species evaluated at the gas channel for an imposed current equal or different from zero, respectively. The conversion overpotential is only dependent on the applied current and the gas composition (124). When all the reactants entering the cell are consumed by the reaction, the so-called limiting current density appears. This parameter is strictly linked to the conversion losses. A conversion rate is usually defined as the ratio between the flow of reactants at the inlet and the reactants consumed by the reaction. This parameter is named fuel utilization (FU) when operating in fuel cell mode, while it is referred as steam conversion (SC) when operating in electrolysis mode.

The diffusion losses are due to the difficulty of the gas species to cross the porous and tortuous structure of the electrode and to reach the active sites. This species transport limitation causes a depletion in the reactants needed for the reaction at the active sites, where the reaction occurs. The diffusion overpotential at the two electrodes are described by the following equations [10] and [11] (111):

$$\eta_{\text{diff}}^{\text{H}_2\text{ electrode}} = \frac{\text{R} \cdot T}{2 \cdot \text{F}} \ln\left(\frac{a_{\text{H}_2}^{\text{ch}} \cdot a_{\text{H}_2\text{O}}}{a_{\text{H}_2} \cdot a_{\text{H}_2\text{O}}^{\text{ch}}}\right) \quad [10]$$

$$\eta_{\text{diff}}^{\text{O}_2\text{ electrode}} = \frac{\text{R} \cdot T}{4 \cdot \text{F}} \ln\left(\frac{a_{\text{O}_2}}{a_{\text{O}_2}^{\text{ch}}}\right) \quad [11]$$

Where a_{j}^{ch} and a_{j} are the chemical activities of the j-th species evaluated for an imposed current different from zero at the gas channel and at the active sites, respectively.

Overall, the cell voltage considers all the losses defined previously. The overpotential terms are subtracted in fuel cell mode and summed in electrolysis mode. Accordingly, the cell voltage can be expressed as follows:

$$U_{\text{cell}} = U_{\text{OCV}} \pm \eta_{\text{act}} \pm \eta_{\text{ohm}} \pm \eta_{\text{conc}} \quad [12]$$

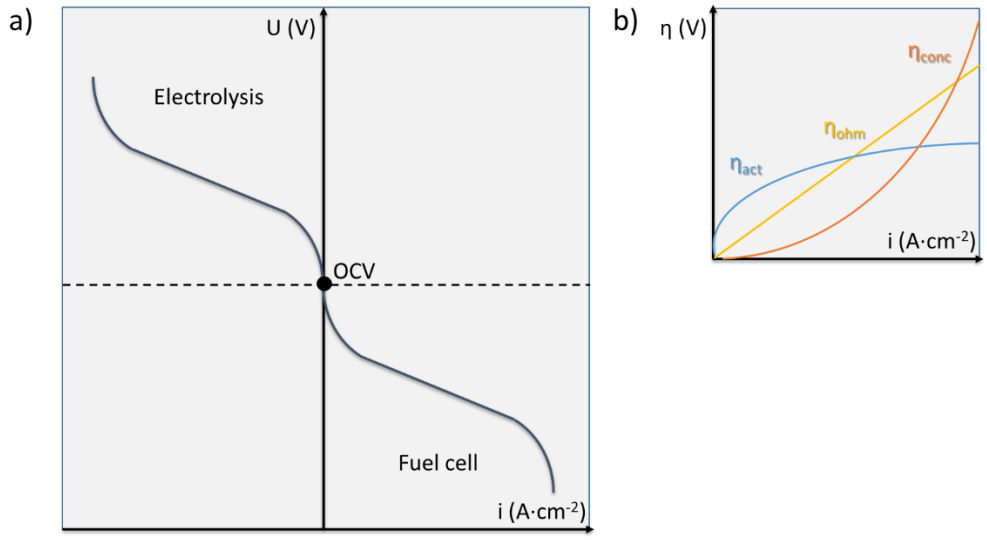

Figure 1-8. Schematics of a) polarization curves for both electrolysis and fuel cell modes and b) overpotentials.

1.6 Cell performance and durability

For industrial applications, the voltage as a function of current and the voltage evolution over time define the performance and the durability of the cell, respectively. In the following sections, the state of the art on the cell performance and durability is presented. The state of the art on the cell performance includes a brief description of the most used electrochemical characterization techniques, namely polarization curves and electrochemical impedance spectroscopy (EIS). The state of the art on the cell durability includes the current status of the targets in terms of degradation rate (DR) and lifetime.

1.6.1 State of the art on cell performance

Typical performance for solid oxide cells depends on operating parameters, including the temperature, current density, gas flow rate and gas composition. They can be defined in terms of cell voltage at given current density, or vice versa, as well as in terms of power density or area specific resistance (ASR). Table 1-1 summarizes the performance of some selected cell. Additional cell performance can be found in the publication of Graves et al. (125) and Udomsilp et al. (126).

Table 1-1. Reported performance for SOCs operated in SOFC and SOEC modes.

SOFC	SOEC
0.75-0.9 V and 1-1.5 Ω·cm^2 at 0.3 A·cm^{-2}, 750 °C, 50/50 %vol. H_2/H_2O (127)	1.1-1.25 V and 3-4 Ω·cm^2 in SOEC mode at -0.3 A·cm^{-2}, 750 °C, 50/50 %vol. H_2/H_2O (127)
0.75-0.85 V and 0.25-0.7 Ω·cm^2 at 0.25 A·cm^{-2}, 800 °C, 63.6/36.4 %vol. H_2/H_2O (128)	1.0-1.1 V and 0.3-0.7 Ω·cm² at -0.25 A·cm^{-2}, 800 °C, 63.6/36.4 %vol. H_2/H_2O (128)
ca. 0.8 V at 1 A·cm^{-2}, 850 °C, 50/50 %vol. H_2/H_2O (129)	ca. 1.2 V at -1 A·cm^{-2}, 850 °C, 50/50 %vol. H_2/H_2O (129)

The SOC performance can be evaluated by performing electrochemical characterizations. Polarization curves and electrochemical impedance spectra are among the most common characterizations to assess the electrochemical response of the cell. In the next sections, general information about these two types of characterizations are briefly presented.

1.6.1.1 Polarization curves

A polarization (or i-V) curve consists of plotting the cell voltage as function of the applied current (see Figure 1-8). The shape of the i-V curve depends on several processes occurring under an imposed DC current, as described in the previous section 1.5. The i-V curves give important information about the electrochemical performance of a cell. The slope of the curve in the linear part, corresponds to the ASR.

1.6.1.2 Electrochemical impedance spectroscopy (EIS)

The electrochemical response of a cell can be assessed with the EIS technique, which consists of applying a sinusoidal perturbation to the studied system and measuring the output signal. Considering the application of an alternating current (AC) as perturbation, the response of the cell can be defined as follows:

$$i(t) = i_{\mathrm{DC}} + i_{\mathrm{AC}} \cdot \sin(2\pi f t)\,, U(t) = U_{\mathrm{DC}} + U_{\mathrm{AC}} \cdot \sin(2\pi f t + \varphi) \qquad [13]$$

Where f is frequency, φ is the phase shift, i_{AC} and U_{AC} are the amplitudes for the AC current and voltage, respectively, and i_{DC} and U_{DC} are the imposed DC current and voltage, respectively. By applying a sufficiently perturbation, the response of the system can be considered within the linear domain, so that the cell impedance can be defined as follows:

$$Z(f) = |Z| \cdot \mathrm{e}^{\mathrm{j}\cdot\varphi(f)} = Z_{\mathrm{Re}}(f) + \mathrm{j} \cdot Z_{\mathrm{Im}}(f) \qquad [14]$$

Where Z_{Re} and Z_{Im} are the real part and the imaginary part of the cell impedance, respectively. The impedance spectrum is usually represented by the so-called Nyquist plot, or by the Bode plot as shown in Figure 1-9.

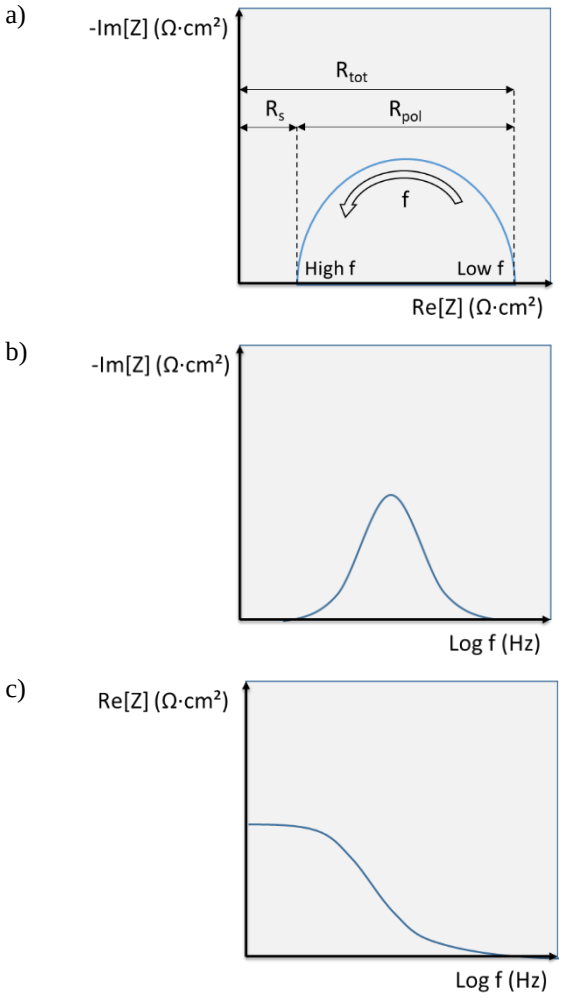

Figure 1-9. a) Nyquist and b) Bode plots for representing the impedance spectrum.

Thanks to the EIS, it is possible to extract important information about the electrochemical performance of the cell, such as the series resistance (R_s), the polarization resistance (R_{pol}) and the total resistance ($R_{tot} = R_s + R_{pol}$). The series resistance corresponds to the intercept of the Nyquist plot with the real axis at high frequencies, and it is related to the cell ohmic resistance (130). The intercept of the Nyquist plot with the real axis at low frequencies is related to the total cell resistance, which corresponds to the ASR. The polarization resistance corresponds to the length of the segment below the impedance arc in between the two intercepts of the Nyquist plot with the real axis (i.e. the difference between R_{tot} and R_s), and it is related to the resistive processes occurring in the electrodes (131). Additionally, the impedance spectra can provide information about the rate determining steps (RDS) in the electrodes, knowing that the various kinetic processes in the reaction mechanism start to appear at different frequency ranges in the EIS, depending on their speed (131).

The impedance spectrum is usually post treated with different techniques to extract the useful information about the electrochemical response of the cell. One possibility is to fit the impedance spectrum with an equivalent electric circuit model (EECM) built with electrical

elements such as electric resistance, inductance, capacitance connected in series or in parallel (132). Another way is to use the distribution of relaxation times (DRT) analysis, which is a statistical approach to deconvolute and identify the contributions in the impedance diagram (133). Finally, physics-based models can be used to account for the kinetic processes in the reaction mechanism to predict the response of the cell and identify the RDS in the EIS diagram (106). In the frame of this thesis, as it will be detailed in **Chapter II**, the raw EIS are first corrected using an EECM and, then, they are analysed by a physics-based multiscale model.

1.6.2 State of the art on cell durability

The durability curves are obtained by performing long-term tests at given operating conditions to observe the evolution over time of the cell electrochemical response in terms of voltage (or current) in galvanostatic (or potentiostatic) mode. Figure 1-10 displays an example of a durability curve for a SOC operated in electrolysis mode under galvanostatic conditions. According to the literature, cell performance degradation (e.g. voltage increase for tests under SOEC mode in galvanostatic mode) slows down over time (134–136) following a non-linear trend (137). Hence, a faster degradation occurs at the beginning of the durability test (Zone I), with a gradual decrease over time (Zone II). The slowdown of degradation rate is probably ascribed to a slower evolution of the material degradation (e.g. Ni coarsening or active site poisoning) (138, 139).

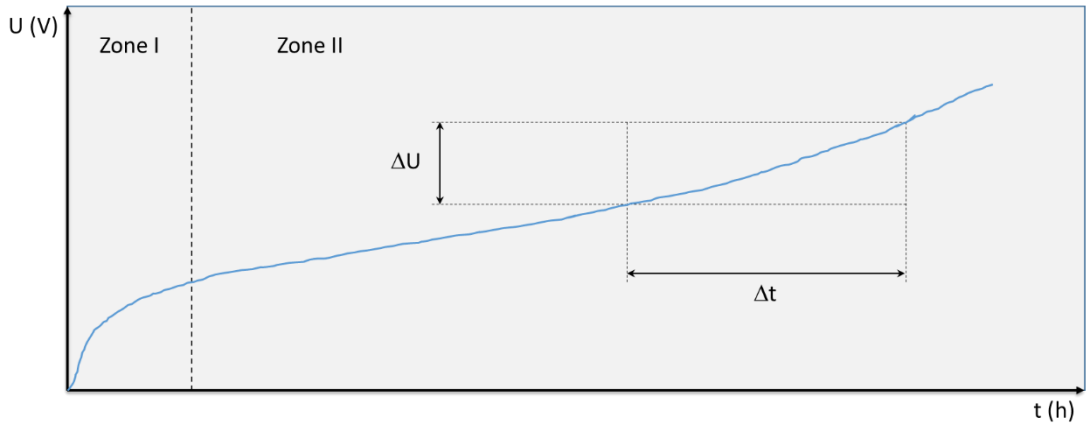

Figure 1-10. Representation of a durability curve under SOEC mode in galvanostatic mode.

From the durability curve, the degradation rate (DR) can be extracted, which provides information about the performance degradation after a given amount of time. The DR is usually expressed in $mV \cdot kh^{-1}$ or $\%\cdot kh^{-1}$ and it is defined as the ratio between the cell voltage evolution over a given time and the initial voltage:

$$DR(t) = \frac{\Delta U(t)}{U(t_0)} \cdot \frac{1}{\Delta t} = \frac{U(t) - U(t_0)}{U(t_0)} \cdot \frac{1}{t - t_0} \quad (\mathrm{mV \cdot kh^{-1}}) \qquad [15]$$

In the literature, hydrogen electrode supported cells show DR values around 2 – 5 $\%\cdot kh^{-1}$ in SOEC mode (140–143) and in the range of 0.5 – 2 $\%\cdot kh^{-1}$ in SOFC mode (144, 145). Currently, the longest durability test has reached more than 100'000 hours (more than 10 years) of operation in SOFC mode at 700 °C, 0.5 $A\cdot cm^{-2}$, 21/79 %vol. H_2/H_2O, 40 % FU, cell active area 81 cm^2 (137, 146, 147), with a DR of 0.5 $\%\cdot kh^{-1}$. The targets for SOFC systems in terms of durability are 80'000 – 90'000 hours (148, 149) with DR lower than 0.2 $\%\cdot kh^{-1}$ (150, 151).

Considering the operation in SOEC mode, the DR is commonly observed to be higher compared to the SOFC operation (58, 152, 153). Schefold et al. (19) reported 34'000 h of operation in electrolysis mode at 780-800 °C, -0.6 $A \cdot cm^{-2}$, 25/75 %vol. H_2/H_2O, 50 % SC, cell active area 45 cm^2, with a DR of around 4 $mV \cdot kh^{-1}$. The targets set for SOEC are 80'000 hours lifetime with DR around 1.6 $\%\cdot kh^{-1}$ with cell performance equal to -2 $A \cdot cm^{-2}$ at 1.28 V (154). Finally, the 2030 targeted durability for reversible solid oxide cells (rSOC) is set to be 40'000 hours (155). A summary of the current status of durability and degradation rates for SOFC, SOEC and rSOC can be found in the manuscript from Lamagna et al. (156).

Table 1-2. State of the art and targets on cell durability in SOFC and SOEC operation.

Mode of operation	SoA	Targets
SOFC	100'000 h, 0.5 $\%\cdot kh^{-1}$ (137, 146, 147)	80'000 – 90'000 h (148, 149), < 0.2 $\%\cdot kh^{-1}$ (150, 151)
SOEC	34'000 h, 4 $mV \cdot kh^{-1}$ (19)	80'000 h, 1.6 $\%\cdot kh^{-1}$ (154)

In order to shorten the duration of long-term tests and address the study of the degradation in SOCs within reasonable time, accelerate stress test (AST) protocols have been recently explored to hasten the degradation phenomena (157–159). Many factors are known to aggravate the degradation in SOCs, such as high current density (160), temperature (161) and water content in air (162). Nevertheless, the AST protocol need first to be validated in order to reproduce the same degradation impact effect on the cell as under non-accelerated conditions. Additionally, the impact of some factors on the cell degradation is not yet understood, such as the operating temperature, as presented in the detail in the next section 1.7 related to the state of the art on the degradation phenomena.

1.7 Degradation phenomena in solid oxide cells

As can be seen, despite the promising features of SOCs, their limited durability remains the main bottleneck for the large-scale commercialization. Various degradation phenomena may occur during operation causing a deterioration of the electrochemical performance and shortening the lifetime of the cell, with a direct impact on the economic viability. Most efforts in the research community are focused on the understanding of the degradation mechanisms and their impact on the cell performance loss. Nowadays, the degradation mechanisms remain unclear and the role of the manufacturing and the operating conditions on the stability needs to be better understood. The degradation phenomena manifest themselves in the form of microstructural evolution (138, 163), active site poisoning (164–166), material decomposition (58, 167), reactivity and inter-diffusion at the interfaces (40, 61, 168). Some of these phenomena occur already during the cell fabrication. The manufacturing conditions can play an important role on the cell durability, as reviewed in (169). Upon operation, the SOC degradation is strongly dependent on the temperature (170), the current density (171–173) and the humidity content in the air (162, 174–176).
The following sections describe the main electrodes degradation phenomena. Particular attention is paid to the oxygen electrode degradation, which is the main focus of this thesis.

1.7.1 Hydrogen electrode degradation

The degradation phenomena observed in the Ni-YSZ hydrogen electrode take place in the form of microstructural evolution, including Ni agglomeration and Ni migration (55, 147, 153, 177–181). Both Ni agglomeration and Ni migration are reported to cause an increase in the cell polarization resistance after operation (182, 183). Additionally, an increase in the ohmic losses in the EIS was attributed to the Ni migration occurring in SOEC mode (55, 160). The Ni agglomeration (or coarsening) consists in the Ni particles growth after operation (177). Hubert et al. (178) observed a higher Ni agglomeration at higher operating temperatures. The formation of a Ni-depleted zone at the interface with the electrolyte is observed already after few hundreds hours of operation in SOEC mode (180). The Ni migrates from the interface with the electrolyte towards the bulk of the electrode in electrolysis mode (181). An opposite trend is observed in SOFC mode, where a slight Ni accumulation is found at the interface with the electrolyte after very long ageing time in the order of 10^5 h (147). According to Wang et al. (183), Ni migration is affected by the local humidity, overpotential, operating temperature and current density. Only few works studied the impact of temperature on the Ni migration with contradictory conclusions (140, 160, 179, 184, 185). Indeed, it is still not clear whether the high operating temperature is aggravating (160) or alleviating (185) the Ni migration in SOEC mode. Hoerlein et al. (160) observed a lower Ni depletion in the sample aged at 750 °C, compared to those aged at higher operating temperatures. They explained that this should be related to the higher electrode overpotential at such lower temperature.

1.7.2 Oxygen electrode degradation

Among the different degradation processes at the cell level, those related to the oxygen electrode are reviewed in Table 1-3. It has been shown that the oxygen electrode explains a substantial part of the cell degradation in performances (145, 152). For the LSCF/GDC/YSZ or LSC/GDC/YSZ system, the main degradation phenomena are ascribed to Cr poisoning, LSCF decomposition and secondary phase formation at the GDC/YSZ interface such as $SrZrO_3$ (SZO). Additionally, nano-pores formation in the YSZ has been attributed to elemental diffusion and interpreted as Kirkendall voids (186, 187).

Table 1-3. Main degradation phenomena in SOC oxygen electrode

Phenomenon	Description	Region	Impact on performance	Countermeasures	References
Demixing	Release of cations	Perovskite lattice	Surface passivation, loss of activity Decrease of the ionic conductivity (Dchem)	Change of materials, surface decoration	(33, 41, 43, 44, 58, 188–190)
Reactivity	Formation of new phases: $SrZrO_3$ (SZO), inter-diffusion layer (IDL)	Interfaces between layers with different composition	Additional resistive layer	Diffusion barrier layer, manufacturing conditions	(59, 186, 191–193, 193, 194, 40, 195–197, 58, 62, 198, 42, 168, 199, 61)
Delamination	Detachment of the electrode from the electrolyte due to high oxygen partial pressures or thermal stress at the electrode/electrolyte interface	Electrode/electrolyte interface	Catastrophic failure of the cell	Change material	(32, 200)
Poisoning	Deposition of contaminants such as Cr and S	Interconnect/electrode interface	Blocking the electrochemical active sites, inhibition of the oxygen surface diffusion	Coatings, Cr-getters	(165, 166, 201, 202)

1.7.2.1 Decomposition of the LSCF

LSCF demixing. During manufacture and operation at high temperature, the LSCF demixing consists in a change in the composition of the material in the bulk and/or at the surface (203, 204). The latter consists of segregation of cations (e.g. Sr, Co) from the lattice of the material to the outermost surface, with the subsequent formation of passivating layer as oxides (such as SrO), hydroxides or carbonates layer at the surface. This layer is known to limit the electron transfer and slow down the oxygen surface exchange kinetics (43) and sub-surface oxygen bulk diffusion (205).

The release of cations from the lattice and their consequent segregation to the surface arise from the well-documented decomposition of the LSCF (33, 40–44, 58, 59, 188–191, 193). The Sr segregation is one of the most reported detrimental phenomena for this type of material (41, 44, 206–211). The LSCF decomposition with the consequent Sr segregation are found to be aggravated under humid air conditions as reported in literature (162, 174–176) and more

generally by the atmosphere surrounding the cell (212). Monaco et al. (40) observed an aggravated destabilization of the LSCF after operating in SOEC mode at high temperature. According to this finding, they suggested that the LSCF decomposition is activated by the high operating temperature.

In addition to Sr segregation, many studies reported Co segregation under SOFC and SOEC operation at different current densities, under different operating temperatures between 800-900°C (58, 59, 199, 207, 213–217). A Raman spectroscopy study has shown that segregated cobalt was in the form of Co_3O_4 (218). Moreover, the study of Mahmud et al. (219) suggested that structural change of the LSCF perovskite occurs with the formation of Co_3O_4, a partial reduction of Co^{4+} to Co^{3+} and of Fe^{4+} to Fe^{3+}. However, the Co segregation was found also in the form of Co-Fe oxides (58, 207). In the literature, Co was observed mainly in the GDC (58, 59), with a lower amount in the electrolyte (59), but also on the LSCF surface in dense bar samples (214) and porous electrodes (207).

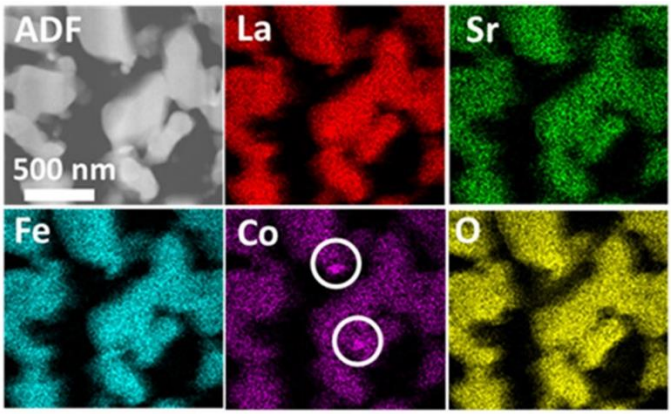

Figure 1-11. Cobalt-enrichment at the LSCF surface in porous electrodes. Reprinted (adapted) with permission from {N. Ni, S. J. Cooper, R. Williams, N. Kemen, D. W. McComb, and S. J. Skinner, *ACS Appl. Mater. Interfaces*, **8**, 27, 17360–17370 (2016)}. Copyright {2016} American Chemical Society.

Villanova et al. (59) found Co in the GDC, as well as in the YSZ in a minor way, already after the cell manufacture. The authors explained that this phenomenon could take part in the long-term degradation. A further Co and Fe cations diffusion after operation was highlighted in the work of Bernadet et al. (63). According to Mahmood et al. (217), the loss of Co from LSCF could have an impact on the electrochemical properties of the material, in terms of electro-catalytic activity, as well as electronic and ionic conductivities. However, Laurencin et al. (58) observed that the Co segregation was occurring with the formation of Co-Fe-based particles in the GDC barrier layer. They suggested that the good electrical conductivity of such particles was not the reason for the major performance degradation, compared to Sr segregation that had a significant impact. Accordingly, Shen et al. (220) reported improved performance by intentionally increasing the Co content in the $SrZrO_3$ that was artificially added at the interface with the electrolyte.

The main driving forces for cations segregation are the elastic and electrostatic interactions, which arise in the presence of strain in the structure (elastic interactions) or in case of a variation in the surface charge (electrostatic interactions) (70, 188, 221–227). According to Lee et al. (221), the driving force related to the electrostatic energy minimization is linked to the electrostatic interactions between the cations and the surface charged defects, while the driving force related to the elastic energy minimization is more important when the size mismatch, in terms of ionic radii (see Table 1-4), between the dopant and host cation (i.e. La) is larger. Ding et al. (188) stated that Sr segregation was hindered by imposing a compressive strain in the structure (elastic interactions) and by minimizing the surface charge (electrostatic interactions).

Table 1-4. Crystal ionic radii in pm (228, 229).

La	Sr	Co	Fe	Gd	Ce	Y	Zr	Ni
$^{3+}$: 117.2	$^{2+}$: 132	$^{2+}$: 79 ls, 88.5 hs $^{3+}$: 68.5 ls, 75 hs $^{4+}$: 67 hs	$^{2+}$: 75 ls, 92 hs $^{3+}$: 69 ls, 78.5 hs $^{4+}$: 72.5	$^{3+}$: 107.5	$^{3+}$: 115 $^{4+}$: 101	$^{3+}$: 104	$^{4+}$: 86	$^{2+}$: 83 $^{3+}$: 70 ls, 74 hs $^{4+}$: 62 ls

ls = low spin, hs = high spin

According to some authors (230–232), electrostatic interactions seem to be the dominant driving forces for Sr segregation in LSCF. Koo et al. (233) also proposed that the redistribution of cations in LSCF or LSC could be due to electrostatic interactions. Indeed, the surface charge related to the loss of symmetry at the surface, in comparison to the bulk, may drive the Sr segregation. Moreover, the perovskite oxides readily form oxygen vacancies, which may accumulate on the surface. Thus, the negatively charged Sr is attracted by the positively charged surface oxygen vacancies according to Coulomb's law, causing cation segregation. According to Harrison et al. (225), the surface charge minimization may occur due to a change in the charge state of B-site elements or to a change in the surface termination. The latter can be obtained either by increasing the Sr concentration or depleting the La at the surface. Ding et al. (188) suggested that the substitution of Fe with Co can induce an additional tensile strain and increase in the surface charge, thus increasing Sr segregation and SrO formation (by increasing Co content that replace Fe). Accordingly, Kwon et al. (226) suggested that A-site cation segregation is hindered when smaller B-site cations, such as Ni or Co, are employed. In addition, Ding et al. (188) stated that A-site deficiency plays a role in the material stability, causing both the two types of interactions. Accordingly, Lu et al. (70), performed a study on the comparison of two configuration: stoichiometric LSCF and 5% A-site deficient LSCF. A higher amount of SZOs was observed in the stoichiometric LSCF compared to the 5% A-site deficient LSCF. The reason behind this finding was related to the improved sintering of the deficient perovskite. In addition, they reported that A-site deficiency plays a role in the material stability, causing both elastic and electrostatic interactions.

The LSCF demixing with the release of cations is reported to cause a change in the crystal structure and a chemical expansion of the lattice (234–238). The increase in the LSCF lattice unit cell volume (UCV) can be ascribed to the LSCF destabilization and more specifically to the loss of Sr and Co (234–238). The increase in the LSCF UCV was observed in a previous work performed in our laboratory (40) on a cell with same materials but different manufacturing conditions, after ageing in SOEC mode at 850 °C. The change in the LSCF lattice parameter is in general affected by different factors, such as composition, temperature and oxygen non-stoichiometry (234, 235). Tai et al. (234, 237) observed an increase in the LSCF lattice parameter with decreasing the Sr content in the $La_{1-x}Sr_xCo_{0.2}Fe_{0.8}O_3$ or increasing the Fe content in the $La_{0.8}Sr_{0.2}Co_{1-y}Fe_yO_3$. They explained that the increase in Sr content, replacing the La, cause an increase in the average size of the A-site cations and a charge imbalance. For this reason, B-site cations oxidize (i.e. Fe^{3+} and Co^{3+} from to Fe^{4+} and Co^{4+}) to go back to electro-neutrality, resulting in a decrease in the average size of the B-site cations and the consequent net decrease in the global ABO_3 perovskite lattice volume. Nevertheless, Chen et al. (238) suggested that the chemical expansion of the lattice cannot be explained only by the role of ionic radii and the state of oxidation. They state that multiple factors as the preferential coordination and the local lattice distortions should be considered.

Effect of operating temperature - Concerning the effect of the operating temperature on the degradation, Monaco (57) stated that higher operating temperatures could involve higher Sr excorporation, which would be thus thermally activated. On the other hand, Endler-Schuck et al. (170) have claimed that the LSCF degradation increases with decreasing the operating temperature. Moreover, Wang et Barnett (44) found that the amount of strontium increase with the temperature from 700°C to 750°C, while at 950°C the Sr segregation decreases. On the one hand, Sr could be more easily removed from the LSCF surface at high temperatures by the formation of volatile species. Lee et al. (221) studied the effect of the annealing temperature for $La_{0.8}D_{0.2}MnO_3$ (D = Ca, Sr, Ba) dense thin films deposited on single-crystal SrTiO3 substrates via pulsed laser deposition (PLD). They suggested that lowering the annealing temperature could help reducing cation segregation. Koo et al. (233) explained in their review paper that lowering the operating temperature would be an effective way to prevent the segregation. As can be seen, the effect of temperature is still controversial as different studies have different operating parameters and manufacturing conditions.

Effect of sintering temperature - Another aspect to be considered is the cell manufacturing. According to many authors (58, 59, 64, 186, 206, 233, 239), the LSCF phase demixing with the diffusion of cations and the formation of secondary phases occur already during the manufacturing processes with the LSCF sintering step due to high temperatures around 1000-1200 °C (64). Conversely, their contributions to the long-term degradation can be neglected (239). According to Oh et al. (190), the amount of segregated SrO phases increase with increasing the heat treatment temperature from 600°C to 900°C. Cai et al. (206) stated that partially crystalline $La_{0.6}Sr_{0.4}CoO_{3-\delta}$ (LSC) thin films deposited at 450 °C by pulsed laser deposition have higher stability compared to fully crystalline LSC films deposited at 650°C. This was attributed to the lower cation segregation in a partially crystalline structure.

Effect of polarization - Kim et al. (227) put in evidence the role of electrochemical polarization on the elastic and electrostatic driving forces for the segregation in doped lanthanum manganite materials. They observed transition from elastic-dominated driving force under anodic polarization to electrostatic-dominated driving force under cathodic polarization. The transition was defined at the minimum of a U-shaped curve, which reported the trend of dopant segregation with the polarization. Under anodic polarization, the increase in surface segregation was related to the elastic strain. Under cathodic polarization, the increase in segregation was attributed to the electrostatic attraction of negatively charged dopants towards the positively charged oxygen vacancies at the surface. In their review, Chen et Jiang (60) highlighted the important role of surface properties of the electrode on the Sr segregation according to the applied polarization. They explained that, under anodic polarization, the lower amount of positively charged oxygen vacancies at the surface cause a lower attraction of the negatively charged lattice Sr towards the surface. Thus, the electrostatic attraction of bulk oxygen vacancies prevails over the elastic interactions, resulting in a lower Sr surface segregation. According to Monaco et al. (40), the operation in electrolysis mode promote LSCF demixing and the Sr migration towards the electrolyte to form SZO. Laurencin et al. (58) observed that higher degradation rates could be related to the formation of SZO after operation in electrolysis compared to fuel cell mode. They suggested that the depletion of oxygen vacancies, which is higher during SOEC mode, could favour the Sr release. This is in agreement with the results obtained by Frey et al. (152), who stated that LSCF demixing were accelerated in SOEC mode compared to SOFC mode. However, some other works (41, 213, 240, 241) stated the opposite that higher Sr segregation occurs under cathodic polarization, while it is inhibited under anodic polarization. Pan et al. (41) have reported an improvement in the stability of LSCF electrode performance under anodic polarization, that could be ascribed to a decrease in Sr species at the surface. In addition, the electrostatic interaction between Sr and oxygen vacancies in the bulk

could prevail over the driving force associated with the elastic interaction, leading to lower Sr segregation (60). Villanova et al. (59) observed a limited growth in the volume of secondary phases related to Sr, Gd and Ce, at the GDC/YSZ interface in a fuel electrode supported cell aged for 6100h under anodic polarization during SOEC operation. They also stated that, conversely to LSCF demixing, the formation of secondary phases should not affect the electrochemical response of the cell. Mutoro et al. (213) studied the surface composition of dense $La_{0.8}Sr_{0.2}CoO_{3-\delta}$, $(La_{0.5}Sr_{0.5})_2CoO_{4\pm\delta}$ thin films grown by pulsed laser deposition by in situ synchrotron-based XPS and they found SrO-like and CoO_x-like phases on the surface under cathodic polarization.

Effect of humidity in the air - Among the different impacting factors, it has been suggested that a higher water content in the air inlet flow implies a higher degradation (162, 174–176, 242). This has been found to be related to the formation of volatile $Sr(OH)_2$ (174, 175). Indeed, $Sr(OH)_2$ is the dominant Sr containing species in the gas form according to thermodynamics calculations and its amount is determined by the presence of water vapor in the air flow (70). The volatile $Sr(OH)_2$ species may then easily diffuse to the GDC barrier layer through the pores (69, 216). An 100 h test at 1000°C with humidified oxygen (i.e. 20% H_2O and 80% O_2) showed that the presence of water molecules in the gas phase promotes the formation of secondary phases (162). Most studies have been performed on symmetrical (162, 176, 243) and complete (244) cells in SOFC mode, whereas no studies can be found in SOEC mode for complete cells.

1.7.2.2 Inter-diffusion and reactivity at the LSCF/GDC/YSZ interfaces

A. GDC/YSZ interface

The LSCF demixing under operation would not only be related to the formation of a Sr enriched passivation layer on the LSCF surface, but also to the subsequent formation of secondary phases at the interface between the barrier layer and the electrolyte (186, 191–194). Indeed, at the interface, Sr can react with Zr coming from the electrolyte to produce phases such as SZO and $La_2Zr_2O_7$ (LZO) with low ionic conductivity (see Table 1-5). Wankmüller et al. (168) stated that the transport of Sr towards the electrolyte can occur in three possible ways: (i) via bulk and (ii) surface diffusion along LSCF and GDC phases or (iii) via gas diffusion in the form of $Sr(OH)_2$ in the pores.

Table 1-5. Ionic conductivities of different phases at 800°C

Phase	Ionic conductivity (S/m)	Refs.
GDC	8.70	(22)
YSZ	5.40	(22)
SZO	1.87×10^{-4}	(245)
LZO	4.2×10^{-3} (at 900°C)	(246)
IDL	1.25×10^{-1}	(22)

The formation of such phases possibly occurs in the regions where Sr is released from LSCF (186, 247) and it is known to contribute to a decrease in the cell performance, when forming a

continuous layer with lower ionic conductivity (194, 197, 199). However, Laurencin et al. (58) observed SZOs were formed only in the open porosity of the GDC, so that they should not affect the cell performance. Moreover, Tietz et al. (62) found that the durability was not affected that much by the presence or absence of SZOs. Indeed, thanks to a dense barrier layer by physical vapour deposition (PVD), the Sr diffusion towards the electrolyte along with the formation of secondary phases was almost suppressed, without substantial enhancement in the cell durability. Therefore, they stated that the LSCF decomposition contribute in a major manner to the cell decrease in performance compared to the formation of secondary phase at the electrolyte interface. In addition to avoid SZO formation, Tietz et al. (62) observed higher initial performance for dense GDC layer obtained with PVD, compared to porous sintered GDC layer. Accordingly, Bernadet et al. (63) reported that a dense GDC barrier layer, obtained by PLD, can prevent cations inter-diffusion and formation of secondary phases, leading to improved cell performance and durability. The structure of the GDC barrier layer can also affect the formation of secondary phases. The barrier layer can be porous or dense. Higher performance and small or absent reactivity with the electrolyte was observed for dense GDC layer (62, 67, 68). Indeed, according to literature (69, 70), in the case of porous diffusion barrier the formation of secondary phases mainly occurs because of volatile $Sr(OH)_2$, which is the most present species and it can diffuse easily through the pores of the barrier to reach the electrolyte. Some authors performed a study comparing dense and porous GDC barrier layer, highlighting the advantages of a dense barrier layer in terms of performance and reactivity with the electrolyte with the formation of SZO (61, 62, 66, 68). The effect of the thickness of the barrier layer was also investigated, pointing out the trade-off between additional ohmic resistance in the case of too thick layer and reactivity in the case of too thin layer (67, 248). To summarize, the formation of the SZO layer at the interface with the electrolyte is dependent on the manufacturing conditions.

The formation of the IDL at the GDC/YSZ interface is another phenomenon that has been observed in literature (40, 59, 193, 195, 196). It has been shown that the formation of the IDL can arise due to the diffusion of Zr and Y from the YSZ electrolyte towards the GDC layer and the diffusion of Gd and Ce from the GDC barrier layer towards the electrolyte (168, 193). As mentioned above for the secondary phases formation, the application of a dense GDC layer by PLD was found to inhibit the IDL formation (64, 65). However, it is not clear if it could be deleterious for the cell performance by inducing an increase in ohmic losses due to a decrease of the ionic conductivity (198) or if it could help by acting as a protective layer against the formation of secondary phases (42, 168, 199). Wilde et al. (199) found that the IDL is composed of two sublayers. From GDC to YSZ, they observed first a sublayer composed of Gd with a substantial amount of Ce and poor amount of Zr, followed by a second sublayer with Gd, almost no Ce and richer in Zr. The Gd content was found to be almost constant in the IDL, with a drop at the interface with the electrolyte. In this way, the Zr-rich phase (YSZ) and the Sr-rich phase ($Sr(OH)_2$ volatile species in the pores of the GDC barrier layer) are effectively separated, and their reactivity is prevented. They also observed a microstructural change of the IDL after LSCF sintering, mainly when the GDC is sintered at low temperature. Moreover, it was proposed that the diffusion of Zr^{4+} from YSZ, associated to the formation of secondary phases as SZO upon operation, could also trigger the inter-diffusion of Gd and cause a decrease in local ionic conductivity (40, 249–251). In addition, it was suggested that such mechanism may partly explain the larger increase in the ohmic resistance observed for the cell operated in electrolysis mode compared with the fuel cell mode, at high temperatures (40). Nevertheless, the authors concluded that further characterizations at the nanometre length scale are required to finely investigate the IDL and its evolution after long term operation.

In addition to the IDL, nano-porosities form at the interface between the electrolyte and the diffusion barrier, which are named Kirkendall voids (186, 187, 252, 253). According to The et al. (186) it could be related to the Zr^{4+} diffusion from the electrolyte to the interface with the

diffusion barrier, while Mitsuyasu et al. (187) stated that such voids resulted from the diffusion of Ce into the YSZ.

Effect of sintering temperature - As discussed in section 1.2, manufacturing conditions affect also the reactivity with the electrolyte. It has been shown that the IDL is strongly affected by the GDC sintering temperature (42, 168, 199). According to Wankmüller et al. (168), at high sintering temperatures (1400°C), the thickness of the IDL increase and the formation of SZO decreases, while at lower sintering temperatures (1100-1200°C) a continuous layer of SZOs was observed. Moreover, Xu et al. (196) observed in NiO-YSZ/GDC/YSZ half cells prepared via tape casting and then sintered that inter-diffusion at the GDC/YSZ interface takes place especially during the sintering process performed at two different sintering temperatures (i.e. 1250°C and 1315°C), whereas its impact on the cell degradation was negligible during long-term operation at lower temperature (i.e. 700°C for 2000h). They also found that the inter-diffusion was promoted at high sintering temperature.

Effect of sintering time - Another factor to be considered during manufacturing processes is the sintering time. Indeed, a possible way for suppressing the Sr cation diffusion and SZO formation is to obtain the LSCF electrode via flash light sintering technique, which is characterized by an extremely short processing time period of a few seconds, during which the diffusion of elements is not sufficient for secondary phase formation (254).

B. LSCF/GDC interface

It has been shown that additional inter-diffusion and reactivity can occur at the LSCF/GDC interface (197, 247, 255–257). Develos-Bagarinao et al. (255) reported that the use of a dense GDC, instead of a nanocolumnar structure, both obtained by PLD, can limit the cations diffusion at the LSCF/GDC interface. De Vero et al. (197) observed an increase in Gd content in the LSCF that was counterbalanced by the release of La towards the GDC layer to maintain the same A/B perovskite ratio. According to Shaula et al. (258), the perovskite A-site deficiency can promote the introduction of Ce and Gd into LSCF. Lower electrical conductivity was reported for Gd-based perovskites $Gd_{0.4}Sr_{0.6}Co_{0.8}Fe_{0.2}O_{3-\delta}$ as compared to $La_{0.4}Sr_{0.6}Co_{0.8}Fe_{0.2}O_{3-\delta}$ (259). According to Uhlenbruck et al. (61), the diffusion of Gd from the GDC to the LSCF is a possible cause for the cell performance degradation. They observed in the GDC barrier layer a content of 5 at.% Gd, which was much lower compared to the nominal value (i.e. 20 at.%). Additionally, they reported a change in the LSCF structure after adding 1 at.% Gd to form $La_{0.58}Sr_{0.4}Gd_{0.01}Co_{0.2}Fe_{0.8}O_{3-\delta}$. On the other hand, Zhang et al. (46) observed an improved performance and durability, with the suppression of Sr segregation, when Ce and La mutually diffused in the LSCF-CeO_2 nanofiber-based electrode. As can be seen, the conflicting conclusions among the different studies indicate that the role of GDC elements incorporation into the LSCF on the durability of the cell materials is not fully clarified.

1.7.2.3 Mitigation strategies

In the literature, there are many suggestions about what is needed to be addressed in order to reduce the Sr segregation and its effect on performance. For instance, Chen et Jiang (60)

highlighted the role of surface chemistry, oxygen nonstoichiometry, cation segregation and phase changes. According to Sun et al. (260), the use of GDC electrolyte allows reducing the amount of Sr segregation. Nevertheless, they found surface segregation of Co was promoted under the cathodic polarization, with the consequent formation of isolated CoO_x particles like CoO and Co_3O_4 in the LSCF electrode and no segregation at the interface with GDC electrolyte. Conversely, accumulation of Sr and Zr was found at the interface with the YSZ electrolyte. Moreover, a limited impact on the LSCF activity and stability was observed. Another possible way to reduce the effect of segregated species is the chemical etching, which has been described by many authors (206, 261–263). This technique allows recovering the performance of the cell removing the Sr-segregated phases. Lu et al. (263) found that treatment with ultrapure water allowed the polarization resistance to be reset to the initial value. However, they stated that possible challenges could arise to apply a cleaning process on a stack and not just on a lab-scale cell. Villanova et al. (59) studied two different cell configurations operated in different conditions, namely a cathode supported cell (CSC) made of LSCF/GDC/8YSZ/Ni-YSZ and an electrolyte supported cell (ESC) made of LSCF/GDC/6Sc1CeSZ/GDC/Ni-GDC. In both architectures, diffusion of elements was observed already after the sintering process. According to their results, a clear accumulation of Sr was found at the interface in the case of the CSC, compared to the ESC, for which the GDC barrier prevented the Sr diffusion at the interface. Co diffusion was found in both architectures, but in the CSC operated for 6'100 h it was limited in the GDC barrier, while in the ESC it reached the electrolyte after an operation of 23'000 h. In addition, the adoption of A-site deficiency, A-site or B-site doping (e.g. B-site doping with high valence cations) in the typical perovskite structure ABO_3 demonstrated a remarkable reduction of the Sr surface segregation and enhance the structural stability of LSCF (60, 70, 188, 264). Moreover, Li et al. (261) reviewed the impact of LSCF surface decoration by nanoparticles in order to mitigate the cation segregation. Indeed, they stated that surface decoration can be a relevant solution to combine a high catalytic activity for the electrochemical reaction and a good electrode stability. For instance, Gong et al. (265) observed a high stability over 4000 h of operation for the $La_{0.6}Sr_{0.4}CoO_{3-\delta}$ electrode surface decorated with ZrO_2 overcoats using atomic layer deposition (ALD).

However, some contradictory results were reported regarding the effectiveness of surface decoration to prevent Sr segregation, as reviewed by Li et al. (261). Overall, the discrepancies in the literature are due to the fact that Sr segregation is critically influenced by the employed material, the environmental conditions (e.g. temperature, strain, polarization, gas environment, etc.) and several other factors (e.g. manufacturing, surface chemistry, surface strains, morphology, atmospheres, impurities and polarizations) (60, 261). This is in accordance with statements from Koo et al. (233), according to whom Sr segregation can have different formations and structures depending on the compositions of the perovskite oxide, the synthesis processes, and the measurement conditions. This seems to be the key point, as any comparison should relate to both manufacturing and operating parameters.

1.8 Chapter conclusions: thesis objectives and methodology

This chapter was devoted to the state of the art on SOC technology and the related degradation phenomena occurring in the different layers of the cell. On the basis of this literature review, notwithstanding the electrochemical performance and the various advantages of using SOCs,

further research is needed to fulfil the requirements in terms of cell durability and envisage a large-scale deployment of this technology. The degradation phenomena in SOCs are observed in form of microstructural evolution, kinetic demixing and decomposition of the materials, poisoning, elemental inter-diffusion and formation of secondary phases. It was highlighted the important role of manufacturing and operating conditions on the material stability. Nevertheless, the effect of operating temperature on the cell performance deterioration and material degradation is not yet fully clarified, especially in SOEC mode. Additionally, the reason behind a stronger material degradation in SOEC mode has to be investigated. The use of AST protocols and the identification of the aggravating parameters is essential for understanding the degradation phenomena upon operation. Finally, this review has highlighted the crucial importance of multiscale modelling, long-term testing and advanced post-test characterizations as means to unravel the intricate processes that occur during cell manufacture and operation. Additionally, the impact of degradation phenomena on the cell lifetime according to the operating conditions can be studied with the aforementioned methods in a combined approach to progress in this research direction and deepen the knowledge on the SOCs durability.

In the frame of this problematic, the thesis aims to better understand the governing degradation phenomena in SOCs and to study their effect on the cell response depending on the operating conditions. The studied cell has a planar design with a hydrogen electrode supported cell architecture. The cell is made of a LSCF-GDC oxygen electrode, a 8YSZ electrolyte, a GDC diffusion barrier layer, and a Ni-YSZ hydrogen electrode. A detailed cell description will be provided in the **Chapter II**. To achieve the thesis objectives addressing the problem of degradation, a three-fold methodology based on multiscale physics-based modelling, long-term electrochemical testing, and post-test characterizations is adopted (see Figure 1-12). (i) The multiscale physics-based model available at the laboratory has been adapted to the studied cell, validated on the experimental data, and used to simulate the cell operation in electrolysis and fuel cell modes. In the frame of this thesis, the electrodes morphology was obtained from 3D reconstructions of the two electrodes. More specifically, the stationary model has been validated on polarization (or i-V) curves. The activated reaction pathways associated with the elementary steps in the active layers have been investigated depending on the position along the cell radius. Additionally, the model has been extended to simulate the dynamic response of the cell and it has been validated on the experimental EIS. Herein, special attention was given to the simulation of the complete cell impedance diagram, in order to interpret the experimental EIS evolution after operation and study the cell performance degradation. Indeed, EIS-based measurements and modelling are powerful tools to analyse the kinetic and transport phenomena, as well as to diagnose the SOCs state-of-health for long-term operation (73, 79, 82). In the framework of this thesis, the model is used to identify the different contributions arising in the EIS, namely the RDS in the considered full-elementary reaction mechanism, and to investigate their evolution after ageing in various operating conditions. Hence, the model enables discerning the dominant degradation phenomena and, thus, the component that is most responsible for the cell performance loss. (ii) The studied single complete cells are tested for long-term operation to assess the impact of various industrially relevant operating conditions on the performance deterioration and on the complex set of material degradation phenomena. Electrochemical characterizations (i.e. i-V curves and EIS, before and after ageing) are

performed to assess the performance deterioration in various operating conditions. After that, the experimental data from the electrochemical characterizations performed in various operating conditions are used to validate the multiscale physics-based model. In order to extend the study to relevant open questions, long-term tests were performed in various operating conditions, including different temperatures (750, 800 and 850 °C), ageing time (1000, 2000 and 5000 h), operating modes (electrolysis and fuel cell), and water content in air (dry, 3% humid air and 8% humid air). The increased water content in the air flow has been chosen as an aggravating factor in the frame of the AST protocols to induce harsh operating conditions for the cell and exacerbate the oxygen electrode degradation. In order to compare the tests performed at different operating conditions, the electrochemical response is evaluated at reference conditions (i.e. 750°C and 800°C, 10/90 vol.%H_2/H_2O, H_2O+H_2=12 $NmL \cdot min^{-1} \cdot cm^{-2}$). (iii) Finally, in order to verify the model findings in terms of components degradation and to better understand the type of degradation phenomena encountered after ageing in the various operating conditions, advanced post-test characterizations are required. Indeed, the post-test characterizations are essential to detect and evaluate the signs of material degradation in the cell after ageing in different operating conditions, such as the microstructural evolution and material decomposition. More specifically, high-resolution advanced techniques are required to understand the phenomena occurring in the oxygen electrode. This thesis comprises characterization techniques performed in large-scale facilities, of which synchrotron nanoscale X-ray fluorescence (nano-XRF) and X-ray diffraction (nano-XRD) performed at the European Synchrotron Radiation Facility (ESRF, ID16B beamline, France) (266), as well as synchrotron microscale XRD (μXRD) performed at the Swiss Light Source (SLS) of Paul Scherrer Institute (PSI, microXAS beamline, Switzerland). A larger range of information was acquired by using complementary techniques in laboratory-based instruments, including inductively coupled plasma mass spectroscopy (ICP-MS), scanning electron microscopy (SEM), 3D focused ion beam-SEM (FIB-SEM), X-ray photoelectron spectroscopy (XPS), high-resolution secondary ion mass spectroscopy (SIMS) imaging, atom probe tomography (APT), and scanning transmission electron microscopy (STEM) coupled with energy dispersive X-ray spectroscopy (EDS). The reason behind the choice of the various techniques is reported in the following. SEM and 3D FIB-SEM techniques has been selected to perform the microstructural analysis on the two electrodes. More specifically, 3D FIB-SEM is used to assess the hydrogen electrode microstructural evolution after ageing. The chemical analysis was performed using ICP-MS, XPS, SIMS and synchrotron XRF. ICP-MS was used to verify the LSCF powders stoichiometry. XPS analysis was carried out to collect information on the oxidation state of the surface and to identify the formation of passivating layers on the surface of the perovskite material in the oxygen electrode. SIMS and synchrotron XRF techniques have been used to map the elements in the oxygen electrode, barrier layer and hydrogen electrode. Additionally, synchrotron XRD crystallographic data were collected concurrently with XRF data, integrating elemental mapping and point-by-point structural analysis. Finally, APT and STEM-EDS have been used to perform a chemical analysis of the oxygen electrode material with high-resolution, down to the atomic scale. Specifically, APT technique enables obtaining 3D imaging and atomic concentration profiles of the prepared samples, and it can be used to identify interfacial intermixing at atomic scale (267). STEM-EDS results consist of 2D maps that can be used to study the cations ordering and periodicity (267, 268). The coupling of both APT and STEM techniques is reported to improve the analysis as compared to their use without mutual

correlation (267). Overall, the heterogeneity of the selected techniques allows collecting microstructural, chemical (bulk and surface) and crystallographic information at different length-scales (micro, nano and atomic), which are necessary to understand the degradation phenomena involved in the cell materials. Additionally, the set of various post-test characterizations enables complementing and validating each other by ensuring the reliability of the results coming from each technique separately.

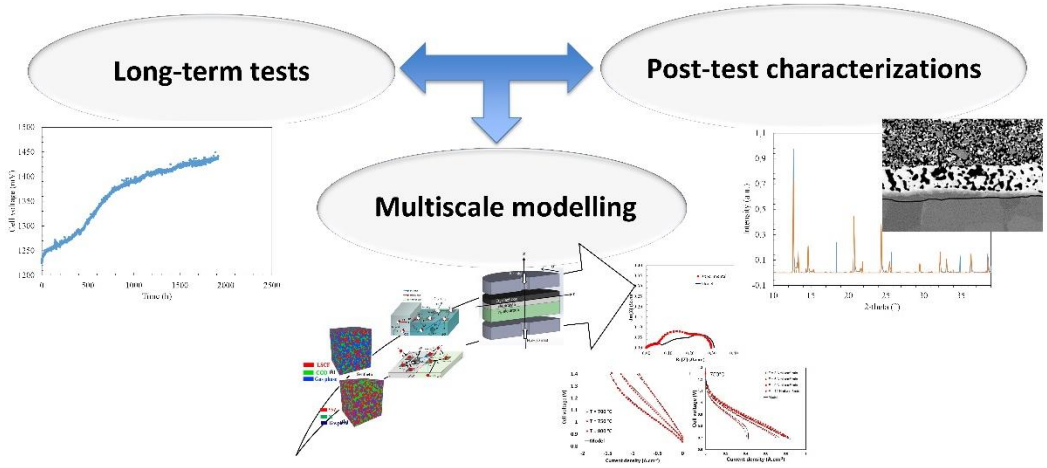

Figure 1-12. Scheme of the three-fold methodology used in the thesis.

Chapter II will provide a detailed description of the various electrochemical and post-test characterizations used within the three-fold methodology. **Chapter III** will present the multiscale physics-based model validated on the stationary (i.e. i-V curves) and dynamic (i.e. EIS) response of the cell. **Chapter IV** will report the electrochemical and post-test characterizations for the cells tested under dry air to investigate the effect of operating temperature on the cell durability. **Chapter V** will address the study the effect of humid air and operating mode on the cell durability. Finally, **Chapter VI** will summarise the main the results collected during the thesis to highlight the knowledge gain by this thesis, along with the conclusions and perspectives.

References

1. N. Q. Minh, *Solid State Ionics*, **174**, 271–277 (2004).
2. S. P. S. Badwal and K. Foger, *Ceramics International*, **22**, 257–265 (1996).
3. N. Q. Minh and T. Takahashi, *Science and Technology of Ceramic Fuel Cells*, p. 379, Elsevier, (1995).
4. P. Singh and N. Q. Minh, *International Journal of Applied Ceramic Technology*, **1**, 5–15 (2004).
5. L. S. Mahmud, A. Muchtar, and M. R. Somalu, *Renewable and Sustainable Energy Reviews*, **72**, 105–116 (2017).
6. L. Blum, W. A. Meulenberg, H. Nabielek, and R. Steinberger-Wilckens, *International Journal of Applied Ceramic Technology*, **2**, 482–492 (2005).
7. R. Hino, K. Haga, H. Aita, and K. Sekita, *Nuclear Engineering and Design*, **233**, 363–375 (2004).
8. T.-L. Wen, D. Wang, H. Y. Tu, M. Chen, Z. Lu, Z. Zhang, H. Nie, and W. Huang, *Solid State Ionics*, **152–153**, 399–404 (2002).
9. *Bloom Energy* https://newsroom.bloomenergy.com/news/bloom-energy-demonstrates-hydrogen-production-with-the-worlds-largest-and-most-efficient-solid-oxide-electrolyzer.
10. *CORDIS | European Commission* https://cordis.europa.eu/project/id/101056723.
11. V. Venkataraman, M. Pérez-Fortes, L. Wang, Y. S. Hajimolana, C. Boigues-Muñoz, A. Agostini, S. J. McPhail, F. Maréchal, J. Van Herle, and P. V. Aravind, *Journal of Energy Storage*, **24**, 100782 (2019).
12. G. Min, S. Choi, and J. Hong, *Applied Energy*, **328**, 120145 (2022).
13. *CORDIS | European Commission* https://cordis.europa.eu/project/id/875123.
14. *Sunfire* https://www.sunfire.de/en/news/detail/renewable-hydrogen-project-multiplhy-worlds-largest-high-temperature-electrolyzer-from-sunfire-successfully-installed.
15. M. C. Tucker, *Journal of Power Sources*, **195**, 4570–4582 (2010).
16. M. Singh, D. Zappa, and E. Comini, *International Journal of Hydrogen Energy*, **46**, 27643–27674 (2021).
17. B. Timurkutluk, C. Timurkutluk, M. D. Mat, and Y. Kaplan, *Renewable and Sustainable Energy Reviews*, **56**, 1101–1121 (2016).
18. K. Kendall and M. Kendall, *High-Temperature Solid Oxide Fuel Cells for the 21st Century: Fundamentals, Design and Applications*, p. 522, Elsevier, (2015).
19. J. Schefold, H. Poepke, and A. Brisse, *ECS Trans.*, **97**, 553 (2020).
20. R. I. Tomov, M. Krauz, A. Tluczek, R. Kluczowski, V. V. Krishnan, K. Balasubramanian, R. V. Kumar, and B. A. Glowacki, *Mater Renew Sustain Energy*, **4**, 14 (2015).
21. V. V. Kharton, F. M. B. Marques, and A. Atkinson, *Solid State Ionics*, **174**, 135–149 (2004).
22. A. Tsoga, A. Gupta, A. Naoumidis, and P. Nikolopoulos, *Acta Materialia*, **48**, 4709–4714 (2000).
23. A. Tsoga, A. Gupta, A. Naoumidis, D. Skarmoutsos, and P. Nikolopoulos, *Ionics*, **4**, 234–240 (1998).
24. A. Nakamura and J. B. Wagner, *J. Electrochem. Soc.*, **133**, 1542 (1986).
25. M. Ghatee, M. H. Shariat, and J. T. S. Irvine, *Solid State Ionics*, **180**, 57–62 (2009).
26. E. Lay-Grindler, J. Laurencin, G. Delette, J. Aicart, M. Petitjean, and L. Dessemond, *International Journal of Hydrogen Energy*, **38**, 6917–6929 (2013).
27. A. Weber and E. Ivers-Tiffée, *Journal of Power Sources*, **127**, 273–283 (2004).
28. J. Zhang, C. Lenser, N. H. Menzler, and O. Guillon, *Solid State Ionics*, **344**, 115138 (2020).

29. S. Yu, H. Bi, J. Sun, L. Zhu, H. Yu, C. Lu, and X. Liu, *Journal of Alloys and Compounds*, **777**, 244–251 (2019).
30. M. B. Hanif, S. Rauf, M. Motola, Z. U. D. Babar, C.-J. Li, and C.-X. Li, *Materials Research Bulletin*, **146**, 111612 (2022).
31. S. B. Adler, *Chem. Rev.*, **104**, 4791–4844 (2004).
32. A. V. Virkar, *International Journal of Hydrogen Energy*, **35**, 9527–9543 (2010).
33. E. Effori, H. Moussaoui, F. Monaco, R. K. Sharma, J. Debayle, Y. Gavet, G. Delette, G. S. Larbi, E. Siebert, J. Vulliet, L. Dessemond, and J. Laurencin, *Fuel Cells*, **19**, 429–444 (2019).
34. A. Mineshige, M. Kobune, S. Fujii, Z. Ogumi, M. Inaba, T. Yao, and K. Kikuchi, *Journal of Solid State Chemistry*, **142**, 374–381 (1999).
35. A. Mineshige, M. Inaba, T. Yao, Z. Ogumi, K. Kikuchi, and M. Kawase, *Journal of Solid State Chemistry*, **121**, 423–429 (1996).
36. Y. Fukuda, (2009) https://iopscience.iop.org/article/10.1149/1.3205790/meta.
37. Q. Xu, D. Huang, W. Chen, F. Zhang, and B. Wang, *Journal of Alloys and Compounds*, **429**, 34–39 (2007).
38. M. M. Natile, F. Poletto, A. Galenda, A. Glisenti, T. Montini, L. D. Rogatis, and P. Fornasiero, *Chem. Mater.*, **20**, 2314–2327 (2008).
39. Y. Leng, S. H. Chan, and Q. Liu, *International Journal of Hydrogen Energy*, **33**, 3808–3817 (2008).
40. F. Monaco, D. Ferreira-Sanchez, M. Hubert, B. Morel, D. Montinaro, D. Grolimund, and J. Laurencin, *International Journal of Hydrogen Energy* (2021).
41. Z. Pan, Q. Liu, L. Zhang, X. Zhang, and S. H. Chan, *J. Electrochem. Soc.*, **162**, F1316 (2015).
42. J. Szász, F. Wankmüller, V. Wilde, H. Störmer, D. Gerthsen, N. H. Menzler, and E. Ivers-Tiffée, *J. Electrochem. Soc.*, **165**, F898 (2018).
43. D. Kim, J. W. Park, B.-H. Yun, J. H. Park, and K. T. Lee, *ACS Appl. Mater. Interfaces*, **11**, 31786–31792 (2019).
44. H. Wang and S. A. Barnett, *J. Electrochem. Soc.*, **165**, F564 (2018).
45. F. Baiutti, F. Chiabrera, M. Acosta, D. Diercks, D. Parfitt, J. Santiso, X. Wang, A. Cavallaro, A. Morata, H. Wang, A. Chroneos, J. MacManus-Driscoll, and A. Tarancon, *Nat Commun*, **12**, 2660 (2021).
46. W. Zhang, H. Wang, K. Guan, Z. Wei, X. Zhang, J. Meng, X. Liu, and J. Meng, *ACS Appl. Mater. Interfaces*, **11**, 26830–26841 (2019).
47. H. Jia, X. Zhang, Y. Xu, L. Zou, J.-M. Kim, P. Gao, M. H. Engelhard, Q. Li, C. Niu, B. E. Matthews, T. L. Lemmon, J. Hu, C. Wang, and W. Xu, *ACS Appl. Mater. Interfaces*, **13**, 44339–44347 (2021).
48. J. Song, W. Yan, H. Cao, Q. Song, H. Ding, Z. Lv, Y. Zhang, and Z. Sun, *Journal of Cleaner Production*, **215**, 570–581 (2019).
49. S. M. Hayes and E. A. McCullough, *Resources Policy*, **59**, 192–199 (2018).
50. G. Corbel, S. Mestiri, and P. Lacorre, *Solid State Sciences*, **7**, 1216–1224 (2005).
51. B. Fan, J. Yan, and X. Yan, *Solid State Sciences*, **13**, 1835–1839 (2011).
52. N. H. Menzler, F. Tietz, S. Uhlenbruck, H. P. Buchkremer, and D. Stöver, *J Mater Sci*, **45**, 3109–3135 (2010).
53. J. Jeong, A. K. Azad, H. Schlegl, B. Kim, S.-W. Baek, K. Kim, H. Kang, and J. H. Kim, *Journal of Solid State Chemistry*, **226**, 154–163 (2015).

54. Y.-F. Sun, Y.-Q. Zhang, B. Hua, Y. Behnamian, J. Li, S.-H. Cui, J.-H. Li, and J.-L. Luo, *Journal of Power Sources*, **301**, 237–241 (2016).
55. A. Sciazko, T. Shimura, Y. Komatsu, and N. Shikazono, *Journal of Thermal Science and Technology*, **16**, JTST0013–JTST0013 (2021).
56. A. Léon, S. Schlabach, and J. Villanova, *Journal of Power Sources*, **581**, 233410 (2023).
57. F. Monaco, thesis, Université Grenoble Alpes (2020) https://www.theses.fr/2020GRALI034.
58. J. Laurencin, M. Hubert, D. F. Sanchez, S. Pylypko, M. Morales, A. Morata, B. Morel, D. Montinaro, F. Lefebvre-Joud, and E. Siebert, *Electrochimica Acta*, **241**, 459–476 (2017).
59. J. Villanova, S. Schlabach, A. Brisse, and A. Léon, *Journal of Power Sources*, **421**, 100–108 (2019).
60. K. Chen and S. P. Jiang, *Electrochem. Energ. Rev.*, **3**, 730–765 (2020).
61. S. Uhlenbruck, T. Moskalewicz, N. Jordan, H.-J. Penkalla, and H. P. Buchkremer, *Solid State Ionics*, **180**, 418–423 (2009).
62. F. Tietz, Q. Fu, V. A. C. Haanappel, A. Mai, N. H. Menzler, and S. Uhlenbruck, *International Journal of Applied Ceramic Technology*, **4**, 436–445 (2007).
63. L. Bernadet, J. Segura-Ruiz, L. Yedra, S. Estrade, F. Peiró, D. Montinaro, M. Torrell, A. Morata, and A. Tarancón, *Journal of Power Sources*, **555**, 232400 (2023).
64. A. Mai, V. A. C. Haanappel, S. Uhlenbruck, F. Tietz, and D. Stöver, *Solid State Ionics*, **176**, 1341–1350 (2005).
65. R. Knibbe, J. Hjelm, M. Menon, N. Pryds, M. Søgaard, H. J. Wang, and K. Neufeld, *Journal of the American Ceramic Society*, **93**, 2877–2883 (2010).
66. N. Jordan, W. Assenmacher, S. Uhlenbruck, V. A. C. Haanappel, H. P. Buchkremer, D. Stöver, and W. Mader, *Solid State Ionics*, **179**, 919–923 (2008).
67. J. Railsback, S. H. Choi, and S. A. Barnett, *Solid State Ionics*, **335**, 74–81 (2019).
68. K. M. Paciejewska, Y. Yu, S. Kühn, A. Weber, and M. Kleber, *Journal of the Ceramic Society of Japan*, **123**, 171–177 (2015).
69. F. Tietz, A. Mai, and D. Stöver, *Solid State Ionics*, **179**, 1509–1515 (2008).
70. Z. Lu, S. Darvish, J. Hardy, J. Templeton, J. Stevenson, and Y. Zhong, *J. Electrochem. Soc.*, **164**, F3097 (2017).
71. J. P. Stempien, Q. Sun, and S. H. Chan, *Journal of Power Technologies*, **Vol. 93** (2013).
72. Z. Li, H. Zhang, H. Xu, and J. Xuan, *Renewable and Sustainable Energy Reviews*, **141**, 110863 (2021).
73. S. B. Beale, M. Andersson, C. Boigues-Muñoz, H. L. Frandsen, Z. Lin, S. J. McPhail, M. Ni, B. Sundén, A. Weber, and A. Z. Weber, *Progress in Energy and Combustion Science*, **85**, 100902 (2021).
74. P. Fan, G. Li, Y. Zeng, and X. Zhang, *International Journal of Thermal Sciences*, **77**, 1–10 (2014).
75. T. Abdullah and L. Liu, *International Journal of Hydrogen Energy*, **41**, 13632–13643 (2016).
76. H. Moussaoui, J. Laurencin, Y. Gavet, G. Delette, M. Hubert, P. Cloetens, T. Le Bihan, and J. Debayle, *Computational Materials Science*, **143**, 262–276 (2018).
77. Z. Yan, A. He, S. Hara, and N. Shikazono, *Energy Conversion and Management*, **198**, 111916 (2019).
78. T. Parhizkar and S. Hafeznezami, *Energy Conversion and Management*, **158**, 81–91 (2018).
79. A. Donazzi, S. De Pascali, F. Garavaglia, and M. Bracconi, *Electrochimica Acta*, **365**, 137346 (2021).
80. X. Wu and Q. Ye, *Journal of Power Sources*, **321**, 47–56 (2016).
81. S. Gao, J. Li, and Z. Lin, *Journal of Power Sources*, **255**, 144–150 (2014).

82. J. I. Gazzarri and O. Kesler, *Journal of Power Sources*, **167**, 100–110 (2007).
83. A. Cadi-Essadek, A. Roldan, and N. H. de Leeuw, *Faraday Discussions*, **208**, 87–104 (2018).
84. S. N. Rashkeev and M. V. Glazoff, *International Journal of Hydrogen Energy*, **37**, 1280–1291 (2012).
85. Y. Sun, C. Wang, and Y. Chen, *Journal of Power Sources*, **233**, 131–138 (2013).
86. M. S. Sohal, A. V. Virkar, S. N. Rashkeev, and M. V. Glazoff, *Modeling Degradation in Solid Oxide Electrolysis Cells*, Idaho National Laboratory (INL), (2010).
87. L. Ma, P. Priya, and N. R. Aluru, *J. Electrochem. Soc.*, **165**, F1232 (2018).
88. B. Ren, J. Li, G. Wen, L. Ricardez−Sandoval, and E. Croiset, *J. Phys. Chem. C*, **122**, 21151–21161 (2018).
89. X. Liu, C. L. Martin, G. Delette, J. Laurencin, D. Bouvard, and T. Delahaye, *Journal of Power Sources*, **196**, 2046–2054 (2011).
90. G. Gaiselmann, M. Neumann, L. Holzer, T. Hocker, M. R. Prestat, and V. Schmidt, *Computational Materials Science*, **67**, 48–62 (2013).
91. S. Kakaç, A. Pramuanjaroenkij, and X. Y. Zhou, *International Journal of Hydrogen Energy*, **32**, 761–786 (2007).
92. C. O. Colpan, I. Dincer, and F. Hamdullahpur, *International Journal of Energy Research*, **32**, 336–355 (2008).
93. C. Bao, Y. Wang, D. Feng, Z. Jiang, and X. Zhang, *Progress in Energy and Combustion Science*, **66**, 83–140 (2018).
94. V. M. Janardhanan and O. Deutschmann, *Journal of Power Sources*, **162**, 1192–1202 (2006).
95. G. Hawkes, J. O'Brien, C. Stoots, and B. Hawkes, *International Journal of Hydrogen Energy*, **34**, 4189–4197 (2009).
96. H. Paradis, M. Andersson, J. Yuan, and B. Sundén, *Journal of Fuel Cell Science and Technology*, **8** (2011).
97. A. Al-Masri, M. Peksen, L. Blum, and D. Stolten, *Applied Energy*, **135**, 539–547 (2014).
98. H. Geisler, A. Kromp, A. Weber, and E. Ivers-Tiffée, *J. Electrochem. Soc.*, **161**, F778 (2014).
99. M. Peksen, *International Journal of Hydrogen Energy*, **39**, 5137–5147 (2014).
100. H. K. Versteeg and W. Malalasekera, *An Introduction to Computational Fluid Dynamics: The Finite Volume Method*, p. 530, Pearson Education, (2007).
101. *SimScale* https://www.simscale.com/docs/simwiki/cfd-computational-fluid-dynamics/what-is-cfd-computational-fluid-dynamics/.
102. D. Grondin, J. Deseure, P. Ozil, J.-P. Chabriat, B. Grondin-Perez, and A. Brisse, *Journal of Power Sources*, **196**, 9561–9567 (2011).
103. J. H. Kim, W. K. Liu, and C. Lee, *Comput Mech*, **44**, 683–703 (2009).
104. G. Reiss, H. L. Frandsen, W. Brandstätter, and A. Weber, *Journal of Power Sources*, **273**, 1006–1015 (2015).
105. L. Wang, M. Pérez-Fortes, H. Madi, S. Diethelm, J. V. herle, and F. Maréchal, *Applied Energy*, **211**, 1060–1079 (2018).
106. A. Bertei, G. Arcolini, J. P. Ouweltjes, Z. Wuillemin, P. Piccardo, and C. Nicolella, *Electrochimica Acta*, **208**, 129–141 (2016).
107. W. G. Bessler, S. Gewies, and M. Vogler, *Electrochimica Acta*, **53**, 1782–1800 (2007).

108. E. Effori, J. Laurencin, E. D. R. Silva, M. Hubert, T. David, M. Petitjean, G. Geneste, L. Dessemond, and E. Siebert, *J. Electrochem. Soc.*, **168**, 044520 (2021).
109. F. Monaco, E. Effori, M. Hubert, E. Siebert, G. Geneste, B. Morel, E. Djurado, D. Montinaro, and J. Laurencin, *Electrochimica Acta*, **389**, 138765 (2021).
110. L. Bernadet, J. Laurencin, G. Roux, D. Montinaro, F. Mauvy, and M. Reytier, *Electrochimica Acta*, **253**, 114–127 (2017).
111. J. Laurencin, D. Kane, G. Delette, J. Deseure, and F. Lefebvre-Joud, *Journal of Power Sources*, **196**, 2080–2093 (2011).
112. E. D. R. Silva, M. Hubert, B. Morel, H. Moussaoui, J. Debayle, and J. Laurencin, *ECS Trans.*, **103**, 893 (2021).
113. S. H. Chan and Z. T. Xia, *Journal of Applied Electrochemistry*, **32**, 339–347 (2002).
114. A. V. Virkar, J. Chen, C. W. Tanner, and J.-W. Kim, *Solid State Ionics*, **131**, 189–198 (2000).
115. A. Godula-Jopek, *Hydrogen Production: by Electrolysis*, p. 436, John Wiley & Sons, (2015).
116. J. Udagawa, P. Aguiar, and N. P. Brandon, *Journal of Power Sources*, **166**, 127–136 (2007).
117. R. Guidelli, R. G. Compton, J. M. Feliu, E. Gileadi, J. Lipkowski, W. Schmickler, and S. Trasatti, *Pure and Applied Chemistry*, **86**, 245–258 (2014).
118. J. O. Bockris and Z. Nagy, *J. Chem. Educ.*, **50**, 839 (1973).
119. J. A. V. Butler, *Trans. Faraday Soc.*, **19**, 729 (1924).
120. J. A. V. Butler, *Trans. Faraday Soc.*, **19**, 734 (1924).
121. T. Erdey-Grúz and M. Volmer, *Zeitschrift für Physikalische Chemie*, **150A**, 203–213 (1930).
122. S. Primdahl and M. Mogensen, *J. Electrochem. Soc.*, **145**, 2431 (1998).
123. H. Zhu and R. J. Kee, *Journal of Power Sources*, **117**, 61–74 (2003).
124. J. Laurencin, M. Hubert, K. Couturier, T. L. Bihan, P. Cloetens, F. Lefebvre-Joud, and E. Siebert, *Electrochimica Acta*, **174**, 1299–1316 (2015).
125. C. Graves, S. D. Ebbesen, M. Mogensen, and K. S. Lackner, *Renewable and Sustainable Energy Reviews*, **15**, 1–23 (2011).
126. D. Udomsilp, C. Lenser, O. Guillon, and N. H. Menzler, *Energy Technology*, **9**, 2001062 (2021).
127. M. Preininger, B. Stoeckl, V. Subotić, and C. Hochenauer, *Energy Conversion and Management*, **203**, 112215 (2020).
128. X. Zhang, J. E. O'Brien, R. C. O'Brien, and G. K. Housley, *Journal of Power Sources*, **242**, 566–574 (2013).
129. S. H. Jensen, P. H. Larsen, and M. Mogensen, *International Journal of Hydrogen Energy*, **32**, 3253–3257 (2007).
130. A. Nechache, A. Mansuy, M. Petitjean, J. Mougin, F. Mauvy, B. A. Boukamp, M. Cassir, and A. Ringuedé, *Electrochimica Acta*, **210**, 596–605 (2016).
131. D. Montinaro, A. R. Contino, A. Dellai, and M. Rolland, *International Journal of Hydrogen Energy*, **39**, 21638–21646 (2014).
132. S. Khan, S. M. A. Rizvi, and S. Urooj, in *2016 3rd International Conference on Computing for Sustainable Global Development (INDIACom)*,, p. 1563–1567 (2016).
133. P. Caliandro, A. Nakajo, S. Diethelm, and J. Van herle, *Journal of Power Sources*, **436**, 226838 (2019).
134. A. Hauch, S. H. Jensen, S. Ramousse, and M. Mogensen, *J. Electrochem. Soc.*, **153**, A1741 (2006).

135. S.-D. Kim, H. Moon, S.-H. Hyun, J. Moon, J. Kim, and H.-W. Lee, *Journal of Power Sources*, **163**, 392–397 (2006).
136. A. Hauch, K. Brodersen, M. Chen, and M. B. Mogensen, *Solid State Ionics*, **293**, 27–36 (2016).
137. Q. Fang, L. Blum, and D. Stolten, *J. Electrochem. Soc.*, **166**, F1320 (2019).
138. D. Simwonis, F. Tietz, and D. Stöver, *Solid State Ionics*, **132**, 241–251 (2000).
139. J. P. Trembly, R. S. Gemmen, and D. J. Bayless, *Journal of Power Sources*, **169**, 347–354 (2007).
140. A. Hauch, S. D. Ebbesen, S. H. Jensen, and M. Mogensen, *J. Electrochem. Soc.*, **155**, B1184 (2008).
141. X. Sun, P. V. Hendriksen, M. B. Mogensen, and M. Chen, *Fuel Cells*, **19**, 740–747 (2019).
142. J. Schefold, A. Brisse, and F. Tietz, *J. Electrochem. Soc.*, **159**, A137 (2011).
143. G. Schiller, A. Ansar, M. Lang, and O. Patz, *J Appl Electrochem*, **39**, 293–301 (2009).
144. L. Blum, U. Packbier, I. C. Vinke, and L. G. J. de Haart, *Fuel Cells*, **13**, 646–653 (2013).
145. F. Tietz, V. A. C. Haanappel, A. Mai, J. Mertens, and D. Stöver, *Journal of Power Sources*, **156**, 20–22 (2006).
146. C. Dellen, S. Tardif, R. Purohit, J.-S. Micha, O. Guillon, and N. H. Menzler, *ECS Trans.*, **111**, 1845 (2023).
147. N. H. Menzler, D. Sebold, Y. J. Sohn, and S. Zischke, *Journal of Power Sources*, **478**, 228770 (2020).
148. D. Vladikova, B. Burdin, A. Sheikh, P. Piccardo, M. Krapchanska, D. Montinaro, and R. Spotorno, *Energies*, **15**, 3287 (2022).
149. A. Hagen, in *Fuel Cells : Data, Facts and Figures*,, p. 304–320, John Wiley & Sons, Ltd (2016).
150. Department of Energy, DOE Technical Targets for Fuel Cell Systems for Stationary (Combined Heat and Power) Applications, *Energy.gov* (2023), https://www.energy.gov/eere/fuelcells/doe-technical-targets-fuel-cell-systems-stationary-combined-heat-and-power.
151. M. M. Whiston, I. M. L. Azevedo, S. Litster, C. Samaras, K. S. Whitefoot, and J. F. Whitacre, *Joule*, **3**, 2060–2065 (2019).
152. C. E. Frey, Q. Fang, D. Sebold, L. Blum, and N. H. Menzler, *J. Electrochem. Soc.*, **165**, F357 (2018).
153. M. Trini, A. Hauch, S. De Angelis, X. Tong, P. V. Hendriksen, and M. Chen, *Journal of Power Sources*, **450**, 227599 (2020).
154. Department of Energy, Technical Targets for High Temperature Electrolysis, *Energy.gov* (2023), https://www.energy.gov/eere/fuelcells/technical-targets-high-temperature-electrolysis.
155. Department of Energy, Reversible Fuel Cell Targets, *Energy.gov* (2023), https://www.hydrogen.energy.gov/pdfs/20001-reversible-fuel-cell-targets.pdf.
156. M. Lamagna, D. Groppi, and B. Nastasi, *International Journal of Hydrogen Energy*, **48**, 27033–27058 (2023).
157. B. Königshofer, M. Höber, G. Nusev, P. Boškoski, C. Hochenauer, and V. Subotić, *Journal of Power Sources*, **523**, 230982 (2022).
158. B. Königshofer, G. Pongratz, G. Nusev, P. Boškoski, M. Höber, Đ. Juričić, M. Kusnezoff, N. Trofimenko, H. Schröttner, C. Hochenauer, and V. Subotić, *Journal of Power Sources*, **497**, 229875 (2021).
159. E. Dogdibegovic, Y. Wang, and X.-D. Zhou, *Next Energy*, **1**, 100001 (2023).
160. M. P. Hoerlein, M. Riegraf, R. Costa, G. Schiller, and K. A. Friedrich, *Electrochimica Acta*, **276**, 162–175 (2018).
161. A. Ploner, A. Hagen, and A. Hauch, *Journal of Power Sources*, **395**, 379–385 (2018).
162. M. Kim, H. Muroyama, T. Matsui, and K. Eguchi, *J. Electrochem. Soc.*, **166**, F1269 (2019).

163. E. Lay-Grindler, J. Laurencin, J. Villanova, P. Cloetens, P. Bleuet, A. Mansuy, J. Mougin, and G. Delette, *Journal of Power Sources*, **269**, 927–936 (2014).
164. A. Hauch, S. H. Jensen, J. B. Bilde-Sørensen, and M. Mogensen, *J. Electrochem. Soc.*, **154**, A619 (2007).
165. B. Wei, K. Chen, L. Zhao, Z. Lü, and S. P. Jiang, *Phys. Chem. Chem. Phys.*, **17**, 1601–1609 (2014).
166. J. A. Schuler, H. Yokokawa, C. F. Calderone, Q. Jeangros, Z. Wuillemin, A. Hessler-Wyser, and J. Van herle, *Journal of Power Sources*, **201**, 112–120 (2012).
167. H. Yokokawa, N. Sakai, T. Kawada, and M. Dokiya, *Solid State Ionics*, **52**, 43–56 (1992).
168. F. Wankmüller, J. Szász, J. Joos, V. Wilde, H. Störmer, D. Gerthsen, and E. Ivers-Tiffée, *Journal of Power Sources*, **360**, 399–408 (2017).
169. S. J. McPhail, S. Frangini, J. Laurencin, E. Effori, A. Abaza, A. K. Padinjarethil, A. Hagen, A. Léon, A. Brisse, D. Vladikova, B. Burdin, F. R. Bianchi, B. Bosio, P. Piccardo, R. Spotorno, H. Uchida, P. Polverino, E. A. Adinolfi, F. Postiglione, J.-H. Lee, H. Moussaoui, and J. Van herle, *Electrochemical Science Advances*, **2**, e2100024 (2022).
170. C. Endler-Schuck, A. Leonide, A. Weber, S. Uhlenbruck, F. Tietz, and E. Ivers-Tiffée, *Journal of Power Sources*, **196**, 7257–7262 (2011).
171. R. Knibbe, M. L. Traulsen, A. Hauch, S. D. Ebbesen, and M. Mogensen, *J. Electrochem. Soc.*, **157**, B1209 (2010).
172. M. Z. Khan, R.-H. Song, A. Hussain, S.-B. Lee, T.-H. Lim, and J.-E. Hong, *Journal of the European Ceramic Society*, **40**, 1407–1417 (2020).
173. M. Z. Khan, M. T. Mehran, R.-H. Song, S.-B. Lee, and T.-H. Lim, *International Journal of Hydrogen Energy*, **43**, 12346–12357 (2018).
174. E. Bucher and W. Sitte, *Solid State Ionics*, **192**, 480–482 (2011).
175. P. Hjalmarsson, M. Søgaard, and M. Mogensen, *Solid State Ionics*, **179**, 1422–1426 (2008).
176. R. R. Liu, S. H. Kim, S. Taniguchi, T. Oshima, Y. Shiratori, K. Ito, and K. Sasaki, *Journal of Power Sources*, **196**, 7090–7096 (2011).
177. R. Vaßen, D. Simwonis, and D. Stöver, *Journal of Materials Science*, **36**, 147–151 (2001).
178. M. Hubert, J. Laurencin, P. Cloetens, B. Morel, D. Montinaro, and F. Lefebvre-Joud, *Journal of Power Sources*, **397**, 240–251 (2018).
179. F. Monaco, M. Hubert, J. Vulliet, J. P. Ouweltjes, D. Montinaro, P. Cloetens, P. Piccardo, F. Lefebvre-Joud, and J. Laurencin, *J. Electrochem. Soc.*, **166**, F1229 (2019).
180. M. B. Mogensen, A. Hauch, X. Sun, M. Chen, Y. Tao, S. D. Ebbesen, K. V. Hansen, and P. V. Hendriksen, *Fuel Cells*, **17**, 434–441 (2017).
181. L. Rorato, Y. Shang, S. Yang, M. Hubert, K. Couturier, L. Zhang, J. Vulliet, M. Chen, and J. Laurencin, *J. Electrochem. Soc.*, **170**, 034504 (2023).
182. Q. Fang, C. E. Frey, N. H. Menzler, and L. Blum, *J. Electrochem. Soc.*, **165**, F38–F45 (2018).
183. Y. Wang, C. Wu, B. Zu, M. Han, Q. Du, M. Ni, and K. Jiao, *Journal of Power Sources*, **516**, 230660 (2021).
184. Y. Lei, Y.-L. Lee, W. K. Epting, J. H. Mason, T.-L. Cheng, H. Abernathy, G. Hackett, and Y.-H. Wen, *Journal of Power Sources*, **545**, 231924 (2022).
185. V. Bilalis, B. Li, H. L. Frandsen, and M. Chen, *ECS Trans.*, **111**, 429 (2023).
186. D. The, S. Grieshammer, M. Schroeder, M. Martin, M. Al Daroukh, F. Tietz, J. Schefold, and A. Brisse, *Journal of Power Sources*, **275**, 901–911 (2015).

187. H. Mitsuyasu, Y. Nonaka, and K. Eguchi, *Solid State Ionics*, **113–115**, 279–284 (1998).
188. H. Ding, A. V. Virkar, M. Liu, and F. Liu, *Physical Chemistry Chemical Physics*, **15**, 489–496 (2013).
189. W. Jung and H. L. Tuller, *Energy & Environmental Science*, **5**, 5370–5378 (2012).
190. D. Oh, D. Gostovic, and E. D. Wachsman, *Journal of Materials Research*, **27**, 1992–1999 (2012).
191. L. C. Baqué, A. L. Soldati, E. Teixeira-Neto, H. E. Troiani, A. Schreiber, and A. C. Serquis, *Journal of Power Sources*, **337**, 166–172 (2017).
192. R. Knibbe, A. Hauch, J. Hjelm, S. Ebbesen, and M. Mogensen, *Green*, **1**, 141 (2011).
193. M. Morales, V. Miguel-Pérez, A. Tarancón, A. Slodczyk, M. Torrell, B. Ballesteros, J. P. Ouweltjes, J. M. Bassat, D. Montinaro, and A. Morata, *Journal of Power Sources*, **344**, 141–151 (2017).
194. W.-H. Kim, H.-S. Song, J. Moon, and H.-W. Lee, *Solid State Ionics*, **177**, 3211–3216 (2006).
195. A. Martínez-Amesti, A. Larrañaga, L. M. Rodríguez-Martínez, A. T. Aguayo, J. L. Pizarro, M. L. Nó, A. Laresgoiti, and M. I. Arriortua, *Journal of Power Sources*, **185**, 401–410 (2008).
196. H. Xu, K. Cheng, M. Chen, L. Zhang, K. Brodersen, and Y. Du, *Journal of Power Sources*, **441**, 227152 (2019).
197. J. C. De Vero, K. Develos-Bagarinao, H. Kishimoto, T. Ishiyama, K. Yamaji, T. Horita, and H. Yokokawa, *Journal of Power Sources*, **377**, 128–135 (2018).
198. T. Shimura, A. He, and N. Shikazono, *J. Electrochem. Soc.*, **166**, F821 (2019).
199. V. Wilde, H. Störmer, J. Szász, F. Wankmüller, E. Ivers-Tiffée, and D. Gerthsen, *ACS Appl. Energy Mater.*, **1**, 6790–6800 (2018).
200. K. Park, S. Yu, J. Bae, H. Kim, and Y. Ko, *International Journal of Hydrogen Energy*, **35**, 8670–8677 (2010).
201. Z. Sun, R. Wang, A. Y. Nikiforov, S. Gopalan, U. B. Pal, and S. N. Basu, *Journal of Power Sources*, **378**, 125–133 (2018).
202. M. A. Uddin, A. Aphale, B. Hu, S. J. Heo, U. Pasaogullari, and P. Singh, *J. Electrochem. Soc.*, **164**, F1342 (2017).
203. C. Endler-Schuck, J. Joos, C. Niedrig, A. Weber, and E. Ivers-Tiffée, *Solid State Ionics*, **269**, 67–79 (2015).
204. B. Wang, B. Zydorczak, D. Poulidi, I. S. Metcalfe, and K. Li, *Journal of Membrane Science*, **369**, 526–535 (2011).
205. J. Druce, H. Téllez, M. Burriel, M. D. Sharp, L. J. Fawcett, S. N. Cook, D. S. McPhail, T. Ishihara, H. H. Brongersma, and J. A. Kilner, *Energy & Environmental Science*, **7**, 3593–3599 (2014).
206. Z. Cai, M. Kubicek, J. Fleig, and B. Yildiz, *Chem. Mater.*, **24**, 1116–1127 (2012).
207. N. Ni, S. J. Cooper, R. Williams, N. Kemen, D. W. McComb, and S. J. Skinner, *ACS Appl. Mater. Interfaces*, **8**, 17360–17370 (2016).
208. M. Niania, R. Podor, B. Britton, S. Skinner, and J. Kilner, in *European Microscopy Congress 2016: Proceedings*,, p. 834–835, American Cancer Society (2016).
209. Y. Chen, H. Téllez, M. Burriel, F. Yang, N. Tsvetkov, Z. Cai, D. W. McComb, J. A. Kilner, and B. Yildiz, *Chem. Mater.*, **27**, 5436–5450 (2015).
210. E. Mutoro, E. J. Crumlin, M. D. Biegalski, H. M. Christen, and Y. Shao-Horn, *Energy & Environmental Science*, **4**, 3689–3696 (2011).
211. W. Lee and B. Yildiz, *ECS Trans.*, **57**, 2115 (2013).

212. M. Siebenhofer, T. M. Huber, G. Friedbacher, W. Artner, J. Fleig, and M. Kubicek, *J. Mater. Chem. A*, **8**, 7968–7979 (2020).

213. E. Mutoro, E. J. Crumlin, H. Pöpke, B. Luerssen, M. Amati, M. K. Abyaneh, M. D. Biegalski, H. M. Christen, L. Gregoratti, J. Janek, and Y. Shao-Horn, *J. Phys. Chem. Lett.*, **3**, 40–44 (2012).

214. L. Zhao, J. Drennan, C. Kong, S. Amarasinghe, and S. Ping Jiang, *Journal of Materials Chemistry A*, **2**, 11114–11123 (2014).

215. S. M. Choi, J. Ahn, J.-W. Son, J.-H. Lee, B.-K. Kim, K. J. Yoon, and H.-I. Ji, *ACS Appl. Mater. Interfaces*, **10**, 39608–39614 (2018).

216. M. Z. Khan, R.-H. Song, M. T. Mehran, S.-B. Lee, and T.-H. Lim, *Ceramics International*, **47**, 5839–5869 (2021).

217. A. Mahmood, S. Bano, J. H. Yu, and K.-H. Lee, *Energy*, **90**, 344–350 (2015).

218. L. Zhao, J. Zhang, T. Becker, and S. P. Jiang, *J. Electrochem. Soc.*, **161**, F687 (2014).

219. A. Mahmoud, M. Al Daroukh, M. Lipinska-Chwalek, M. Luysberg, F. Tietz, and R. P. Hermann, *Solid State Ionics*, **312**, 38–43 (2017).

220. J. Shen, B. Miao, Q. Liu, Y. Wu, S. H. Chan, Z. Zhong, and Z. Pan, *International Journal of Hydrogen Energy* (2022).

221. W. Lee, J. W. Han, Y. Chen, Z. Cai, and B. Yildiz, *J. Am. Chem. Soc.*, **135**, 7909–7925 (2013).

222. E. Yu. Konysheva, X. Xu, and J. T. S. Irvine, *Advanced Materials*, **24**, 528–532 (2012).

223. Z. Liu, L. Cheng, and M.-F. Han, *Journal of Power Sources*, **196**, 868–871 (2011).

224. K. K. Hansen and K. V. Hansen, *Solid State Ionics*, **178**, 1379–1384 (2007).

225. W. A. Harrison, *Phys. Rev. B*, **83**, 155437 (2011).

226. H. Kwon, W. Lee, and J. Woo Han, *RSC Advances*, **6**, 69782–69789 (2016).

227. D. Kim, R. Bliem, F. Hess, J.-J. Gallet, and B. Yildiz, *J. Am. Chem. Soc.*, **142**, 3548–3563 (2020).

228. R. D. Shannon, *Acta Cryst A*, **32**, 751–767 (1976).

229. *Saylor Academy* (2023) https://www.saylor.org.

230. E. J. Crumlin, E. Mutoro, Z. Liu, M. E. Grass, M. D. Biegalski, Y.-L. Lee, D. Morgan, H. M. Christen, H. Bluhm, and Y. Shao-Horn, *Energy & Environmental Science*, **5**, 6081–6088 (2012).

231. J. Kuyyalil, D. Newby, J. Laverock, Y. Yu, D. Cetin, S. N. Basu, K. Ludwig, and K. E. Smith, *Surface Science*, **642**, 33–38 (2015).

232. N. Tsvetkov, Q. Lu, L. Sun, E. J. Crumlin, and B. Yildiz, *Nature Materials*, **15**, 1010–1016 (2016).

233. B. Koo, K. Kim, J. K. Kim, H. Kwon, J. W. Han, and W. Jung, *Joule*, **2**, 1476–1499 (2018).

234. L.-W. Tai, M. M. Nasrallah, H. U. Anderson, D. M. Sparlin, and S. R. Sehlin, *Solid State Ionics*, **76**, 273–283 (1995).

235. S. Hashimoto, Y. Fukuda, M. Kuhn, K. Sato, K. Yashiro, and J. Mizusaki, *Solid State Ionics*, **186**, 37–43 (2011).

236. K. Świerczek, B. Dabrowski, L. Suescun, and S. Kolesnik, *Journal of Solid State Chemistry*, **182**, 280–288 (2009).

237. L.-W. Tai, M. M. Nasrallah, H. U. Anderson, D. M. Sparlin, and S. R. Sehlin, *Solid State Ionics*, **76**, 259–271 (1995).

238. Chen, Yu, and S. B. Adler, *Chem. Mater.*, **17**, 4537–4546 (2005).

239. R. Kiebach, W.-W. Zhang, W. Zhang, M. Chen, K. Norrman, H.-J. Wang, J. R. Bowen, R. Barfod, and P. V. Hendriksen, *Journal of Power Sources*, **283**, 151–161 (2015).

240. Z. He, L. Zhang, S. He, N. Ai, K. Chen, Y. Shao, and S. P. Jiang, *Journal of Power Sources*, **404**, 73–80 (2018).

241. S. He, M. Saunders, K. Chen, H. Gao, A. Suvorova, W. D. A. Rickard, Z. Quadir, C. Q. Cui, and S. P. Jiang, *J. Electrochem. Soc.*, **165**, F417–F429 (2018).

242. D. Zhang, M. L. Machala, D. Chen, Z. Guan, H. Li, S. Nemsak, E. J. Crumlin, H. Bluhm, and W. C. Chueh, *Chem. Mater.*, **32**, 2926–2934 (2020).

243. S.-S. Liu, K. Develos-Bagarinao, R. Achmad Budiman, T. Ishiyama, H. Kishimoto, and K. Yamaji, *Journal of Materials Chemistry A*, **11**, 21983–22000 (2023).

244. J. S. Hardy, C. A. Coyle, J. F. Bonnett, J. W. Templeton, N. L. Canfield, D. J. Edwards, S. M. Mahserejian, L. Ge, B. J. Ingram, and J. W. Stevenson, *Journal of Materials Chemistry A*, **6**, 1787–1801 (2018).

245. F. Willy Poulsen and N. van der Puil, *Solid State Ionics*, **53–56**, 777–783 (1992).

246. J. A. Labrincha, J. R. Frade, and F. M. B. Marques, *Solid State Ionics*, **99**, 33–40 (1997).

247. F. Wang, M. E. Brito, K. Yamaji, D.-H. Cho, M. Nishi, H. Kishimoto, T. Horita, and H. Yokokawa, *Solid State Ionics*, **262**, 454–459 (2014).

248. M. Z. Khan, M. T. Mehran, R.-H. Song, J.-W. Lee, S.-B. Lee, T.-H. Lim, and S.-J. Park, *Ceramics International*, **42**, 6978–6984 (2016).

249. T. Matsui, S. Li, Y. Inoue, N. Yoshida, H. Muroyama, and K. Eguchi, *ECS Trans.*, **91**, 1247 (2019).

250. V. M. Bekale, A. M. Huntz, C. Legros, G. Sattonnay, and F. Jomard, *Philosophical Magazine*, **88**, 1–19 (2008).

251. M. Kilo, G. Borchardt, B. Lesage, O. Kaïtasov, S. Weber, and S. Scherrer, *Journal of the European Ceramic Society*, **20**, 2069–2077 (2000).

252. M. Hubert, thesis, Université Grenoble Alpes (2017) https://tel.archives-ouvertes.fr/tel-01689775.

253. F. Tietz, D. Sebold, A. Brisse, and J. Schefold, *Journal of Power Sources*, **223**, 129–135 (2013).

254. Y. Lim, J. Park, H. Lee, M. Ku, and Y.-B. Kim, *Nano Energy*, **90**, 106524 (2021).

255. K. Develos-Bagarinao, R. A. Budiman, S.-S. Liu, T. Ishiyama, H. Kishimoto, and K. Yamaji, *Journal of Power Sources*, **453**, 227894 (2020).

256. J. C. D. Vero, K. Develos-Bagarinao, H. Kishimoto, T. Ishiyama, K. Yamaji, T. Horita, and H. Yokokawa, *J. Electrochem. Soc.*, **164**, F259 (2017).

257. M. Izuki, M. E. Brito, K. Yamaji, H. Kishimoto, D.-H. Cho, T. Shimonosono, T. Horita, and H. Yokokawa, *Journal of Power Sources*, **196**, 7232–7236 (2011).

258. A. L. Shaula, V. V. Kharton, F. M. B. Marques, A. V. Kovalevsky, A. P. Viskup, and E. N. Naumovich, *J Solid State Electrochem*, **10**, 28–40 (2006).

259. H. Y. Tu, Y. Takeda, N. Imanishi, and O. Yamamoto, *Solid State Ionics*, **117**, 277–281 (1999).

260. Y. Sun, S. He, M. Saunders, K. Chen, Z. Shao, and S. P. Jiang, *International Journal of Hydrogen Energy*, **46**, 2606–2616 (2021).

261. Y. Li, W. Zhang, Y. Zheng, J. Chen, B. Yu, Y. Chen, and M. Liu, *Chemical Society Reviews*, **46**, 6345–6378 (2017).

262. M. Kubicek, A. Limbeck, T. Frömling, H. Hutter, and J. Fleig, *J. Electrochem. Soc.*, **158**, B727 (2011).

263. M. Y. Lu, J. G. Railsback, H. Wang, Q. Liu, Y. A. Chart, S.-L. Zhang, and S. A. Barnett, *Journal of Materials Chemistry A*, **7**, 13531–13539 (2019).

264. K. Chen, S. He, N. Li, Y. Cheng, N. Ai, M. Chen, W. D. A. Rickard, T. Zhang, and S. P. Jiang, *Journal of Power Sources*, **378**, 433–442 (2018).

265. Y. Gong, D. Palacio, X. Song, R. L. Patel, X. Liang, X. Zhao, J. B. Goodenough, and K. Huang, *Nano Lett.*, **13**, 4340–4345 (2013).

266. G. Martinez-Criado, J. Villanova, R. Tucoulou, D. Salomon, J.-P. Suuronen, S. Laboure, C. Guilloud, V. Valls, R. Barrett, E. Gagliardini, Y. Dabin, R. Baker, S. Bohic, C. Cohen, and J. Morse, *Journal of Synchrotron Radiation*, **23**, 344–352 (2016).

267. H. Kim, Y. Meng, J.-L. Rouviére, D. Isheim, D. N. Seidman, and J.-M. Zuo, *Journal of Applied Physics*, **113**, 103511 (2013).

268. S. Iijima, I. Ohnishi, and Z. Liu, *Sci Rep*, **11**, 18022 (2021).

2. Materials and methods

This chapter is dedicated to the description of the studied cell, the experimental setup, as well as the tools used in the frame of the three-fold methodology presented in **Chapter I**. The testing protocol is described, along with the employed electrochemical characterizations and the operating conditions selected for the long-term tests. A brief description of the multiscale physics-based model is reported as well. Finally, the list of post-test characterization techniques is detailed.

2.1 Cell description

Figure 2-1 shows a schematic of a hydrogen electrode supported cell used in this thesis, which has a circular shape and an active area of 9.08 cm^2. The cells manufactured at CEA Le Ripault consist of a dense ceramic electrolyte sandwiched between two porous electrodes. The electrolyte is made of 8% yttria stabilized zirconia $Y_{0.16}Zr_{0.84}O_{1.92}$ (8YSZ) and it is ca. 8 µm thick. The oxygen electrode comprises a ca. 20 µm current collecting layer (CCL) made of lanthanum strontium cobaltite ferrite $La_{0.6}Sr_{0.4}Co_{0.2}Fe_{0.8}O_{3-\delta}$ (LSCF) and a ca. 20 µm functional layer (FL) made of 50/50 wt.% LSCF-$Ce_{0.8}Gd_{0.2}O_{2-\delta}$ (LSCF-GDC) composite material. A ca. 3 µm thick porous diffusion barrier layer (BL) in gadolinium-doped ceria $Ce_{0.8}Gd_{0.2}O_{2-\delta}$ (GDC) is added between the oxygen electrode and the electrolyte to minimize the inter-diffusion of elements between the oxygen electrode and the electrolyte, and the formation of insulating phases. The hydrogen electrode is made of a cermet material and it comprises a ca. 25 µm FL made of 54/46 wt.% Ni-8YSZ and a ca. 280 µm support layer (or substrate) made of 44/56 wt.% Ni-3YSZ.

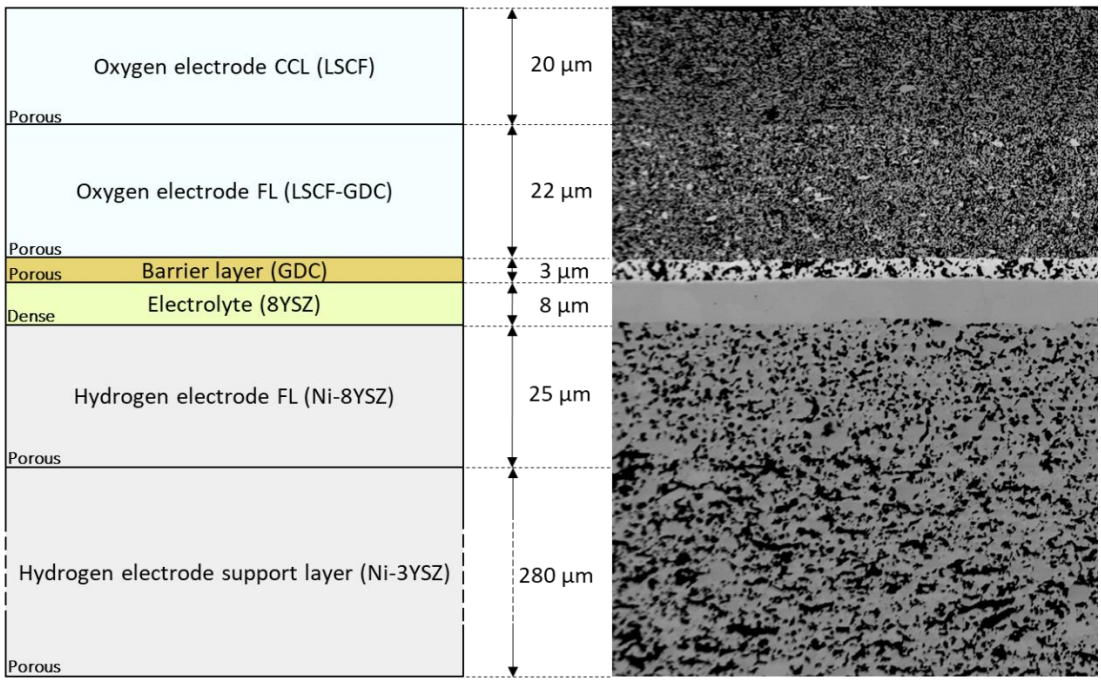

Figure 2-1. Schematics of the hydrogen electrode supported cell used in this work.

The nomenclature of the samples studied in this thesis is reported in Table 2-1, while the detailed operating conditions are presented in the Testing protocol section.

Table 2-1. Nomenclature for the samples studied in the thesis

Sample label	Description
Reference	Non-operated cell that has undergone cermet reduction
Aged750	Cell operated at 750 °C in SOEC, dry air, 2000 h
Aged800	Cell operated at 800 °C in SOEC, dry air, 2000 h
Aged850	Cell operated at 850 °C in SOEC, dry air, 2000 h
SOECdry	Cell operated at 800 °C in SOEC, dry air, 1000 h
SOEC3%	Cell operated at 800 °C in SOEC, 3% humid air, 1000 h
SOEC8%	Cell operated at 800 °C in SOEC, 8% humid air, 1000 h
SOFC8%	Cell operated at 800 °C in SOFC, 8% humid air, 1000 h
SOFCdry	Cell operated at 800 °C in SOFC, dry air, 2000 h
SOEC5k	Cell operated at 800 °C in SOEC, dry air, 5000 h

2.2 Electrochemical characterizations and long-term tests

The long-term tests under dry air conditions, along with the related electrochemical characterizations, were performed in collaboration with Léa Rorato during her Ph.D. in CEA.

2.2.1 Description of the experimental setup

Long-term tests were performed in an in-house test bench (see Figure 2-2). The circular cell is placed in a metallic housing inside a furnace. The fuel compartment of the cell is separated from the air compartment by a glass sealant (Schott G018-311) deposited at the periphery of the cell (1, 2). On both sides, the inlet gas flows are supplied by mass flow controllers (Brooks SLA5850S) at the cell centre and then they are distributed along the electrodes in a radial co-flow configuration. In order to collect the current at the electrodes surface, a Ni grid (100 meshes·cm^{-2}) and two gold grids (100 meshes·cm^{-2}) are used for the hydrogen electrode and the oxygen electrode, respectively. A ceramic Cr-free holder on top of the oxygen electrode is used to avoid the well-known Cr-poisoning effect (3) (see Figure 2-2a). In order to measure local i-V curves along the cell radius without cell segmentation (4), a specific interconnect design has been used at the air side (see Figure 2-2b) based on Ni alloy. More specifically, the current is measured at various positions along the cell radius. This was achieved using interconnect with nine cavities to allow the current-related wires to pass through the interconnect itself (2). An additional voltage-related wire is used to measure the voltage drop at the different positions. In order to decrease the contact resistance, a mechanical load of 600 g·cm^{-2} is applied on the cell.

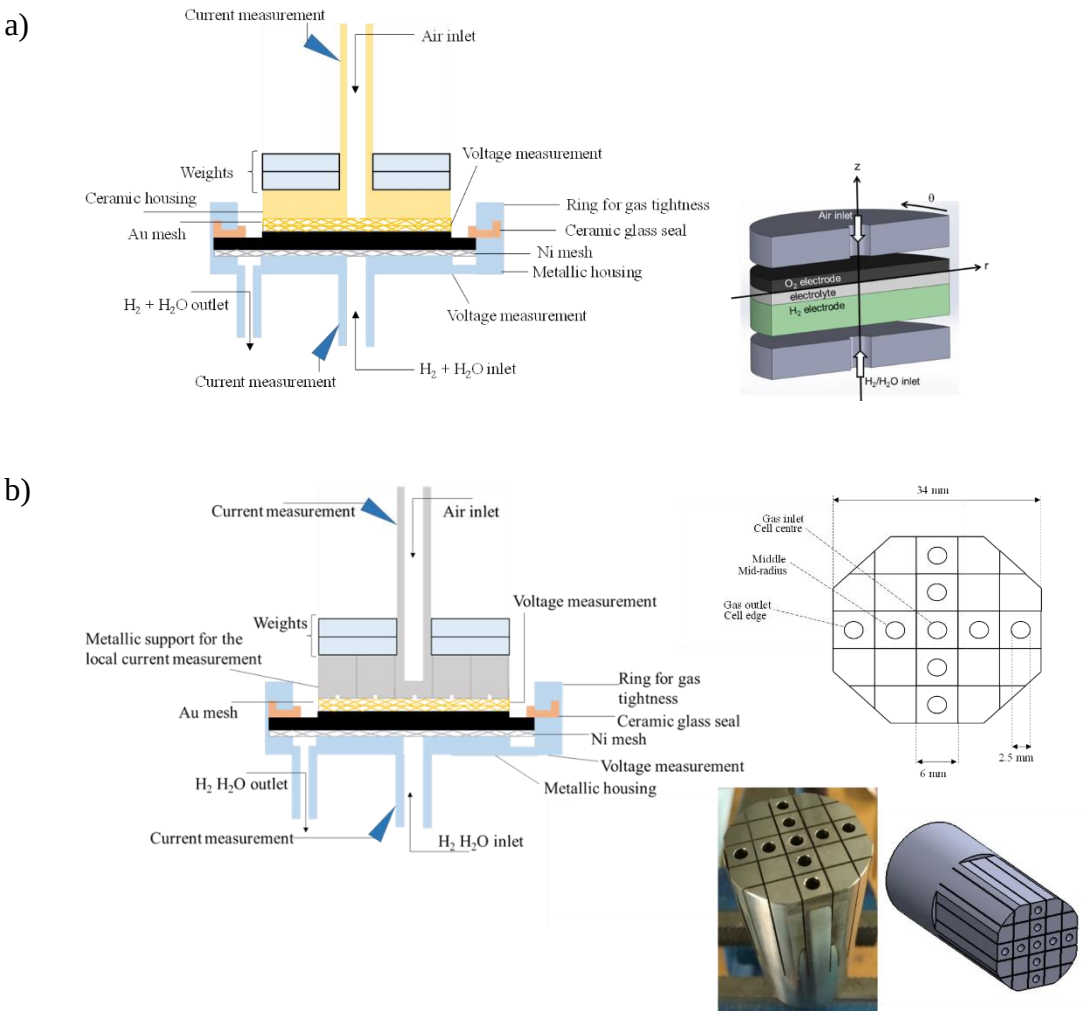

Figure 2-2. Cell housing and interconnects for collecting a) global measurements, b) local measurements along the cell radius.

The general scheme of the experimental setup is shown in Figure 2-3. The local temperatures along the whole experimental setup are measured using K-type thermocouples. The cell temperature is also measured with a K-type thermocouple, which is positioned close to the tested cell at the fuel outlet (T1 in Figure 2-3c).

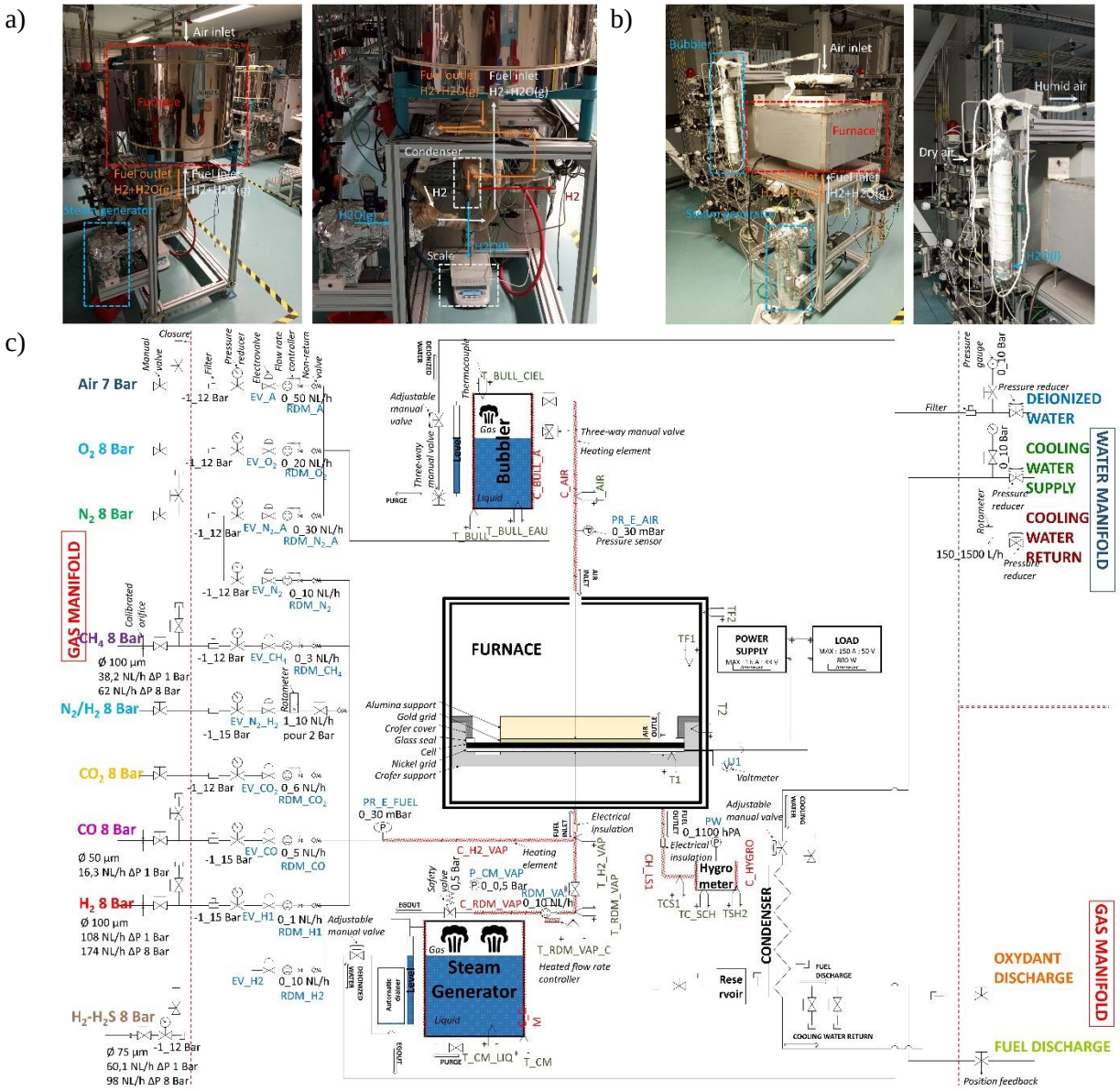

Figure 2-3. Test bench used for the long-term tests in a) dry air and b) humid air. c) Overall piping and instrumentation diagram (P&ID) of the experimental setup.

The local network available in the laboratory supplies liquid deionized water and gases to the setup. The quality of the employed deionized water and gases is reported in Table 2-2.

Table 2-2. Deionized water and gases quality.

Liquid deionized water	H_2	N_2
Ultra-pure water	N45 = 99.99995%	N51 = 99.999991%
Resistivity = 18 MΩ·cm	Impurities < 50 ppm	Impurities < 9 ppm

A steam generator operating under saturated vapour conditions allows the water phase change from liquid water to steam. The steam flow rate is controlled with a modified mass flow

controller that can operate at a temperature as high as 100 °C, with a maximum temperature of the mass flow controller equal to 60 °C (5). The steam is then mixed with hydrogen before entering fuel compartment of the cell. Compressed air is supplied in dry conditions, compliant with class [1:1:1] according to ISO 8573-1 (see Table 2-3). A bubbler is installed upstream of the inlet at the air compartment of the cell to introduce moisture into the air stream (see Figure 2-3b), for operation in humid air. A membrane made of a metallic porous medium is positioned inside the bubbler to produce micro water bubbles in the air flow. The bubbler temperature is controlled to reach the targeted air absolute humidity level, i.e. 24 °C and 41.5 °C to obtain 3% and 8% humid air, respectively. In order to avoid any possible condensation along the pipelines upstream and downstream the cell chamber, heating elements are wrapping the pipes and heated up to around 120-140 °C. At the outlet of the setup, a condenser is employed to separate the liquid water from the gas flow. In order to verify that the steam flow rate provided by the mass flow controller is correct, a weighing scale is used to measure the amount of condensed water over time.

Table 2-3. Air quality according to ISO 8573-1 class [1:1:1].

Solid particles			Water	Oil
Max. number of particles per m^3			Dew point under pressure	Total oil content (liquid, aerosols and vapours) in mg/m^3
0,1 - 0,5 microns	0,5 - 1 microns	1 - 5 microns		
≤ 20 000	≤ 400	≤ 10	≤ -70 °C	0.01

2.2.2 Testing protocol

The experiment starts with the mounting of the cell in its housing and applying the glass ceramic sealant to separate the fuel and air compartments. After that, the furnace is heated up to 860 °C at a heating rate of 1 $°C \cdot min^{-1}$ and held at this temperature for 90 minutes to complete the glass sealing process. During this process, 0.5 $Nl \cdot h^{-1}$ of N_2 and 0.5 $Nl \cdot h^{-1}$ of compressed dry air are supplied to the hydrogen and oxygen electrodes, respectively. Subsequently, the flow rates at the two electrodes are increased from 0.5 $Nl \cdot h^{-1}$ to 4 $Nl \cdot h^{-1}$ and the temperature is lowered to 800 °C to perform the cell cermet reduction. During this step, the N_2 gas flow at the hydrogen electrode is gradually replaced by H_2. To ensure the complete reduction of NiO to metallic Ni, a H_2 flow rate of 4 $Nl \cdot h^{-1}$ is maintained for at least 16 hours. Thereafter, initial electrochemical characterizations are carried out and, successively, the long-term test is started. The operating conditions are defined in the next section 2.2.2.2. Finally, at the end of the ageing test and after performing the final electrochemical characterizations, the setup is cooled down to room temperature at a cooling rate of 1 $°C \cdot min^{-1}$. During the cooling down, a mixture of nitrogen and hydrogen is supplied to the hydrogen electrode to maintain the cermet in its reduced state and prevent possible re-oxidation.

2.2.2.1 Electrochemical characterizations

As aforementioned, before and after the long-term tests, polarization curves (i-V) and electrochemical impedance spectroscopy (EIS) were selected as electrochemical characterizations. The reference and operating conditions for the electrochemical characterizations are defined in Table 2-4. The list of these electrochemical characterizations are presented in Table 2-5. Finally, the summary of the electrochemical characterizations and the related operating conditions at which they have been acquired is reported in Table 2-6.

Table 2-4. Reference and operating conditions for the electrochemical characterizations.

Parameters	Reference condition 1	Reference condition 2	Operating conditions
Temperature (°C)	750	800	Test*
H_2+H_2O flow ($NmL \cdot min^{-1} \cdot cm^{-2}$)	12	12	12
H_2/H_2O (%vol.)	10/90	10/90	Test*
Air flow ($NmL \cdot min^{-1} \cdot cm^{-2}$)	36	36	36
Humidity in air (%)	0	0	Test*

Test*: operating condition selected for the long-term test

Table 2-5. List of the electrochemical characterizations.

Parameters	EIS at OCV	EIS under polarization		i-V	
Operating mode	OCV	SOEC	SOFC	SOEC	SOFC
H_2/H_2O (%vol.)	10/90	10/90	90/10	10/90	90/10
DC current density to acquire the EIS ($A \cdot cm^{-2}$)	0	- 0.2	+ 0.2	-	-
i-V voltage limits (V)	-	-	-	1.4	0.7

Table 2-6. Summary of the electrochemical characterizations acquired in the various conditions.

Parameters	EIS at OCV			EIS under polarization			i-V		
Temperature (°C)	Test*	750	800	Test*	750	800	Test*	750	800
Operating mode	OCV	OCV	OCV	Test*	SOEC	SOEC	Test*	SOEC	SOEC
DC current density to acquire the EIS ($A \cdot cm^{-2}$)	0	0	0	+/- 0.2	- 0.2	- 0.2			
i-V voltage limits (V)							0.7 or 1.4	1.4	1.4
H_2+H_2O flow ($NmL \cdot min^{-1} \cdot cm^{-2}$)	12	12	12	12	12	12	12	12	12
H_2/H_2O (%vol.)	Test*	10/90	10/90	Test*	10/90	10/90	Test*	10/90	10/90
Air flow ($NmL \cdot min^{-1} \cdot cm^{-2}$)	36	36	36	36	36	36	36	36	36
Humidity in air (%)	Test*	0	0	Test*	3	8	Test*	0	0

Test*: operating condition selected for the long-term test

A. Polarization curves

The i-V curves were measured in galvanostatic mode before and after the long-term tests, using a controlled power supply in SOEC mode, which can work as an electric load as well for the SOFC mode. The employed current ramp has a rate equal to 20 $mA \cdot s^{-1}$, and the voltage limits are equal to 0.7 V in SOFC and 1.4 V in SOEC modes, respectively. As reported in Table 2-6, the polarization curves were performed in the reference conditions and in the conditions selected for each long-term test (see Table 2-4). The area specific resistance (ASR) in $ohm \cdot cm^2$ defined as $abs\left(\frac{dU}{di}\right)_{i_{DC}}$ can be extracted from i-V and compared to EIS measurements.

B. Electrochemical impedance spectroscopy

The EIS were performed in reference conditions to compare the different sets of experiments carried out at different operating conditions. In addition, impedance spectra are collected during the durability test every 500 hours at the operating conditions. The EIS were acquired using a potentiostat/galvanostat (Autolab PGSTAT-302N) equipped with a frequency response analyzer module (FRA) and a 20 A current booster. The EIS measurements were performed at the open circuit voltage (OCV) by imposing a sinusoidal current with an amplitude of 100 mA, and under polarization at +/- 0.2 $A \cdot cm^2$ with an amplitude of 50 mA, in the frequency range of 10^{-2} to 10^4 Hz. The raw data were collected using the NOVA ver. 1.11 software. Thereafter, the raw impedance spectra at OCV were post-treated by using the Zview ver. 2.70 software based on equivalent electric circuit model (EECM) (see Figure 2-4) to remove the inductive behaviour due to electrical wiring. The frequency range of the corrected EIS has been extended compared to the raw EIS, from 10^{-2} – 10^4 Hz to 10^{-3} – 10^6 Hz.

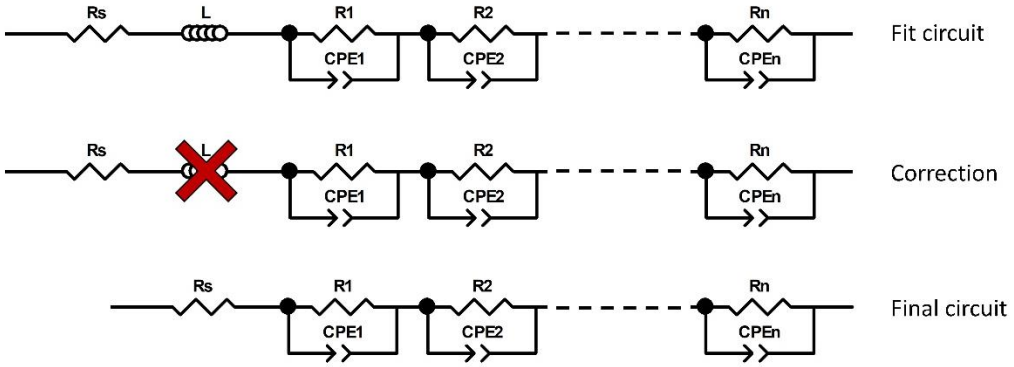

Figure 2-4. Equivalent electric circuit model (EECM) used to fit and correct the experimental EIS.

2.2.2.2 Long-term tests

Long-term tests were conducted under various operating conditions to evaluate the effect of operating temperatures (i.e. 750°C, 800°C and 850°C), SOFC and SOEC operating modes, and harsh conditions for the oxygen electrode by introducing 3-8% moisture at the air side. The tests performed in dry air conditions have a duration of 2000 h, while the ageing time for the tests in humid air conditions is 1000 h. The inlet flow at the hydrogen electrode is 12 $NmL \cdot min^{-1} \cdot cm^{-2}$ with a composition of 10/90 H_2/H_2O in SOEC or 90/10 H_2/H_2O in SOFC for the hydrogen electrode. At the oxygen electrode side, 36 $NmL \cdot min^{-1} \cdot cm^{-2}$ of compressed air are supplied in both SOEC/SOFC modes. Finally, the operating current density is +1 $A \cdot cm^{-2}$ in SOFC mode and -1 $A \cdot cm^{-2}$ in SOEC mode. The list of the long-term tests carried out in the frame of this thesis on complete cells is reported in Table 2-7. The 5000 h test carried out during the thesis will be discussed in the perspectives at the end of the manuscript. The related durability curve and EIS evolution are reported in the **Annex** of this manuscript.

Table 2-7. Long-term tests operating conditions for complete cells

Parameters	Aged750	Aged800	Aged850	SOECdry	SOEC3%	SOEC8%	SOFC8%	SOFCdry	SOEC5k
Ageing time (h)	2000	2000	2000	1000	1000	1000	1000	2000	5000
Temperature (°C)	750	800	850	800	800	800	800	800	800
Operating mode	SOEC	SOEC	SOEC	SOEC	SOEC	SOEC	SOFC	SOFC	SOEC
Current density ($A \cdot cm^{-2}$)	-1	-1	-1	-1	-1	-1	+1	+1	-1
Gas flow H_2+H_2O ($NmL \cdot min^{-1} \cdot cm^{-2}$)	12	12	12	12	12	12	12	12	12
Gas composition H_2/H_2O (%vol.)	10/90	10/90	10/90	10/90	10/90	10/90	90/10	90/10	10/90
Gas flow air ($NmL \cdot min^{-1} \cdot cm^{-2}$)	36	36	36	36	36	36	36	36	36
Humidity introduced in the air (%)	0	0	0	0	3	8	8	0	0

2.3 Multiscale physics-based model

As reported in **Chapter I**, the multiscale physics-based model available at the laboratory has been adapted on the studied cell. It includes a morphology model able to reproduce the electrode microstructures, a microscale electrode kinetic model describing the reaction mechanism in elementary steps, and a macroscale cell-level model that takes into account the design of the experimental setup under study. Within the thesis, the model is used to simulate the electrochemical response of the cell, in terms of both i-V curves (local and global) and impedance spectra. It allows the interpretation of the EIS experimental data by identifying the various contributions considered in the reaction mechanism and investigating their evolution after ageing. A more detailed description of the multiscale physics-based model is presented in the **Chapter III** of the manuscript. The work on the multiscale model was done in collaboration with Eduardo Da Rosa Silva during his post-doc in CEA.

2.4 Post-test characterization techniques

The morphology and the microstructure of the cell were studied by using SEM and FIB-SEM techniques. In order to investigate the elemental composition, the surface chemistry and the

chemical environment of the cell, SIMS, EDS and XPS techniques were selected. Finally, APT and STEM-EDS techniques were employed to achieve the atomic scale resolution and study the phenomena involved within the oxygen electrode.

The post-test characterizations presented in this thesis were performed in the frame of a collaboration with other laboratories. Thomas David (3D FIB-SEM and STEM-EDS), Laure Guetaz (STEM-EDS) and Anass Benayad (XPS) carried out the characterizations at the CEA DTNM in France. Katherine Develos-Bagarinao performed the SIMS analyses at AIST in Japan. Isabelle Martin did APT characterizations at CAMECA in the United States. Vincent Martin performed ICP-MS analysis at the LEPMI EIP in France.

The data acquisition of the synchrotron post-test characterizations was carried out with the help of Dario Ferreira Sanchez at PSI in Switzerland and with the help of Julie Villanova at ERSF in France. The data treatment was performed in our laboratory, in the frame of this thesis. This work was done in collaboration with Ozden Celikbilek, especially for the XPS and XRD analyses.

2.4.1 Electrode morphology observation

2.4.1.1 SEM

A field emission gun scanning electron microscope (FEG-SEM Zeiss Merlin, Germany) was used to study the microstructure of the electrodes. The accelerating voltage was 3 kV and the working distance was approximately 8-10 mm. The samples were first impregnated with a polymer resin (Epofix, Denmark) to fill the pores and then polished using a 0.25 mm diamond spray. To prevent charging, the polished cross-section was coated with a thin layer of carbon.

2.4.1.2 3D FIB-SEM

3D FIB-SEM data were obtained using a Zeiss Crossbeam 550 system. The three-dimensional images of each sample have a pixel size of 10 nm and an inter-slice distance of 10 nm, covering in a cubic voxel of 10x10x10 nm^3. The FIB milling was performed at 30 kV with a current of 3 nA, while operating the electron column at 1.5 kV and 1 nA. Images from both InLens and SE2 detectors were collected at the same time. Image processing prior to segmentation were done using home-made Python scripts based on common image processing Python libraries, such as numpy and scikit-image. This image pre-treatment included aligning each slice, homogenising contrast and brightness in all three directions, as well as curtain effect correction. In addition, resampling in the z-direction were performed to correct for inhomogeneous distances between slices during milling and imaging. The segmentation was carried out using machine learning-based random forest classifier on the Ilastik software (1, 6), considering the ‘pixel classification’ workflow. Sub-volumes measuring 100-300 pixels in all directions were selected for the annotation and training phase.

2.4.2 Chemical and structural analyses

2.4.2.1 ICP-MS

Inductively coupled plasma mass spectroscopy (ICP-MS, PerkinElmer NexION 2000) was used to study the LSCF powder composition. For this purpose, 0.1 g of LSCF powder was dissolved in 100 ml of a 2% nitric acid solution.

2.4.2.2 EDS

Energy-dispersive X-ray spectroscopy (EDS) detection is based on the emission of photons due to the interaction between the incident electrons and the atoms within the sample. Each element is defined by its EDS spectrum. A specific EDS detector is used to analyse these photons related to the elements contained in the sample and to provide the spectra of the different elements-related peaks. EDS cartographies of La, Sr, Co, Fe, Ce, Gd and O elements were acquired to investigate their distribution over the oxygen electrode on the SOEC8% and the Reference samples. The analysis was performed by Ozden Celikbilek and Manon Prioux, during their post-doc at the CEA laboratory.

2.4.2.3 XPS

XPS analysis was used to study the surface chemistry of the LSCF. Both the oxygen electrode CCL top surface and FL were analysed. Specifically, the FL was accessed by using a scalpel to scrape approximately 25 µm of material starting from the surface. The samples were analysed using a VersaProbe-II apparatus from ULVAC-Phi. A monochromatic Al Kα radiation (1486.6 eV) was employed, with an emission current of 4 mA and an X-ray beam diameter of 200 µm. The instrument worked under ultra-high vacuum conditions ($p < 10^{-7}$ Pa) at room temperature. The spectrometer calibration is conducted by taking into account the gold photo-emission lines (Au4f7/2 emission at 83.9 eV, relative to Fermi level). In order to record the survey spectra and the core-level peaks, two constant pass energies of 117.9 eV and 23.3 eV were considered, respectively. To minimize the surface charging effect, electron and argon charge neutralizer guns were used. All spectra were calibrated against carbon C 1s emission at 285.0 eV. CasaXPS software (7) was used to fit XPS spectra and to perform the quantitative analyses. For the peaks fitting, a combined Gaussian (80%) and Lorentzian (20%) distribution was selected, considering a Shirley background. An energy separation of 1.8 eV and a branching ratio of 1.5 were maintained between the Sr 3d5/2 and 3d3/2 doublets to fit the Sr core-level spectra. In order to consider the transmission function of the spectrometer, the X-ray source relative sensitivity factors (RSF) were exported from the MultiPak library.

2.4.2.4 SIMS

High-resolution secondary ion mass spectrometry imaging (SIMS, NanoSIMS 50L, Ametek CAMECA) is employed to evaluate the elemental distribution along the cross sections of the samples studied in this thesis. Sample preparation involves infiltrating the porous layers with a high-vacuum-compatible resin. After that, a diamond slurry was used to polish the cross-section surface. The scanning of the cross-sections is carried out using a Cs^+ primary ion beam, with a current of ≈ 23 nA and a diameter of ≈ 100 nm. Two raster areas of 20 µm x 20 µm and 10 µm x 10 µm, spanning from the electrode FL to the electrolyte, have been defined as regions of

interest (ROIs) for both electrodes. For simultaneous collection of all the secondary ion mass species in the cell, a multi-collection system is employed. Image processing is done using the WinImage ver. 4.6 software by Ametek, Cameca.

2.4.2.5 XRF and XRD synchrotron characterizations

XRF and XRD are two complementary characterization techniques that provide information on materials chemistry and crystallographic structure, respectively. On the one hand, the fluorescence phenomenon, due to the interaction of a medium with an X-ray beam, enables probing the elemental composition of the samples studied with a detection limit in the range of 10 ppm (8). It can be combined with imaging techniques to obtain elemental maps of the sample. On the other hand, the diffraction phenomenon is used to identify the crystalline structure of the material by measuring the intensity of the scattered X-rays and the angle between the incident and diffracted beams. For a given photon energy, the angle is a function of the distance between parallel lattice planes according to the Bragg's law (9). In a sample with a given crystalline structure, the diffraction occurs when the scattered vector is equal to a reciprocal lattice vector. The scattered vector depends on the geometry of the experiment, while the reciprocal lattice vector is given by the orientation and lattice parameter of the crystalline structure.

Synchrotron µXRD. Synchrotron µXRD was performed using the setup of the microXAS beamline at the Swiss Light Source (SLS). To this end, a plasma-focused ion beam (pFIB) Vion (FEI^{TM}) instrument, coupled with a Xe^+ ion source, was used to extract relatively thin lamellae from the cells. The size of the lamellae in the three dimensions are approximately 80 µm wide (in the X direction), 50 µm high (in the Y direction) and 20 µm thick (in the Z direction). Afterwards, the lamella was secured onto an aluminium pin. The beamline setup comprises a motorized sample holder, on which the sample is positioned. Kirkpatrick-Baez (KB) mirrors are used to focus the X-ray beam both horizontally and vertically. The beam energy was 17.995 keV. During the horizontal scans, a spot size of 1 µm was adopted, while in the vertical scans, a size of 0.5 µm was used. The beamline allows collecting XRD and XRF data simultaneously. For the XRF data acquisition, a silicon drift diode detector (SDD, Ketek GmbH, Germany) is placed at 50° to the beam. For the XRD data collection an XRD detector was placed behind the sample, on the opposite side as referred to the coming beam direction. The beam passes through the relatively thin sample before reaching the XRD detector, allowing the XRD data to be acquired in transmission mode. Azimuthal integration processing was performed on the 2D powder diffraction patterns using the pyFAI Python library to generate the 1D diffractograms (10). Approximatively 60 scans in the horizontal direction and 130 scans in the vertical direction were recorded. Subsequently, an integration of all horizontal scans on the same axis were done to generate a collection of 1D diffractograms. Thereafter, Le Bail fitting method (11) was performed in the FullProf software (12) for the phases detection analysis.

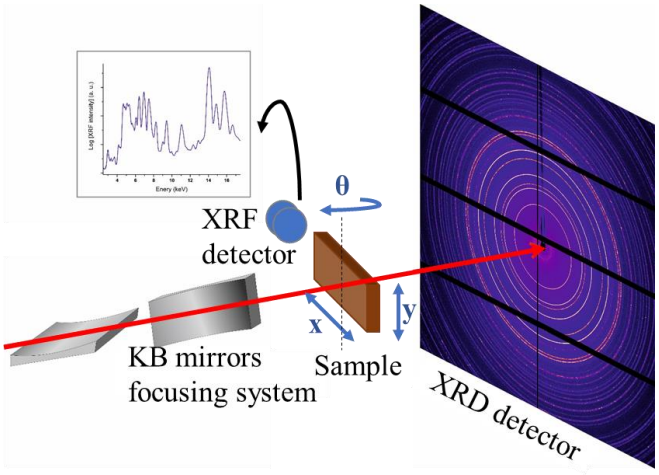

Figure 2-5. Scheme of the microXAS beamline at the SLS, PSI, Switzerland (13). "Reprinted from Publication Journal of Power Sources, 450, Nur Istiqomah Khamidy,Jérôme Laurencin,Dario Ferreira Sanchez,Federico Monaco,Frederic Charlot,Elisabeth Djurado, Durability of nanostructured LaPrNiO4+δ electrode for solid oxide cells: Electrochemical, microstructural, and structural investigation, Pages No. 227724, Copyright (2020), with permission from Elsevier [OR APPLICABLE SOCIETY COPYRIGHT OWNER]."

Synchrotron nanoscale XRF and XRD. The 2 µm-thick lamellae for the synchrotron XRD and XRF nanoscale analyses were extracted from the cells using a Xe^+ pFIB Vion (FEI™). The lamella samples preparation was done using a protocol similar to the one detailed in references (1, 13). Specifically, the samples were prepared under vacuum in a pFIB machine dedicated chamber. The lamella size are approximately 60 × 60 × 2 μm^3 for the horizontal dimension (X), the vertical dimension (Y) and the thickness (Z), respectively. Subsequently, a 10 µm protective layer made of Pt was applied on top of the lamella with a current of 59 nA. A higher current of 470 nA was used to mill the area surrounding the sample, while a lower current of 180 nA was used for the lamella surface refinement to ensure that the sample remains undamaged. A micromanipulator was used for extracting the lamella from the cell using an ion current of 180 nA. Finally, a Pt deposition was used to fix the extracted sample onto an aluminium pin.

The XRF and XRD analyses at the nanoscale were conducted at the ID16B beamline within the European Synchrotron Radiation Facility (ESRF) (14) (see Figure 2-6). Data acquisition was carried out at the ID16B beamline. The beamline comprises double white beam mirror and double-crystal monochromator primary optics, close to the source, and a KB mirror nano-focusing optics, close to the sample. The sample is positioned over a motorized stage. The focused X-ray beam is provided at high flux (10^{12} ph/s), and it has a spot size of 60×60 nm^2. For this study, an energy of 29.6 keV was chosen to analyse all cell elements.

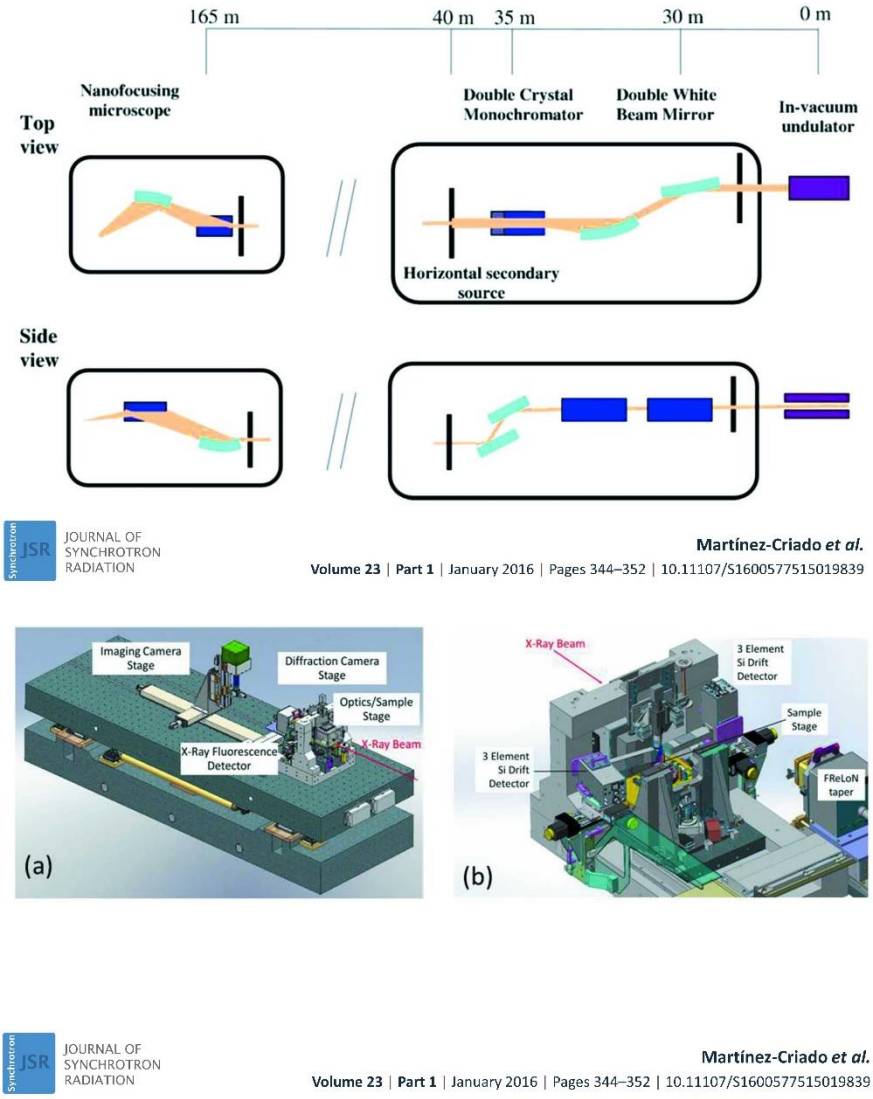

Figure 2-6. Scheme of the ID16B beamline at the ESRF, France. Figures reused with permission from (14).

Multiple XRF detectors were placed at the two sides of the sample, on a perpendicular axis compared to the incoming beam direction. Fluorescence spectra were acquired for each point of the 2D maps using two silicon drift detectors (three and seven elements respectively). The placement of the two detectors on both sides of the sample, with an angle of 13° between the sample surface and the detector, enable them to attain a resolution of 145–150 eV full width at half maximum (FWHM) (14). At such resolution, it is possible to discriminate the signal coming from X-ray emission lines of components with close energies (8). An XRD detector was positioned behind the sample on the same axis of the incoming beam. The data acquisition for the diffraction detector was possible in transmission mode because of the thin lamellae (i.e. ca. 2 µm).

Two main type of scans were considered for the acquisition of XRF and XRD data. (i) 2D maps of XRF and XRD signals were acquired simultaneously, considering a step size of 50 nm (i.e. 50×50 nm^2 resolution) and an exposure time of 1000 ms per point. A ROI of 7×8 μm^2 (6×8 μm^2 for the Reference sample) ranging from the LSCF-GDC/GDC interface to the GDC/YSZ interface was selected to study the elemental inter-diffusion. (ii) 1D line scans along the horizontal direction (X) were acquired to gather XRD data with the so-called zapline method, considering a 50 nm resolution and 1000 ms per point exposure time. For the line scans, three positions were selected at the top of the LSCF CCL, in te middle of the LSCF CCL and in the

middle of the LSCF-GDC FL, targeting the detection of an evolution in the LSCF lattice parameter through the oxygen electrode and the formation of secondary phases.

The fluorescence data fitting was done with the software PyMca (15). The 1D line profiles across the cell layers (in the Y direction) were obtained from each 2D XRF elemental map by averaging and integrating the signal along the horizontal direction (X). The diffraction rings underwent azimuthal integration using the software XRDUA (16) to obtain 2D diffractogram maps. The 2D diffractograms are then integrated along the cell layers (Y direction) and fitted by Le Bail method using FullProf software (17, 18). The XRD results consist in 1D local diffraction patterns.

2.4.2.6 Laboratory XRD

Complementary XRD was performed by Romain Bodeux at the Institute of Photovoltaic France (Paris, France). The XRD data were recorded on a Panalytical empyrean in the θ-2θ Bragg-Brentano geometry ($10° < 2\theta < 90°$ and step 0.02°). The incident X-ray beam with CuKα1 radiation (1.54057 Å) had a spot size of ~ 5 x 5 mm². The PIXcel3D detector consisted of 256 strips to provide the best resolution and linearity. The 8 cm diameter sample holder was capable of translation in the x, y, z axes and rotation in the phi and chi axes. The XRD results consist in diffraction patterns taken on top of the oxygen electrode LSCF CCL, for the Reference and SOEC8% samples. The Le Bail method using FullProf software (17, 18) were used to fit the diffractograms.

2.4.3 Atomic-scale characterizations

2.4.3.1 STEM-EDS

STEM-EDS analyses were conducted on a FEI-Themis microscope equipped with a probe aberration corrector and a super-X detection system. The samples were embedded in an epoxy resin. The extraction of thin lamellae from the LSCF-GDC/GDC/YSZ area was carried out via FIB milling. The Cliff-Lorimer method in the Esprit Bruker Software was used to perform semi-quantitative analyses on the Co, Fe and Y K line profiles, as well as on the La, Sr, Ce, Zr and Gd L line profiles.

2.4.3.2 APT

Atom probe tomography was performed on a CAMECA LEAP 6000XR atom probe. This technique allowed collecting 3D atomic elemental maps. The samples preparation was performed using standard top down lift-out methodology (19) on a Helios 660 FIB-SEM. The analysis was done at the LSCF-GDC/GDC/YSZ interfaces. For data acquisition, a detection rate of 1%, a temperature of 30 K, and a pulsed laser operated at 30 pJ and 100 kHz. Data analysis was carried out on CAMECA's AP Suite 6.3 Analysis software.

2.5 Chapter conclusions

This chapter was dedicated to the description of the studied cell and the methods employed in the thesis. Accordingly, the cell architecture, the experimental setup and the testing protocol were detailed. Electrochemical characterisations were acquired to assess the electrochemical response of the cell. To this end, both i-V curves and EIS were performed in various conditions. The long-term tests were listed along with the related operating conditions. The multiscale physics-based model has been briefly described in this chapter and will be deeper exposed in the next chapter (**Chapter III**) of this thesis. Finally, the set of post-test characterizations used to assess the material degradation in the cell have been reported. The collaboration with different institutes at the international level enabled accessing very powerful techniques able to acquire various type information at the different length scales.

The use of various instruments, tools and techniques enable achieving the objectives of the thesis. Indeed, the multimodal approach is essential to have a complete and cross-validated conclusion on the collected result. The experimental results will be thoroughly detailed later on in the manuscript, from **Chapter III** to **Chapter V**.

References

1. F. Monaco, D. Ferreira-Sanchez, M. Hubert, B. Morel, D. Montinaro, D. Grolimund, and J. Laurencin, *International Journal of Hydrogen Energy* (2021).
2. E. Da Rosa Silva, G. Sassone, M. Prioux, M. Hubert, B. Morel, and J. Laurencin, *Journal of Power Sources*, **556**, 232499 (2023).
3. B. Wei, K. Chen, L. Zhao, Z. Lü, and S. P. Jiang, *Phys. Chem. Chem. Phys.*, **17**, 1601–1609 (2014).
4. W. G. Bessler, S. Gewies, C. Willich, G. Schiller, and K. A. Friedrich, *Fuel Cells*, **10**, 411–418 (2010).
5. F. Monaco, Analysis of the degradation in solid oxide cells operated in fuel cell and electrolysis modes: microstructural evolution and stability of the electrodes materials, thesis, Université Grenoble Alpes (2020).
6. C. Sommer, C. Straehle, U. Köthe, and F. A. Hamprecht, in *2011 IEEE International Symposium on Biomedical Imaging: From Nano to Macro*, p. 230–233 (2011).
7. N. Fairley, V. Fernandez, M. Richard-Plouet, C. Guillot-Deudon, J. Walton, E. Smith, D. Flahaut, M. Greiner, M. Biesinger, S. Tougaard, D. Morgan, and J. Baltrusaitis, *Applied Surface Science Advances*, **5**, 100112 (2021).
8. J. Villanova, S. Schlabach, A. Brisse, and A. Léon, *Journal of Power Sources*, **421**, 100–108 (2019).
9. R. E. Dinnebier and S. J. L. Billinge, *Powder Diffraction: Theory and Practice*, p. 606, Royal Society of Chemistry, (2008).
10. G. Ashiotis, A. Deschildre, Z. Nawaz, J. P. Wright, D. Karkoulis, F. E. Picca, and J. Kieffer, *J Appl Cryst*, **48**, 510–519 (2015).
11. A. Le Bail, *NIST Special Publication*, **846**, 142–153 (1992).
12. J. Rodríguez-Carvajal, *Commission on Powder Diffraction (IUCr). Newsletter*, **26**, 12–19 (2001).
13. N. I. Khamidy, J. Laurencin, D. Ferreira Sanchez, F. Monaco, F. Charlot, and E. Djurado, *Journal of Power Sources*, **450**, 227724 (2020).
14. G. Martinez-Criado, J. Villanova, R. Tucoulou, D. Salomon, J.-P. Suuronen, S. Laboure, C. Guilloud, V. Valls, R. Barrett, E. Gagliardini, Y. Dabin, R. Baker, S. Bohic, C. Cohen, and J. Morse, *Journal of Synchrotron Radiation*, **23**, 344–352 (2016).
15. V. A. Solé, E. Papillon, M. Cotte, Ph. Walter, and J. Susini, *Spectrochimica Acta Part B: Atomic Spectroscopy*, **62**, 63–68 (2007).
16. W. De Nolf, F. Vanmeert, and K. Janssens, *J Appl Cryst*, **47**, 1107–1117 (2014).
17. A. Le Bail, H. Duroy, and J. L. Fourquet, *Materials Research Bulletin*, **23**, 447–452 (1988).
18. J. R. Carvajal, *Newsletter*, **26**, 12–19 (2001).
19. K. Thompson, D. Lawrence, D. J. Larson, J. D. Olson, T. F. Kelly, and B. Gorman, *Ultramicroscopy*, **107**, 131–139 (2007).

3. Multiscale physics-based model

This chapter is devoted to the validation of the multiscale physics-based model adapted to the studied cell. As aforementioned in **Chapter I**, the model account for different length scales, and it is used to reproduce the electrochemical response at the cell level in terms of i-V curves and EIS within the thesis. The chapter is divided in two parts, which are dedicated to the validation of the stationary model and dynamic model, respectively.

The first part (Part I) is dedicated to the simulation of the stationary response of the cell. The stationary model is validated on local and global i-V curves. Local measurements were possible thanks to the use of a specific design of the interconnect at the air side, as described in **Chapter II**. Hence, experimental i-V curves collected in various conditions provided the global and local response of the cell. In this way, a cross-validation of the experimental setup and the stationary multiscale physics-based model was achieved. This part of the work was done in collaboration with Eduardo Da Rosa Silva, who was working on the multiscale physics-based model at the laboratory as a post-doctorate. The work on the stationary model has been published in the Journal of Power Sources (2023) (1).

In the second part (Part II) the model has been extended to the simulation of the dynamic response in terms of impedance spectra at the cell-level. The validation was performed on the experimental EIS collected at the OCV under specific conditions (i.e. 750 °C, 10/90 %vol. H_2/H_2O at the hydrogen electrode). The different contributions arising in the EIS were identified. This analysis allowed investigating the evolution of the electrochemical response in terms of EIS after ageing in various conditions. This part of the work has been published in The Electrochemical Society Transactions (2023) (2).

Reference

1. E. Da Rosa Silva, G. Sassone, M. Prioux, M. Hubert, B. Morel, and J. Laurencin, *Journal of Power Sources*, **556**, 232499 (2023).
2. G. Sassone, E. D. R. Silva, M. Prioux, M. Hubert, B. Morel, A. Léon, and J. Laurencin, *ECS Trans.*, **111**, 649 (2023).

Part I: A Multiscale model validated on local current measurements for understanding the solid oxide cells performances

E. Da Rosa Silva[1], G. Sassone[1], M. Prioux[1], M. Hubert[1], B. Morel[1], J. Laurencin[1,*]

(1) Univ. Grenoble Alpes, CEA/LITEN, 17 Avenue des Martyrs, 38054 Grenoble/France

Abstract. A physical-based model has been developed and validated to unravel the complex relationships between the global solid oxide cells response and the reaction mechanisms taking place in the electrodes. This numerical tool combines three length-scales modules from the electrode microstructure up to the single repeat unit. This model allows computing the local distribution of reaction kinetic rates, current densities, and gas composition as function of the cell operating conditions. To validate the multiscale model, a special experimental setup has been developed to measure the local polarization curves along the cell length. For this purpose, a specific design of the interconnect has been proposed in order to probe the local current density on standard cells. A good agreement has been found between the experimental and simulated data for different operating conditions. The fully validated model has been used to analyze the cell operation in electrolysis and fuel cell modes. The activated reaction pathways associated with the elementary steps in the active layers have been investigated depending on the position along the cell length.

Keywords. Solid Oxide Electrolysis Cell, Solid Oxide Fuel Cell, Multiscale Modeling, Local Polarization Curves.

*Corresponding author: Telephone: +33 4 38 78 22 10,

E-mail: jerome.laurencin@cea.fr

1. Introduction

In a scenario with growing energy demand and a tendency to reduce fossil fuel consumption, hydrogen is considered as an important energy vector for the transition toward a low-carbon energy market [1]. In this context, High-Temperature Steam Electrolysis (HTSE) based on Solid Oxide Cells (SOCs) technology presents a great potential to produce H_2 at a low cost and high efficiency [2]. SOCs are electrochemical devices that can operate in fuel cell mode (SOFC) and electrolysis mode (SOEC) with a large range of fuels and no utilization of expensive catalysts [3]. Due to its reversibility, this technology can also be used to match the fluctuations between electricity demand and production, mainly during the consumption peaks [4]–[6]. Classical SOCs are composed of a dense electrolyte sandwiched between two porous electrodes. The reactions of hydrogen oxidation and steam reduction occur in the fuel electrode (Eq. 1a), whereas the oxygen is consumed or produced in the air electrode (Eq. 1b). A porous Nickel and Yttria-Stabilized Zirconia (Ni-YSZ) cermet is typically used for the fuel electrode, while the air electrode is composed of a Mixed Ionic and Electronic Conductor (MIEC). Nowadays the most common material for the air electrode is a composite of Lanthanum Strontium Cobalt Ferrite ($La_xSr_{1-x}Co_yFe_{1-y}O_{3-\delta}$ - LSCF) and Gadolinium-doped Ceria ($Gd_xCe_{1-x}O_{2-\delta}$ - CGO) [3], [7], [8]. The electrolyte is a pure ionic conductor, which allows the migration of oxygen vacancies ($V_O^{\bullet\bullet}(YSZ)$), and it is usually made of Yttria-Stabilized Zirconia with 8.mol% of yttria (8YSZ) [9].

$$H_2(g) + O_o^x(YSZ) \underset{SOEC}{\overset{SOFC}{\rightleftarrows}} H_2O(g) + V_o^{\bullet\bullet}(YSZ) + 2e^- \quad [1a]$$

$$\frac{1}{2}O_2(g) + V_o^{\bullet\bullet}(YSZ) + 2e^- \underset{SOEC}{\overset{SOFC}{\rightleftarrows}} O_o^x(YSZ) \quad [1b]$$

To reach economic viability, the cell performances still need to be improved while the degradation rate should be limited to 0.5 %.kh^{-1} in SOEC mode (for an operating current density of -1.5 A.cm^{-2} [10]) and 0.2 %.kh^{-1} in SOFC mode [11]. However, degradation rates measured at current densities lower than 1 A.cm^{-2} have been reported in the literature in the range of 1 – 3 %.kh^{-1} [12] and 2 – 10 %.kh^{-1} [13] for SOFC and SOEC operation, respectively. Degradation phenomena can be caused by different factors such as microstructural evolution, electroactive site poisoning, and chemical decomposition [14]. Those phenomena can be aggravated by harsh

operating conditions at high current density and/or high fuel utilization/steam conversion, which can result in strong gradients of concentration along the cell length.

In general, the electrochemical characterization techniques (e.g. polarization curves and Electrochemical Impedance Spectroscopy (EIS)) are used to measure the global cell response without any information on the spatial distributions arising in the electrodes [7]. Hence, current inhomogeneities that are associated with locally-critical conditions are not detected. To overcome this limitation, specific experimental setups must be designed for local electrochemical analyses. The most extensively applied method for local measurements is the electrode segmentation [15]–[22]. It consists in the segmentation of the air electrode into small disconnected zones, which are electronically isolated from each other. For this purpose, the electrode layer is printed over the entire surface of the electrolyte in insulated segments, allowing the measurements in distinct areas of the cell [7], [20].

Although the electrode segmentation technique has been extensively applied for other types of cells (e.g. proton exchange membrane fuel cells), the same abundant quantity of data is not found for SOCs application [17], [23]. This under-utilization of segmented cells for the high temperature applications lies in difficulties to change the design of the air electrode and to probe the current and/or temperature in each segment. Besides, the air electrode partitioning can induce heterogeneities of current and potential that can affect the cell behavior [17]. Hence, new experimental facilities must be developed to perform local analysis using standard cells by avoiding any type of modification in the cell geometry.

The relevance of spatially resolved electrochemical measurements can be significantly enhanced when applied in combination with mathematical modelling. Indeed, the simulation also gives the possibility to have an access to local parameters that are not easily measured (e.g. partial pressures repartition inside the porous media or distribution of overpotentials along the cell length) [17], [20], [21]. In this sense, numerical modeling of SOCs is becoming crucial for a deeper insight into the processes that occur within the electrodes. Accordingly, a significant number of models have been presented in the literature with different approaches and length scales.

For instance, mathematical models have been developed to emulate representative electrode microstructures [24]–[26]. These models can be useful to identify microstructural corrections that control the electrode efficiency [26]. In terms of electrochemical response, some microscale electrochemical models have been proposed to describe precisely the electrode reaction

mechanism including mass and charge transfer within the active functional layer [3], [27]–[30]. On the other hand, many macroscale models have been developed to take into account the full geometry of the single repeating unit (SRU) [23], [31], [32] or stack [33]–[35] including the complete cell, the flow channel and the interconnect. As a general matter, these macro-models present a rather simplified description of the reaction mechanisms, whereas a special attention is paid to describe accurately the fluid distribution in the system and how it can affect the performances.

One possibility to increase the complexity of the SOCs models is to combine the different length scales in a multiscale approach [4]. Complex descriptions from a microscale approach (e.g. microstructure emulation and complex reaction mechanisms) can be coupled with the macro description to better understand the role of microstructure and the reaction mechanism on performances and degradation. In the recent years, some multiscale models have been developed for the SOCs application [33], [36]–[40], showing the power and the potential of these numeric tools. However, it is still necessary to develop an integrated model including (i) a microstructural description of the electrodes, (ii) a decomposition of the reaction pathways in pure elementary steps for both electrodes and (iii) a global description of the SRU geometry. Moreover, despite all the works dedicated to the SOCs modeling in the literature, only a small quantity of them [41]–[43] have bridged the multiscale approach to a spatial resolved electrochemical analysis. To the best of our knowledge, only the group of G. Schiller have published a series of articles, in which a multiscale model [44] was applied to analyze the local polarization curves acquired in a segmented setup [41]–[43].

In this work, a coupled experimental and multiscale model approach has been proposed in order to unravel the relationships between a classical SOC response and the mechanisms that take place in the electrodes. The multiscale model is composed of three different length-scale modules. The first one emulates digital twins of the electrode microstructure, giving the possibility to have a complete description of the morphology of the electrodes. It is linked to two microscale models for both electrodes. They take into consideration the reaction mechanisms in a sequence of pure elementary steps associated with charge and mass transport phenomena in the active layers. Finally, all the modules are linked to a macroscopic description that takes into account the SRU design including the gas channels. The multiscale model has been validated using global and local polarization curves using a standard cell (i.e. fuel electrode supported cell made of the classical materials). For this purpose, an innovative design of the air electrode interconnect is proposed in order to probe the local distribution of the current

without any kind of electrode segmentation. After validation, the model has been used to analyze the evolution of the reaction mechanism in the electrode along the cell length.

2. Materials and methods

2.1 Cell description

In this study, a 'standard' fuel electrode-supported cell was studied. The cell has a circular shape with an active area of 9.08 cm². A thin and dense electrolyte made of 8YSZ with a thickness of 8 µm was sandwiched between two porous electrodes. The air electrode is a bilayer with a current collector made of LSCF (ca. 20 µm tick) and an active layer in LSCF-CGO (ca. 20 µm thick). A 3 µm barrier layer of CGO is inserted between the electrolyte and the air electrode to avoid the formation of secondary phases. The fuel electrode is composed a thin functional layer in Ni-8YSZ (ca. 25 µm) and a thick support layer (ca. 280 µm) made of Ni-3YSZ cermet.

2.2 Setup description

All tests were carried out in an in-house test bench depicted in Figure 3-1a. The circular cell is positioned in a metallic housing. Both anodic and cathodic gases are introduced at the cell center and are distributed along the electrodes in a radial co-flow configuration. The inlet gas fluxes are delivered by mass flow controllers (Brooks SLA5850S).

On the fuel side, a Ni grid (100 meshes.cm^{-2}) is used to collect the current at the electrode surface. A ceramic glass seal (Schott G018-311) is deposited on the edge of the cell to ensure the gas tightness of the hydrogen compartment. It can be noticed that steam is produced using a steam generator operated in saturated vapor conditions. In parallel, hydrogen is introduced and mixed with the steam before entering the cell. At the cell outlet, a heat exchanger allows separating the water from the dry gas.

At the air side, a specific design of the metallic interconnect is applied in order to measure the local current distribution along the cell radius. This setup is made of Inconel Ni-based alloy and its geometry is displayed in Figure 3-1b-c. The metallic support is divided into numerous pins that are positioned from the gas inlet to the edge of the electrode. Nine of those pins are drilled to allow the passage of wires that are welded in the extremity of each pin. Another wire is welded to the opposite surface of the interconnect and used as a reference for the voltage measurement. With this configuration, when a current density is imposed to the cell under

operation, the voltage drop can be measured for each pin. Since the geometry and the electrical conductivity of the interconnect material is known precisely, it is possible to calculate accurately the local current density passing through by each pin (corresponding to the local current collected by the pin on the electrode). Hence, this modification in the interconnect geometry offers the advantage to perform local current measurements (and consequently, local polarization curves) using classical cells without any specific segmentation of the air electrode [15]–[17], [19], [45]. Finally, it is worth mentioning that two gold grids (100 meshes.cm^{-2}) with a diameter of 34 mm are inserted between the interconnect and the electrode surface to improve the electrical contact. Moreover, a mechanical pressure of 600 g.cm^{-2} is also applied on the setup to further decrease the contact resistances.

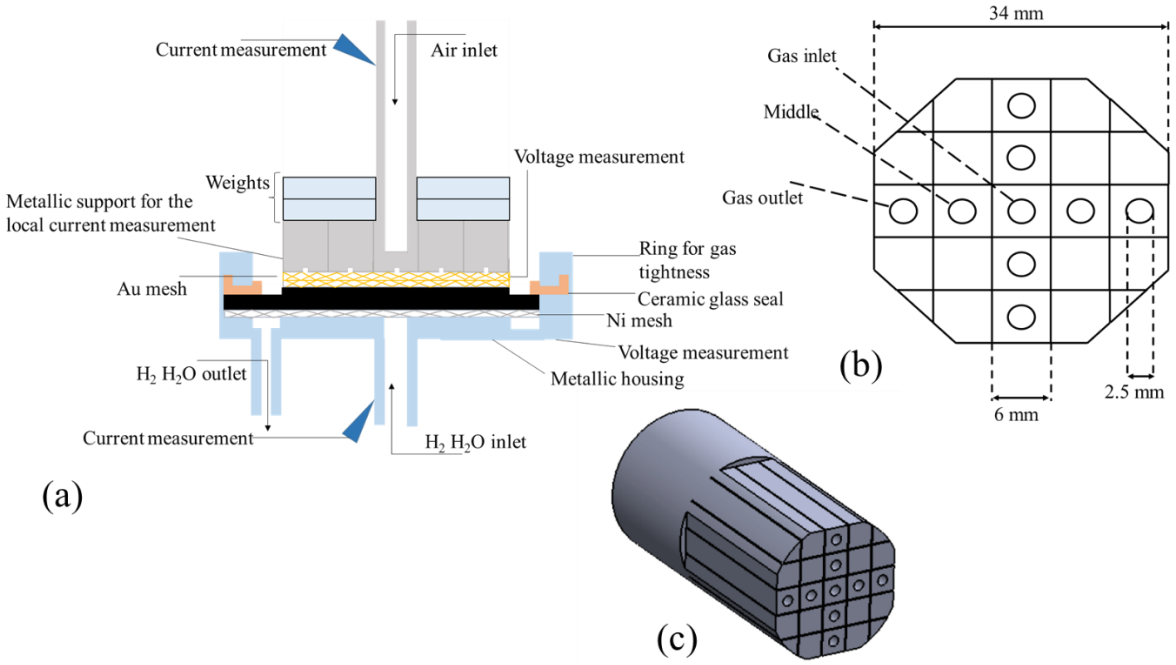

Figure 3-1 - Schematic illustration of (a) the testing setup, (b) cross-section and, (c) 3D view of the interconnect at the oxygen side for the local current measurements.

2.3 Protocol description

The experiment procedure started with the cell heating at a rate of 1 °C.min^{-1} up to 860 °C under a nitrogen and air sweeping at the fuel and air sides, respectively. Then, the cell was maintained at this temperature for 90 min to form the glass sealing. After, the temperature was lowered to 800 °C to start the cermet reduction. For this purpose, the hydrogen concentration at the inlet was increased gradually up to reach the full conversion of Nickel oxide into metallic Nickel.

Polarization curves were performed in fuel cell and electrolysis mode. For electrolysis mode, a ratio of $P(H_2)/P(H_2O)$ = 10/90 was used, whereas, in SOFC mode, the anode was supplied with dry hydrogen. In both cases, the air electrode was always supplied with synthetic air with a constant flux of 41 $NmL.min^{-1}cm^{-2}$. The measurements were performed in galvanostatic mode (Autolab PGSTAT-302N) with a current rate of 21 $mA.s^{-1}$ and a 20 A current booster. The current local distribution was measured using a multichannel data logger HIOKI LR8400-20, able to record simultaneously the 9 voltage pins measurements. The data were acquired at different temperatures (700, 750 and, 800 °C) and for various inlet fluxes at the fuel electrode (3, 6, 9, and 12 $NmL.min^{-1}cm^{-2}$).

In order to assess the contact resistance (R_c) between the electrodes and the grids, electrochemical impedance spectroscopy has been also performed at the Open Circuit Voltage (OCV) for the three investigated temperatures (i.e. 700, 750 and, 800 °C and for an inlet flux at the fuel electrode of 12 $NmL.min^{-1}cm^{-2}$). The contact resistances have been calculated as a function of the temperature by removing the electrolyte ohmic resistance from the serial resistance measured on the impedance diagrams (i.e. high frequency intercept with the real axis in the Nyquist plot). The diagrams were also acquired in galvanostatic mode by imposing a sinusoidal current with an amplitude of 110 $mA.cm^{-2}$ in the frequency range of 10^{-2}-10^4 Hz.

3. Model descriptions

3.1 General assumptions and multiscale model

A multiscale model was developed in order to unravel the complex relationships between the SOC response and the mechanisms that take place in the electrodes. This model is composed of three different length-scale modules that can achieve an exhaustive analysis of the cell performance in both SOEC and SOFC modes. The first module allows generating 3D digital twins of electrode microstructures made of classical materials. It can provide all the necessary morphological information for the other modules. The second module is a micro-scale model that takes into consideration the elementary reactions coupled with the mass and charge transfer in the active layer of both electrodes. Finally, the third module is a macro-scale model that can compute all the polarization curves and local current distribution along the cell radius.

The connections between the modules are established in different arrangements as it can be seen in Figure 3-2. The microstructural model provides all the morphologic inputs that are needed for the other modules. Moreover, the micro-scale modules provide the parameters of

the ‘apparent’ or ‘global’ exchange current densities (i.e. activation energies and exponents - cf. Eqs. 4 and 5) for the calculation of the electrode activation overpotential in the macro-scale model. It can be noticed that the functional layers are not described at the macroscopic scale. Therefore, the partial pressure distributions taken at the electrolyte interface in the macro-model are used in the micro-model as boundary conditions applied at the top of the functional layer. The model description at the microscopic scale must include a full description of the micro-processes involved in the reaction mechanism. In this approach, the parameters for the ‘global’ exchange current densities are identified in order to match with the electrode overpotential calculated in the active layer with the microscale models. Thanks to this method, all the processes in the functional layer are thus included in the apparent exchange current density of the Butler-Volmer equation for the macroscale model. In other words, it is possible to guarantee that the activation overpotentials in the macro-model take into consideration all microscopic processes arising in the electrode functional layers.

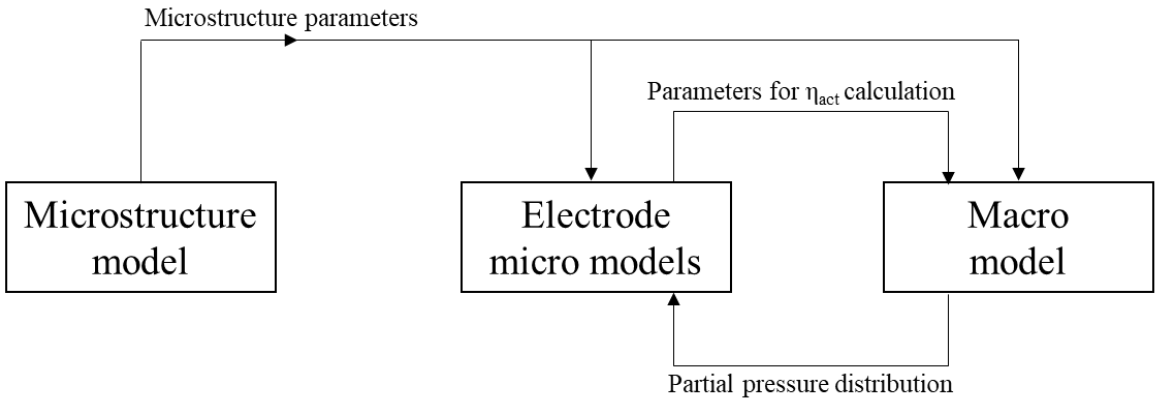

Figure 3-2 – General flowchart of the multiscale model

3.2 Microstructure model

To obtain digital twins of the real electrode structures, geostatistical simulations were carried out using a model based on a truncated plurigaussian random field method [24], [46]. In this method, each phase is represented by a random field, which is generated by the convolution of random noise with a weight function. Hence, the fields are jointly thresholded according to a specific procedure to obtain the synthetics microstructures [46]. This model was validated by comparison with 3D reconstructions of real electrodes performed by X-ray holotomography [27]. More details about the model and its validation can be found in [24]. In this work, we used the digital twins of the real electrodes as input for the electrochemical simulations.

3.3 Micro-scale models: electrodes functional layer

The micro-scale models are able to describe all the microscopic processes that take place in the active functional layer of both electrodes. These models are essential to understand the role of the microstructure and the operating conditions (polarization, temperature, etc.) on the reaction mechanisms and electrode performances. Two models were developed considering the state-of-the-art materials with the LSCF-CGO [28], [47] composite and Ni-YSZ [48] cermet for the air and fuel electrodes, respectively. Both models were built up considering a slice of porous electrode described as a homogenous medium. A special attention was paid to describe the electrode kinetics in a sequence of elementary steps that can evolve in different reaction pathways depending on the polarization. The list of reactions implemented in the models are listed in Table 3-1 for both electrodes. All the kinetic constants are thermally activated and expressed with an Arrhenius law. Activations energies were already calculated and published in [28] and [48] for the air and fuel electrodes, respectively.

For the hydrogen electrode, the model is based on a hydrogen spillover mechanism proposed and validated in [49]. In this case, the reactions mechanism is co-limited by the charge transfer at Triple Phase Boundary lines (TPBls), the oxygen vacancies migration in the YSZ network and a pure chemical surface process depending on the polarization [48]. According to this model, steam can interact with the surface of both Ni and YSZ in two parallel pathways. Considering cathodic polarization (electrolysis mode), steam can adsorb on the Ni surface (cf. reaction R1 in Table 3-1), where it is reduced at the TPBls into one hydrogen adatom H_{Ni} attached on the Ni surface and one hydroxyl ions OH^-_{YSZ} on the YSZ surface (reaction R5). The hydroxyl ion OH^-_{YSZ} is then further reduced at the TPBls into a second hydrogen on the Ni surface and an oxygen ion O^{2-}_{YSZ} attached on the YSZ surface (reaction R6). Then, two hydrogens H_{Ni} can be associated and desorbed into H_2 molecules (reaction R4), while the oxygen ions O^{2-}_{YSZ} are incorporated into the YSZ lattice (reaction R7). In parallel, steam molecules can also adsorb on the YSZ surface (reaction R2). In this second pathway, the adsorbed water molecule can react with the oxygen ions available at the YSZ surface to produce hydroxyl ions OH^-_{YSZ} (reaction R3). As previously described, the hydroxyl ions can be reduced at TPBls according to reaction R6. It has been shown [50] that the first pathway (steam adsorption on Ni surface) is preferentially activated under electrolysis mode while the water desorption from YSZ (second pathway) is predominant in fuel cell mode. Nevertheless, the prevalence of one pathway should also depend on the local operating condition along the cell length that still need to be investigated.

Regarding the air electrode, the reaction mechanism proposed and validated in [28] is also divided into two parallel pathways. For an operation in electrolysis mode, the so-called bulk path starts by the ionic transfer reaction at the LSCF/CGO interface (reaction R8 in Table 3-1) that supplies the electrode material in oxygen atoms $O^{x}_{O_{(LSCF)}}$. After a transport by solid-state diffusion in LSCF, the incorporated oxygen is released from the bulk to generate ad-ions $O^{-}_{(LSCF)}$ on the LSCF surface (reaction R9). For the second path, hereafter called surface path, the oxygens coming from the electrolyte material (i.e. CGO) are directly oxidized at the TPBls to produce oxygen ad-ions (reaction R10). Finally, the oxygen ad-ions are reduced in oxygen ad-atoms in a second reaction of charge transfer (reaction R11) which is common to the two pathways. The oxygen is then associated on the LSCF surface (reaction R12) before to be desorbed into the porosity (reaction R13). For a composite electrode, it has been shown that the surface path is dominant whatever the polarization even if the contribution of the bulk path is significantly enhanced in fuel cell mode [28]. As for the fuel electrode, the reaction mechanism is expected to change as a function of the local condition along the cell radius.

For both electrodes, mass and charge balances have been considered for all species. They constitute a set of partial differential equations that are implemented and solved using COMSOL Multiphysics®. Besides, all the equations for the transport and the kinetic rates are expressed as a function of the electrode microstructural properties. They are extracted from the digital twins obtained with the truncated random field, establishing a link between the two-length scales. Finally, it is worth noting that all the equations and the details for this module of the multiscale model have been already published in [48] and [28] for the fuel and the air electrodes, respectively. In these previous studies, a special attention was paid to validate the mechanisms using experimental results obtained on symmetrical cells tested in a three-electrode set-up.

Table 3-1 – Reactions and fitted values for the kinetic constants for T = 750 °C

Fuel electrode			
$H_2O_{(gas)} + 1s_{Ni} \underset{k^{ADS}_{H_2O_{Ni}}}{\overset{k^{DES}_{H_2O_{Ni}}}{\leftrightarrows}} H_2O_{Ni}$	Steam adsorption on the Ni surface (R1)	Ni interaction pathway	1.18 x 10^6 (s^{-1})
$H_2O_{(gas)} + 1s_{YSZ} \underset{k^{ADS}_{H_2O_{YSZ}}}{\overset{k^{DES}_{H_2O_{YSZ}}}{\leftrightarrows}} H_2O_{YSZ}$	Steam adsorption on the YSZ surface (R2)	YSZ interaction pathway	9.28 x 10^3 (s^{-1})
$H_2O_{YSZ} + O^{2-}_{YSZ} \underset{k^{DISS+}_{H_2O_{YSZ}}}{\overset{k^{DISS-}_{H_2O_{YSZ}}}{\leftrightarrows}} 2OH^-_{YSZ}$	H_2O dissociation on YSZ surface (R3)	YSZ interaction pathway	6.87 x 10^{16} ($m^2.s^{-1}.mol^{-1}$)
$2H_{Ni} \underset{k^{DES}_{H_2Ni}}{\overset{k^{ADS}_{H_2Ni}}{\leftrightarrows}} H_{2(gas)} + 2s_{Ni}$	Hydrogen desorption from Ni surface (R4)	Common pathway	3.69 x 10^{12} ($m^2.s^{-1}.mol^{-1}$)
$H_2O_{Ni} + 1s_{YSZ} + 1e^- \underset{k^{red}_1}{\overset{k^{ox}_1}{\leftrightarrows}} OH^-_{YSZ} + H_{Ni}$	First charge transfer reaction (R5)	Ni interaction pathway	8.5 x 10^4 ($m^3.s^{-1}.mol^{-1}$)
$OH^-_{YSZ} + s_{Ni} + 1e^- \underset{k^{red}_1}{\overset{k^{ox}_2}{\leftrightarrows}} O^{2-}_{YSZ} + H_{Ni}$	Second change transfer reaction (R6)	Common pathway	5.5 x 10^5 ($m^3.s^{-1}.mol^{-1}$)
$O^{2-}_{YSZ} + V^{\bullet\bullet}_{(YSZ)} \underset{k^{EXC}_{O^{2-}_{YSZ}}}{\overset{k^{INC}_{O^{2-}_{YSZ}}}{\leftrightarrows}} O^x_{O(YSZ)} + s_{YSZ}$	Oxygen incorporation in the YSZ lattice (R7)	Common pathway	1.3 x 10^8 ($m^3.s^{-1}.mol^{-1}$)
Air electrode			
$O^x_{O(CGO)} + V^{\bullet\bullet}_{(LSCF)} \underset{k_+}{\overset{k_-}{\leftrightarrows}} O^x_{O(LSCF)} + V^{\bullet\bullet}_{(CGO)}$	Ionic transfer at LSCF/CGO interface (R8)	Bulk pathway	50 ($mol.m^{-2}.s^{-1}$)
$O^x_{O(LSCF)} + 1h^\bullet + 1s_{LSCF} \underset{k^{LSCF/gas}_{ox}}{\overset{k^{LSCF/gas}_{red}}{\leftrightarrows}} V^{\bullet\bullet}_{O(LSCF)} + O^-_{LSCF}$	Oxygen excorporation reaction (R9)	Bulk pathway	9 x 10^{-5} ($m^3.s^{-1}.mol^{-1}$)
$O^x_{O(CGO)} + 1h^\bullet + 1s_{LSCF} \underset{k^{TPBls}_{ox}}{\overset{k^{TPBls}_{red}}{\leftrightarrows}} V^{\bullet\bullet}_{O(CGO)} + O^-_{LSCF}$	Oxygen oxidation reaction at the TPBls (R10)	Surface pathway	2.25 x 10^{-4} (s^{-1})
$O^-_{LSCF} + 1h^\bullet \underset{k_{deion}}{\overset{k_{ion}}{\leftrightarrows}} O_{LSCF}$	Oxygen deionization reaction (R11)	Common pathway	8.74 x 10^5 (s^{-1})
$2O_{LSCF} \underset{k_{ass}}{\overset{k_{diss}}{\leftrightarrows}} O_{2LSCF} + 1s_{LSCF}$	Oxygen association reaction (R12)	Common pathway	1.5 x 10^{15} ($m^2.s^{-1}.mol^{-1}$)
$O_{2LSCF} \underset{k_{des}}{\overset{k_{ads}}{\leftrightarrows}} O_{2(gas)} + 1s_{LSCF}$	Oxygen desorption reaction (R13)	Common pathway	3.12 x 10^6 (s^{-1})

3.4 Macro-scale model: SRU and interconnects

In the macroscale model, the cell design and the geometry of the gas channels are taken into account considering a 2D approach as already detailed in [31], [32]. It couples locally fluidic and electrochemical steps, allowing the analysis of the distribution of gas composition and current density along the cell radius. In this macroscopic approach, the active functional layers are not described and they are limited to the electrode/electrolyte interface. The Dusty Gas

Model (DGM), which takes into consideration the molecular and Knudsen diffusions, is used to describe the gas transport through the current collector in LSCF at the air side and the thick Ni-YSZ substrate at the hydrogen side. All the diffusion coefficients are calculated as a function of the microstructural properties [31], [32]. The main features of this macroscale model are briefly reminded hereafter.

Since the metallic interconnects present a very good electrical conductivity, the cell voltage (U_{cell}) is considered constant all along the cell length. In this way, Eq. 2 is applied to calculate the local current density along the cell radius *r*:

$$U_{cell}=E_{i=0}+\eta_{conc}^{O_2 electrode}(r)-\eta_{conc}^{H_2 electrode}(r)+\eta_{act}^{O_2 electrode}(r)-\eta_{act}^{H_2 electrode}(r)-\eta_{ohm}(r) \quad (2)$$

where $E_{i=0}$ is the Open Circuit Voltage (OCV), which is calculated by Nernst's equation. The terms η_{conc}, η_{act} and, η_{ohm} are the concentration, activation and, ohmic overpotential, respectively. Those terms increase the cell voltage in electrolysis conditions and decrease the cell voltage in fuel cell conditions. The ohmic overpotential includes (*i*) the contact resistances (R_C) arising between the electrodes and the interconnects, (*ii*) the ionic resistance of the electrolyte and (*iii*) the electronic resistances for the LSCF current collector and Ni-YSZ support.

The difficulty to maintain the gas composition at the active sites is taken into account in the concentration overpotential. This term is the sum of the gas diffusion overpotential (η_{diff}) and the gas conversion overpotential (η_{conv}). The first contribution is due to the losses ascribed to the gas transfer through the porous media (i.e. LSCF current collector and Ni-YSZ support described at this macroscale). The second contribution is related to the thermodynamic losses that are induced by the change in the gas composition due to the consumption or production of the gaseous species along the cell length. Finally, the activation overpotentials must take into account all the microscopic processes occurring in the Ni-YSZ and LSCF-CGO functional layers (i.e. all the reactions convoluted with the mass and charge transfers as described in the microscale models). For this purpose, they are calculated using a phenomenological Butler-Volmer equation as shown in Eq. 3.

$$\left|\eta_{act}^{O2\ electrode}\right|+\left|\eta_{act}^{H2\ electrode}\right|=\frac{RT}{F}sinh^{-1}\left\{\frac{|i(r)|}{2i_0^{O2\ electrode}(r)}\right\}+\frac{RT}{F}sinh^{-1}\left\{\frac{|i(r)|}{2i_0^{H2\ electrode}(r)}\right\} \quad (3)$$

The terms $i_0^{O2\ electrode}(r)$ and $i_0^{H2\ electrode}(r)$ are defined as the 'global' exchange current densities for each electrode. They are a function of the local partial pressure p_i taken at the electrode/electrolyte interface, as can be seen in Eqs. 4 and 5.

$$i_0^{H_2\ electrode}=\mathrm{A}\times\left(p_{H_2}(r)\right)^{\mathrm{m}}\times\left(p_{H_2O}(r)\right)^{\mathrm{n}}\times\mathrm{e}^{\left(-\frac{\mathrm{E_a}^{H_2 electrode}}{\mathrm{RT}}\right)} \quad (4)$$

$$\mathrm{i}_0^{O_2 electrode}=\mathrm{B}\times\left(p_{O_2}(r)\right)^{\mathrm{p}}\times\mathrm{e}^{\left(-\frac{\mathrm{E_a}^{O_2 electrode}}{\mathrm{RT}}\right)} \quad (5)$$

The parameters *m*, *n* and, *p* denote the exponent on the partial pressures dependency whereas $\mathrm{E_a}^{O_2 electrode}$ and $\mathrm{E_a}^{H_2 electrode}$ are the activation energy for the oxygen and hydrogen electrodes, respectively. The computation of these parameters is carried out using the microscale model as detailed in section 3.1, in such a way that the macroscale model takes into account all the electrochemical phenomena occurring in the electrode functional layers.

4. Results

4.1 Microstructural modeling

The digital twins of the LSCF current collector and the LSCF-CGO and Ni-YSZ functional layers are compared in Figure 3-3 and Figure 3-4 to the reconstructions of the real electrodes obtained by FIB-SEM (Focused Ion Beam-Scanning Electron Microscopy) tomography according to the protocol already published in [27]. As expected, it can be observed that the synthetic microstructures seem to mimic accurately the real ones. As a verification, the microstructural properties listed in Table 3-2 have been calculated on both types of volume using the numerical procedures thoroughly detailed in [24]. The computations have been carried out on volumes as large as 15^3 µm^3, which can be considered as a Representative Volume

Element (RVE) for this type of microstructures [24]. Whatever the studied layer, a good match has been found between the two sets of data. For instance, the mean error between the parameters computed on the real and synthetic microstructures for the LSCF-CGO does not exceed 10%. Moreover, it has been also checked that the mean error for the LSCF and Ni-YSZ microstructures lies in the range of a few percent. Therefore, these results validate the generation of synthetic microstructures for the standard cell tested in this work.

The Ni-YSZ support has been reconstructed by synchrotron X-ray tomography according to procedure given in [50]. As shown in Figure 3-4, this technique allows obtaining a large reconstructed volume, required to be representative of this coarse microstructure [51]. The microstructural properties for the support have been computed on several sub-volumes extracted from the whole reconstruction [51]. Knowing that the standard deviation on the data is very small, only the mean value for the parameters is given in Table 3-2. It can be noticed in Figure 3-4 that the porosity of the support exhibits a large pore size distribution. This particular feature is explained by the utilization of pore former during the manufacturing. Because of this characteristic, the truncated random field method fails to reproduce correctly the microstructure. In this case, models based on sphere packing are more adapted to reproduce microstructures exhibiting a multi-modal distribution of pore size [51].

Finally, it is worth noting that all the data given in Table 3-2 provide a complete description of the electrode microstructures, which are necessary for the electrochemical simulations described hereafter.

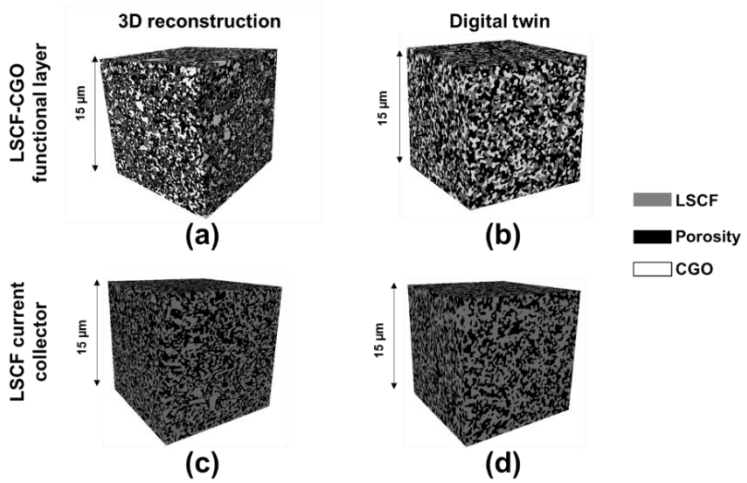

Figure 3-3 – Comparison between the microstructures of the LSCF-CGO functional layer obtained by 3D reconstruction (a) and by the microstructural modeling (b); and for the LSCF current collector microstructures obtained by 3D reconstruction (c) and by the microstructural modeling (d).

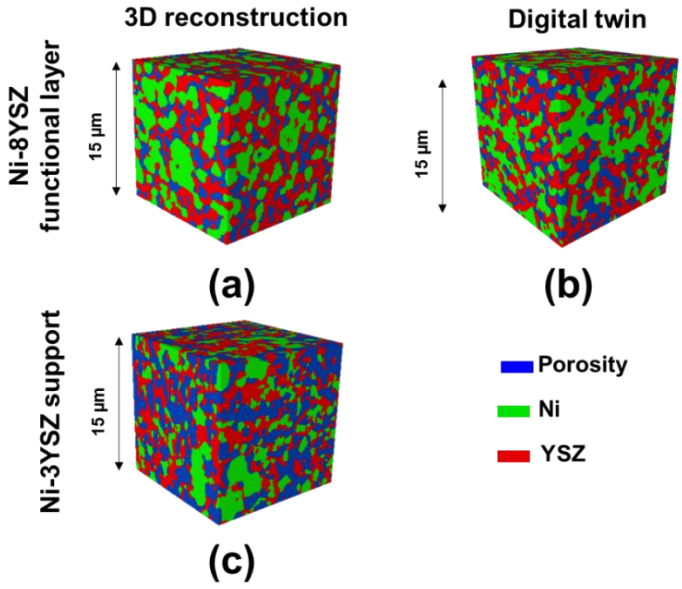

Figure 3-4 – Comparison between the microstructures of the Ni-8YSZ functional layer obtained by 3D reconstruction (a) and by the microstructural modeling (b) and a 3D reconstruction of the Ni-3YSZ support (c).

Table 3-2 – Microstructure properties of the fuel and air electrodes

Properties of the connected phases	**Ni-8YSZ functional layer**	**Ni-3YSZ support**	
Pores volume fraction (ε_{pores})	0.234	0.39	(%)
Nickel volume fraction (ε_{Ni})	0.329	0.26	(%)
YSZ volume fraction (ε_{YSZ})	0.425	0.35	(%)
Specific surface area between YSZ and pores ($Sp_{YSZ-pores}$)	1.49	1.44	(μm^{-1})
Specific surface area between pores and Ni ($Sp_{pores-Ni}$)	0.343	0.60	(μm^{-1})
Specific surface area between Ni and 8YSZ (Sp_{Ni-YSZ})	0.984	1.38	(μm^{-1})
Mean pore radius ($\bar{r}_{pore}$)	0.14	0.325	(µm)
Pores tortuosity factor (τ_{pore})	5.3	3.74	(-)
Ni tortuosity factor (τ_{Ni})	6.5	8.88	(-)
YSZ tortuosity factor (τ_{YSZ})	2.45	3.53	(-)
Triple phase boundary length density (ξ_{TPB})	3.15	-	(μm^{-2})
Properties of the connected phases	**LSCF-CGO functional layer**	**LSCF current collector**	
Pores volume fraction (ε_{pores})	0.459	0.476	(%)
LSCF volume fraction (ε_{LSCF})	0.263	0.524	(%)
CGO volume fraction (ε_{CGO})	0.254	-	(%)
Specific surface area between LSCF and pores ($Sp_{LSCF-gas}$)	2.61	6.09	(μm^{-1})
Specific surface area between LSCF and CGO ($Sp_{LSCF-CGO}$)	1.05	-	(μm^{-1})
Mean pore radius ($\bar{r}_{pore}$)	0.068	0.074	(µm)
Triple phase boundary length density (ξ_{TPB})	17.81	-	(μm^{-2})
Pores tortuosity factor (τ_{pore})	1.89	1.86	(-)
LSCF tortuosity factor (τ_{LSCF})	9.5	2.27	(-)
CGO tortuosity factor (τ_{CGO})	13.15	-	(-)

4.2 Model calibration

The calibration of the multiscale model was performed in order to match the activation overpotentials calculated at the cell level and the overpotentials induced by all the processes in

the active functional layers. To achieve this goal, the following procedure has been applied for both electrodes operated in SOFC and SOEC modes:

• First, the kinetic constants for the reactions implemented in the validated microscale models have been scaled up to reach the performances required at the cell level, using the polarization resistance measured by EIS at OCV and 750 °C as reference. This step consisted to multiply all the kinetic constants, previously determined on symmetrical cells [28], [48], by a correcting factor. Indeed, this correction is necessary since the electrode performances measured in a symmetrical setup are usually lower than those determined for the complete cell. Nevertheless, it is worth mentioning that neither the activation energies nor the reaction mechanism has been changed by this procedure. The values of the calibrated kinetic constants for the studied cell are given in Table 3-1 for both electrodes, considering electrolysis mode.

• The microscale models were then used to generate a large database of electrode polarization curves as function of the operating temperature and the gas partial pressures taken at the top of the active layers. To build this database, simulations were carried out by increasing the temperature from 700°C to 800°C. Furthermore, the partial pressures were changed from $P(H_2)/P(H_2O)$=10/90 to 90/10 for the fuel electrode and from $P(O_2)/P(N_2)$=10/90 to 100/0 for the air electrode.

• The parameters for the 'global' exchange current densities given by Eqs. (4) and (5) have been finally obtained by adjusting the activation overpotentials given by Eq (3) on the database related to the electrode polarization curves established for the active functional layers.

The fitted partial pressure exponents (*m* and *n* for the hydrogen side and *p* for the air side) and activation energy of the exchange current density are provided in Table 3-3 for both electrodes in SOFC and SOEC modes. For the hydrogen side, it can be noted that the steam presents a stronger impact than the hydrogen on the current exchange density. Similar results have been published in [52] and [53] with exponents m=0.11 and n=0.67 for SOFC polarization. For the air electrode, the value of the exponent is also consistent with the literature. For instance, exponents of 0.25 [52] and 0.26 [54] have been reported for the SOFC and SOEC modes, respectively. For the fuel electrode, the fitted activation energies are also consistent with the ones given in [55] and [56], with values of 100 $kJ.mol^{-1}$ and 140 $kJ.mol^{-1}$ in SOFC and SOEC modes, respectively. Finally, for the air electrode, the activation energies reported in [54] (83 $kJ.mol^{-1}$) and in [55] (120 $kJ.mol^{-1}$) for SOEC and SOFC modes, respectively, are in relative good agreement with the fitted values.

In this procedure for the model calibration, it is worth noting that the contact resistances deduced from the experimental impedance spectra have been introduced as inputs data in the simulations. As expected, R_C values have been found to decrease with the temperature [57] (values of 0.244 Ω.cm², 0.181 Ω.cm², and 0.131 Ω.cm² were measured for 700 °C, 750 °C and 800 °C, respectively).

Table 3-3 – Parameters for exchange current densities

		Partial pressure exponent	Activation energy (kJ mol^{-1})	Pre-exponential factors
SOFC	H_2 electrode	m = 0.06 and n = 0.48	100	A=1.26x10^9 (A.m^{-2}.atm$^{-(m+n)}$)
	O_2 electrode	p = 0.21	112	B=8.12x10^9 (A.m^{-2}.atm^{-p})
SOEC	H_2 electrode	m = 0.10 and n = 0.80	130	A=2.63x10^{10} (A.m^{-2}.atm$^{-(m+n)}$)
	O_2 electrode	p = 0.16	88	B=1.1x10^{12} (A.m^{-2}.atm^{-p})

4.3 Model validation

The polarization curves of the complete cell have been measured in SOEC ($P(H_2)/P(H_2O)$ = 10/90) and SOFC ($P(H_2)/P(H_2O)$ = 100/0) modes for different fluxes introduced at the inlet of the fuel electrode (Figure 3-5a-b) and for different temperatures (Figure 3-5c-d). As a general matter, the experimental results are found to be coherent with the ones expected for this type of cell [3], [32]. It can be noticed that the OCV values are in excellent agreement to the theoretical values given by the Nernst equation (considering $P(H_2)/P(H_2O)$ = 10/90 for SOEC and $P(H_2)/P(H_2O)$ > 99/1 for SOFC mode). Moreover, the OCV values remained constant when changing the total inlet flux for the fuel electrode during the experiments. These statements point out that there was no significant leakage between the electrode compartments so that the gas tightness of the glass seal was considered satisfactory.

As expected, the cell presents higher performances when the operating temperature and the gas inlet flux at the hydrogen side are increased. For instance, at the thermo-neutral voltage (≈1.3 V [58]) in SOEC mode, the absolute value of the current density at 750 °C is increased

from -0.39 A.cm^{-2} to -1.05 A.cm^{-2} when the inlet flux is increased from 3 NmL.min^{-1}cm^{-2} to 12 NmL.min^{-1}cm^{-2} (Figure 3-5a).

The comparison between the experimental and simulated polarization curves is also provided in Figure 3-5. It can be seen that the model is able to predict all the experimental data in both SOFC and SOEC polarizations without any type of fitting. Therefore, the model can reproduce accurately the effect of temperature and inlet flux on the cell performance. Nonetheless, a minor difference between the shape of the simulated and experimental curves can be observed in the region of the cell limiting current density. This slight discrepancy must be probably ascribed to small uncertainties in the determination of the microstructural properties on the 3D reconstruction on the cell support (i.e. pore radius and tortuosity factor). Indeed, as they control the mass transfer across the tick substrate, even a small change of one of these parameters can affect significantly the diffusion process, which can increase the concentration overpotential and decrease the cell performances [32], [59].

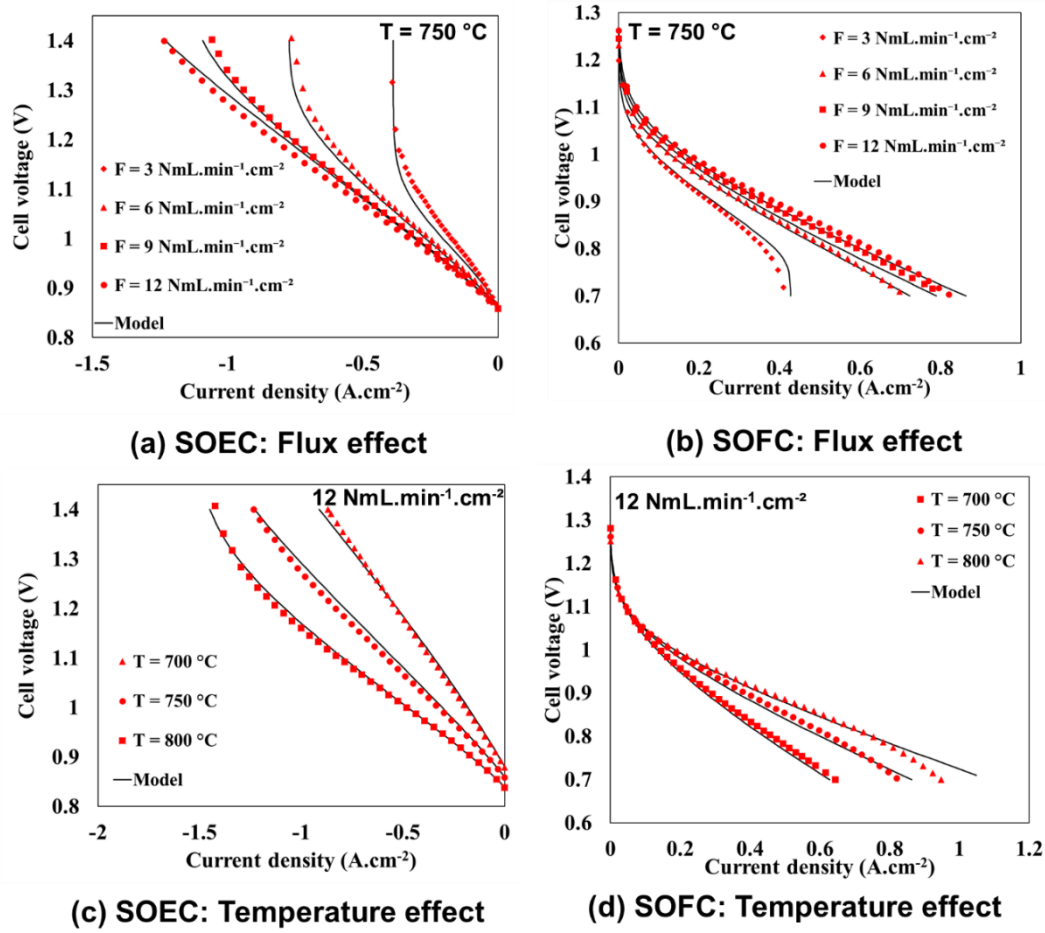

Figure 3-5 – Polarization curves showing the effect of the inlet gas flux at 750 °C in (a) SOEC and (b) SOFC modes, and effect of the temperature for a flux of 12 NmL.min^{-1}.cm^{-2} at 750 °C in (c) SOEC and (d) SOFC modes.

To go deeper in the model validation, the local polarization curves have been measured with our specific setup at the cell inlet, middle and outlet. The results obtained in SOEC modes are compared in Figure 3-6a-c to the local polarization curves extracted from the simulations in the same operating conditions than the experiments. It can be noted that the cell response is strongly heterogeneous along the electrode radius, the performances decrease continuously from the gas inlet (cell center) up to the outlet (cell periphery). Moreover, it can be observed that this evolution of the local polarization curves is enhanced when the temperature is increased. This heterogeneity along the electrode radius is mainly induced by the loss in performance caused by the steam consumption and depletion from the inlet to the outlet [17], [41]. Indeed, the strong gradient in steam partial pressure along the cell radius (cf. Figure 3-8)

increases the local concentration overpotentials, which in turn lead to decrease the local current densities. In the most critical condition (i.e. T = 800 °C, curve related to the edge position), it becomes possible to observe the beginning of a turning back behavior of the curves as shown in Figure 3-6c. This phenomenon was already reported by [17], using a segmented electrode in SOFC operations. It is related to the local current density distribution in the cell and its evolution with the polarization. At low polarization, the repartition of the current is quite homogeneous all along the cell length. In this condition, the local current densities increase with the polarization even in the cell outlet. However, the gradient becomes more and more pronounced with the polarization, due to the fuel shortage (or starvation) close to the cell outlet (i.e. at high fuel utilization in SOFC mode or steam conversion in SOEC mode). Therefore, after increasing, the local current density at the cell outlet starts to decrease. This 'bell-shaped' evolution for the local current density at the cell outlet explains the turning-back behavior in the local cell polarization at the cell outlet.

It is worth mentioning that a very good agreement is found between the experimental data and simulations for all the investigated conditions in Figure 3-6a-c. The model is thus able to predict the heterogeneity along the electrode radius measured in SOEC mode. Moreover, the simulations reproduce correctly the shape of the curves changing with the temperature. For instance, the turning back behavior highlighted at 800°C is well caught by the model.

The same analysis has also been conducted in SOFC mode at 750 °C and 800°C (Figure 3-6d-e). As stated for the SOEC mode, the comparison between the experimental data and the computations also confirms that the model simulates quite precisely the evolution of the local polarization curves along the cell radius in SOFC mode. As expected, the local cell performances are decreased from the inlet to the outlet due to the consumption of hydrogen.

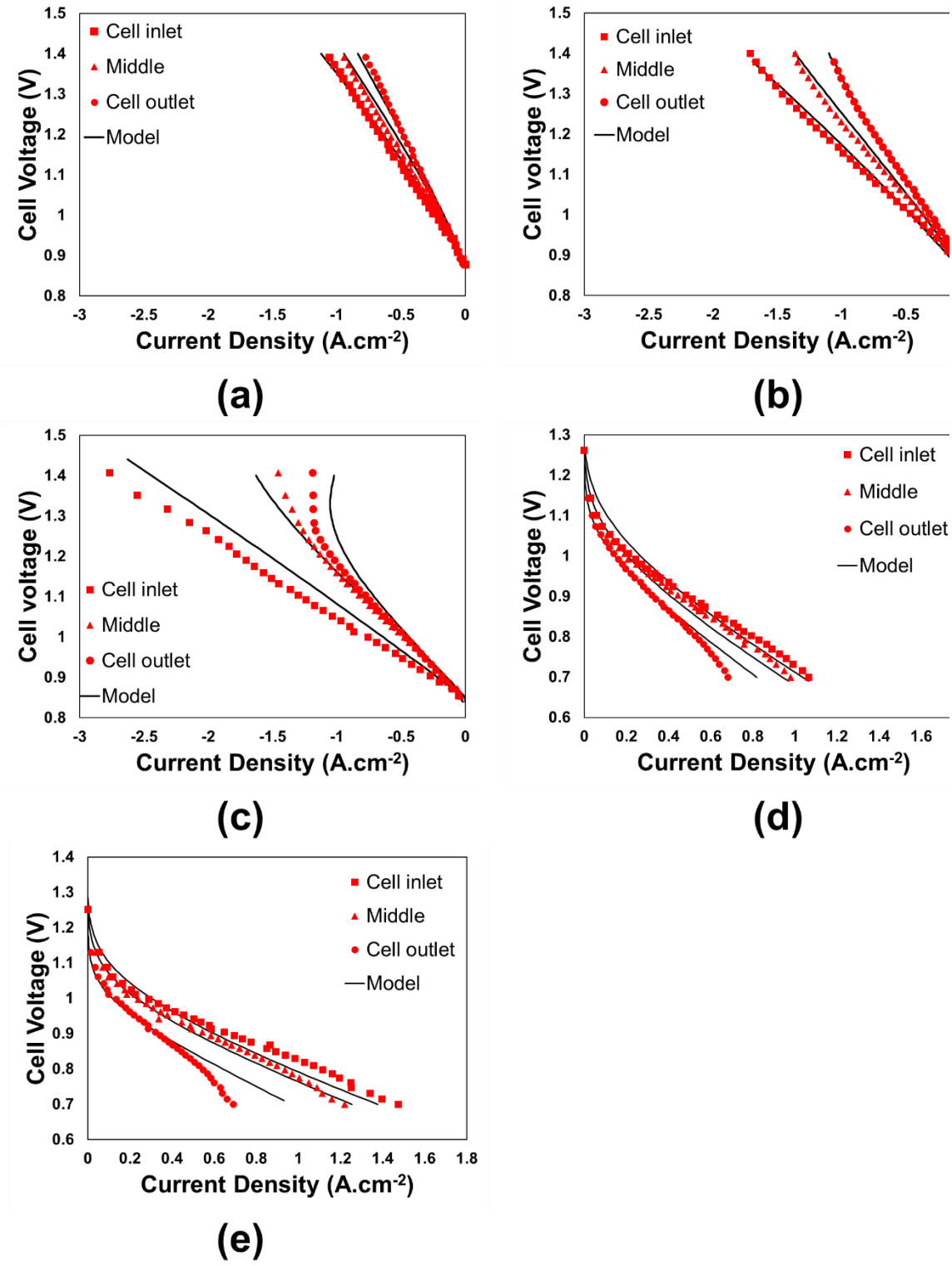

Figure 3-6 – Local polarization curves of cell inlet, middle and outlet for a flux of 12 $NmL.min^{-1}.cm^{-2}$ in SOEC mode at (a) 700 °C, (b) 750 °C and (c) 800 °C and in SOFC mode at 750°C (d) and 800 °C (e).

In Figure 3-7a-c, the local current densities have been plotted as function of the position along the electrode radius in SOEC mode at 700 °C, 750 °C, and 800 °C. Different conditions of cell voltage were chosen for the analysis: one in the region of higher current densities at 1.3 V and the other for an intermediate polarization at 1 V. The experimental data are represented by the red and blue segments, which are related to the local current density measured in each pin at 1.3 and 1 V, respectively. In all situations, the current density profile decreases from the gas inlet in the direction of the cell periphery. This behavior, which is more pronounced at higher temperatures and cell voltage, is in perfect line with the evolution of the local polarization curves. Indeed, as already explained, this evolution of the current density along the cell radius is due to the consumption of steam, which is favored at higher temperatures and higher cell voltages. With this representation, it can be seen that the computed currents along the cell radius are fully consistent with the measurements. Indeed, the simulated curves cross all the segments except at the cell inlet were experimental data are slightly above the predicted currents. This slight discrepancy could be explained by the contact resistances between the grids and the electrodes, which could not be perfectly homogenous in the experiments. It is thus proposed that the contact resistance below the pin at the cell inlet would be slightly lower in such a way that the current density would be higher (and hence, the simulated current systematically lower). Finally, it is worth noting that the same behavior is observed in SOFC mode under polarization at 0.8 V and 1 V at 750 °C and 800 °C (Figure 3-7d-e).

As a general mater, when analyzing the global polarization curves in Figure 3-5 together with the local results shown in Figure 3-6and Figure 3-7, it is possible to conclude that the multiscale model is validated with the global and local measurements obtained for various operating conditions. Moreover, it has been shown that the experimental data obtained using the special setup is consistent with the expected results for this type of cell. Hence, it is possible to state that there is a mutual validation between the experimental data and the multiscale model. In other words, the general good agreement between the modeling results and the experimental data can be seen as a cross validation of the model with our specific setup proposed to measure the local polarization curves.

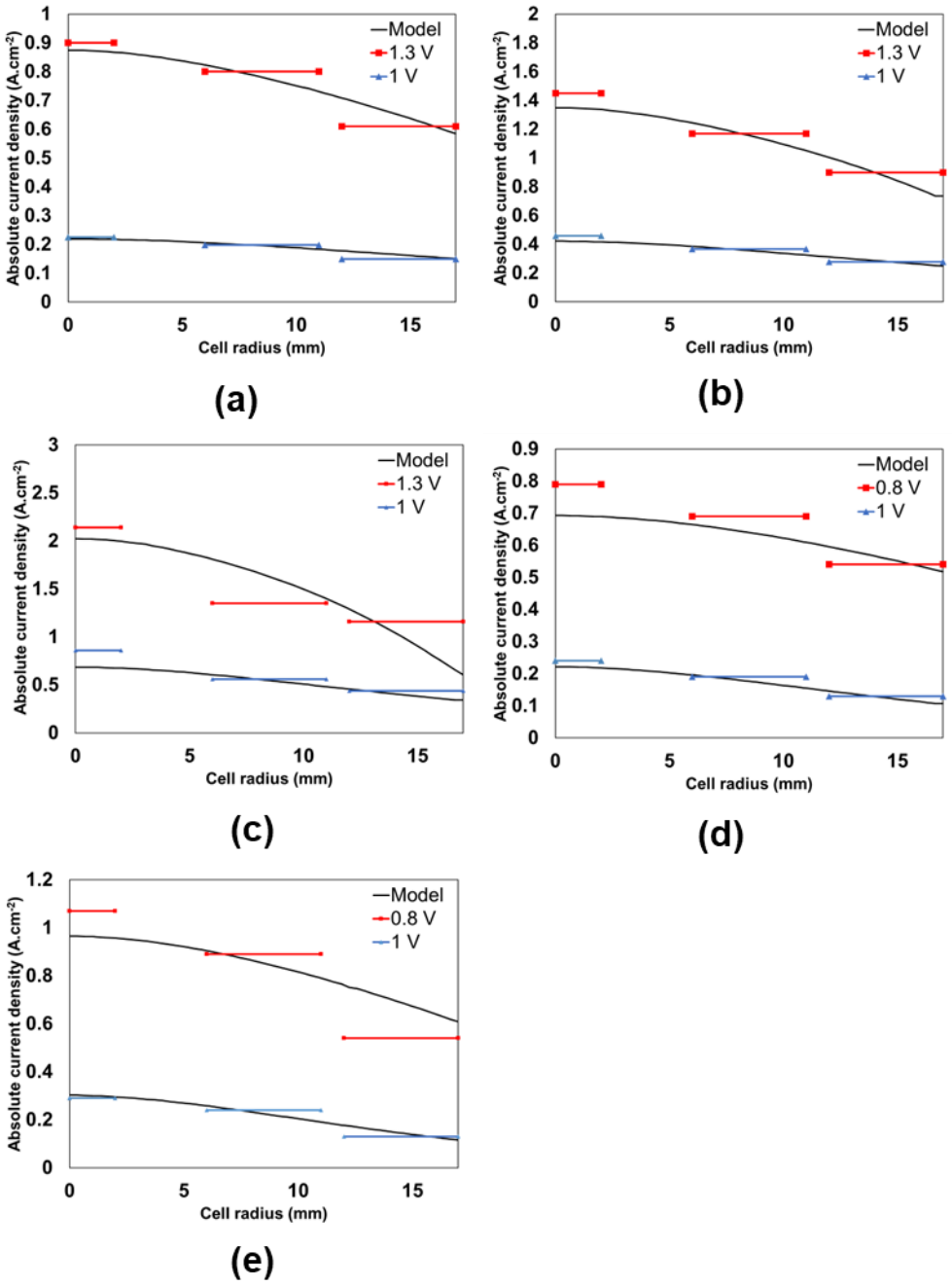

Figure 3-7 – Radial distribution of the current in SOEC mode (cell voltage of 1.3 V and 1 V, inlet flux = 12 NmL.min^{-1}cm^{-2}, P(H_2)/P(H_2O) = 10/90) at (a) 700 °C, (b) 750 °C and (c) 800 °C and in SOFC mode (cell voltage of 0.8 V and 1 V, inlet flux = 12 NmL.min^{-1}cm^{-2}, P(H_2)/P(H_2O) = 100/0) at (d) 750 °C and (e) 800°C.

5. Discussion

5.1 Partial pressures distribution

The multiscale model offers the possibility to compute all the quantities in the electrodes such as the radial distribution of the partial pressure under different conditions of inlet flux, polarization and temperature. As an illustration, the steam and hydrogen partial pressures have been plotted in Figure 3-8a-b at the interface between the electrolyte and the fuel electrode. These distributions have been determined at 750 °C for a current density of ± 0.5 $A.cm^{-2}$ in both SOEC ($P(H_2)/P(H_2O)$ = 10/90) and SOFC modes ($P(H_2)/P(H_2O)$ = 90/10) and for two different inlet fluxes (6 and 12 $NmL.min^{-1}.cm^{-2}$). As expected, in SOEC mode, hydrogen partial pressure increases in the direction of the cell outlet, while the steam partial pressure decreases, since they are respectively produced and consumed by the electrochemical reactions. In SOFC mode, the partial pressures distribution follows an opposite evolution with a decrease of hydrogen concentration and an increase of steam concentration at the cell outlet.

The effect of the inlet flux for the fuel electrode is also shown in Figure 3-8a-b. When the steam and hydrogen supply is lowered, the depletion of reactants in both modes is higher for a given current density. In that condition, the gradients along the cell radius are more pronounced as shown in Figure 3-8a-b. At high fuel utilization in SOFC mode, the starvation of hydrogen at the cell outlet can accelerate the processes of cermet degradation with the local Ni re-oxidation into NiO [60].

The distributions of the oxygen and nitrogen partial pressures in the air electrode are also shown in Figure 3-8c-d. It can be noticed that the gradients of partial pressures along the cell radius are not strongly affected by the cell operation in both modes. These slight evolutions are explained by the high inlet flux of air (41 $NmL.\ min^{-1}.cm^{-2}$) that guarantees a supply of oxygen all along the electrode radius.

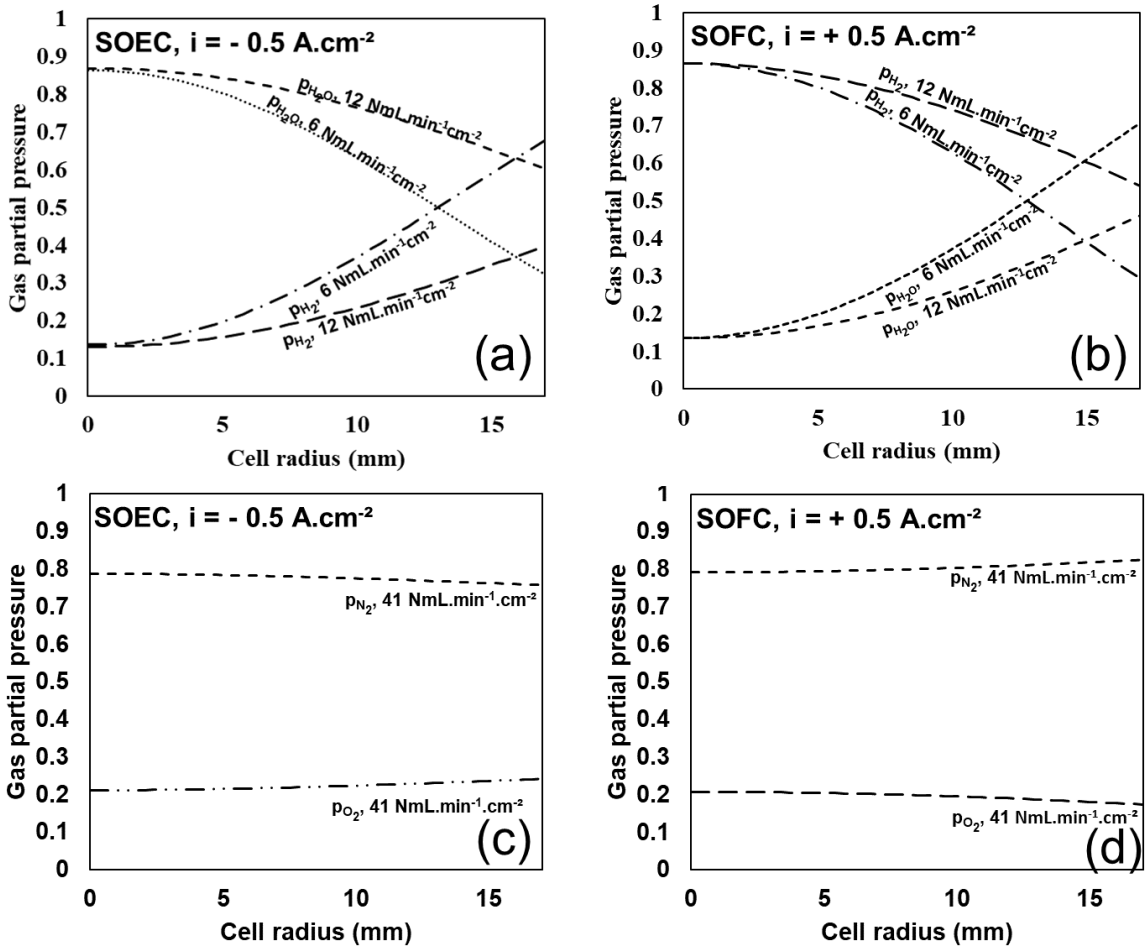

Figure 3-8 – Partial pressures of H_2 and H_2O along the cell radius for 6 NmL.min^{-1}cm^{-2} and 12 NmL.min^{-1}cm^{-2} at 750 °C under (a) cathodic polarization and partial pressure in the gas inlet of $P(H_2)/P(H_2O)$ = 10/90, and (b) anodic polarization and partial pressure in gas inlet of $P(H_2)/P(H_2O)$= 90/10. Partial pressures of O_2 and N_2 along the cell radius for 41 NmL.min^{-1}cm^{-2} at 750 °C under (c) anodic polarization and partial pressure in the gas inlet of $P(O_2)/P(N_2)$ = 21/79, and (d) cathodic polarization and partial pressure in the gas inlet of $P(O_2)/P(N_2)$ = 21/79.

5.2 Reaction mechanism in the fuel electrode

The extent of the active reaction zone in the fuel electrode can be quantified by plotting as a function of the electrode thickness the local ionic (i_{io}) and electronic (i_{el}) current densities in YSZ and Ni [61]. These evolutions have been extracted from the simulating results for the three positions along the electrode radius at the cell inlet, middle and outlet. They are reported in Figure 3-9 for a cell operating at 750°C and ±0.5 A.cm^{-2} in SOFC and SOEC mode. As

expected, the electronic current density increases from the electrolyte interface up to the current collector while the ionic current density follows the opposite evolution. With the studied microstructure, it can be noticed that the reactions spread over a distance of around 15 µm in the cermet thickness when operated in electrolysis mode (Figure 3-9a). Moreover, it is found that the repartition of the current density in the active layer is not significantly impacted by the position along the cell radius. From a practical point of view, this statement means that it is not necessary to tune the thickness of the functional layer from the cell inlet to the outlet during manufacturing. Finally, it can be noticed that the same statement has been found when the cell is operated in fuel cell mode (Figure 3-9b). Nevertheless, the extension of the reaction zone in the electrode is slightly lower than in SOEC mode. This difference is related to a change in the activated reaction mechanism, which is detailed hereafter.

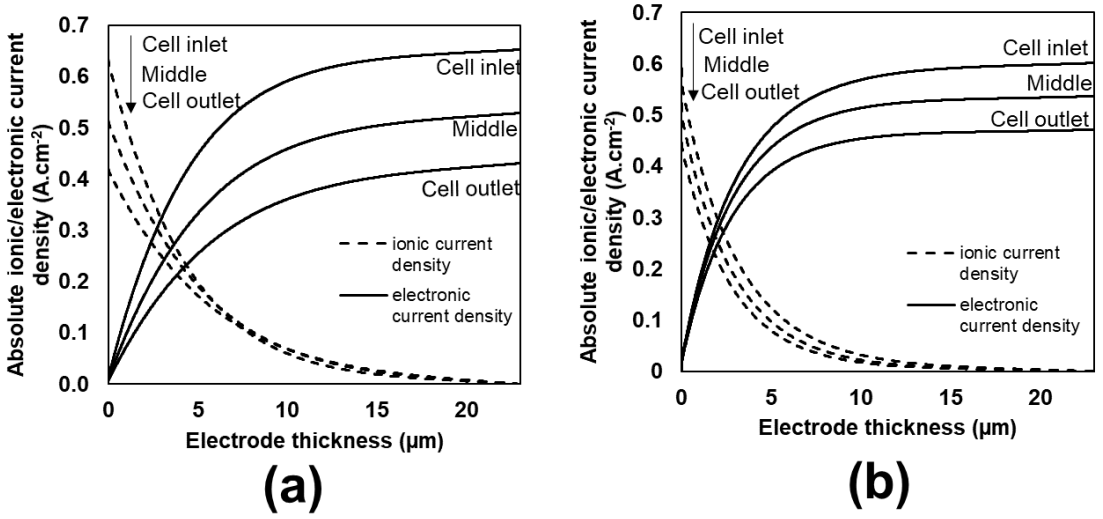

Figure 3-9 – Distribution of the ionic and electronic currents along the electrode thickness for different radial positions with an inlet gas flux of 12 NmL.min^{-1}.cm^{-2}, T = 750 °C and P(H_2)/P(H_2O) = 50/50 in (a) SOEC mode at -0.5 A.cm^{-2} and (b) SOFC mode at +0.5 A.cm^{-2}.

To highlight the effect of the position on the reaction mechanism, the ratio (ξ) between the kinetic rates of steam adsorption/desorption on YSZ (v_{R2}) and Ni (v_{R1}) (cf. Table 3-1) has been computed at the cell inlet, middle and outlet:

$$\xi(r) = \frac{\int_{z=0}^{z=FL} v_{R2}(z,r)\,dz}{\int_{z=0}^{z=FL} v_{R1}(z,r)\,dz} \quad (6)$$

A ratio higher than one means that the mechanism is mainly controlled by the reaction pathway related to the steam interaction with YSZ. On the contrary, a ratio lower than one indicates that reaction mechanism is dominated by the pathway related to the steam interaction with Ni.

This ratio is plotted in Figure 3-10a for an operation in SOFC mode at 750°C and i=+ 0.5 A.cm^{-2}. As already explained in [48], the majority of the steam is produced in fuel cell mode by the water desorption from the YSZ surface (ξ>1). Nevertheless, the ratio between the two pathways decreases in the direction of the cell outlet. This evolution in the reaction mechanism along the cell radius can be explained by the inspection of the surface coverages on the Ni and YSZ (Figure 3-11). For the water molecules, it can be remarked that both coverages on Ni and YSZ increases from the inlet up to the outlet (Figure 3-11a-b) since the steam partial pressure is higher at the cell periphery (Figure 3-8b). However, it is worth noting that the increase of Θ_{H_2O} at the cell outlet is stronger for the Ni surface than for the YSZ. Indeed, an increase of 4.5x is found for Ni surface between the inlet and outlet (Figure 3-11a), whereas in the same conditions, an increase of 2.3x is found for the local coverage on YSZ surface (Figure 3-11b). This evolution points out that, compared to the cell inlet, the capability of the YSZ surface at the cell outlet to accept additional water molecules becomes limited. This trend is related to the very high coverage of hydroxyl ions resulting in low available sites on the YSZ surface when the steam partial pressure is increased (Figure 3-11c-d). On the other hand, the available site on Ni tends to increase at the cell outlet due to the decrease of hydrogen ad-atom surface concentration (Figure 3-11e-f). As a result, the reaction pathway with the steam desorption from YSZ becomes more and more bounded in the direction of the cell outlet while the one from Ni surface becomes favored. Finally, it can be noticed that the decrease of the ratio along the cell radius is enhanced when the inlet gas flux is lowered (Figure 3-10a). Indeed, the higher fuel utilization leads to a stronger gradient of gas partial pressure along the electrode radius, and hence, a higher steam partial pressure at the cell outlet (cf. Figure 3-8b).

Regarding an operation in SOEC mode, the ratio has been computed along the cell radius at 750°C and i=-0.5 A.cm^{-2} (Figure 3-10b). It can be noted that the ratio follows an opposite behavior when compared to the SOFC mode. Indeed, it increases in the direction of the cell

outlet, changing the prevailing mechanism of interaction between steam molecules and the electrode surface. At the cell inlet, the mechanism is mainly controlled by the adsorption of steam on Ni surface (i.e. $\xi<1$) while, at the cell outlet, the mechanism becomes more and more dominated by the steam adsorption on YSZ (i.e. $\xi>1$). As for the SOFC mode, this behavior can also be explained by analyzing the distribution of surface coverages on YSZ and Ni. For instance, the evolution of Θ_{H_2O} along the cell radius is shown in Figure 3-12a-b on both materials. A decrease of 60% is found for the surface coverage on Ni from the inlet to the outlet. On the other hand, the decrease in the steam coverage is only about 35% for YSZ. Hence, the quantity of steam associated with the YSZ surface increases as a function of the electrode radius, which favors the reaction pathway that takes into consideration the adsorption on the YSZ surface, increasing the ratio ξ.

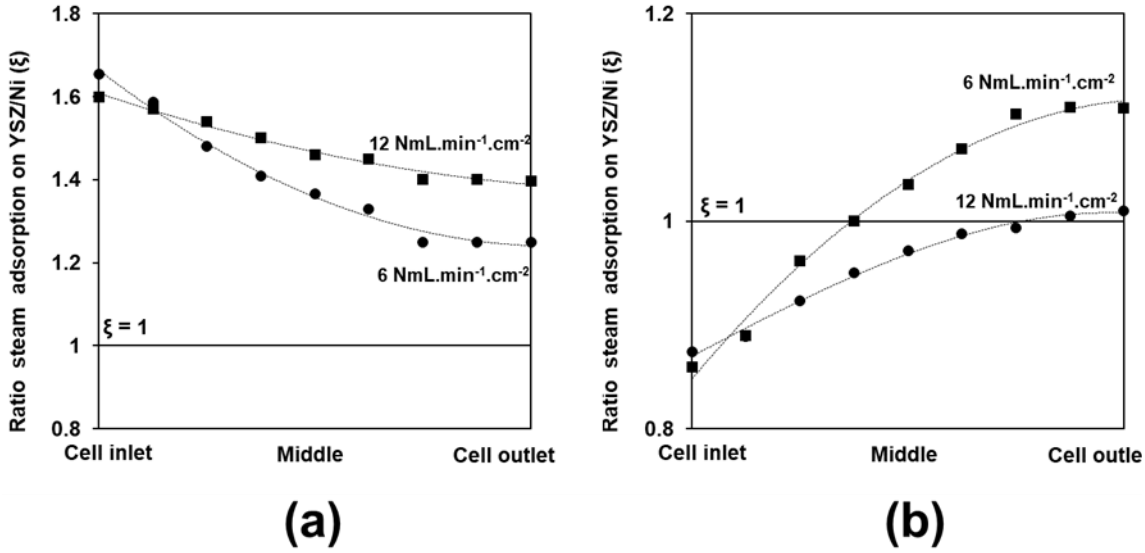

Figure 3-10 – (a) Ratio between the kinetic rates of steam desorption on Ni and YSZ surfaces as a function of the cell radius at 750 °C, with an inlet gas flux of 6 NmL.min^{-1}.cm^{-2} and 12 NmL.min^{-1}.cm^{-2} in (a) SOFC mode ($P(H_2)/P(H_2O)$ = 90/10) at i = +0.5 A.cm^{-2}, and (b) SOEC mode ($P(H_2)/P(H_2O)$ = 10/90) at i = -0.5 A.cm^{-2}.

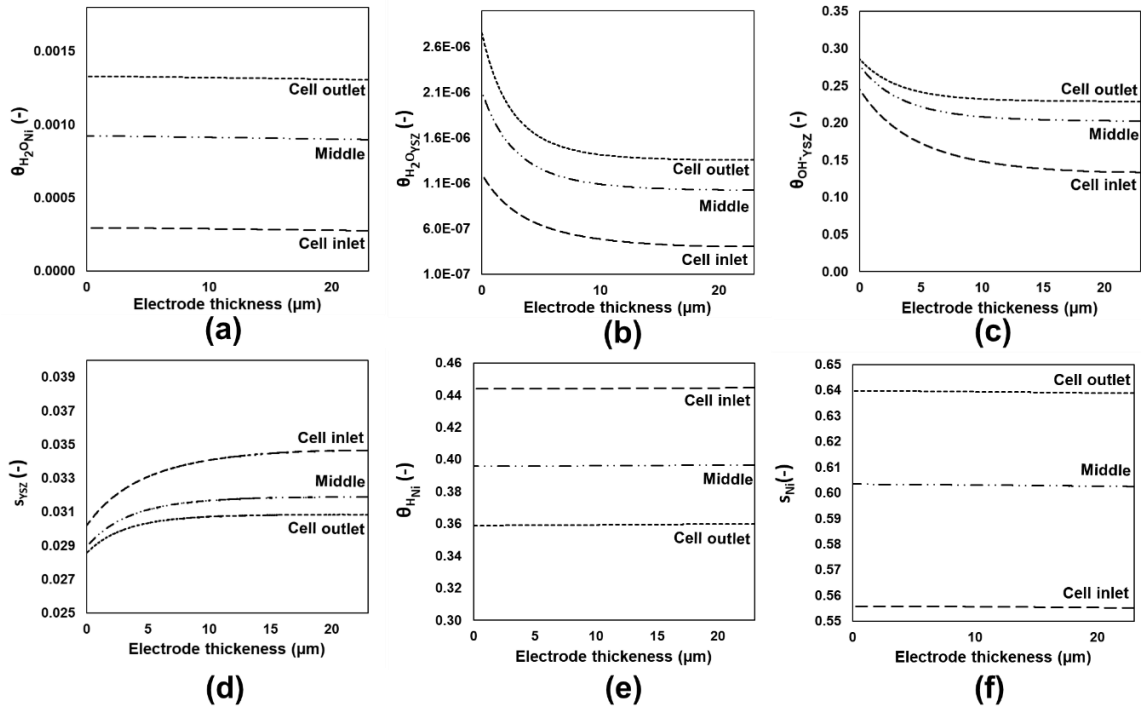

Figure 3-11 – Evolution of the surface coverage on YSZ and Ni surfaces in SOFC mode ($P(H_2)/P(H_2O)$ = 90/10) at 750 °C, i = +0.5 $A.cm^{-2}$ and with an inlet gas flux of 6 $NmL.min^{-1}.cm^{-2}$ for: (a) H_2O molecules on Ni surface, (b) H_2O molecules on YSZ surface, (c) OH^- ions on YSZ surface, (d) free sites on YSZ surface, (e) hydrogen ad atom on Ni surface, and (f) free sites on Ni surface.

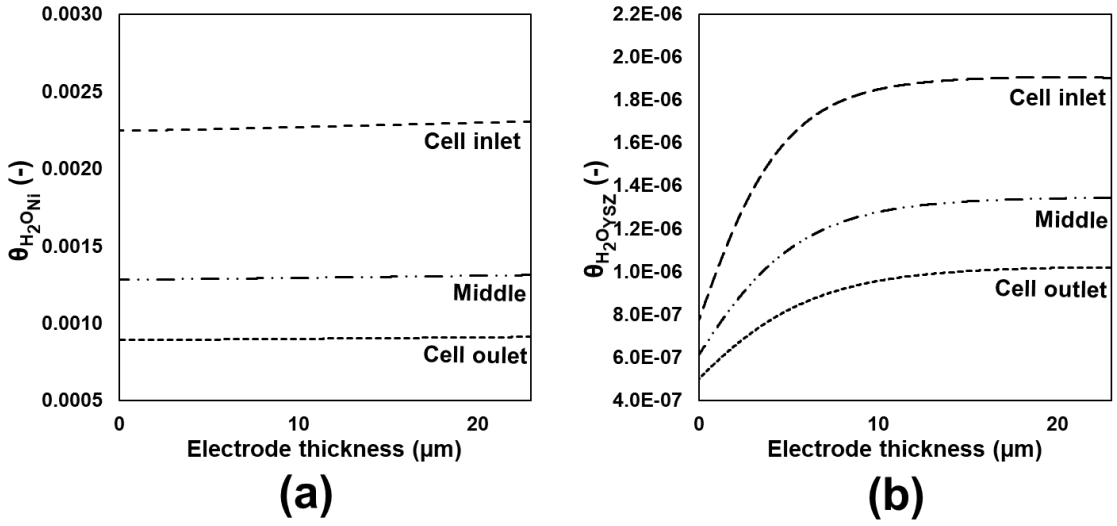

Figure 3-12 – Evolution of the surface coverage on YSZ and Ni surfaces in SOEC mode ($P(H_2)/P(H_2O) = 10/90$) at 750 °C, i = -0.5 A.cm^{-2} and with an inlet gas flux of 6 NmL.min^{-1}.cm^{-2} for: (a) H_2O molecules on Ni surface, (b) H_2O molecules on YSZ surface.

5.3 Reaction mechanism in the air electrode

The local electronic current densities in LSCF and the sum of the ionic current densities in LSCF and CGO have been taken from the simulated dataset for an operation at 750°C and a cell current of ± 0.5 A.cm^{-2} in SOFC/SOEC mode. The profiles in the electrode thickness are plotted in Figure 3-13a (SOFC) and Figure 3-13b (SOEC) for the cell inlet, middle and outlet. With the microstructure of the studied LSCF-CGO composite, the reaction zone in the functional layer spreads over a limited distance of a few micrometers and does not exceed 10 µm in electrolysis mode (Figure 3-13a). Moreover, as for the fuel electrode, the repartition of the local current densities is not significantly impacted by the position along the cell radius. It can be also noticed that the thickness of the reaction zone in fuel cell mode is roughly similar to the one in SOEC mode. Indeed, in this case, the reaction mechanism remains identical for both polarizations as detailed hereafter.

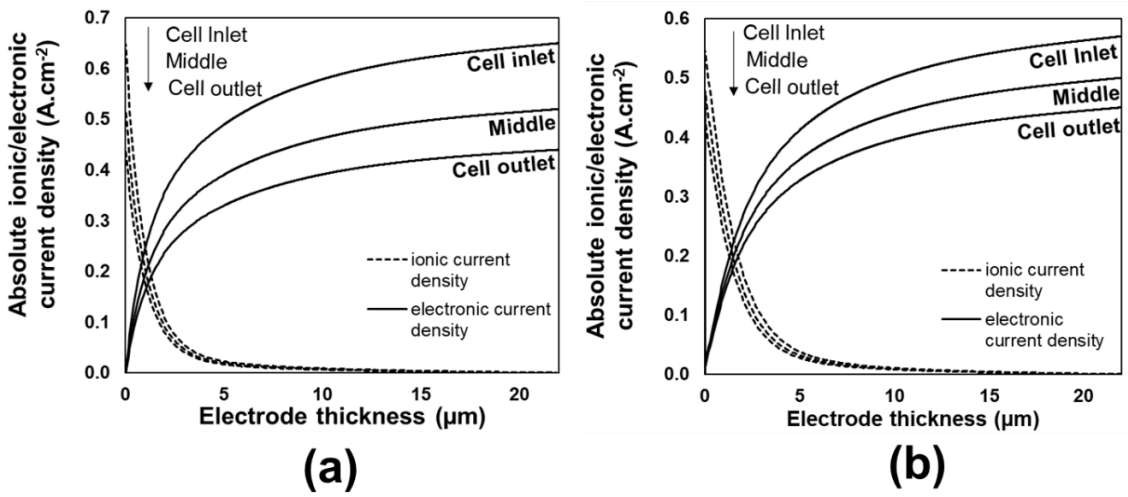

Figure 3-13 –Distribution of the ionic and electronic currents along the cell thickness for different radial positions with an inlet gas flux of 41 NmL.min^{-1}.cm^{-2}, T = 750 °C and P(O_2)/P(N_2) = 50/50 in (a) SOFC mode (i = +0.5 A.cm^{-2}) and (b) SOEC mode (-0.5 A.cm^{-2}).

The multiscale model has been also applied to analyze the activated reaction mechanism depending on the position along the cell radius. For this purpose, the ratio between the surface to the bulk path has been defined as follows [28]:

$$\zeta(r) = \frac{\int_{z=0}^{z=FL} v_{R10}(z,r)dz}{\int_{z=0}^{z=FL} v_{R9}(z,r)dz} \quad (7)$$

where v_{R9} and v_{R10} denote the kinetic rates for the reactions R9 and R10, respectively (Table 3-1). When $\zeta > 1$, the mechanism is mainly controlled by the surface path related to the charge transfer at TPBls, whereas $\zeta < 1$ means that the mechanism is governed by the bulk path related to the oxygen incorporation/excorporation at the LSCF surface.

The ratio ζ is plotted as function of the cell radius in Figure 3-14a-b for a cell operated in SOFC and SOEC modes, respectively (at 750°C and i=+/-0.5 A.cm^{-2}). Whatever the position in the cell, it can be noted that the mechanism is completely dominated by the surface path ($\zeta >$ 1) for both operating modes. This result is explained by the high density of active TPBls in the LSCF-CGO composite that favors the surface path [26], [28].

Under SOEC mode, it can be observed that the ratio decreases in the direction of the cell outlet (Figure 3-14b). This evolution is driven by the concentration of incorporated oxygen atoms in the LSCF that has been computed from the inlet to the cell outlet. As shown in Figure 3-14d, this concentration decreases along the cell length due to the decrease of the local current density (cf. Figure 3-7). Therefore, the lower concentration of oxygen atom in LSCF, which is directly related to a higher concentration of vacancies, tends to promote the bulk path as already detailed in [28]. Under SOFC mode, the opposite behavior is observed. The oxygen reduction at the TPBls (i.e. surface path) is promoted at the cell outlet compared to the cell inlet (Figure 3-14a). This behavior is linked to the increase in the concentration of incorporated oxygen in the direction of the cell outlet as shown in Figure 3-14c [14].

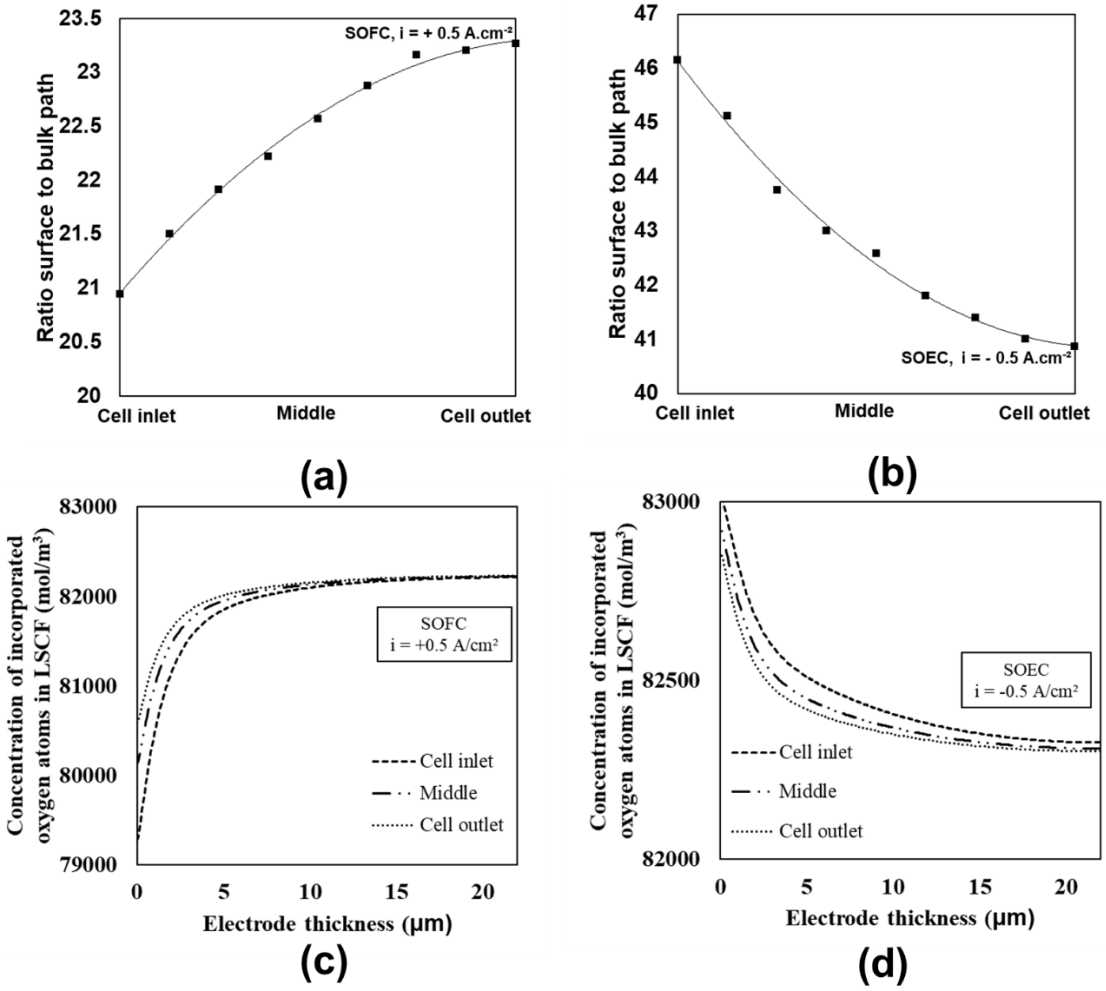

Figure 3-14 – Ratio between the surface and bulk pathways along the functional layer thickness for different regions of the cell radius at 750 °C and inlet flux of 41 NmL.min^{-1}cm^{-2} in (a) SOFC mode (i = +0.5 A.cm^{-2}) and (b) SOEC mode (i = -0.5 A.cm^{-2}). Concentration of oxygen atoms incorporated in LSCF along the functional layer thickness for different regions of the cell radius at 750 °C and inlet flux of 41 NmL.min^{-1}cm^{-2} in (c) SOFC mode (i = +0.5 A.cm^{-2}) and (d) SOEC mode (i = -0.5 A.cm^{-2}).

6. Conclusion

A coupled experimental and numerical approach has been adopted to elucidate the complex relationships between the global SOC response and the reaction mechanisms taking place in the electrodes. To perform this study, an in-house multiscale model has been developed and

validated. This physical-based model consists of a combination of three different length-scales. The first module is devoted to the generation of synthetic microstructures for the morphological description of both electrodes. The second module describes all the microscopic processes arising in the electrodes functional layers. They take into account the reaction mechanisms divided in elementary steps together with the mass and charge transfer in the electrode phases. These kinetic models are linked to the third module that allows the simulation of the global cell response. The multiscale model offers the possibility to study the impact of the cell design on the local distribution of reaction kinetic rates, current densities, gas composition, etc.

To validate the multiscale model, a special setup has been developed to measure the local polarization curves along the cell length. For this purpose, a specific design of the interconnect has been proposed in order to probe the local current density in the cell without any segmentation of the electrodes. This setup has been used to characterize a typical cell made of the classical SOCs materials (i.e. Ni-YSZ//YSZ//LSCF-CGO). Global and local polarization curves have been recorded in both SOFC and SOEC modes between 700 °C and 800 °C and for a large range of inlet flux for the fuel electrode (3-12 $NmL.min^{-1}.cm^{-2}$). As expected, it has been found that the cell performances are improved with increasing the H_2/H_2O inlet flux and the temperature. The local measurements have confirmed that the local current density decreases along the cell length from the inlet to the outlet.

The cell response has been computed with the model in the same conditions than the experiments. For this purpose, the model has been applied to the studied cell by considering an accurate description of the electrode microstructures. It has been found that the model is able to simulate accurately the global and local polarization curves obtained in SOFC and SOEC modes. A good agreement has been found between the simulated local current densities and the ones measured along the cell for various cell voltages. These results constitute a cross validation of the model and the specific setup proposed to measure the local current densities.

The model has been applied to study the fuel and air electrode operation as a function of the cell length. For the fuel electrode, it has been highlighted that the extension of the reactions in the functional layer is almost independent on the position along the cell length. However, the reaction mechanism evolves continuously from the cell inlet to the outlet. In SOEC mode, this evolution leads to a change in the mechanism. Indeed, the steam molecules adsorb preferentially on the Ni surface at the inlet; whereas the adsorption on YSZ becomes dominant at the outlet. In SOFC mode, the steam interaction with YSZ surface is favored whatever the position, although the contribution of the Ni surface on the reaction pathways is enhanced along the cell

length. All these evolutions have been discussed and explained with the distribution of adsorbates on both surfaces. Regarding the air electrode, it has been also found that the thickness of the reaction zone in the functional layer is almost the same along the cell length. Moreover, the reaction mechanism remains mainly controlled by the so-called surface path related to the charge transfer at the TPBls. Nevertheless, in SOEC mode, the relative weight of the bulk path associated to the charge transfer at the LSCF surface is increased along the cell length. The opposite trend has been found in SOFC mode. These evolutions have been explained by the change of oxygen content in the LSCF material.

Acknowledgments

The research leading to these results has received funding from Fuel cells and Hydrogen Joint Undertaking under Grant Agreement n° 875047 (RUBY Project), grand agreement n° 101007175 (REACTT project) and grant agreement n° 874577 (NewSOC project). The work has also been supported by Genvia and the project CELCER-EHT.

Nomenclature

Roman symbols

A	Exchange density pre-exponential factor in the hydrogen electrode, (A.cm^{-2})
B	Exchange density pre-exponential factor in the air electrode, (A.cm^{-2})
$C_{O_O^x}^{max.}$	Maximum concentration of oxygen incorporated in LSCF, (mol.m^{-3})
E_a^i	Activation energy of the exchange current density for the electrode *i*, (J.mol^{-1})
$E_{i=0}$	Open circuit voltage, (V)
e^-	Electron, (-)
F	Faraday's constant, (C.mol^{-1})
i	Cell current density, (A.cm^{-2})
i_{io}	Local ionic current density, (A.cm^{-2})
i_{el}	Local electronic current density, (A.cm^{-2})
i_0^i	Exchange current density in the electrode *i*, (A.cm^{-2})
k	Kinetic constant of the reaction, (units shown in Table 3-1)
m	Exchange density exponent for the hydrogen partial pressure, (-)
n	Exchange density exponent for the steam partial pressure, (-)
p	Exchange density exponent for the oxygen partial pressure, (-)
p_i	Partial pressure of the specie *i*, (atm)
R	Universal gas constant, (J.mol^{-1}.K^{-1})
R_c	Contact resistance, (Ω.cm^2)
$\overline{r_i}$	Radius of the phase i, (µm)
s_i	Free site on the surface for the phase *i* (-)
Sp_{i-j}	Specific surface area between phase *i* and *j*, (µm^{-1})
T	Absolut temperature, (K)
U_{cell}	Cell voltage, (V)

Chemical species

$H_2(g)$	Gaseous hydrogen, (-)
$H_2O(g)$	Gaseous water, (-)
H_{Ni}	H attached on Ni surface, (-)
H_2O_{Ni}	H_2O attached on Ni surface, (-)
H_2O_{YSZ}	H_2O attached on YSZ surface, (-)

$h^{\bullet}$	Hole defect in the LSCF, (-)
$O_2(g)$	Gaseous oxygen
O_{YSZ}^{2-}	O^{2-} attached on YSZ surface, (-)
$O_O^x(YSZ)$	Oxygen in the YSZ lattice, (-)
OH_{YSZ}^{-}	OH^- attached on YSZ surface, (-)
$O_O^x(CGO)$	Oxygen in CGO lattice
$O_O^x(LSCF)$	Oxygen in LSCF lattice
O_{LSCF}^{-}	Oxygen ad-ion on the LSCF surface
O_{LSCF}	Oxygen ad-atom on the LSCF surface
$O_{2_{LSCF}}$	Oxygen ad-molecule on the LSCF surface
$V_O^{\bullet\bullet}(YSZ)$	Oxygen vacancies in the YSZ lattice, (-)
$V_O^{\bullet\bullet}(LSCF)$	Oxygen vacancy in the LSCF lattice, (-)
$V_O^{\bullet\bullet}(CGO)$	Oxygen vacancy in the CGO lattice, (-)

Greek symbols

ε_i	Volume fraction of the phase *i*, (-)
ζ	Ratio between surface and bulk path, (-)
ξ	Ratio between steam adsorption/desorption on Ni and YSZ, (-)
ξ_{TPB}	Triple phase boundary length density, (μm^{-2})
η_{conc}^{i}	Concentration overpotential in the electrode *i*, (V)
η_{act}^{i}	Activation overpotential in the electrode *i*, (V)
η_{ohm}	Ohmic overpotential, (V)
η_{diff}	Gas diffusion overpotential, (V)
η_{conv}	Gas conversion overpotential, (V)
θ_{i_j}	Local coverage of the specie i on the surface of the phase *j*, (-)
τ_i	Tortuosity factor of the phase *i*, (-)

List of Abbreviations

3YSZ	Yttria Stabilized Zirconia with 3.mol% of Yttria
8YSZ	Yttria Stabilized Zirconia with 8.mol% of Yttria
CGO	Gadolinium-doped Ceria
DGM	Dusty Gas Model
EIS	Electrochemical Impedance Spectroscopy
HTSE	High-Temperature Steam Electrolysis
LSCF	Lanthanum Strontium Cobalt Ferrite
MIEC	Mixed Ionic and Electronic Conductor
OCV	Open Circuit Voltage
RVE	Representative Volume Element
SOCs	Solid Oxide Cells
SOEC	Solid Oxide Electrolysis Cell
SOFC	Solid Oxide Fuel Cell
SRU	Single Repeating Unit
YSZ	Yttria Stabilized Zirconia

References

[1] A. Godula-Jopek, *Hydrogen Production by Electrolysis*. 2015.

[2] J. Aicart, Z. Wuillemin, B. Gervasoni, D. Reynaud, F. Waeber, C. Beetschen, Y. Antonetti, A. Nesci, and J. Mougin, "Performance evaluation of a 4-stack solid oxide module in electrolysis mode," *Int. J. Hydrogen Energy*, vol. 47, no. 6, pp. 3568–3579, Jan. 2022, doi: 10.1016/j.ijhydene.2021.11.056.

[3] F. Monaco, D. Ferreira-Sanchez, M. Hubert, B. Morel, D. Montinaro, D. Grolimund, and J. Laurencin, "Oxygen electrode degradation in solid oxide cells operating in electrolysis and fuel cell modes: LSCF destabilization and interdiffusion at the electrode/electrolyte interface," *Int. J. Hydrogen Energy*, vol. 46, no. 62, pp. 31533–31549, Sep. 2021, doi: 10.1016/j.ijhydene.2021.07.054.

[4] E. Da Rosa Silva, M. Hubert, B. Morel, H. Moussaoui, J. Debayle, and J. Laurencin, "A Dynamic Multi-Scale Model for Solid Oxide Cells Validated on Local Current Measurements: Impact of Global Cell Operation on the Electrodes Reaction Mechanisms," *ECS Meet. Abstr.*, vol. MA2021-03, no. 1, pp. 164–164, 2021, doi: 10.1149/ma2021-031164mtgabs.

[5] S. J. McPhail, S. Frangini, J. Laurencin, E. Effori, A. Abaza, A. K. Padinjarethil, A. Hagen, A. Léon, A. Brisse, D. Vladikova, B. Burdin, F. R. Bianchi, B. Bosio, P. Piccardo, R. Spotorno, H. Uchida, P.

Polverino, E. A. Adinolfi, F. Postiglione, J. Lee, H. Moussaoui, J . Van Herle, “Addressing planar solid oxide cell degradation mechanisms: A critical review of selected components,” *Electrochem. Sci. Adv.*, no. February, pp. 1–37, Nov. 2021, doi: 10.1002/elsa.202100024.

[6] Q. Cai, C. S. Adjiman, and N. P. Brandon, “Optimal control strategies for hydrogen production when coupling solid oxide electrolysers with intermittent renewable energies,” *J. Power Sources*, vol. 268, pp. 212–224, 2014, doi: 10.1016/j.jpowsour.2014.06.028.

[7] S. B. Beale, M. Andersson, C. Boigues-Muñoz, H. L. Frandsen, Z. Lin, S. J. McPhail, M. Ni, B. Sundén, A. Weber, and A. Z. Weber, “Continuum scale modelling and complementary experimentation of solid oxide cells,” *Prog. Energy Combust. Sci.*, vol. 85, p. 100902, 2021, doi: 10.1016/j.pecs.2020.100902.

[8] A. Nechache and S. Hody, “Alternative and innovative solid oxide electrolysis cell materials: A short review,” *Renew. Sustain. Energy Rev.*, vol. 149, 2021, doi: 10.1016/j.rser.2021.111322.

[9] A. Nechache, M. Cassir, and A. Ringuedé, “Solid oxide electrolysis cell analysis by means of electrochemical impedance spectroscopy : A review,” *J. Power Sources*, vol. 258, pp. 164–181, 2014, doi: 10.1016/j.jpowsour.2014.01.110.

[10] C. H. J. UNDERTAKING, “Strategic Research and Innovation Agenda for RHC, 2013,” *Decis. no. CleanHydrogen-GB-2022-02*, 2020, doi: 10.13140/2.1.4252.7520.

[11] S. D. Vora, W. L. Lundberg, and J. F. Pierre, "Overview of U.S. Department of Energy Office of Fossil Energy’s Solid Oxide Fuel Cell Program," *ECS Trans.*, vol. 78, pp. 3-19, 2017, doi: 10.1149/07801.0003ecst.

[12] Q. Fang, L. Blum, and D. Stolten, “Electrochemical Performance and Degradation Analysis of an SOFC Short Stack Following Operation of More than 100,000 Hours,” *J. Electrochem. Soc.*, vol. 166, no. 16, pp. F1320–F1325, 2019, doi: 10.1149/2.0751916jes.

[13] Y. Wang, W. Li, L. Ma, W. Li, and X. Liu, “Degradation of solid oxide electrolysis cells: Phenomena, mechanisms, and emerging mitigation strategies—A review,” *J. Mater. Sci. Technol.*, vol. 55, pp. 35–55, 2020, doi: 10.1016/j.jmst.2019.07.026.

[14] J. Laurencin, M. Hubert, D. F. Sanchez, S. Pylypko, M. Morales, A. Morata, B. Morel, D. Montinaro, F. Lefebvre-Joud, and E. Siebert, “Degradation mechanism of La0.6Sr0.4Co0.2Fe0.8O3-δ/Gd0.1Ce0.9O2-δ composite electrode operated under solid oxide electrolysis and fuel cell conditions,” *Electrochim. Acta*, vol. 241, pp. 459–476, 2017, doi: 10.1016/j.electacta.2017.05.011.

[15] P. Metzger, K. A. Friedrich, H. Müller-Steinhagen, and G. Schiller, “SOFC characteristics along the flow path,” *Solid State Ionics*, vol. 177, no. 19-25 SPEC. ISS., pp. 2045–2051, 2006, doi: 10.1016/j.ssi.2006.06.019.

[16] F. Ravussin, J. Van herle, N. Autissier, M. Molinelli, D. Larrain, and D. Favrat, “Local current measurement in a solid oxide fuel cell repeat element,” *J. Eur. Ceram. Soc.*, vol. 27, no. 2–3, pp. 1035–1040, 2007, doi: 10.1016/j.jeurceramsoc.2006.05.089.

[17] W. G. Bessler, S. Gewies, C. Willich, G. Schiller, and K. A. Friedrich, “Spatial distribution of electrochemical performance in a segmented SOFC: A combined modeling and experimental study,” *Fuel Cells*, vol. 10, no. 3, pp. 411–418, 2010, doi: 10.1002/fuce.200900083.

[18] P. Tanasini, J. A. Schuler, Z. Wuillemin, M. L. B. Ameur, C. Comninellis, and J. Van Herle, "Segmented cell testing for cathode parameter investigation," *J. Power Sources*, vol. 196, no. 17, pp. 7097–7103, 2011, doi: 10.1016/j.jpowsour.2010.08.034.

[19] Z. Wuillemin, Y. Antonetti, C. Beetschen, O. Millioud, S. Ceschini, H. Madi, and J. Van herle, "Local Activation and Degradation of Electrochemical Processes in a SOFC," *ECS Trans.*, vol. 57, no. 1, pp. 561–570, 2013, doi: 10.1149/05701.0561ecst.

[20] Ö. Aydın, H. Nakajima, and T. Kitahara, "Reliability of the numerical SOFC models for estimating the spatial current and temperature variations," *Int. J. Hydrogen Energy*, vol. 41, no. 34, pp. 15311–15324, 2016, doi: 10.1016/j.ijhydene.2016.06.194.

[21] B. Conti, B. Bosio, S. J. McPhail, F. Santoni, D. Pumiglia, and E. Arato, "A 2-D model for intermediate temperature solid oxide fuel cells preliminarily validated on local values," *Catalysts*, vol. 9, no. 1, 2019, doi: 10.3390/catal9010036.

[22] J. A. Schuler, H. Yokokawa, C. F. Calderone, Q. Jeangros, Z. Wuillemin, A. Hessler-Wyser, and J. Van Herle, "Combined Cr and S poisoning in solid oxide fuel cell cathodes," *J. Power Sources*, vol. 201, pp. 112–120, 2012, doi: 10.1016/j.jpowsour.2011.10.123.

[23] A. Donazzi, S. De Pascali, F. Garavaglia, and M. Bracconi, "A quasi 2D model for the interpretation of impedance and polarization of a planar solid oxide fuel cell with interconnects," *Electrochim. Acta*, vol. 365, p. 137346, 2021, doi: 10.1016/j.electacta.2020.137346.

[24] H. Moussaoui, J. Laurencin, Y. Gavet, G. Delette, M. Hubert, P. Cloetens, T. Le Bihan, and J. Debayle, "Stochastic geometrical modeling of solid oxide cells electrodes validated on 3D reconstructions," *Comput. Mater. Sci.*, vol. 143, pp. 262–276, 2018, doi: 10.1016/j.commatsci.2017.11.015.

[25] H. Moussaoui, J. Laurencin, M. Hubert, R. Sharma, P. Cloetens, G. Delette, Y. Gavet, and J. Debayle, "Stochastic Geometrical and Microstructural Modeling for Solid Oxide Cell Electrodes," *ECS Trans.*, vol. 91, no. 1, pp. 2031–2043, 2019, doi: 10.1149/09101.2031ecst.

[26] E. Effori, H. Moussaoui, F. Monaco, R. K. Sharma, J. Debayle, Y. Gavet, G. Delette, G. Si Larbi, E. Siebert, J. Vulliet, L. Dessemond, and J. Laurencin, "Reaction Mechanism and Impact of Microstructure on Performances for the LSCF-CGO Composite Electrode in Solid Oxide Cells," *Fuel Cells*, vol. 19, no. 4, pp. 429–444, 2019, doi: 10.1002/fuce.201800185.

[27] M. Hubert, J. Laurencin, P. Cloetens, J. C. da Silva, F. Lefebvre-Joud, P. Bleuet, A. Nakajo, and E. Siebert, "Role of microstructure on electrode operating mechanisms for mixed ionic electronic conductors: From synchrotron-based 3D reconstruction to electrochemical modeling," *Solid State Ionics*, vol. 294, pp. 90–107, 2016, doi: 10.1016/j.ssi.2016.07.001.

[28] E. Effori, J. Laurencin, E. D. R. Silva, M. Hubert, T. David, M. Petitjean, G. Geneste, L. Dessemond, and E. Siebert, "An Elementary Kinetic Model for the LSCF and LSCF-CGO Electrodes of Solid Oxide Cells: Impact of Operating Conditions and Degradation on the Electrode Response," *J. Electrochem. Soc.*, vol. 168, no. 4, p. 044520, 2021, doi: 10.1149/1945-7111/abf40a.

[29] S. Gewies and W. G. Bessler, "Physically Based Impedance Modeling of Ni/YSZ Cermet Anodes," *J. Electrochem. Soc.*, vol. 155, no. 9, p. B937, 2008, doi: 10.1149/1.2943411.

[30] A. Donazzi, G. Cordaro, A. Baricci, Z. Bin Ding, and M. Maestri, "A detailed kinetic model for the

reduction of oxygen on LSCF-GDC composite cathodes," *Electrochim. Acta*, vol. 335, p. 135620, 2020, doi: 10.1016/j.electacta.2020.135620.

[31] J. Laurencin, D. Kane, G. Delette, J. Deseure, and F. Lefebvre-Joud, "Modelling of solid oxide steam electrolyser: Impact of the operating conditions on hydrogen production," *J. Power Sources*, vol. 196, no. 4, pp. 2080–2093, 2011, doi: 10.1016/j.jpowsour.2010.09.054.

[32] L. Bernadet, J. Laurencin, G. Roux, D. Montinaro, F. Mauvy, and M. Reytier, "Effects of Pressure on High Temperature Steam and Carbon Dioxide Co-electrolysis," *Electrochim. Acta*, vol. 253, pp. 114–127, 2017, doi: 10.1016/j.electacta.2017.09.037.

[33] O. Babaie Rizvandi, X. Y. Miao, and H. L. Frandsen, "Multiscale modeling of degradation of full solid oxide fuel cell stacks," *Int. J. Hydrogen Energy*, vol. 46, no. 54, pp. 27709–27730, 2021, doi: 10.1016/j.ijhydene.2021.05.204.

[34] R. T. Nishida, S. B. Beale, J. G. Pharoah, L. G. J. de Haart, and L. Blum, "Three-dimensional computational fluid dynamics modelling and experimental validation of the Jülich Mark-F solid oxide fuel cell stack," *J. Power Sources*, vol. 373, no. July 2017, pp. 203–210, 2018, doi: 10.1016/j.jpowsour.2017.10.030.

[35] M. Navasa, X. Y. Miao, and H. L. Frandsen, "A fully-homogenized multiphysics model for a reversible solid oxide cell stack," *Int. J. Hydrogen Energy*, vol. 44, no. 41, pp. 23330–23347, 2019, doi: 10.1016/j.ijhydene.2019.06.077.

[36] M. Andersson, J. Yuan, and B. Sundén, "Review on modeling development for multiscale chemical reactions coupled transport phenomena in solid oxide fuel cells," *Appl. Energy*, vol. 87, no. 5, pp. 1461–1476, 2010, doi: 10.1016/j.apenergy.2009.11.013.

[37] L. Mastropasqua, A. Donazzi, and S. Campanari, "Development of a Multiscale SOFC Model and Application to Axially-Graded Electrode Design," *Fuel Cells*, vol. 19, no. 2, pp. 125–140, 2019, doi: 10.1002/fuce.201800170.

[38] H. Zhu, R. J. Kee, V. M. Janardhanan, O. Deutschmann, and D. G. Goodwin, "Modeling Elementary Heterogeneous Chemistry and Electrochemistry in Solid-Oxide Fuel Cells," *J. Electrochem. Soc.*, vol. 152, no. 12, p. A2427, 2005, doi: 10.1149/1.2116607.

[39] A. Bertei, J. Mertens, and C. Nicolella, "Electrochemical simulation of planar solid oxide fuel cells with detailed microstructural modeling," *Electrochim. Acta*, vol. 146, pp. 151–163, 2014, doi: 10.1016/j.electacta.2014.08.120.

[40] M. Mozdzierz, K. Berent, S. Kimijima, J. S. Szmyd, and G. Brus, "A multiscale approach to the numerical simulation of the solid oxide fuel cell," *Catalysts*, vol. 9, no. 3, pp. 1–27, 2019, doi: 10.3390/catal9030253.

[41] G. Schiller, W. G. Bessler, K. A. Friedrich, S. Gewies, and C. Willich, "Spatially Resolved Electrochemical Performance in a Segmented Planar SOFC," *ECS Trans.*, vol. 17, no. 1, pp. 79–87, 2009, doi: 10.1149/1.3142737.

[42] M. Lang, C. Auer, G. Braniek, F. Wenz, and F. Hauler, "Understanding the Electrochemical Performance of SOFC Stacks," *ECS Meet. Abstr.*, vol. MA2015-03, no. 1, pp. 352–352, 2015, doi: 10.1149/ma2015-03/1/352.

[43] M. Lang, C. Bohn, M. Henke, G. Schiller, C. Willich, and F. Hauler, “Understanding the Current-Voltage Behavior of High Temperature Solid Oxide Fuel Cell Stacks,” *J. Electrochem. Soc.*, vol. 164, no. 13, pp. F1460–F1470, 2017, doi: 10.1149/2.1541713jes.

[44] W. G. Bessler, S. Gewies, and M. Vogler, “A new framework for physically based modeling of solid oxide fuel cells,” *Electrochim. Acta*, vol. 53, no. 4, pp. 1782–1800, 2007, doi: 10.1016/j.electacta.2007.08.030.

[45] G. Rinaldi, A. Nakajo, J. Van herle, P. Burdet, E. Oveisi, and M. Cantoni, “Strontium Migration at the GDC-YSZ Interface of Solid Oxide Cells in SOFC and SOEC Modes,” *ECS Meet. Abstr.*, vol. MA2017-03, no. 1, pp. 299–299, 2017, doi: 10.1149/ma2017-03/1/299.

[46] J. P. Serra, *Image Analysis and Mathematical Morphology: Theoretical advances*. Academic Press, 1982. [Online]. Available: https://books.google.fr/books?id=SfF4zgEACAAJ

[47] J. Laurencin, M. Hubert, K. Couturier, T. Le Bihan, P. Cloetens, F. Lefebvre-Joud, and E. Siebert, “Reactive Mechanisms of LSCF Single-Phase and LSCF-CGO Composite Electrodes Operated in Anodic and Cathodic Polarisations,” *Electrochim. Acta*, vol. 174, pp. 1299–1316, 2015, doi: 10.1016/j.electacta.2015.06.080.

[48] F. Monaco, E. Effori, M. Hubert, E. Siebert, G. Geneste, B. Morel, E. Djurado, D. Montinaro, and J. Laurencin, “Electrode kinetics of porous Ni-3YSZ cermet operated in fuel cell and electrolysis modes for solid oxide cell application,” *Electrochim. Acta*, vol. 389, pp. 1–53, 2021, doi: 10.1016/j.electacta.2021.138765.

[49] D. G. Goodwin, H. Zhu, A. M. Colclasure, and R. J. Kee, “Modeling Electrochemical Oxidation of Hydrogen on Ni–YSZ Pattern Anodes,” *J. Electrochem. Soc.*, vol. 156, no. 9, p. B1004, 2009, doi: 10.1149/1.3148331.

[50] M. Hubert, A. Pacureanu, C. Guilloud, Y. Yang, J. C. Da Silva, J. Laurencin, F. Lefebvre-Joud, and P. Cloetens, “Efficient correction of wavefront inhomogeneities in X-ray holographic nanotomography by random sample displacement,” *Appl. Phys. Lett.*, vol. 112, no. 20, 2018, doi: 10.1063/1.5026462.

[51] H. Moussaoui, J. Debayle, Y. Gavet, P. Cloetens, and J. Laurencin, “Particle-based model for functional and diffusion layers of solid oxide cells electrodes,” *Powder Technol.*, vol. 367, pp. 67–81, 2020, doi: 10.1016/j.powtec.2020.03.040.

[52] A. Yahya, D. Ferrero, H. Dhahri, P. Leone, K. Slimi, and M. Santarelli, “Electrochemical performance of solid oxide fuel cell: Experimental study and calibrated model,” *Energy*, vol. 142, pp. 932–943, 2018, doi: 10.1016/j.energy.2017.10.088.

[53] D. Kanno, N. Shikazono, N. Takagi, K. Matsuzaki, and N. Kasagi, “Evaluation of SOFC anode polarization simulation using three-dimensional microstructures reconstructed by FIB tomography,” *Electrochim. Acta*, vol. 56, no. 11, pp. 4015–4021, 2011, doi: 10.1016/j.electacta.2011.02.010.

[54] T. Fukumoto, N. Endo, K. Mori, Y. Tachikawa, J. Matsuda, S. Taniguchi, and K. Sasaki, “Exchange Current Density of Solid Oxide Electrolysis Cell Electrodes,” *ECS Meet. Abstr.*, vol. MA2021-03, no. 1, pp. 282–282, 2021, doi: 10.1149/ma2021-031282mtgabs.

[55] P. Costamagna, A. Selimovic, M. D. Borghi, G. Agnew, "Electrochemical model of the integrated planar solid oxide fuel cell (IP-SOFC)," *J. Chem. Eng.*, vol. 102, no. 1, pp 61-69, 2004, doi: 10.1016/j.cej.2004.02.005

[56] J. Udagawa, P. Aguiar, N. P. Brandon, "Hydrogen production through steam electrolysis: Model-based steady state performance of a cathode-supported intermediate temperature solid oxide electrolysis cell," *J. Power Sources*, vol. 166, no. 1, pp. 127-136, 2007, https://doi.org/10.1016/j.jpowsour.2006.12.081.

[57] E. Effori, J. Laurencin, V. Tezyk, C. Montella, L. Dessemond, and E. Siebert, "A physically-based modelling to predict the cyclic voltammetry response of LSCF-type electrodes: Impact of the Ohmic Losses and Microstructure," *Solid State Ionics*, vol. 371, no. August, p. 115765, 2021, doi: 10.1016/j.ssi.2021.115765.

[58] M. Reytier, S. Di Iorio, A. Chatroux, M. Petitjean, J. Cren, M. De Saint Jean, J. Aicart, and J. Mougin, "Stack performances in high temperature steam electrolysis and co-electrolysis," *Int. J. Hydrogen Energy*, vol. 40, no. 35, pp. 11370–11377, 2015, doi: 10.1016/j.ijhydene.2015.04.085.

[59] M. Ni, M. K. H. Leung, and D. Y. C. Leung, "Parametric study of solid oxide fuel cell performance," *Energy Convers. Manag.*, vol. 48, no. 5, pp. 1525–1535, 2007, doi: 10.1016/j.enconman.2006.11.016.

[60] J. Laurencin, G. Delette, B. Morel, F. Lefebvre-Joud, and M. Dupeux, "Solid Oxide Fuel Cells damage mechanisms due to Ni-YSZ re-oxidation: Case of the Anode Supported Cell," *J. Power Sources*, vol. 192, no. 2, pp. 344–352, 2009, doi: 10.1016/j.jpowsour.2009.02.089.

[61] F. Usseglio-Viretta, J. Laurencin, G. Delette, J. Villanova, P. Cloetens, and D. Leguillon, "Quantitative microstructure characterization of a Ni-YSZ bi-layer coupled with simulated electrode polarisation," *J. Power Sources*, vol. 256, pp. 394–403, 2014, doi: 10.1016/j.jpowsour.2014.01.094.

Part II: Multiscale Modelling of Solid Oxide Cells Validated on Electrochemical Impedance Spectra and Polarization Curves

G. Sassone[a], E. Da Rosa Silva[a], M. Prioux[a], M. Hubert[a], B. Morel[a], A. Léon[b], and J. Laurencin[a]

[a] Univ. Grenoble Alpes, CEA-Liten, DTCH, 38000 Grenoble, France
[b] European Institute for Energy Research (EIFER), Emmy-Noether-Strasse 11, 76131 Karlsruhe, Germany

Solid oxide cells (SOCs) are high temperature energy-conversion devices, which have attracted a growing interest in the recent years. Indeed, this technology presents a high efficiency and a good reversibility in fuel cell (SOFC) and electrolysis (SOEC) modes. Nevertheless, SOCs durability is still insufficient due to performance degradation during operation. In this context, a physics-based model has been proposed to investigate the impact of operating conditions on the electrodes reaction mechanisms and cell performance. This multiscale model has been developed considering a typical cell composed of a dense electrolyte in $Y_{0.16}Zr_{0.84}O_{1.92}$ (8YSZ) sandwiched between an oxygen electrode in $La_{0.6}Sr_{0.4}Co_{0.2}Fe_{0.8}O_{3-\delta}$-$Ce_{0.8}Gd_{0.2}O_{2-\delta}$ (LSCF-GDC) and a hydrogen electrode made of Ni-YSZ. The model has been validated on global and local polarizations curves in SOFC and SOEC modes, and electrochemical impedance spectra at the open circuit voltage (OCV). The different contributions arising in the impedance spectra have been identified and discussed.

1. Introduction

Solid oxide cells (SOCs) are high temperature energy-conversion devices, which have attracted a growing interest in the recent years. In the context of the transition towards fossil-free energy market, this technology offers technical solutions for the development of a clean hydrogen economy. Indeed, the SOCs present a high efficiency and a good reversibility in fuel cell (SOFC) and electrolysis (SOEC) modes. However, their durability is still insufficient due to severe performance degradation related to different phenomena occurring in the cell components (1–4). Therefore, for large-scale commercialization, it is still required to improve the SOCs lifetime by maintaining high performance. For this purpose, it is necessary to better understand the impact of global operating conditions on the local processes taking place in the cell components. Besides, the role of the electrode microstructure on the reaction mechanism is still not precisely understood. From this point of view, the modelling can be an efficient tool to unravel and better analyze all the microscopic processes involved in the cell operation. In this context, a physics-based model has been proposed to investigate the impact of operating conditions on the electrodes reaction mechanisms and cell performance. This model takes into account (i) a 3D representation of the electrode microstructure (5), (ii) a description of the reaction mechanisms in full elementary steps (6, 7) and (iii) the SOC geometry with the gas flow configuration (8, 9). The validated multiscale model has been used to analyze the cell operation in electrolysis and fuel cell modes. The activated reaction pathways associated with the elementary steps in the active layers have been investigated depending on the position along the cell length. Additionally, the different processes occurring in the cell components, arising in the electrochemical impedance spectra (EIS), have been identified and discussed. In the frame of this work, special attention has been paid to the simulation of the complete cell impedance diagram, since the EIS technique is a powerful tool to analyze the kinetic and transport phenomena, but also to perform a prognosis of degradation for long-term operation (10, 11).

2. Materials and methods

2.1 Cell description

A standard hydrogen electrode-supported cell has been considered for this study. The circular cell has an active area of 9.08 cm². It is composed of a $Y_{0.16}Zr_{0.84}O_{1.92}$ (8YSZ) dense electrolyte (ca. 8 µm) and a Ni-8YSZ fuel electrode functional layer (ca. 25 µm) supported on a thick Ni-3YSZ substrate (ca. 280 µm). The oxygen electrode is a bilayer, which includes a $La_{0.6}Sr_{0.4}Co_{0.2}Fe_{0.8}O_{3-\delta}$-$Ce_{0.8}Gd_{0.2}O_{2-\delta}$ (LSCF-GDC) composite functional layer (ca. 20 µm) and a LSCF current collecting layer (ca. 20 µm). A GDC barrier layer (ca. 3 µm) is added between the electrolyte and the oxygen electrode to limit the reactivity.

2.2 Experimental setup

Electrochemical tests have been performed in an in-house test bench, which is described in (12). The cell was placed in a metallic housing inside a furnace. A glass sealant (Schott

G018-311) was deposited at the cell periphery to ensure the tightness of the fuel compartment. On both sides, the inlet gas was supplied at the cell center by mass flow controllers (Brooks SLA5850S) according to a radial co-flow configuration. A steam generator operated in saturated vapor conditions delivered the steam to the cell. In order to collect the current at the electrodes surface, a Ni grid (100 meshes·cm^{-2}) and two gold grids (100 meshes·cm^{-2}) were used for the hydrogen and the oxygen electrodes, respectively. Local measurements along the cell radius have been performed thanks to a specific design for the metallic interconnect at the air side, which is detailed in (12). In addition, a mechanical load of 600 g·cm^{-2} was applied on the cell to further decrease the contact resistance.

2.3 Experimental protocol

For the experiments, the cell was heated up to 860°C with a heating rate of 1°C·min^{-1} and maintained at this temperature for 90 min to form the glass seal. During this first step, the hydrogen and oxygen electrodes were respectively swept under nitrogen (0.5 Nl·h^{-1}) and air (0.5 Nl·h^{-1}). Subsequently, the temperature was decreased to 800°C for the cermet reduction. For this purpose, the N_2 at the fuel electrode was progressively substituted with H_2 while the flow rates at the two electrodes were gradually increased from 0.5 Nl·h^{-1} to 4 Nl·h^{-1}. The cermet was then maintained in this condition, under pure hydrogen, for 16 h to ensure the full reduction of NiO into Ni. Afterwards, the electrochemical characterizations were carried out in the operating conditions defined in the next section. At the end of the characterizations, the setup was cooled down to room temperature at a rate of 1°C·min^{-1}. During this step, a mixture of nitrogen and hydrogen was supplied to the hydrogen electrode to maintain the cermet in its reduced state and avoid Ni re-oxidation.

2.4 Electrochemical characterizations

In order to validate the model, electrochemical characterizations were performed considering both polarization curves and impedance spectra. As detailed in (12), polarization curves measured in galvanostatic mode were obtained in SOFC and SOEC modes. The local current densities were measured for three zones at center (i.e. gas inlet), middle and edge (i.e. gas outlet) of the circular cell. The data were acquired at different temperatures (700, 750 and 800 °C) and for various inlet flow rates at the hydrogen electrode (3, 6, 9, and 12 NmL·min^{-1}·cm^{-2}). Additionally, EIS at the open circuit voltage (OCV) was measured at 750°C, 10/90 H_2/H_2O, total inlet flow rate of 12 NmL·min^{-1}·cm^{-2} at the hydrogen electrode. The experimental data were acquired using a potentiostat/galvanostat (Autolab PGSTAT-302N) equipped with a frequency response analyzer (FRA) module and a 20 A current booster. The ac current amplitude for the EIS acquisition at OCV was imposed to 100 mA. The raw impedance spectra were collected using the NOVA software and then post-treated with the Zview software (ver. 2.70, Scribner Associates) based on equivalent electric circuit model (EECM) shown in Figure 3-15. The EECM proposed by (13, 14), consists of a resistance that represents the ohmic resistance (R_s) in series with an inductor element (L) that takes into account the inductance of the wires. Four resistance-constant phase element (R-CPE) were used to fit accurately

the different EIS contributions at high frequency (HF), medium (or intermediate) frequency (MF) and low frequency (LF) (Figure 3-15a). It can be noted that the contribution at high frequency is strongly distorted by the inductance related to the wires. To remove this effect, the impedance spectra were simulated with the equivalent circuit without the inductance as shown in Figure 3-15b. It can be noticed that several cells were tested with a very limited scattering on the experimental results. For the sake of clarity, the iV curves and EIS diagrams retained for the analysis correspond to the data with the lowest standard deviation.

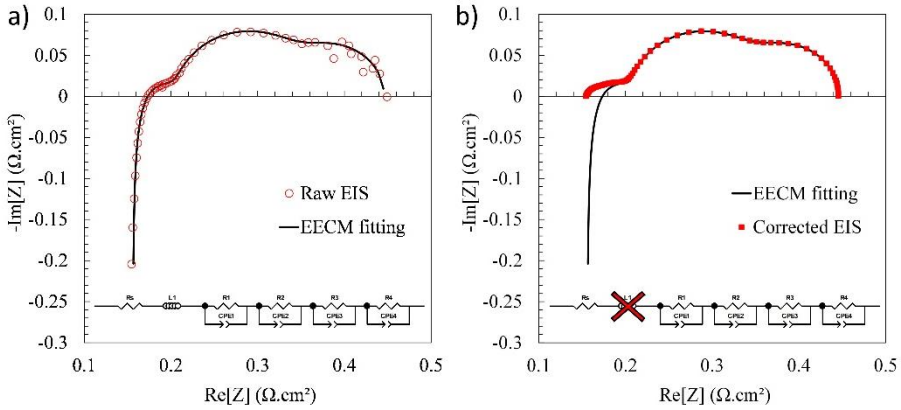

Figure 3-15. EIS at OCV, 750°C, 10/90 H_2/H_2O, 12 $NmL \cdot min^{-1} \cdot cm^{-2}$ total inlet flow rate, a) comparison between the experimental data and the fitted EIS and b) Simulated EIS without the inductance related to the wires.

3. Multiscale model description

The multiscale model has been implemented in COMSOL Multiphysics®, MATLAB® and LiveLink™ software. A 2D axisymmetric geometry has been considered thanks to the circular geometry of the cell and the radial co-flow configuration for the experimental setup. In this approach, the set of partial differential equations (PDEs) is solved in the time domain, keeping the full-non linearity of the system. The model is capable of simulating the cell response in different conditions. It is composed of (i) a morphological model to represent the electrodes microstructures; (ii) two electrode-level models based on elementary reactions; and (iii) a cell-level model considering the geometry and the gas distribution to compute all the local quantities (partial pressures, current, etc.) along the cell radius. The microstructural properties coming from the morphological model are used in the electrode-level and cell-level models. For the stationary simulations, as detailed in (12), the apparent exchange current densities used at the macroscopic scale are computed all along the cell length with the electrode models. The stationary model is used for simulating the polarization curves in SOFC and SOEC as presented in (12). This model has been extended to compute the EIS at OCV and under polarization for the complete cell.

The impedance model accounts for the dynamic response of the different irreversible processes arising in the cell layers together with the reversible gas conversion overpotential. For the two electrode models, a transient term has been added in the mass and charge transfer equations for each species considered for the elementary reactions. All the constitutive equations have been already detailed in (6) and (7) for the oxygen and hydrogen electrodes, respectively. It can be noted that the transient terms related to the gas diffusion in the porous electrodes, the solid-state diffusion in the material, the surface diffusion of adsorbed species along with the electronic and ionic currents have been taken into account (6, 7).

The gas conversion contribution in the impedance spectra is induced by the consumption and production of species that modify the gas composition along the cell length for the two electrodes. In order to consider this contribution in the EIS, the channels distributing the gas over the electrodes are modeled as continuous stirred tank reactors (CSTRs) (6, 15–17). The CSTR model allows computing the boundary conditions in terms of partial pressures that must be applied at the top of the electrode. These boundary conditions are used to simulate the mass transfer within the electrode porous microstructure. For the EIS under polarization, in order to consider the change in composition along the cell radius induced by the reactions, the whole electrode is discretized in *n* annular slices between two radii, *r* and *r+dr*. Therefore, the mass and charge balances in the electrodes associated to the CSTR model for the channels are applied to each slice to calculate the EIS under polarization. For the EIS at OCV, it can be noted that the CSTR is directly computed on the whole electrode, because the composition does not change along the cell radius.

For each slice n of electrode comprised between *r* and *r+dr*, the system of time dependent PDEs related to the processes within the electrode are complemented by equation [16] for the gas channel. It allows computing the molar fraction $y_{\mathrm{i}}(r,t)$ for the i-th species in the channel for the slice *n:*

$$\frac{\mathrm{P_{tot}\,V_{CSTR}}}{\mathrm{R}\,T}\cdot\frac{\partial y_{\mathrm{i}}(r,t)}{\partial t}=F_{\mathrm{inlet}}\cdot y_{\mathrm{i,inlet}}-F_{\mathrm{outlet}}\cdot y_{\mathrm{i}}(r,t)\pm\left|\vec{J}_{\mathrm{i,n}}(r,t)\right|\cdot\mathrm{A_n} \qquad [16]$$

Where t is the time, P_{tot} is the total pressure (Pa), V_{CSTR} is the volume of the CSTR (m^3), R is the ideal gas constant ($J \cdot mol^{-1} \cdot K^{-1}$), T is the operating temperature (K). F_{inlet} and F_{outlet} denote the inlet and outlet total flow rates ($mol \cdot s^{-1}$) of the considered slice n while A_n represents its surface area (m^2). $y_{i,inlet}$ is the inlet molar fraction for the i-th species. The term $\vec{J}_{i,n}$ is the molar flow rate across the gas channel/electrode interface ($mol \cdot m^{-2} \cdot s^{-1}$) for the i-th species at the slice *n* (computed along with the equation of mass transfer in the electrode porosity). In this approach, it is worth noting that F_{inlet}, F_{outlet} and $y_{i,inlet}$ are assumed to be time independent (6, 18). Their evolution along the cell radius (i.e. for each slice n) is calculated with the stationary model and used as inputs in the dynamic model. In order to compute the impedance of the considered electrode for each slice n, a sinusoidal perturbation is applied on the ionic current in the electrolyte:

$$i(r,t) = i_{dc}(r) + i_{ac}(t) \quad \text{with} \quad i_{ac}(t) = A\sin(2\pi f t) \qquad [17]$$

Where A and f are respectively the half-amplitude and the frequency for the sinusoid. The dc current $i_{dc}(r)$ that needs to be applied on each slice comes from the stationary model. Half of the electrolyte thickness is considered in the simulated domain for each slice (at the hydrogen and oxygen sides). The imposed $i(r,t)$ is applied as boundary condition in the electrolyte in such a way that the pure ohmic losses in the dense YSZ are taken into account. The procedure to extract the impedance $Z_n^{O_2}$ (or $Z_n^{H_2}$) for each slice at the oxygen (or hydrogen) sides has been already detailed in (19).

For each frequency, the total impedance $Z_{tot}^{O_2}$ (or $Z_{tot}^{H_2}$) of the whole electrode and half of the electrolyte is calculated knowing that all the local impedances $Z_n^{O_2}$ (or $Z_n^{H_2}$) are in a parallel configuration regarding to the current:

$$\frac{1}{Z_{tot}^{k}} = \frac{1}{A_{tot}} \sum_{n=1}^{N} \frac{A_n}{Z_n^{k}} \quad \text{with} \quad k = O_2 \text{ or } H_2 \qquad [18]$$

Finally, the cell impedance is obtained by the sum of the two contributions:

$$Z_{cell} = Z_{tot}^{O_2} + Z_{tot}^{H_2} \qquad [19]$$

The multiscale model is thus capable of identifying the different contributions related to the different processes in the cell impedance diagram.

4. Results

4.1 Stationary model

The complete validation of the stationary model has been performed on global and local polarization curves. The operating conditions have been explored in terms of cell temperature, SOFC/SOEC operating mode and inlet flow rate at the fuel electrode. All the results have been published elsewhere (12). In Figure 3-16, a comparison between some experimental and simulated polarization curves is shown as an illustration. It can be seen

that the model was able to reproduce the global and local experimental polarization curves. Some deviations were observed approaching the limiting current density, which was mainly ascribed to the uncertainty on the determination of some microstructural properties retrieved from the 3D reconstruction of the Ni-3YSZ support layer (i.e. pore radius and tortuosity factor of the gas phase) (12).

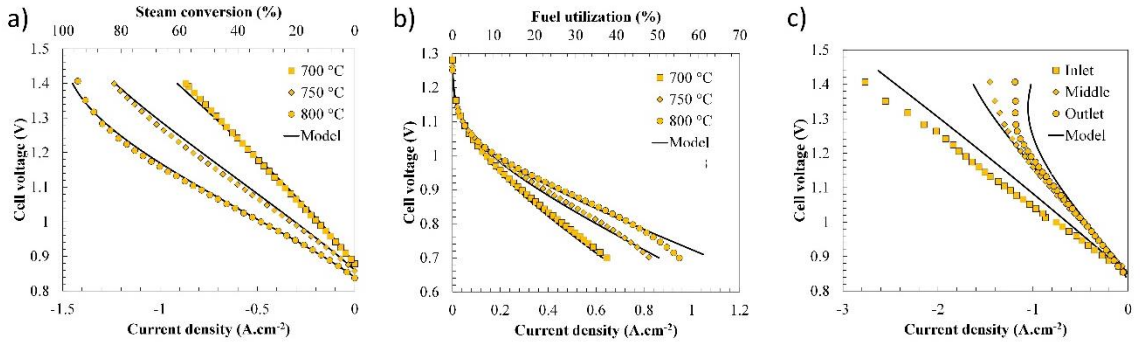

Figure 3-16. Comparison between the simulation and the experimental data obtained on a standard cell made of the classical Ni-YSZ//YSZ//LSCF-GDC materials: global iV curves in a) SOEC and b) SOFC mode at different temperatures (10/90 H_2/H_2O, Total inlet flow rate=12 NmL·min^{-1}·cm^{-2}), c) local iV curves in SOEC mode (800°C, 10/90 H_2/H_2O, Total inlet flow rate=12 NmL·min^{-1}·cm^{-2}) (12).

4.2 Dynamic model

The validation of the impedance model has been performed on the experimental EIS measured at OCV, 750°C, 10/90 H_2/H_2O, total inlet flow rate 12 NmL·min^{-1}·cm^{-2}, after EECM correction. The EIS diagram has been computed in the same conditions as the experimental EIS, without fitting the model input parameters (the kinetic constants for the reactions and the electrode microstructural parameters are given in (12), while diffusion coefficients, ionic and electronic conductivities along with the double layer capacitances are listed in (6, 7)). As shown in the Nyquist plot (Figure 3-17a), a good agreement is obtained between experimental and simulated spectra for the contributions at high and low frequencies. However, a higher mismatch in terms of intensity in the imaginary part is observed for the arc at intermediate frequency. The origins of this mismatch is discussed

in the next section. It can be also noticed, a frequency lag between the simulation and the experimental data, which is visible in the HF region of the Bode plot (Figure 3-17b).

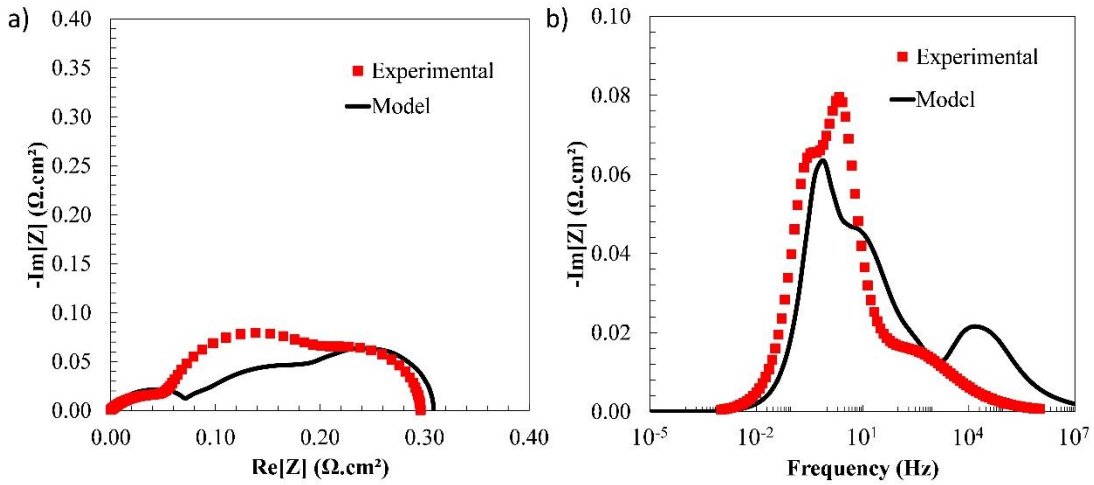

Figure 3-17. Comparison between simulation and experimental data a) Nyquist and b) Bode plots of the EIS at OCV (750°C, 10/90 H_2/H_2O, total inlet flow rate=12 NmL· min^{-1} · cm^{-2}).The ohmic losses have been removed from the impedance diagrams.

To go further in the model validation, the impact of gas composition on the cell response has been assessed in this study. In Figure 3-18a, the experimental and simulated polarization resistances (R_p) taken from the EIS at OCV are plotted as a function of the gas composition introduced at the hydrogen electrode (i.e. $p_{H2}/(p_{H2}+p_{H2O})$ where p_{H2} and p_{H2O} are the hydrogen and steam partial pressures). The evolution of R_p with the gas composition (i.e. $p_{O2}/(p_{O2}+p_{N2})$) is shown in Figure 3-18b for the oxygen electrode. In both cases, a rather good agreement is observed between the experimental data and the simulations. Indeed, the model is able to reproduce the dependency of R_p with the gas composition introduced at the two electrodes. Therefore, despite the deviations observed in Figure 3-17, it can be claimed that the physics-based model can predict quite accurately the cell impedance response at OCV without fitting.

The U-shape of the curve obtained by plotting the R_p evolution with the gas composition has been already discussed in (20). The high R_p values at low hydrogen and steam partial pressures are explained by the depletion in reactants/products, which induces high gas conversion overpotential. Moreover, it can be noticed that the curve is asymmetric, showing a higher R_p at high p_{H2}. This behavior is due to the impact of the hydrogen partial pressure on the electrode activation overpotential related to the complex reaction mechanism in the Ni-YSZ active layer (7). At the oxygen side, the R_p decreases with increasing the oxygen partial pressure. This evolution is explained by both the impact of p_{O2} on the gas conversion overpotential and the activation overpotential associated to the electrochemical processes in the LSCF-GDC electrode (6).

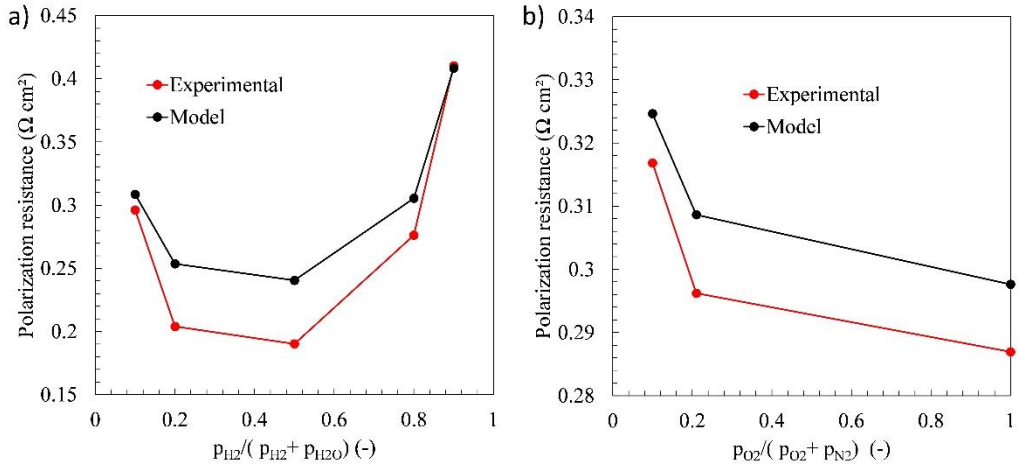

Figure 3-18. Comparison between simulation and experimental data: R_p measured at OCV and 750°C as function of the a) ratio $p_{H2}/(p_{H2}+p_{H2O})$ introduced at the hydrogen electrode hydrogen and b) ratio $p_{O2}/(p_{O2}+p_{N2})$ introduced at the oxygen electrode.

5. Discussion

5.1 Reaction mechanism in the electrodes

It has been found that the physics-based stationary model is able to accurately reproduce the global and local polarization curves in SOFC and SOEC modes (Figure 3-16). Thus, it can be used to investigate the cell operation and the reaction mechanism depending on the position along the cell radius. As shown in (12), a rather high evolution of current density and gas composition along the cell radius was highlighted with both the model and the experimental setup. Besides, the change in the reaction mechanism was identified by a ratio between two specific kinetic rates. For the hydrogen electrode, it corresponds to the ratio of steam adsorption between YSZ and Ni surfaces. This ratio was found to decrease towards the cell outlet in SOFC mode (12). This means that the adsorption on Ni is more favored compared to YSZ, going towards the cell outlet. This behavior was ascribed to the high coverage of hydroxyl ions, resulting in low available sites on the YSZ surface when the steam partial pressure is increased. The opposite trend was observed in SOEC mode. For the air electrode, the ratio between kinetic rates was related to the incorporation/excorporation (i.e. bulk path) and the direct charge transfer at the TPBls (i.e. surface path). Such ratio was found to increase towards the cell outlet in SOFC mode (12), meaning that the surface path is promoted at the outlet. This trend was related to the lower concentration of oxygen vacancies in LSCF due to the lower current densities at the cell outlet. Opposite trend was observed in SOEC mode (12). Nevertheless, in both SOEC and SOFC modes, the ratio was higher than the unity ($\zeta > 1$), meaning that the surface path was always dominating over the bulk path.

5.2 Contributions in the EIS diagrams at OCV

The stationary model has been also extended to compute the impedance spectra by keeping the full description of the reaction mechanisms in elementary steps. This dynamic model, which is able to compute the impedance diagrams at OCV and under polarization, has been compared to the experimental data at OCV with a reasonable agreement. In such conditions, through a sensitivity analysis, the model can be used to identify and unravel all the different contributions entangled in the Nyquist and Bode plots, as shown in Figure 3-19. Moving from the lowest to the highest frequency, the first LF contribution is ascribed to the gas conversion (1*) with a characteristic frequency of ca. 0.8 Hz. This order of magnitude for the characteristic frequency for the gas conversion is consistent with the results reported in (15, 17, 21). After that, the main processes involved in the oxygen electrode (2*) take place in the MF range with a characteristic frequency of ca. 13 Hz. This frequency for the oxygen electrode is also coherent with (18, 22). Subsequently, the gas diffusion (3*) in the fuel electrode support layer arises at ca. 390 Hz. This contribution has been identified by studying the impact of the pore size in the Ni-3YSZ support layer on the cell spectrum. The HF arc is mainly attributed to the hydrogen electrode processes (4*) around 10^4 Hz. This result is also consistent with (21, 23). Lastly, the ionic transfer between LSCF and GDC in the oxygen electrode (5*) arises around $6 \cdot 10^4$ Hz, which is convoluted in the hydrogen electrode contribution. These results are in quite good agreement with the model of Bertei et al. (16) and distribution of relaxation time (DRT) study of Wang et al. (24).

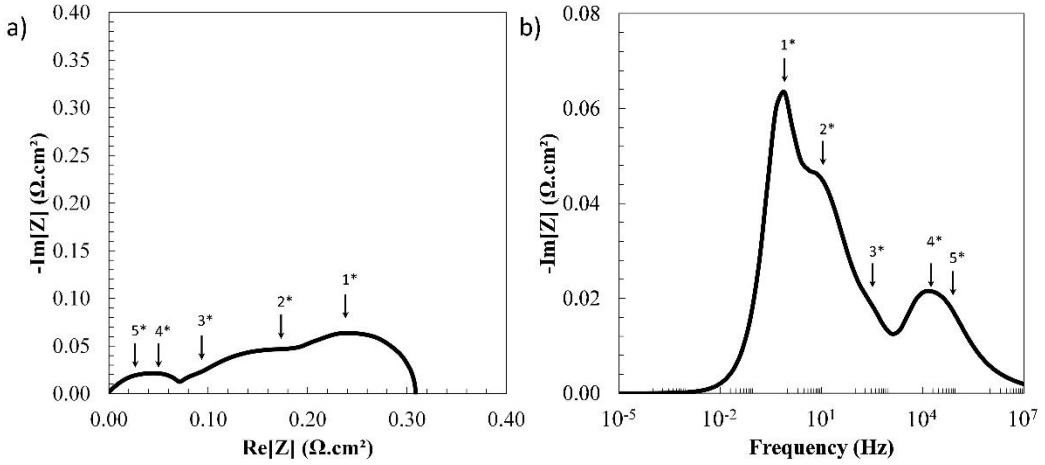

Figure 3-19. Identification of the processes frequency distribution in the a) Nyquist and b) Bode plots for the simulated EIS at OCV (750°C, 10/90 H_2/H_2O, total inlet flow rate=12 $NmL \cdot min^{-1} \cdot cm^{-2}$).

The identification of the HF and MF contributions to the hydrogen and oxygen electrodes with the model has been confirmed by an experimental sensitivity analysis on the impact of partial pressures on the EIS diagrams. Indeed, the change in the pO2 affects mainly the MF arc in the EIS, with a very slight impact on the HF contribution. On the other hand, as found with the model, the change of pH2 affects the three arcs in the experimental EIS. More in detail, the HF arc increases continuously with the increasing pH2, which is

coherent with the aforementioned impact of the pH2 on the hydrogen electrode contribution, as discussed in (7). Concerning the LF arc, the trend is consistent with the U-shape curve shown previously in Figure 3-18a and the findings of Bessler et al. (20). This result is explained by the gas conversion overpotential. The evolution for the MF arc is related to the gas diffusion in the cermet support.

5.3 Impact of gas diffusion contribution on the EIS impedance at OCV

In order to understand the role of the gas diffusion contribution in the fitting of the EIS, a sensitivity analysis was performed on the pore radius of the hydrogen electrode support layer. This parameter has been decreased of an order of magnitude (divided by 10). As shown in Figure 3-20, the discrepancy between the experimental and simulated impedance spectra at the intermediate frequencies has been significantly reduced. In terms of frequency distribution, in the Bode plot (Figure 3-20b), the contribution related to the gas diffusion in the cermet substrate becomes strongly convoluted with the oxygen electrode contribution (since the characteristic frequency of the gas diffusion shifts from ca. 390 Hz down to ca. 70 Hz). Therefore, a possible reason behind the discrepancy between the experimental and simulated EIS in the mid-frequency range, shown in Figure 3-17, can be related to uncertainties in the microstructural properties for the cell substrate (pore radius and tortuosity factor for the gas phase).

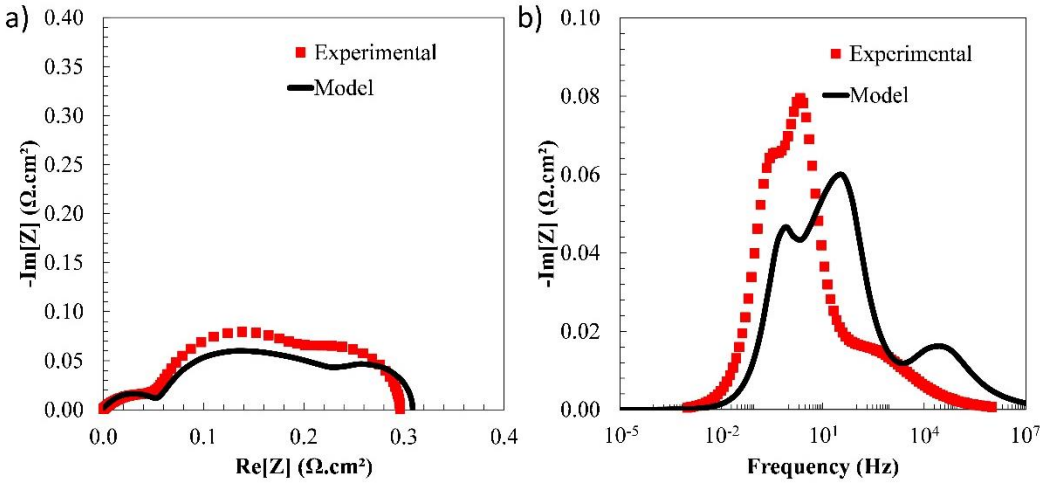

Figure 3-20. Comparison between normalized simulation and experimental EIS at OCV considering a smaller pore radius for the support layer in the fuel electrode: a) Nyquist and b) Bode plots of the EIS at OCV (750°C, 10/90 H_2/H_2O, total inlet flow rate=12 $NmL \cdot min^{-1} \cdot cm^{-2}$).

5.4 Impact of polarization on EIS diagrams

In order to study the impact of polarization on the EIS diagrams, a spectrum has been simulated in SOEC mode at i_{dc}=-0.5 A·cm^{-2} (i.e. SC=32%) and compared to the one computed at OCV in the same conditions (750°C and 12 NmL·min^{-1}·cm^{-2}). As depicted in Figure 3-21, a substantial swelling of the HF arc can be observed, whereas a shrinkage of the LF contribution is found. The MF arc remains almost constant for the two impedance spectra. These evolutions lead to a decrease in the cell polarization resistance under dc current compared to the one at OCV. The increase of the HF arc, which is related to the hydrogen electrode, is explained by the increase in p_{H2} with increasing the dc current in SOEC mode. This higher p_{H2} causes an increase in the hydrogen electrode polarization resistance, as it has been observed in (7). For the MF arc related to the oxygen electrode, it is worth noting that the high air inlet flow rate limits the change in oxygen partial pressure when the polarization is changed. In this condition, the change in the electrode polarization resistance with the potential is rather limited. Finally, the evolution of the LF contribution associated to the gas conversion is explained by the evolution of the reversible voltage U^{rev} (given by the Nernst equation) with the dc current: at the OCV, the polarization resistance, equal to dU^{rev}/di_{dc}, is rather high and tends to decrease for intermediate currents (before increasing again close to the limiting current).

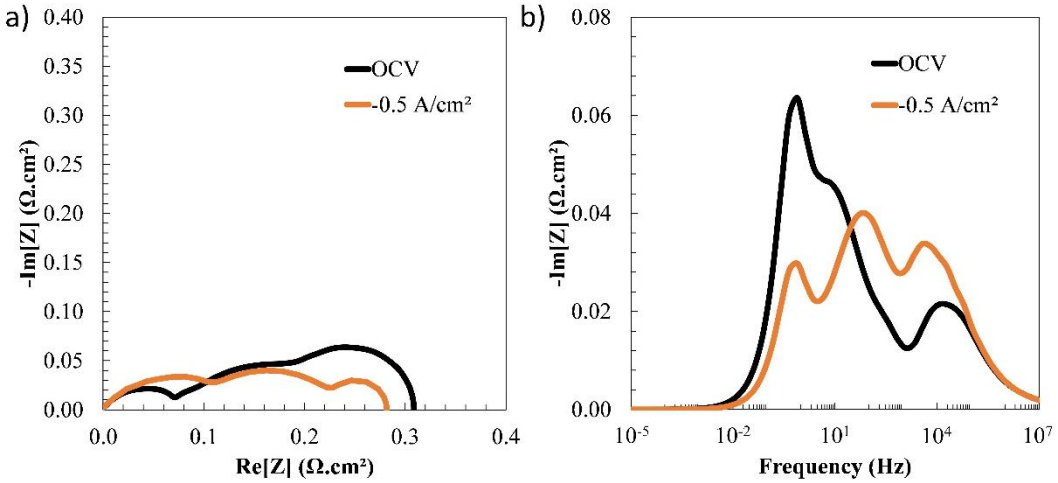

Figure 3-21. Comparison of the simulated EIS spectra at OCV and under polarization at i_{dc} = -0.5 A·cm^{-2} (750°C, 12 NmL·min^{-1}·cm^{-2}).

6. Conclusions

A physics-based multiscale model has been developed to compute the cell polarization curves and the EIS at OCV and under dc current. After validation, the model has been used to study the reaction mechanisms in the electrodes along the cell length. The different contributions in the EIS spectra have been identified and discussed. It has been found that the HF arc is mainly related to the hydrogen electrode, whereas the MF arc is related to the oxygen electrode. The contribution due to the gas diffusion in the cermet support layer

arises between the responses of the two electrodes. The LF arc is induced by the gas conversion overpotential. It has also been highlighted that the uncertainties in the microstructure of the cermet substrate can significantly affect the prediction of the EIS diagrams. Finally, the impact of polarization on the spectra has been discussed.

Acknowledgments

The research leading to these results has received funding from Fuel cells and Hydrogen Joint Undertaking under Grant Agreement n◦ 875047 (RUBY Project), grand agreement n◦ 101007175 (REACTT project) and grant agreement n◦ 874577 (NewSOC project). This work has also been supported by Genvia and by the project CELCER-EHT, grant agreement ANR-PEHY-008, France 2030.

References

1. E. Lay-Grindler, J. Laurencin, J. Villanova, P. Cloetens, P. Bleuet, A. Mansuy, J. Mougin, and G. Delette, *Journal of Power Sources*, **269**, 927–936 (2014).
2. M. Trini, A. Hauch, S. De Angelis, X. Tong, P. V. Hendriksen, and M. Chen, *Journal of Power Sources*, **450**, 227599 (2020).
3. F. Wankmüller, J. Szász, J. Joos, V. Wilde, H. Störmer, D. Gerthsen, and E. Ivers-Tiffée, *Journal of Power Sources*, **360**, 399–408 (2017).
4. H. Wang and S. A. Barnett, *J. Electrochem. Soc.*, **165**, F564 (2018).
5. H. Moussaoui, J. Laurencin, Y. Gavet, G. Delette, M. Hubert, P. Cloetens, T. Le Bihan, and J. Debayle, *Computational Materials Science*, **143**, 262–276 (2018).
6. E. Effori, J. Laurencin, E. D. R. Silva, M. Hubert, T. David, M. Petitjean, G. Geneste, L. Dessemond, and E. Siebert, *J. Electrochem. Soc.*, **168**, 044520 (2021).
7. F. Monaco, E. Effori, M. Hubert, E. Siebert, G. Geneste, B. Morel, E. Djurado, D. Montinaro, and J. Laurencin, *Electrochimica Acta*, **389**, 138765 (2021).
8. L. Bernadet, J. Laurencin, G. Roux, D. Montinaro, F. Mauvy, and M. Reytier, *Electrochimica Acta*, **253**, 114–127 (2017).
9. J. Laurencin, D. Kane, G. Delette, J. Deseure, and F. Lefebvre-Joud, *Journal of Power Sources*, **196**, 2080–2093 (2011).
10. A. Donazzi, S. De Pascali, F. Garavaglia, and M. Bracconi, *Electrochimica Acta*, **365**, 137346 (2021).
11. S. B. Beale, M. Andersson, C. Boigues-Muñoz, H. L. Frandsen, Z. Lin, S. J. McPhail, M. Ni, B. Sundén, A. Weber, and A. Z. Weber, *Progress in Energy and Combustion Science*, **85**, 100902 (2021).
12. E. Da Rosa Silva, G. Sassone, M. Prioux, M. Hubert, B. Morel, and J. Laurencin, *Journal of Power Sources*, **556**, 232499 (2023).
13. A. Nechache, A. Mansuy, M. Petitjean, J. Mougin, F. Mauvy, B. A. Boukamp, M. Cassir, and A. Ringuedé, *Electrochimica Acta*, **210**, 596–605 (2016).
14. F. Monaco, D. Ferreira-Sanchez, M. Hubert, B. Morel, D. Montinaro, D. Grolimund, and J. Laurencin, *International Journal of Hydrogen Energy*, **46**, 31533–31549 (2021).
15. S. Primdahl and M. Mogensen, *Journal of The Electrochemical Society*, **145**, 2431–2438 (1998).

16. A. Bertei, G. Arcolini, J. P. Ouweltjes, Z. Wuillemin, P. Piccardo, and C. Nicolella, *Electrochimica Acta*, **208**, 129–141 (2016).
17. W. G. Bessler, *Journal of The Electrochemical Society*, **153**, A1492 (2006).
18. V. Yurkiv, R. Costa, Z. Ilhan, A. Ansar, and W. G. Bessler, *Journal of The Electrochemical Society*, **161**, F480–F492 (2014).
19. M. Hubert, J. Laurencin, P. Cloetens, J. C. da Silva, F. Lefebvre-Joud, P. Bleuet, A. Nakajo, and E. Siebert, *Solid State Ionics*, **294**, 90–107 (2016).
20. W. G. Bessler and S. Gewies, *J. Electrochem. Soc.*, **154**, B548 (2007).
21. P. Caliandro, A. Nakajo, S. Diethelm, and J. Van herle, *Journal of Power Sources*, **436**, 226838 (2019).
22. S. H. Jensen, A. Hauch, P. V. Hendriksen, M. Mogensen, N. Bonanos, and T. Jacobsen, *Journal of The Electrochemical Society*, **154**, B1325 (2007).
23. G. Nusev, B. Morel, J. Mougin, Đ. Juričić, and P. Boškoski, *Journal of Power Sources*, **489** (2021).
24. Y. Wang, N. Xu, E. Dogdibegovic, T. Su, A. D. Brocato, and X.-D. Zhou, *International Journal of Hydrogen Energy*, **47**, 1917–1924 (2022).

Chapter conclusions

This chapter was devoted to the description and validation of the multiscale physics-based model used in the frame of the thesis. After the model has been adapted to the studied the cell, it was validated on the experimental electrochemical characterizations. More specifically, the stationary and dynamic cell response were studied.

Concerning the first part of this chapter, the stationary model was able to reproduce the experimental i-V curves in various conditions. Additionally, the model was able to predict the local i-V curves measured along the cell radius. In this part, the model the considered reaction mechanisms at the two electrodes and the multiscale approach were described. The model was first calibrated in reference conditions at 750 °C. After this first calibration, the model was able to predict the local and global response of the cell in the other operating conditions. The validation was performed and only slight discrepancies were observed at high current densities, when approaching the limiting current density. This could be associated to the uncertainties on the retrieved microstructural properties, such as the pore radius and tortuosity factor. After its validation, the model was used to investigate the impact of local partial pressures and local currents on the reaction mechanisms at the two electrodes, according to the operating mode and the position along the cell radius. For the hydrogen electrode, the steam adsorption on Ni was found to be more favoured as compared to YSZ in SOFC mode, when going towards the cell outlet. For the oxygen electrode, the direct charge transfer at the TPBls (i.e. surface path) was always dominating compared to the incorporation/excorporation reaction (i.e. bulk path). This behaviour was further promoted towards the cell outlet in SOFC mode. In SOEC mode, both electrodes showed an opposite trend concerning the evolution of the reaction mechanism along the cell radius.

The second part of this chapter was dedicated to the description and validation of the impedance model on the experimental EIS. As for the stationary model, the impedance model considers the reaction mechanisms at the two electrodes with a full-elementary description. Additionally, all the transient terms in the conservation equations are considered in the non-linear system of partial differential equations in the dynamic model. Furthermore, a continuous stirred tank reactor (CSTR) model is used to simulate the conversion losses in the EIS. The validation of the physics-based EIS model at the cell-level enabled the prediction of the EIS in different gas compositions. The various contributions related to the rate determining steps in the reaction mechanisms at the two electrodes were identified in the EIS. Some discrepancies were found at the mid-frequency region, which were attributed to the uncertainties on the microstructural properties, as for the stationary model. A sensitivity analysis was performed to better assess the impact of such uncertainties on the model validation. The findings showed a non-negligible effect of the uncertainties on the goodness of the fit between experimental and simulated EIS. Finally, the EIS model was used to simulate an EIS under polarization in SOEC mode.

To summarize, a good agreement between the experimental and simulated response of the cell was found. Some discrepancies were attributed to the uncertainties on the retrieved microstructural properties. In conclusion, the multiscale physics-based model can successfully predict the stationary and dynamic electrochemical response of the cell.

4. Long-term tests and post-test characterizations of SOCs aged in SOEC mode under dry air

This chapter is dedicated to the electrochemical and post-test characterizations for the cells tested under dry air. A part of the study performed under dry air is focused on ageing of the oxygen electrode and it is reported in **Appendix A**. The main focus of this chapter deals with the effect of operating temperature on the degradation of the various cell layers.

The study presented in **Appendix A** includes one long-term test at 750 °C in SOEC mode at -1 $A \cdot cm^{-2}$ and SC = 64%, along with a set of the post-test characterizations down to the microscale to focus on the oxygen electrode degradation. More specifically, microstructural observations, surface chemistry analyses and structural crystallographic investigations were performed. This part of the work was done in collaboration with Ozden Celikbilek, who works on the long-term testing and post-test characterizations at the laboratory as a post-doctorate. The work done on this part of the chapter has been published in The Electrochemical Society Transactions (2023) (1).

The main core of this chapter is devoted to the study of the effect of operating temperature on the cell degradation. In addition to the test at 750 °C presented in **Appendix A**, two supplementary long-term tests were carried out in the same operating conditions, in SOEC mode at -1 $A \cdot cm^{-2}$ and SC = 64%, at 800 °C and 850 °C. In order to compare the performance degradation of the three tests, electrochemical characterizations were performed in reference conditions (i.e. 750 °C) before and after ageing in the operating conditions. The evolution in the material composition, microstructure and structure in the various layers of the cell was assessed with advanced post-test characterizations techniques with high resolution down to the atomic scale. This part of the work has been published in the Journal of Power Sources (2024) (2).

References

1. O. Celikbilek, G. Sassone, M. Prioux, D. F. Sanchez, A. Benayad, M. Hubert, B. Morel, J. Vulliet, A. Léon, and J. Laurencin, *ECS Trans.*, **111**, 211 (2023).
2. G. Sassone, O. Celikbilek, M. Hubert, K. Develos-Bagarinao, T. David, L. Guetaz, I. Martin, J. Villanova, A. Benayad, L. Rorato, J. Vulliet, B. Morel, A. Léon, and J. Laurencin, *Journal of Power Sources*, **605**, 234541 (2024).

Effect of the Operating Temperature on the Degradation of Solid Oxide Electrolysis Cells

Giuseppe Sassone[a], Ozden Celikbilek[a], Maxime Hubert[a], Katherine Develos-Bagarinao[b], Thomas David[c], Laure Guetaz[c], Isabelle Martin[d], Julie Villanova[e], Anass Benayad[c], Léa Rorato[a], Julien Vulliet[f], Bertrand Morel[a], Aline Léon[g], Jérôme Laurencin[a]

[a] Univ. Grenoble Alpes, CEA, Liten, DTCH, 38000 Grenoble, France
[b] Global Zero Emission Research Center, AIST, Tsukuba, Japan
[c] Univ. Grenoble Alpes, CEA, Liten, DTNM, 38000 Grenoble, France
[d] CAMECA Instruments Inc., 5470 Nobel Drive, Madison, Wisconsin 53711, United States
[e] ESRF the European Synchrotron, CS 40220, 38043, Grenoble Cedex 9, France
[f] CEA, DAM, Le Ripault, F-37260, Monts, France
[g] European Institute for Energy Research (EIFER), Emmy-Noether Strasse 11, 76131 Karlsruhe, Germany

Abstract

The present work aims to better understand the effect of operating temperature on the degradation of Solid Oxide Electrolysis Cells (SOECs). The studied SOECs consist of $La_{0.6}Sr_{0.4}Co_{0.2}Fe_{0.8}O_{3-\delta}$-$Ce_{0.8}Gd_{0.2}O_{2-\delta}$ (LSCF-GDC) oxygen electrode, GDC diffusion barrier layer, $Y_{0.16}Zr_{0.84}O_{1.92}$ (YSZ) electrolyte and Ni-YSZ hydrogen electrode. Durability tests are carried out at 750, 800 and 850 °C for 2000 hours at -1 $A \cdot cm^{-2}$, using 10/90 vol.% H_2/H_2O and dry air at the hydrogen and oxygen electrodes, respectively. The electrochemical impedance spectra measured before and after ageing reveal a strong evolution related to the hydrogen electrode, while the change in the oxygen electrode contribution remains negligible. A set of advanced characterization techniques are employed to study the cell degradation. For the hydrogen electrode, a large Ni depletion is observed after ageing, which increases with the operating temperature. The analysis of the oxygen electrode shows an elemental inter-diffusion between the LSCF-GDC/GDC/YSZ layers on the manufactured cells that seems to not evolve significantly upon operation. Moreover, the presence of $SrZrO_3$ is not detected in the pristine cell and in the operated ones. Besides, only a limited LSCF decomposition is found in good agreement with the electrochemical characterizations. Hypotheses that could explain the good oxygen electrode stability are discussed.

Keywords. Solid Oxide Electrolysis Cell, Durability, Ni migration, LSCF degradation, Long-term Tests

1. Introduction

In the context of the energy transition, solid oxide cells (SOCs) are a promising technology, which offers several advantages, such as high efficiency and fuel flexibility. Thanks to their reversibility, the same device can produce either electricity in fuel cell mode (SOFC) or hydrogen in electrolysis mode (SOEC). The SOCs have thus the potential to be employed as a relevant solution to match the fluctuations between electricity demand and production when using intermittent renewable energy sources.

A typical SOC consists of a dense ceramic electrolyte usually made of yttria-stabilised zirconia (YSZ) sandwiched between two porous electrodes. The state-of-the-art hydrogen electrode is a cermet made of Nickel and YSZ (Ni-YSZ). The oxygen electrode is composed of a mixed ionic electronic conductor (MIEC) [1], such as the typical $La_{1-x}Sr_xCo_{1-y}Fe_yO_{3-\delta}$ (LSCF) material [2]. In general, $Gd_xCe_{1-x}O_{2-\delta}$ (GDC) is mixed with LSCF to improve the performances [2] and to reduce the mismatch in thermal expansion coefficients with the electrolyte [3]. A GDC layer is also added between LSCF and YSZ as a diffusion barrier to mitigate chemical reactivity.

Nowadays, the durability of SOCs is still insufficient and remains a major issue to be addressed for the large-scale industrialisation. For this reason, the research community is currently focused on understanding the degradation processes that occur in the cell during operation. According to the literature, SOC degradation is impacted by various operating parameters, such as temperature [4], applied current [5], presence of contaminants [6], composition of the supplied gases [7], and humidity at the air side [8]. It has also been shown that the degradation rates measured in electrolysis mode are substantially higher compared to the SOFC mode although discrepancy exists depending on the cell architecture or the operating conditions [9,10]. The loss of performances is due to various material deterioration arising in the cell layers upon operation.

In the hydrogen electrode, degradation is mainly due to microstructural evolution within the cermet. A significant Ni particle coarsening is observed in both operating modes that tends to slow down for long operating times [11]. The agglomeration is found to be aggravated with temperature, whereas no relationship is found with polarization [12]. By contrast, Ni migration away from the electrolyte interface to the bulk of the electrode is only observed in electrolysis mode [12–17]. According to the underlying mechanism proposed to explain this Ni relocation in the cermet [17,18], the migration must be driven by the cathodic polarization in SOEC mode.

To date, the effect of operating conditions such as the temperature on Ni migration is still unclear.

Regarding the oxygen electrode, the LSCF is known to decompose and release cations during operation [19–23]. Particularly, the segregation of Sr at the LSCF surface is classically observed after ageing [20,24]. This surface accumulation of Sr results in the formation of a SrO passivation film, which is known to slow down the oxygen surface exchange [22] and decrease the oxygen bulk diffusion coefficient [25]. It has been shown that the strontium release in operation can contribute significantly to the cell degradation [26]. However, contradictory results have been reported on the impact of operating temperature on the Sr segregation. Wen et al. [27] suggested that higher operating temperatures typically promote Sr segregation. By contrast, Wang and Barnett [23] observed a decrease in segregated Sr on the surface of LSCF by increasing the temperature from 550 °C to 950 °C. This result was attributed to a possible Sr volatilization as $Sr(OH)_2$ or to a lower equilibrium Sr coverage at such a high temperature. Additionally, Co migration and segregation have also been detected in many studies [28–31]. Along the electrolyte interface, the formation of secondary phases, such as $SrZrO_3$ (SZO) and $La_2Zr_2O_7$, is observed due to the reactivity between LSCF and YSZ. This reactivity is typically detected after cell manufacturing and can continue upon operation [32–37]. It is related to inter-diffusion of elements at the interfaces between the electrolyte, the barrier layer and the oxygen electrode. At the GDC/YSZ interface, the formation of a GDC-YSZ solid solution is commonly observed after cell manufacturing. This so-called inter-diffusion layer (IDL) is due to the mutual diffusion of Ce and Gd towards YSZ, as well as Y and Zr towards GDC [29,38–41]. As expected, the sintering temperature of the barrier layer can strongly affect its formation [21,41,42]. If sintered at sufficiently high temperature, it has been shown that the IDL could limit and even suppress the formation of SZO [21,29,41–43]. The IDL leads to lower cell performance due to its lower ionic conductivity compared to GDC and YSZ [44]. However, the IDL evolution upon operation and its role on cell durability is still not precisely understood. Monaco et al. [19] suspected a slight evolution of the IDL after operation in electrolysis mode at 850 °C and -0.75 $A \cdot cm^{-2}$, while no change was found at 750 °C. Shimura et al. [37] observed an increase in the ohmic resistance after testing at 800 °C for 100 h, which was attributed to an evolution in the ionic conductivity of the IDL upon operation. Nevertheless, Xu et al. [40] found that the evolution of the IDL and its impact on the cell performance after operation of 2000 hours at 700 °C was negligible. Additional studies are thus needed to better characterize the potential evolution of the IDL as a function of the operating conditions. Finally, inter-diffusion was also observed after manufacturing between LSCF and GDC at the oxygen electrode/barrier

layer interface [45,46]. To elucidate the effect of inter-diffusion on the cell performance, Uhlenbruck et al. [38] purposefully doped 1 % Gd in the LSCF. The authors found that the cell performance decreased along with a change in the lattice structure of LSCF. On the other hand, Zhang et al. [47] observed Ce and La inter-diffusion at the hetero-interface of LSCF-CeO_2 composite electrode with nanofiber microstructure. This phenomenon is suspected by the authors to improve the cell performances.

In this context, this study aims to investigate the impact of the operating temperature in order to clarify the contradictory findings on the cell layers degradation in SOEC mode. For this purpose, long-term tests were carried out at three operating temperatures (750 °C, 800 °C and 850 °C) for 2000 h in SOEC mode at a current density of -1 $A \cdot cm^{-2}$ and a steam conversion (SC) of 64%. To compare the performance loss among the three cells, electrochemical impedance spectra (EIS) were recorded under reference conditions at 750 °C before and after the durability experiments. Thereafter, the samples were characterized using advanced techniques to study the degradation that occurred in different cell layers. Various complementary techniques at the micro-, nano- and atomic scales were selected to provide global and local (point-by-point) information on the microstructure, surface and bulk composition, as well as crystalline structure.

2. Materials and methods

2.1 Cell description

The composition and fabrication of the cells used in this work have been already detailed in reference [48]. Thus, only the materials and dimensions are described hereafter. Circular hydrogen electrode supported cells with an active area of 9.08 cm^2 are used for the experiments. The porous oxygen electrode is made of a ~ 20 µm $La_{0.6}Sr_{0.4}Co_{0.2}Fe_{0.8}O_{3-\delta}$ (LSCF) current collecting layer (CCL) and a ~ 20 µm LSCF-$Ce_{0.8}Gd_{0.2}O_{2-\delta}$ (LSCF-GDC) composite functional layer (FL). A ~ 3 µm thick porous GDC barrier layer (BL), is deposited between the oxygen electrode and the electrolyte. The electrolyte made of $Y_{0.16}Zr_{0.84}O_{1.92}$ (8YSZ) is a dense and thin layer of ~ 8 µm. The porous hydrogen electrode consists of a ~ 280 µm Ni-3YSZ substrate and a ~ 25 µm Ni-8YSZ active layer.

In the following sections, a cell, for which the cermet has been reduced at 800 °C, is referred to as “Reference” whereas the cells aged for 2000 h under high current density in electrolysis mode at three operating temperatures (750 °C, 800 °C and 850 °C) are labelled “Aged750”, “Aged800” and “Aged850”, respectively.

2.2 Experimental setup

The long-term tests have been performed using an in-house test bench. The cell is tested in a furnace using a metallic holder at the hydrogen side while an alumina diffuser is used at oxygen side. A glass ceramic sealant (Schott G018-311) is applied to the periphery of the cell to prevent gas leakage from the hydrogen compartment to the air compartment [19,49]. The gases are supplied at the cell centre and then they are distributed along the electrodes in a radial co-flow configuration. On both hydrogen and air sides, mass flow controllers (Brooks SLA5850S) are used for the gas delivery. A steam generator operated in saturated vapour conditions delivers the steam. Compressed air is supplied in dry conditions, according to ISO 8573-1 class [1:1:1]. In order to distribute the current at the surface of the electrodes, a Ni grid (100 meshes·cm^{-2}) and two gold grids (100 meshes·cm^{-2}) are used for the hydrogen electrode and the oxygen electrode, respectively. A ceramic Cr-free holder is used on top of the oxygen electrode to avoid well-known effects of Cr-poisoning [50]. In addition, a mechanical load of 600 g·cm^{-2} is applied on the cell to further decrease the contact resistance. The pipelines at the inlet and outlet of the cell chamber are heated to avoid any possible condensation. In order to separate the steam from the gas phase at the outlet, a condenser is employed and the collected liquid water is weighed to verify the steam conversion.

2.3 Long-term tests and electrochemical characterizations

2.3.1 Experimental protocol. The cell is first heated up to a temperature of 860 °C at a heating rate of 1 °C·min^{-1}. The temperature is held for 90 minutes to ensure the formation of the glass seal. During this thermal treatment, the hydrogen and oxygen electrodes are supplied with 0.5 NL·h^{-1} of N_2 and 0.5 NL·h^{-1} of compressed dry air, respectively. After the glass formation, the reduction of Ni-YSZ cermet is carried out at 800 °C by keeping a total flow rate of 4 NL·h^{-1} for the two electrodes. During the procedure, the N_2 supplied to the hydrogen electrode is gradually

replaced by H_2 up to the complete substitution of N_2 with H_2. These conditions are then maintained for about 16 h. Once the reduction procedure is completed, the initial electrochemical characterizations are performed. After setting the operating conditions (temperature, current density, gas flows, etc.), the samples are aged for 2000 h. Once the long-term test is finished, the cell is cooled down to room temperature at a rate of 1 °C·min^{-1}. During the cooling, a mixture of N_2 and H_2 is supplied to the hydrogen electrode to preserve the cermet in its reduced state and prevent its potential re-oxidation.

2.3.2 Long-term tests. The three tests have been performed at 750 °C, 800 °C and 850 °C for 2000 h in SOEC mode at a current density of -1 A·cm^{-2} in galvanostatic mode, with 64% steam conversion (SC). During operation, the oxygen and hydrogen electrodes are supplied with 36 NmL·min^{-1}·cm^{-2} of dry compressed air and 12 NmL·min^{-1}·cm^{-2} of a mixture of H_2 and steam, with a composition of 10/90 %vol. H_2/H_2O.

2.3.3 Electrochemical characterizations. Electrochemical impedance spectroscopy (EIS) data were collected at the open circuit voltage (OCV) for the cells tested at the three operating temperatures (750, 800 and 850 °C). Besides, EIS were also measured before and after all the durability experiments at a reference temperature of 750 °C. A potentiostat/galvanostat (Autolab PGSTAT-302N), connected to a frequency response analyzer (FRA) module and a 20 A current booster, was used to apply a sinusoidal current in the frequency range from 10^{-2} to 10^4 Hz. The amplitude of the imposed AC current was set to 100 mA. The NOVA ver. 1.11 software was used to collect the raw data. For the data treatment, the raw EIS spectra were first fitted with an equivalent electrical circuit model (EECM) shown in Figure 4-1 using Zview ver. 2.70 software. In order to remove the inductive part related to cabling and wiring, the spectra were simulated without the inductance. Compared to the raw EIS, the frequency range of the corrected EIS has been extended from 10^{-2} – 10^4 Hz to 10^{-3} – 10^6 Hz.

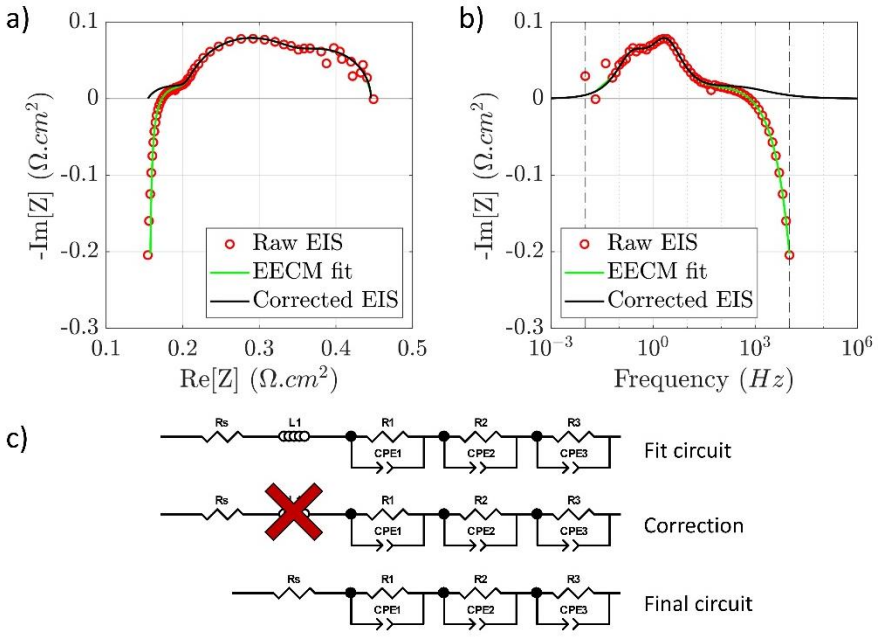

Figure 4-1. Correction of raw EIS spectrum of the sample measured at 750 °C a) Nyquist plot and b) Bode plot using the c) equivalent electric circuit model (EECM). The experimental bounds of the frequency range are marked with dashed lines in the Bode plot.

2.4 Post-test characterization techniques

As stated in the introduction, various complementary techniques have been used to characterize the reference and the operated cells in order to gain microstructural and chemical information at different length scales and resolutions. The techniques used in this study are described shortly in the following.

2.4.1 ICP-MS. The composition of the LSCF powder used for the cell manufacturing was analysed by inductively coupled plasma mass spectroscopy (ICP-MS, PerkinElmer NexION 2000). For this purpose, 0.1 g of LSCF powder was dissolved in 100 mL of a 2% nitric acid solution.

2.4.2 FEG-SEM and EDX. The microstructure of the cross-section was imaged with a field-emission gun scanning electron microscope (FEG-SEM Zeiss Merlin, Germany) equipped with two Energy-Dispersive X-ray detectors (EDX, Bruker XFlash1 Detector 6|60, Berlin, Germany). First, the samples were impregnated in polymer resin (Epofix, Denmark) to fill the pores and then polished to obtain a mirror-like surface using a diamond spray of 0.25 µm. A thin carbon coating was deposited on the surface to avoid charging effect. The images were

acquired in backscattered electron (BSE) mode at an accelerating voltage of 2 kV. For the EDX maps, the accelerating voltage was fixed at 10 kV.

2.4.3 3D FIB-SEM. The microstructure of the hydrogen electrode was reconstructed by Focused Ion Beam - Scanning Electron Microscopy (FIB-SEM) using a Zeiss Crossbeam 550. An accelerating voltage of 30 kV and a current of 3 nA were used for the FIB milling procedure. Regarding the SEM imaging, an accelerating voltage of 1.5 kV and a current of 1 nA were selected for the electron column. For each slice, two types of images were acquired simultaneously using the In-lens and in chamber secondary electron (SE) detectors. They were then combined and processed for the subsequent image segmentation. Image processing consisted of slice-to-slice alignment, homogenization in the three directions of contrast/brightness, correction of the curtaining effect and resampling in the z-direction to correct for non-homogeneous inter-slice distances. Such a post-processing was carried out using custom Python codes, developed with commonly employed Python libraries for image processing, such as numpy and scikit-image. The processed images were then segmented with Ilastik software [19,51], thanks to a machine learning algorithm based on a random forest classifier. The 'pixel classification' workflow was used for this purpose. Sub-volumes of 100-300 pixels in the three directions were selected to perform the annotation and training phase. The final reconstructions have a typical dimension of a few tens of microns with a cubic voxel size of $10 \times 10 \times 10$ nm^3 (resulting from a pixel size of 10 nm for the SEM images and an inter-slice distance of 10 nm).

2.4.4 XPS. The surface chemistry of LSCF was analysed by X-ray Photoelectron Spectroscopy (XPS). The surfaces of current collecting layer and the functional layer (FL) of the electrode were analysed. Access to the FL was obtained by scraping approximately 25 µm of material from the surface with a scalpel. The measurements were performed on a VersaProbe-II instrument from ULVAC-Phi using a focused monochromatic Al Kα radiation (1486.6 eV) with an emission current of 4 mA and an X-ray beam diameter of 200 µm. The spectra were acquired under ultra-high vacuum conditions ($p < 10^{-7}$ Pa) at room temperature. The calibration of the spectrometer was performed considering the gold photo-emission lines (Au $4f_{7/2}$ emission at 83.9eV, with respect to Fermi level). Constant pass energies of 117.9 eV and 23.3 eV were considered for recording the survey spectra and the core-level peaks, corresponding to energy resolution of 1.6 and 0.6 eV, respectively. Electron and argon charge neutralizer guns were employed to minimize the surface charging effect. The calibration of all spectra was performed against the carbon C 1s emission at 285.0 eV. The fitting of XPS spectra and the quantitative

analyses were carried out using the CasaXPS software [52]. A combination of Gaussian (80%) and Lorentzian (20%) distributions was used for fitting the peaks, applying a Shirley background. For the fitting of the Sr core-level spectra, an energy separation of 1.8 eV and a branching ratio of 1.5 were constrained between the Sr $3d_{5/2}$ and $3d_{3/2}$ doublet. Relative sensitivity factors (RSF) for the X-ray source were exported from the MultiPak library to consider the transmission function of the spectrometer.

2.4.5 SIMS imaging. The high-resolution secondary ion mass spectrometry imaging (SIMS, NanoSIMS 50L, CAMECA) was used to study the distribution of the elements along the cross-section of all samples. The sample preparation consisted of infiltrating the porous layers with a high-vacuum-compatible resin and then to polish the surface with a diamond slurry. The cross-sections were scanned using a Cs^+ primary ion beam with a current of ~ 23 nA and a diameter of ~ 100 nm. The scanned region of interests (ROIs) for the two electrodes included a part of the functional layer and the electrolyte, considering raster areas of 20 µm × 20 µm. A multi-collection system was used to collect simultaneously all the secondary ion mass species present in the cell. The WinImage ver. 4.6 software (CAMECA) was used for the image processing.

2.4.6 Synchrotron characterizations. Chemical and structural analyses were performed on the samples by nano-X-ray fluorescence (XRF) and X-ray diffraction (XRD). To ensure a high spatial resolution, a specific sample preparation was required for the synchrotron characterizations. Thin lamellae were extracted from the cells using a Xe^+ plasma-FIB (PFIB) Vion (FEI™). The applied protocol was similar to the one detailed in references [19,53] and is briefly summarized hereafter. Pieces of reference and aged cells were positioned in the vacuum chamber of the PFIB machine and a 10 µm thick Pt protective layer was deposited on top of the sample using a current of 59 nA. The area surrounding the sample was milled with a current of 470 nA. A lower current of 180 nA was used to refine the lamella surfaces, with the target of preventing any damage for the sample. The lamella was then extracted from the cell fragment with a micromanipulator and fixed on an aluminium pin with a platinum deposition. The final dimension of the lamellae was approximately 60 × 60 × 2 μm^3 for the horizontal (X), vertical (Y) and in the thickness (Z) directions, respectively (Figure S-B 1).

The nanoscale XRF and XRD studies were carried out at the European Synchrotron Radiation Facility on the ID16B beamline [54]. The high flux (10^{12} ph·s^{-1}) X-ray beam was focused to a spot size of about 60×60 nm^2. In order to obtain signal from all cell elements in XRF, an energy of 29.6 keV was selected for the incident beam.

XRF spectra were acquired at each point of the 2D maps using two silicon drift detectors, with three and seven elements, respectively. They were positioned on both sides of the sample with an angle of 13° according to the plane of the sample. These detectors provide an energy resolution of 145–150 eV full width half maximum (FWHM) [54]. The XRD data were acquired in transmission mode thanks to the small thickness of the lamellae (i.e. ca. 2 µm). The XRD detector was thus positioned in transmission mode behind the sample.

Two types of scan were performed depending on the position of the ROI in the cell cross-section:

(i) 2D maps were scanned with a 50 nm step size and 1000 ms dwell time per point, recording simultaneously both XRF and XRD data. A ROI of 7×8 µm² (6×8 µm² for the "Reference" sample) was scanned including the barrier layer as well as a part of the 8YSZ electrolyte and LSCF-GDC functional layer.

(ii) 1D XRD line scans in the horizontal direction parallel to the electrolyte interface (X direction) were performed with the so-called zapline method with 1 s dwell time per point. Two lines were acquired in the middle of the CCL and FL to investigate the potential evolution of the LSCF lattice parameter after ageing.

The software PyMca [55] was used to analyse the fluorescence data. The signal extracted from the XRF elemental 2D maps was integrated and averaged along the horizontal direction (X) to obtain 1D line profiles across the cell layers (Y direction). Regarding the XRD data, the diffraction rings were first treated by azimuthal integration with XRDUA [56] to obtain 2D maps of diffractograms. They were then integrated along the cell layers (X direction) and fitted by Le Bail method using FullProf [57,58].

2.4.7 APT. Elemental mapping in 3D was performed with the atom probe tomography (APT). The measurements were done on a CAMECA LEAP 6000XR atom probe. A standard top down lift-out methodology [59] was used on a Helios 660 FIB-SEM to prepare the samples, which were extracted from the area including the LSCF-GDC/GDC/YSZ interfaces. Data acquisition was performed at a temperature of 30 K, with a pulsed laser operated at 100 kHz and 30 pJ, with a detection rate of 0.01 ions/pulse. The CAMECA's AP Suite 6.3 software was used to analyse the data acquired on the "Reference" and "Aged800" samples.

2.4.8 TEM. The oxygen electrode materials were characterized by Transmission Electron Microscopy (TEM) for the "Reference" and "Aged800" cells. The sample preparation consisted of embedding the porous layers in an epoxy resin. Thin lamellae, including a portion of

electrolyte, the GDC barrier layer and a portion of composite oxygen electrode, were then extracted with a FIB-SEM (Zeiss cross-beam 550). A FEI-Themis microscope equipped with a super-X detection system and a probe aberration corrector was employed to perform the scanning transmission electron microscopy and energy dispersive X-ray spectroscopy (STEM-EDS) studies. The Esprit Bruker Software was used to analyse the data of the "Reference" and "Aged800" samples. The Cliff-Lorimer method was applied on the Co, Fe and Y K lines, and on the La, Sr, Ce, Zr and Gd L lines to perform semi-quantitative analyses.

3. Results and discussion

3.1 Long-term test results

The cells performance and degradation were studied at 750, 800 and 850 °C in SOEC mode at -1 $A \cdot cm^{-2}$ with a steam conversion (SC) of 64%. Figure 4-2 displays the durability curves and the electrochemical impedance diagrams recorded at 750 °C before and after the ageing tests. The durability curves show the cell voltage degradation over a period of 2000 hours (Figure 4-2a). Two different regimes can be distinguished. A faster and more variable cell voltage evolution is observed in a first period of approximately 800 h, while in the second period, the voltage degradation slows down and reaches a rather constant rate over time. The degradation rates calculated from the slope of the last five hundred hours give asymptotic limits of around 2.8, 2.0 and 0.8 $\%.kh^{-1}$ for the cells tested at 750, 800 and 850 °C, respectively (the respective degradation rates for the whole ageing time are 9.1, 7.8 and 2.4 $\%.kh^{-1}$). These values lie in the range of the usual degradation rates reported in the literature for comparable cells [60–63]. Interestingly, it can be noticed that the 'apparent' degradation rate decreases with increasing temperature. This result is confirmed by the impedance spectra measured at OCV upon operation for the three samples (Figure S-B 2). Indeed, it can be observed that the evolution of EIS diagrams over the time is higher at 750 °C than 850 °C.

As reported in previous works at 750 °C and 850 °C [12,19], the thermally-activated processes involved in the cell response should be considered when studying the effect of operating temperature on durability. To compare the loss of cell performance after ageing at different operating temperatures, it should be necessary to assess the degradation rate with electrochemical characterizations carried out at a common temperature before and after the

long-term tests. In this work, 750 °C was used as reference temperature to measure the initial and final EIS at OCV (Figure 4-2b-g). This rather 'low' temperature for the reference condition was chosen to exacerbate the thermally activated processes in the cell (mainly the activation overpotentials in both electrodes and ohmic losses in the electrolyte). As discussed thereafter, this choice should allow better highlighting the impact of the material degradation on the cell performance losses.

The degradation rates on the area specific resistance (ASR related to the total resistance measured on the impedance spectra) are reported in Table 4-1 for the reference temperature and for the three operating temperatures. For the long-term test "Aged850", it can be seen that the evolution of the total resistance remains limited when measured in the condition of the durability (i.e. at 850 °C). However, as suspected, when the degradation is measured at the lower reference temperature of 750 °C, the total resistance demonstrates a larger increase.

These results show that the degradation rate is minimized when it is measured at high temperatures. Indeed, for the highest temperatures, the thermally-activated electrode activation overpotential and ohmic losses in the electrolyte become very low compared to the conversion and diffusion losses (which are not thermally activated). Therefore, even if the material evolution (such as the Ni migration, etc.) is significant, the impact on the cell voltage losses can be rather low. In contrast, if the performances are estimated at lower temperature, the impact of the material degradation is much more pronounced. Therefore, it is essential to measure the degradation rates using a common reference condition for all the long-term tests. This reference condition allows a relevant comparison of the degradation rates between the experiments conducted at different temperatures. To illustrate this effect, a theoretical assessment of the degradation rates at different temperatures is reported in section 3.2.1 considering the microstructural evolution in the hydrogen electrode.

The value of the degradation rate is thus dependent of the chosen temperature at which it is measured. In this condition, when the degradations are all estimated at the reference temperature of 750 °C (cf. Table 4-1), it is worth noting that the degradation rates increase with increasing the operating temperature of the durability test. Therefore, a higher temperature induces a higher 'intrinsic' material degradation. In other words, the material deterioration is accelerated for higher operating temperature as already mentioned in several articles [12,19].

Table 4-1. Performance degradation extracted from EIS total resistance (R_{tot}) measured at the operating temperature of the long-term tests and at the reference temperature of 750 °C.

Tested cell		Rs ($\Omega \cdot cm^2$)	Rp ($\Omega \cdot cm^2$)	R_{tot} ($\Omega \cdot cm^2$)	ΔR_{tot} ($\Omega \cdot cm^2$)	Performance loss (%.kh^{-1})
EIS measured at the reference temperature (750°C)						
"Aged750"	$t_{initial}$	0.16	0.29	0.45	0.11	12
	t_{final}	0.21	0.35	0.56		
"Aged800"	$t_{initial}$	0.17	0.28	0.45	0.16	18
	t_{final}	0.27	0.34	0.61		
"Aged850"	$t_{initial}$	0.19	0.32	0.51*	0.24	23.5
	t_{final}	0.32	0.43	0.75		
EIS measured at the temperature of the durability experiment (750°C, 800°C or 850°C)						
"Aged750"	$t_{initial}$	0.16	0.29	0.45	0.11	12
	t_{final}	0.21	0.35	0.56		
"Aged800"	$t_{initial}$	0.11	0.28	0.40	0.09	11
	t_{final}	0.19	0.30	0.49		
"Aged850"	$t_{initial}$	0.11	0.33	0.44	0.06	7
	t_{final}	0.17	0.33	0.50		

** Lower initial performance of this cell compared to the other two cells is explained by the use of a different test-bench*

As shown in Figure 4-2b-d, the degradation leads to an increase in both the series and polarization resistances in the Nyquist plots. The impedance spectra display three main arcs at high-frequency (HF), mid-frequency (MF) and low-frequency (LF) regions. The characteristic frequencies of the three arcs in the impedance spectra deduced from the EECM fitting shown in Figure 4-1c are in the order of (i) 0.2 Hz for the LF contribution, (ii) 2-3 Hz for the MF contribution, and (iii) evolves during ageing from 120-310 Hz to 1430-1650 Hz for the HF contribution. The limiting electrochemical processes involved in each region were identified thanks to a multiscale and physics-based model. This work is thoroughly detailed in reference [64], and therefore only the key findings are summarised in the following. The HF arc was mainly ascribed to the rate determining steps in the hydrogen electrode, while the MF arc was attributed to the oxygen electrode and the gas diffusion in the Ni-YSZ support. The LF arc was found to be related to the gas conversion overpotential.

As shown in Figure 4-2e-g, the increase in the series resistance is also concomitant with an enlargement of the HF arc related to the hydrogen electrode. This evolution of the HF contribution also becomes more pronounced as the ageing temperature increases. According to literature reports for cells operated in electrolysis mode, the increase in both ohmic and HF

resistances can be ascribed to Ni agglomeration and Ni migration away from the electrode/electrolyte interface towards the bulk of the hydrogen electrode [65,66]. Bode plots in Figure 4-2e-g further confirm the distinct separation of the three arcs. Similar to the Nyquist plots, the HF region shows a clear evolution, whereas the MF and LF regions show a very limited variation. Therefore, in our case, the dominant degradation is likely related to the hydrogen electrode, which is accelerated with increasing operating temperature. On the other hand, the degradation due to the oxygen electrode remains very limited.

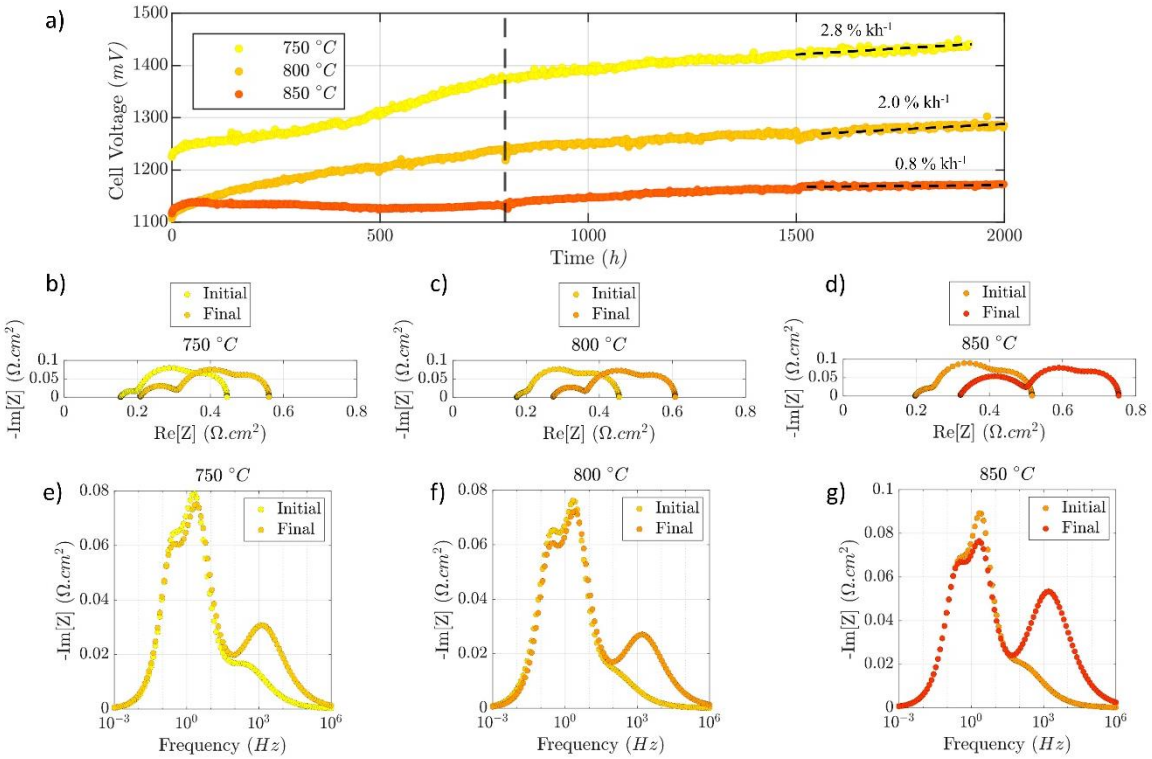

Figure 4-2. a) Durability curves showing the cell voltage evolution for the cells aged at 750, 800 and 850 °C during 2000 h in SOEC mode at -1 A·cm^{-2}, 64% SC, 10/90 vol.% H_2/H_2O. b-d) Nyquist plots and e-g) Bode plots acquired at 750 °C before and after 2000 h of ageing at 750 °C, 800 °C and 850 °C, respectively.

3.2 Post-test characterizations

Post-test characterizations allows complementing the EIS data by analysing the degradation that has occurred in the different layers of the cell.

3.2.1 Microstructural evolution in the hydrogen electrode. SEM images of the hydrogen electrode cross-sections are shown in Figure 4-3 for all the samples. In the SEM images of the aged cells, a substantial Ni coarsening can be observed, as highlighted by the dashed circles. In addition to the agglomeration, the cross sections (Figure 4-3b-d) also indicate a strong Ni

migration away from the dense electrolyte resulting in an almost completely depleted zone, as evidenced by dark contrast (i.e. increase of porosity). The thickness of the Ni depleted zone is found to be higher for the cell tested at 850 °C compared to 750 °C (cf. Figure 4-3b and 3d). These findings agree well with the SIMS analyses (see Figure 4-6) that were reported in a previous article [48]. Indeed, both Ni agglomeration and Ni migration, as well as a growing Ni-depleted zone with increasing temperature were observed. Moreover, the cermet microstructure at the gas inlet is compared to the outlet for the cell operated at 800 °C in electrolysis mode in Figure 4-3c and Figure 4-3e. It can be seen that the Ni migration is more pronounced at the cell inlet, where the current density is the highest. Indeed, using the model adapted for the studied cell and setup [49], the local current density has been computed along the cell radius. It was found that under our experimental conditions of 800 °C, SC=64% and 1.2 V, the current density at the inlet is approximately 1.9 times higher than at the outlet.

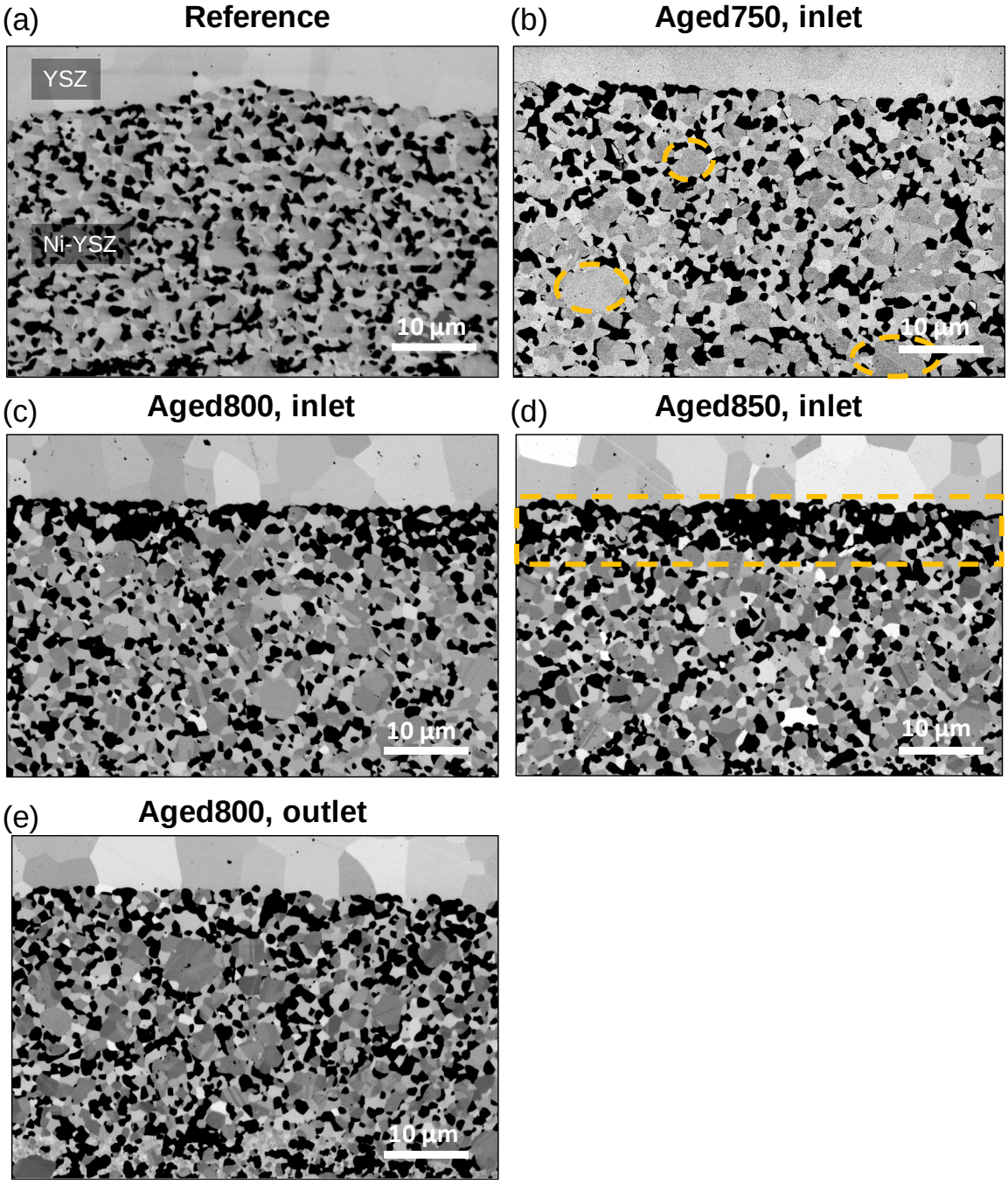

Figure 4-3. SEM observations of the Ni-YSZ/YSZ interface performed on (a) “Reference”, (b) “Aged750”, (c) “Aged800”, (d) “Aged850” samples at the gas inlet and (e) “Aged800” at the gas outlet. As an example, Ni coarsening is indicated by dashed circles and Ni migration by dashed rectangle. Porosity is black, YSZ is light grey and Ni is dark grey.

The Ni-YSZ cermet microstructure including a part of the electrolyte were reconstructed by FIB-SEM tomography. All the reconstructions were taken at a position around 0.7 cm from the cell centre. Figure 4-4a displays the rendered volumes for the “Reference” and the aged samples. The visual inspection of these reconstructions confirms the Ni coarsening and migration that were observed by SEM and SIMS. To quantify the microstructural evolution, the

density of active triple phase boundary length (TPBl) and the mean Ni particle diameter have been computed on the whole reconstructions using existing algorithms [67]. According to the data reported in Table 4-2, the density of active TPBl decreases and the mean Ni particle diameter increases with increasing the operating temperature from 750 °C to 850 °C. These evolutions in the cermet can be partially explained by the Ni coarsening, which is a thermally activated process [12,68,69]. They are fully consistent with the increase of the HF arc in the EIS. Furthermore, the local Ni volume fraction has also been measured on the 3D volumes as a function of the electrode thickness and plotted in Figure 4-4b from the electrolyte interface up to around 20 µm in the electrode. The curves confirm the Ni depletion near the electrolyte interface. Besides, it is evident that Ni migration is greater at 850 °C compared to 750 °C under the conditions of this study. Therefore, the increase in the ohmic resistance with increasing the operating temperature from 750 °C to 850 °C (cf. Figure 4-2) could be explained by the growth of the Ni depleted zone at the electrolyte interface.

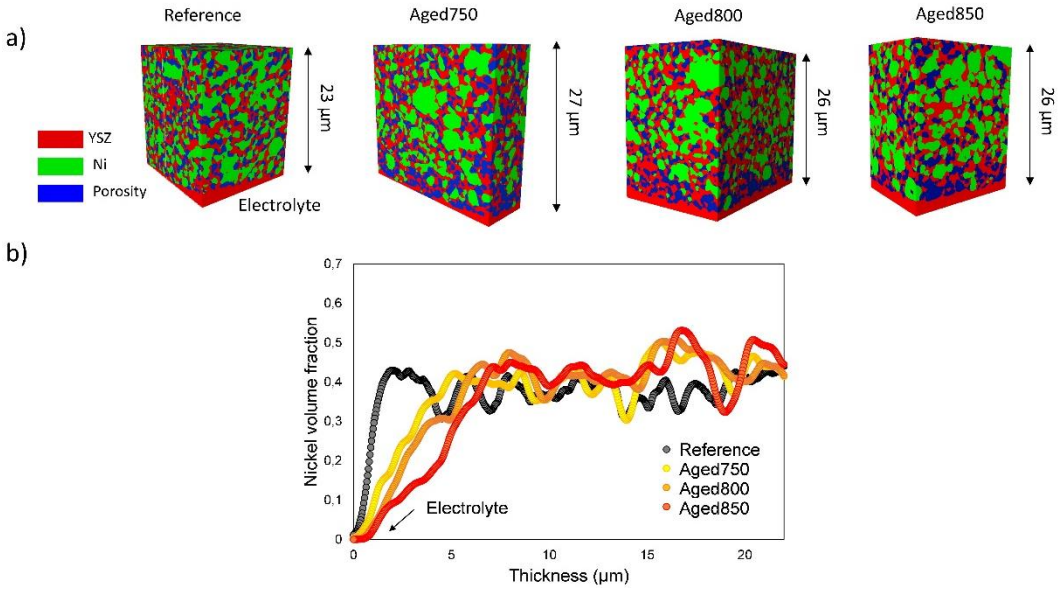

Figure 4-4. a) 3D FIB-SEM reconstructions of the hydrogen electrode performed on the "Reference", "Aged750", "Aged800" and "Aged850" samples; b) Ni volume fraction evolution along the hydrogen electrode thickness (electrolyte interface at 0 µm) calculated from the 3D FIB-SEM reconstructions.

Table 4-2. The density of active triple phase boundary length (TPBl) and the mean Ni particle diameter calculated from the 3D FIB-SEM reconstructions.

Sample ID	TPBl (µm/µm^3)	Ni particle size (µm)
"Reference"	2.85	0.57
"Aged750"	2.57	0.67
"Aged800"	1.72	0.76
"Aged850"	1.31	0.79

To quantify the impact of the Ni migration on the ohmic resistance, the depleted thickness l_{d} has been measured on EDX maps collected for the hydrogen electrodes. These cartographies were taken on large surface area (≈ 300 × 40 µm^2) at the cell inlet. The results are given in Table 4-3 for the different samples. It should be noted that the thicknesses are in good agreement with the local 3D reconstructions. The increase of the ohmic resistance due to the Ni migration, ΔR_{d}, is then estimated using Eq. [1]:

$$\Delta R_{\mathrm{d}}(\Omega \cdot \mathrm{cm}^2) = \frac{l_{\mathrm{d}}}{\frac{\varepsilon_{\mathrm{YSZ}}}{\tau_{\mathrm{YSZ}}} \cdot \sigma_{\mathrm{YSZ}}} \quad [20]$$

where $\varepsilon_{\mathrm{YSZ}}$, τ_{YSZ} and σ_{YSZ} are the volume fraction, tortuosity factor and ionic conductivity for the 8YSZ backbone. The calculated resistances are compared with the experimental values retrieved from the EIS at 750 °C in Table 4-3. It can be noted that the evolution of ohmic losses due to Ni depletion is consistent with the EIS series resistance measurements. This comparison implies that most of the degradation associated with the increase in series resistance is due to Ni migration.

Table 4-3. Estimation of the Ni depleted zone and the related contribution in the ohmic losses

Sample ID	Ni depletion thickness (µm)	Increase in the ohmic losses due to the Ni depletion calculated using Eq. [1] (Ω·cm²)	Increase in the EIS series resistance (Ω·cm²)
"Aged750"	2±1	0.047±0.02	0.054
"Aged800"	5±1	0.097±0.02	0.099
"Aged850"	6±1	0.118±0.02	0.123

Regarding the hydrogen electrode, it was found that the microstructural change in the cermet is responsible for most of the cell degradation. Indeed, the strong Ni migration and coarsening, which appear to be accelerated by increasing temperature, is fully consistent with the evolution

of the impedance spectra. As previously shown, the higher Ni depletion observed at 850 °C is fully consistent with the higher increase in the ohmic losses and the HF arc found for the sample aged at this temperature. Therefore, under the experimental conditions of this study, Ni migration is significantly aggravated by increasing the temperature. This statement is in good agreement with the findings of Hoerlein et al. [70], who observed less Ni depletion at 750 °C compared to 800 °C and 850 °C after operation at -1.5 $A \cdot cm^{-2}$ in SOEC mode. However, these results are not coherent with the study of Bilalis et al. [71] who reported a higher migration at 750 °C compared to 850 °C. Nevertheless, it can be pointed out that their conclusions on Ni migration were based on an apparent degradation extracted from EIS performed at different temperatures.

It has also been found that the Ni migration is higher at the cell inlet where the current density is higher. This last result is also in good agreement with the observations of Hoerlein et al. [70], who reported that the migration is aggravated when the current density in SOEC mode is increased. This dependency is coherent with the mechanism for Ni migration which must be driven by the electrode overpotential [17]. However, according to this mechanism, it could be expected that the Ni migration becomes very limited at high temperatures (since the electrode overpotentials strongly decreases with the temperature), which is contradictory with our observations. This apparent discrepancy between theory and experiment could be explained by the temperature dependency of the Ni surface diffusion coefficient. Indeed, the surface diffusion coefficient of Ni increases with increasing temperature [72]. However, as pointed out in [17], the underlying mechanisms for Ni migration are complex and involve several processes depending on the experimental conditions and the tested cermet which are still not precisely understood. From this point of view, additional tests and characterizations over a larger range of temperatures, gas compositions and cermet microstructures are still necessary to better understand the impact of Ni migration on the cell response.

To illustrate the impact of the selected temperature to assess the degradation before and after the durability test, theoretical calculations have been performed considering the aforementioned microstructural evolution in the hydrogen electrode.

On the one hand, the variation in ohmic losses due to the Ni depletion has been estimated for the test carried out at 850 °C. This calculation has been performed considering a temperature of 750 °C and 850 °C. For this purpose, Eq. [1] has been applied using as inputs (i) the depleted layer thickness given in Table 4-3 and (ii) the YSZ ionic conductivity taken at the two temperatures [73]. As shown in Table 4-4, the variation ΔRs becomes larger when estimated at

750 °C due to the thermally activated ionic conductivity of YSZ. This result shows that the increase in series resistance is much higher when the impedance is measured at 750 °C compared to 850 °C. Therefore, this effect contribute to the fact that the degradation rate measured at 850 °C is lower than the one measured at 750 °C for the cell "Aged850".

Table 4-4. Increase in Ohmic losses due to the Ni depletion for the cell "Aged850" calculated at 750 °C and 850 °C and impact on the ASR

Temperature for assessing the degradation (°C)	Variation in series resistance ΔRs (Ohm.cm²)	Degradation rate on the ASR $\Delta Rs/(R_{tot}.\Delta t)$ (%.kh^{-1})
750	0.118	11.5
850	0.049	5.5

On the other hand, the variation in polarisation resistance at OCV due to the loss of active TPBl in the hydrogen electrode has been estimated for the test carried out at 850 °C. The resistance due to the hydrogen electrode has been calculated according to the following equation [74]:

$$R_p^{H2\ electrode} = \frac{RT}{zF}\frac{1}{i_0^{H2\ electrode}} \quad [2]$$

where $i_0^{H2\ electrode}$ is the exchange current density calibrated for our studied cells considering number of exchange electron z=2 and that depends on the temperature according an Arrhenius law with an activation energy of 130 kJ.mol^{-1} [64]. Moreover, $i_0^{H2\ electrode}$ has been assumed proportional to the density of active TPBl [75,76]. Using this approach, the increase in $R_p^{H2\ electrode}$ has been estimated for the cell "Aged850" at 850°C and 750°C. The results provided in Table 4-5 show that the degradation rate on the ASR estimated at OCV is higher when calculated at low temperature. Therefore, this effect also explains the dependency of the degradation rates with the reference temperature at which the degradation is measured.

Table 4-5. Increase in the polarisation resistance at OCV induced by loss of TPBl in the cermet for the cell "Aged850" calculated at 750 °C and 850 °C

Temperature for assessing the degradation (°C)	Variation in polarisation resistance $\Delta R_p^{H2\ electrode}$ (Ohm.cm²)	Degradation rate on the ASR $\Delta R_p^{H2\ electrode}/(R_{tot}.\Delta t)$ (%.kh^{-1})
750	0.073	7.1
850	0.021	2.4

3.2.2 Inter-diffusion and reactivity at the barrier layer. The elemental intermixing and the presence of secondary phases at the GDC barrier layer (BL) interfaces were investigated applying SEM, SIMS, STEM-EDS, synchrotron XRF, and synchrotron XRD.

SEM images including the barrier layer, a part of the electrolyte and the electrode are shown in Figure 4-5 for the pristine and the aged cells. A line of small grains can be observed in all the samples at the interface between the electrolyte and the barrier layer which is usually attributed to the inter-diffusion layer (IDL) [9,42]. At the spatial resolution of the SEM, the thickness of this layer does not seem to evolve significantly upon operation even after the ageing at 850 °C and -1A.cm^{-2}. Besides, no secondary phases are detected in the porosity of the barrier layer.

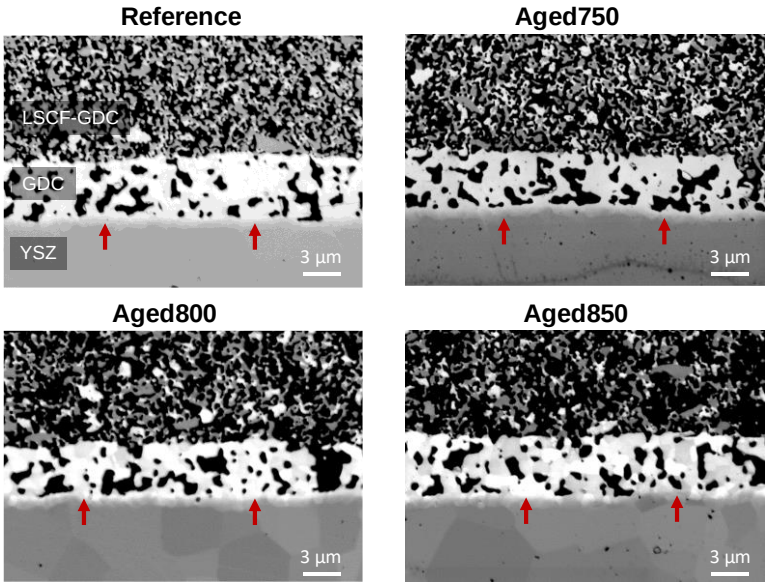

Figure 4-5. SEM images for the barrier layer for the pristine and aged cells. The arrows show the IDL between the electrolyte and the barrier layer.

Figure 4-6 displays the SIMS imaging of Ni, Co, Sr, Zr and Gd signals ranging from the hydrogen to the oxygen electrodes. In this way, elemental inter-diffusion can be highlighted

across all layers. Besides, to complement the SIMS imaging and cross-validate the results, the distribution of the chemical elements in the same region of interest was also measured by synchrotron XRF. Figure 4-7 shows the XRF maps along the LSCF-GDC/GDC/YSZ interfaces.

Several notable observations can be made from these chemical element analyses:

(i) Firstly, Gd maps in Figure 4-6e and Figure 4-7e reveal the formation of a Gd-rich layer at the GDC/YSZ interface which is related to the IDL as observed in the SEM images. The extent of this layer is roughly the same for all samples, confirming that IDL thickness is stable upon operation in our experimental conditions.

(ii) Secondly, looking at the Sr and Zr maps in Figure 4-6c-d and Figure 4-7c-d, it can be seen that these two elements do not accumulate at the interface between the barrier layer and the electrolyte. This observation means that the formation of an insulating phase such as $SrZrO_3$ in the GDC BL close to YSZ electrolyte is very limited even after an operation at 850 °C and -1A.cm^{-2}.

(iii) Thirdly, Figure 4-6a and Figure 4-7a reveal that Ni from the hydrogen electrode has diffused into the YSZ grains in the electrolyte and farther into the oxygen electrode. Besides, Co and Gd have been observed along the YSZ grain boundaries (GB) in the electrolyte (Figure 4-6b and Figure 4-7b).

Since all these inter-diffusions are already observed in the reference cell, it can be concluded that they occurred during the cell manufacturing. However, it is worth noting that no significant evolution is detected after ageing at the SIMS and XRF spatial resolution (around 60-100 nm).

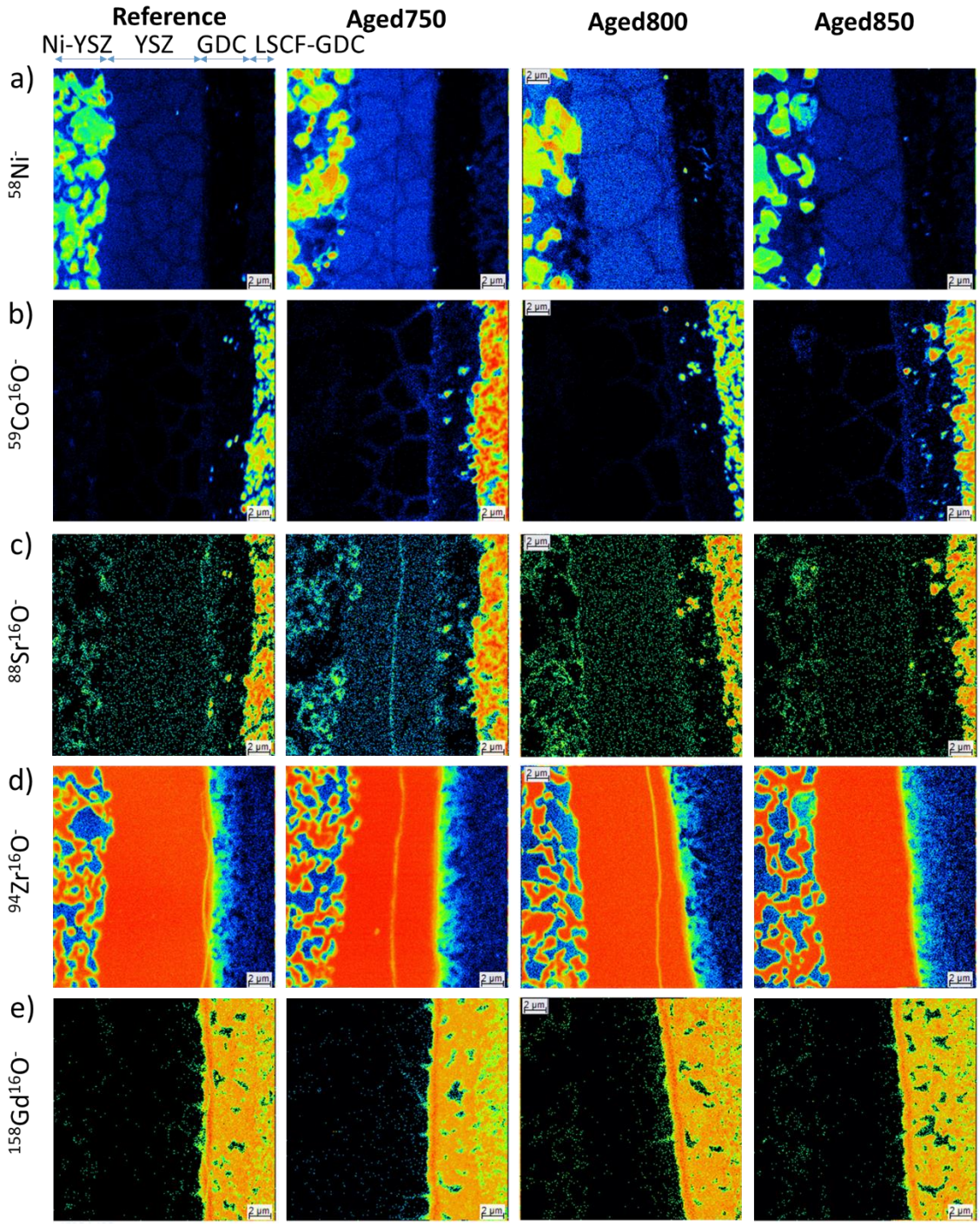

Figure 4-6. SIMS analysis performed at the Ni-YSZ/YSZ/GDC/LSCF-GDC interfaces, reporting a) Ni, b) Co, c) Sr, d) Zr, and e) Gd signals for the "Reference", "Aged750", "Aged800", "Aged850" samples. The raster size is 20x20 µm^2.

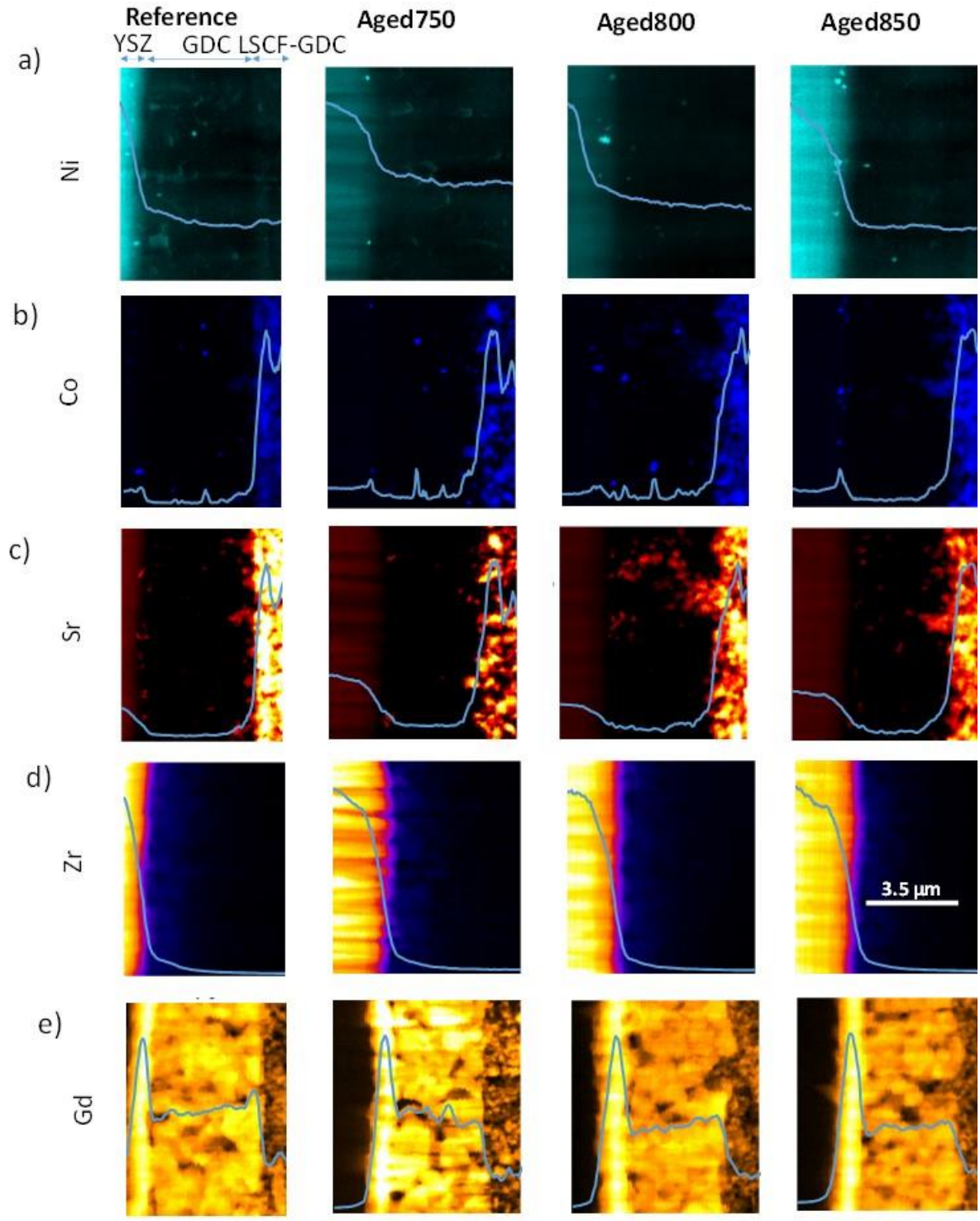

Figure 4-7. Nanoscale XRF elemental maps of the LSCF-GDC/GDC/YSZ interfaces, reporting a) Ni, b) Co, c) Sr, d) Zr, and e) Gd signals acquired on the "Reference", "Aged750", "Aged800", "Aged850" samples. The line plots are normalized elemental line profiles, they provide only qualitative information. The scans were performed with a spot size of 50 nm and an area of 6x8 μm^2 for the reference sample and 7x8 μm^2 for the aged samples.

Point-by-point synchrotron nanoXRD measurements were carried out to complement the elemental maps in order to investigate a potential structural evolution of the IDL upon operation and formation of secondary insulating phases in the barrier layer such as $SrZrO_3$.

The XRD patterns integrated over the IDL region are shown in Figure 4-8 for all the samples. The diffractograms consist of a convoluted set of peaks which may be primarily related to the GDC and YSZ. However, it can be seen that the peak positions are visibly shifted away from the reported ICDD positions for the GDC and the YSZ even for the reference sample. Besides, the peaks of YSZ and GDC are not well separated. Indeed, it is known that the inter-diffusion at the barrier layer interface results in a shoulder on the GDC peak [19,77]. In other words, these shoulders are related to the presence of the IDL in all the samples. A noticeable evolution in the patterns can be observed before and after ageing. Indeed, the YSZ and GDC peaks appear more and more convoluted when the ageing temperature is increased from 750 °C to 850 °C. This observation would mean that the crystal structure around the IDL has evolved with ageing, especially at the highest operating temperature. All these results would thus indicate a slightly accelerated inter-diffusion upon operation, which was not detected by the SIMS and XRF characterizations.

The same analyses were also conducted integrating the data over the BL region. The XRD patterns for the reference and aged cells are reported in the supplementary (Figure S-B 3). As expected, the main peaks are related to the GDC phase. Although there are a few unidentified peaks of low abundance, the presence of secondary phases such as Co_3O_4, CoO, $SrCO_3$, and $SrZrO_3$ in the barrier layer can be ruled out.

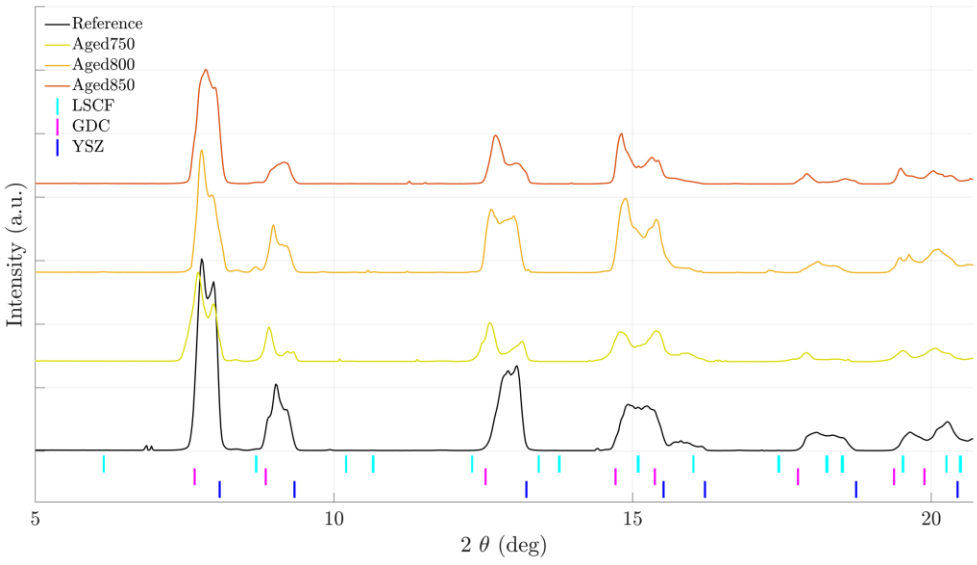

Figure 4-8. Synchrotron XRD patterns of the IDL region of all the samples. The representative phases shown below correspond to $La_{0.6}Sr_{0.4}Co_{0.2}Fe_{0.8}O_3$ ICDD no: 00-064-0218, $Ce_{0.8}Gd_{0.2}O_2$ ICDD no: 01-080-5535, YSZ ICDD no: 04–001–9395.

Finally, the local structure and the elemental composition of the BL and the IDL were analysed at the nanoscale by STEM-EDS [48]. In the analysed lamellae for the "Reference" and the "Aged800" samples, Sr signal was not detected in the barrier layer close to the electrolyte interface, thus excluding the presence of $SrZrO_3$ at the GDC/YSZ interface in good agreement with the other analyses. The bright field (BF)/STEM images of the IDL, that is around 0.6-1 µm thick, show that its microstructure is composed of one or two grains in the thickness for the two samples (cf. Figure 4-9a for the cell aged at 800°C). Regarding its elemental composition, TEM-EDS line-scan analyses revealed a gradient across the layer (Figure 4-9b). As expected, the Gd and Ce diffuse from the barrier layer resulting in a solid solution of Gd, Ce, Zr and Y for the IDL. In addition, the STEM-EDS elemental maps for the "Reference" sample revealed Co, Fe and Gd enrichment along the GBs between two GDC grains (Figure S-B 4). We observed a similar behaviour in a previous study by APT [48]. It appears that the oxygen electrode components (La, Sr, Co and Fe) primarily migrate into the barrier layer through the GDC grain boundaries during the cell fabrication.

It has been suggested by several authors [40,41] that the IDL might be useful in mitigating the formation of secondary phases such as SZO. To test this idea, Kim et al. [78] deliberately added a $Ce_{0.43}Zr_{0.43}Gd_{0.1}Y_{0.04}O_{2-\delta}$ (CZGY) contact layer between YSZ and GDC. The authors observed not only improved cell stability and reduced Sr accumulation between the CZGY and YSZ interface, but also improved electrochemical performances. Some other studies suggested that the sintering temperature of the barrier layer may have a direct impact on the amount of elemental inter-diffusion (IDL) and reactivity at the electrolyte interface [40,41]. For instance, Wankmüller et al. [41] found an increase in the IDL thickness and a decrease in the presence of SZOs when the GDC sintering temperature is increased from 1100 °C to 1400 °C. It can therefore be proposed that the absence of secondary phases observed after ageing in our cells made from standard materials would be due to the relatively thick IDL formed during the manufacturing process. This would suggest that the IDL could act as a dense 'barrier layer' preventing the formation of zirconates even when the cell is tested under harsh conditions (high current density at 850 °C in electrolysis mode).

In addition, we observed that the elements in LSCF, in particular Co and Fe, diffuse into the BL, mainly in the GBs of GDC in the "Reference" sample. Earlier investigations found discrete Co particles in the BL and attributed these observations to the degradation of LSCF [9,29,43]. However, Wang et al. [79] investigated the potential effect of Co and Fe diffusion in the GBs of GDCs. The authors have suggested that Co and Fe may cause a delay in the GB diffusion of

Sr and Zr, and hence, in the formation of insulating $SrZrO_3$. Therefore, the presence of these elements in the BL may also have a mitigating effect on the formation of secondary phases during operation. This point suggests that the local chemistry due to intermixing at the BL/electrolyte interface during the cell manufacturing must play a key role in the formation of insulating phases upon operation.

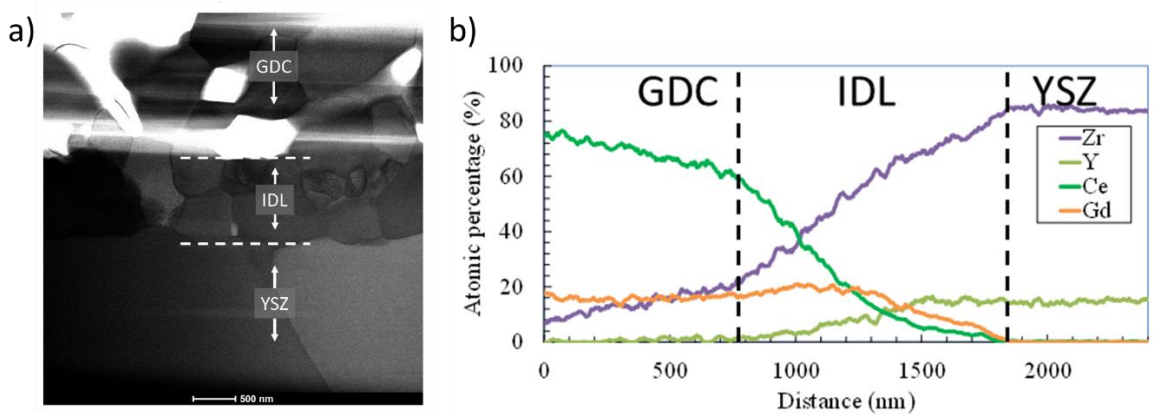

Figure 4-9. a) BF/STEM images of the "Aged800" samples focusing on the GDC/YSZ interface. b) The STEM-EDS line profiles of Gd, Ce, Y and Ze (in at.%) for the "Aged800" sample.

3.2.3 Inter-diffusion between LSCF/GDC in the oxygen electrode. To explore the inter-diffusion between LSCF and GDC particles, structural and elemental analyses were carried out at the atomic scale using APT and TEM techniques. APT enables mapping the local elemental concentrations via a three-dimensional reconstruction. Figure 4-10 shows the atomic distribution and line profiles across a grain boundary between LSCF and GDC in the functional layer (close to the BL). A considerable amount of elemental intermixing between LSCF and GDC has been detected in both samples. In particular, a significant amount of Ce and Gd has diffused into the bulk of the LSCF grain. On the contrary, the signal of LSCF atoms decreases rapidly after a few nm into the GDC phase. In complementarity with the line profile, the 3D dynamic elemental maps of Ce, O, Gd, Fe and Sr for both samples (cf. Supporting Data) show how Ce and Gd diffuse uniformly into the LSCF and how the Fe and Sr counts are close to zero in the GDC grain. Table 4-6 reports the atomic concentrations of elements within the LSCF and GDC phases. It can be seen that 4.4 at. % Ce and 3.9 at. % Gd are found in the LSCF grain of the "Reference" sample, whereas LSCF elements and impurities constitute < 1 at. % in the GDC grain. In the "Aged800" sample, the Ce concentration decreases to 1.3 % whereas Gd concentration remains stable. These results show that a substantial diffusion of Gd and Ce into

LSCF already occurred during the cell manufacturing. However, this intermixing does not seem to evolve upon operation.

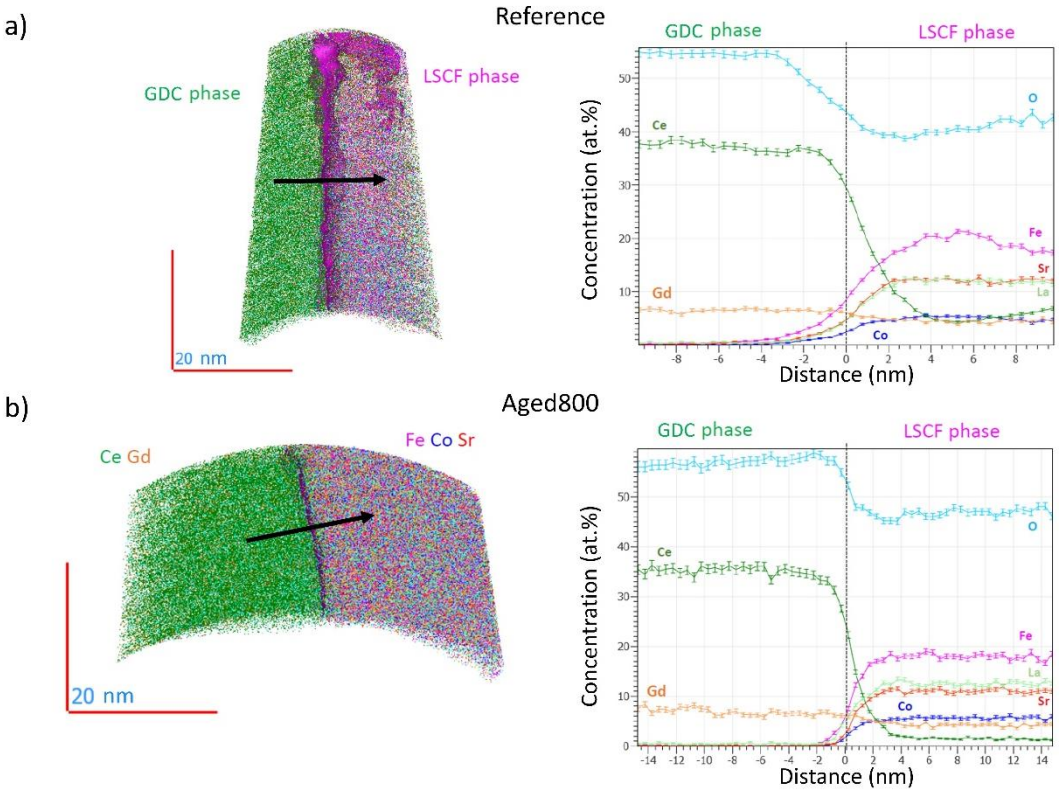

Figure 4-10. 3D atomic map of the LSCF and GDC phases and line profile orthogonal to the grain boundary obtained from APT analyses on a) "Reference" and b) "Aged800" samples.

Table 4-6. Atomic concentration of elements (at. %) in the LSCF and GDC phases in the FL of oxygen electrode for the "Reference" and "Aged800" samples measured by APT.

Sample	Phase	O	Ce	Gd	La	Sr	Co	Fe	Impurities
Reference	GDC	54.2	38.0	7.1	0.2	0.1	-	0.2	0.3
	LSCF	41.2	4.4	3.9	12.0	12.3	5.2	20.1	0.8
Aged800	GDC	57.3	35.4	6.4	0.4	0.13	< 0.1	0.15	0.19
	LSCF	47.2	1.3	4.1	12.8	10.8	5.5	18.0	0.3

Complementing APT, TEM analyses were performed to provide further information on the atomic arrangement and elemental composition.

To investigate the elemental composition, STEM-EDS elemental mapping was performed on neighboring LSCF and GDC grains for the "Reference" and the "Aged800" samples (Figure S-B 5). In good agreement with the APT analyses, it was found that Ce and, in particular, Gd, are clearly present inside the LSCF grain in both samples. It can be noted that secondary phases related to Sr and/or Co oxides were not detected within the studied volume for both samples.

In the following, a high resolution HAADF/STEM image was recorded for a LSCF particle in the "Reference" sample. As expected for an ABO_3-type crystal lattice, La and Sr were found to occupy the same position in the A-site of the perovskite, while Co and Fe were found to occupy the same B-site position. Therefore, in the high resolution HAADF/ STEM image (Figure 4-11a), the La and Sr are located in the atomic columns imaged with large spots whereas the Fe and Co in the columns imaged with a small spot. This is confirmed by the EDS elemental maps and the line profiles extracted from them (Figure 4-11). The Gd elemental map and the line profile also show that the Gd is located on the A-site of the ABO_3-type structure. This observation would thus indicate that Gd diffuse in LSCF through A-site vacancies. It is also clear from the line profiles in Figure 4-11b that the last atomic layer on the surface is enriched in Gd. This last result needs to be confirmed by further studies, as this enrichment could be due to Gd redeposition during FIB sample preparation.

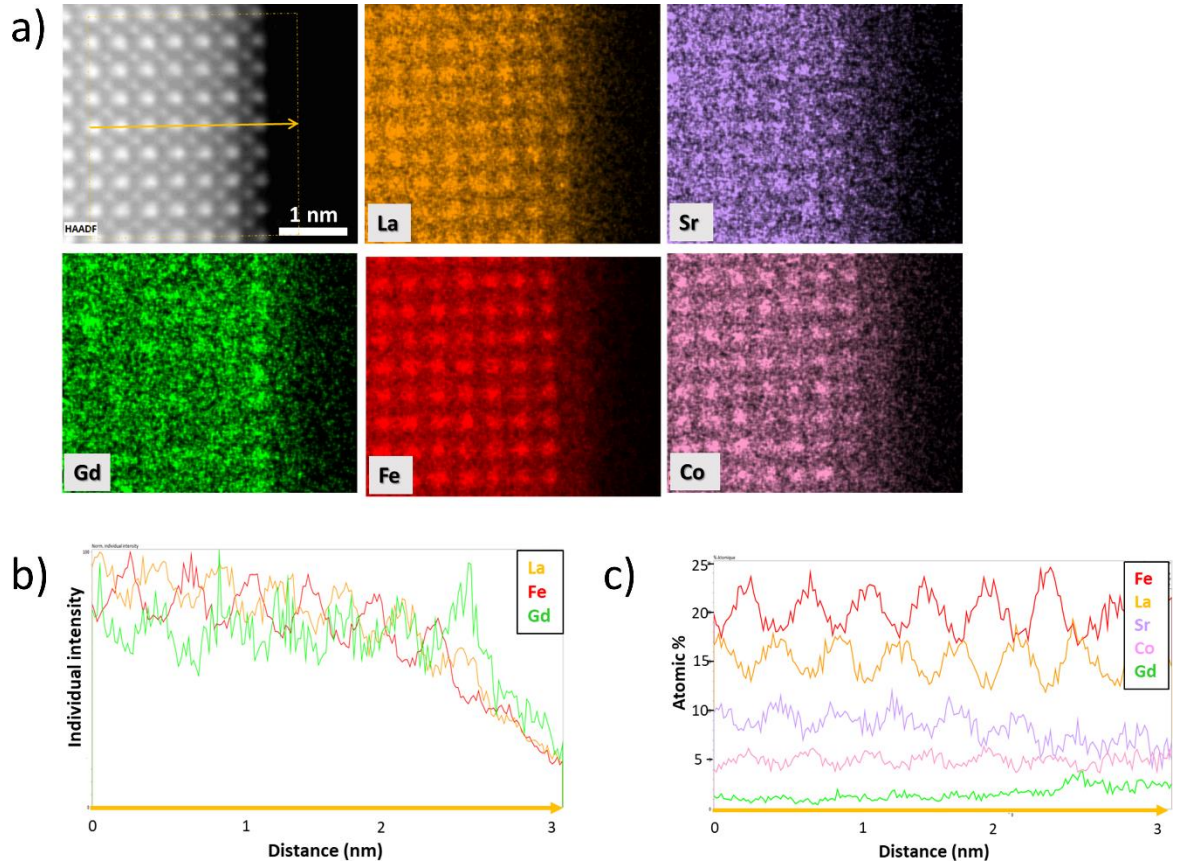

Figure 4-11. High resolution STEM-EDS analysis performed on an LSCF crystal of the Reference sample. a) HAADF and EDS elemental map of La, Sr, Gd, Fe and Co. b) La, Fe and Gd elemental line profiles (individually normalized raw intensities) extracted from the EDS elemental map along the yellow arrow drawn on the HAADF image in a). c) La, Fe, Sr, Co and Ge line profiles in atomic % similar to b).

3.2.4 LSCF decomposition and surface segregation in the oxygen electrode. As already discussed, EIS analyses found no evidence of oxygen electrode-related degradation. As expected for these ceramic materials [80], the cross-sectional SEM micrographs of all the samples have not revealed any microstructural change of the oxygen electrode (Figure 4-5). Moreover, in our testing conditions, the previous characterizations have shown that the inter-diffusion occurred during the cell layers sintering without significant evolution upon ageing. To investigate a potential impact of the cell operation on the LSCF crystalline structures in both the FL and CCL, the synchrotron XRD data were integrated along the line scans parallel to the electrolyte interface (X direction as shown in Figure S-B 1). The resulting patterns are displayed in Figure S-B 6 for the "Reference" and the aged cells. In the CCL, it can be observed that all the peaks are assigned to the LSCF phase. Moreover, the peaks for the FL diffractograms are only related to the LSCF and GDC phases. In other words, no secondary phases were detected even after operation at 850 °C.

Fitted lattice parameters (LSCF space group: $R\bar{3}c$ GDC space group: $Fm\bar{3}m$) are shown in Table 4-7. Considering the experimental uncertainty, the lattice parameters of LSCF and GDC in both layers do not change significantly with ageing. Knowing that the LSCF unit cell volume increases with the Sr release [19], this observation means that the LSCF was not subjected to a strong decomposition upon operation. This statement is in good agreement with the fact that no secondary phases were observed at the electrolyte interface and in the electrode.

Table 4-7. Fitted lattice parameters in Å of LSCF and GDC in the centre of FL and CCL of the oxygen electrode (ICDD no: 00-064-0218: number of the formula units in the unit cell z=6 for LSCF and ICDD no: 04-011-7336 with z=4 for GDC).

Sample	FL			CCL	
	LSCF		GDC	LSCF	
	a	c	a	a	c
"Reference"	5.53	13.51	5.42	5.53	13.53
"Aged750"	5.53	13.53	5.42	5.52	13.50
"Aged800"	5.52	13.50	5.42	5.52	13.48
"Aged850"	5.51	13.49	5.42	5.51	13.49

XPS analysis was carried out to investigate the surface composition and the chemical environment of the LSCF for reference and the aged cells. XPS probes a thickness typically from ~5 to 10 nm deep from the top surface and therefore provides surface sensitive information. To analyse the surface of the LSCF grains in the FL, the CCL were gently scraped from the surface using a scalpel.

The C 1s, O 1s and Sr 3d XPS spectra of the "Reference" sample are shown in Figure 4-12. All the results of the analyses of the "Reference" and the "Aged850" samples collected for the CCL and the FL are presented in Table S-B 1 – S-B 4 as binding energy (BE), full-width half maximum (FWHM), area, atomic concentration percentage (at.%). The C 1s core level spectrum in Figure 4-12 shows four components at 285, 286.4, 288.7, 289.8 eV which are assigned to carbon contamination, in particular carboxylic and/or carbonates groups (O–C=O, $(CO_3)^{2-}$) [81]. The O 1s core-level spectrum shows a sharp peak at the lower BE at ~528.7 eV (O–M1) which is usually attributed to the lattice oxygen in the bulk of the LSCF [82,83]. The smaller peak at a higher BE ~529.4 eV (O–M2) is related to the surface oxygen typically assigned to sub-oxide groups [82,83]. The peak observed at ~531.3 eV is usually attributed to the carbonates, hydroxides and oxides [82]. The Sr 3d core-level spectrum consists of a doublet with $3d_{5/2}$ at the lower BE (~131.9eV) and $3d_{3/2}$ at the higher BE (~133.6 eV). They are attributed to the lattice-bound Sr and the surface-bound Sr, respectively [84]. According to the literature [85], all the surface species found in the spectra indicate the presence of strontium surface segregation in the forms of $SrCO_3$ and $Sr(OH)_2$. Easy hydroxylation of SrO at room temperature makes it difficult to detect this oxide using ambient-temperature XPS measurements [83].

The ratio of surface-bound Sr to the sum of all Sr for both the CCL and the FL is given in Table 4-8 for all the samples. It can be seen that the ratio in the CCL has slightly increased from ~0.45 in the "Reference" sample to ~0.58 in the aged samples. In the FL, the ratio is increased with increasing the operating temperature. Indeed, the highest ratio of surface-bound Sr (0.68) is obtained in the cell aged at 850 °C. All these results indicate a slight increase in the Sr segregation to the surface with ageing, in good agreement with cells tested under similar conditions [20]. Nevertheless, the limited evolution of the Sr segregation is not expected to affect significantly the cell performance, which is in good agreement with the EIS results. Therefore, no significant LSCF decomposition occurred in the electrode after an operation for 2000 h at -1A.cm^{-2} and for a temperature ranging between 750 °C and 850 °C. This statement must explain the good electrode stability in terms of electrochemical performances in our testing conditions.

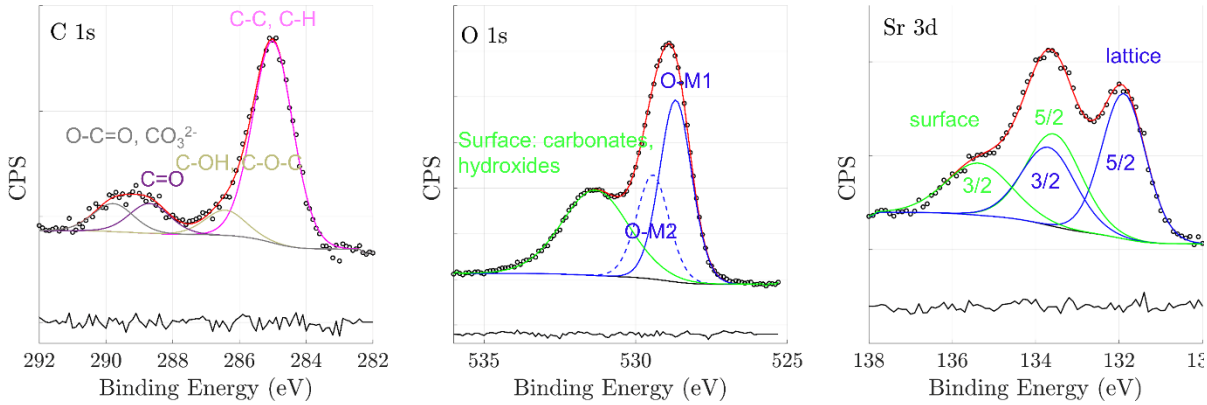

Figure 4-12. X-ray photoelectron spectra of the C 1s, O 1s, and Sr 3d core-level spectra of the "Reference" sample. The measurements were taken in the functional layer.

Table 4-8. Ratio of surface-bound Sr to the sum of lattice-bound Sr and surface-bound Sr deduced from XPS analyses.

Sample ID	Analysis position	
	CCL	FL
"Reference"	0.45	0.47
"Aged750"	0.56	0.51
"Aged800"	0.62	0.54
"Aged850"	0.55	0.68

Focusing on the composite oxygen electrode (LSCF-GDC), we do not detect a substantial Sr segregation and LSCF decomposition. However, in agreement with previous studies [45,46,86–91], a considerable intermixing between LSCF and GDC, in particular diffusion from GDC to LSCF, was observed already in the "Reference" cell. This inter-diffusion can strongly affect the crystal lattice parameters, grain growth and cell performance [38,92]. For instance, lattice parameter of GDC was observed to increase with increasing LSCF content in the LSCF-GDC composite [91]. This was attributed to the incorporation of La and Sr from the LSCF phase into GDC. On the other hand, the lattice parameter of LSCF in the LSCF-GDC composite was found to be lower than a single-phase LSCF [19,93–96]. Moreover, Uhlenbruk et al. found that purposefully doped Gd in the LSCF results in a decrease of the cell performance [38]. In that view, the Gd diffusion into LSCF, which was extensively observed in the bulk of the LSCF particle for all the samples, could lower the electrode performance.

However, it cannot be excluded that Gd diffusion into the A-site of the LSCF, as observed in this work, could improve the lattice stability, and supress the Sr segregation. Indeed, the Gd substitution on the A-site could influence the elastic lattice strain, and hence, stabilise the structure. To illustrate this assumption, Baiutti et al. [97] investigated the stability of LSM-SDC

(Sm-doped ceria) composites. They found increased electrochemical stability due to reduced Sr segregation. Detailed characterisations revealed extensive elemental inter-diffusion, particularly along the grain boundaries. Notably, a high concentration of Sm was found within the LSM. Through density functional theory (DFT) calculations, they provided evidence that Sm substitution in the A-site of LSM reduces the elastic driving force for Sr surface segregation.

Moreover, it is worth mentioning that the LSCF powder used for the cell manufacturing was analysed by ICP-MS. The analysis has revealed a slight A-site deficiency (A=La+Sr, B=Co+Fe, A/B=0.986). This deficiency could explain the Gd diffusion from GDC into the LSCF through the A-site vacancies. Moreover, it could be another key factor that might have an impact on the chemical stability against Sr segregation. For instance, A-site deficient $La_{0.8}Sr_{0.2}MnO_3$ (LSM) thin films was shown to exhibit higher stability against thermal annealing in terms of surface structures and chemistry [98]. Accordingly, a lower amount of SZO was found in the 5% A-site deficient LSCF compared to the stoichiometric LSCF [99]. Besides, the A-site deficiency can limit the formation of SrO [100].

Finally, it is worth reminding that the long-term tests were conducted using dry air. This specific experimental condition could be a key parameter controlling the electrode durability. Indeed, most of the published studies, which have reported Sr segregation, were carried out in ambient air without any control on the humidity. However, it has been shown that the humidity in the air can strongly accelerate the LSCF decomposition [8,101–103]. Therefore, it can be also proposed that the use of dry air could explain the very good LSCF stability highlighted in this work despite harsh operating conditions.

These discussions highlight the fact that a variety of factors affects the LSCF stability, which could explain the apparent conflicting results reported in the literature. Under these circumstances, it is still necessary to combine durability experiments, advanced characterisations, and modelling to assess the impacts of all these factors on the oxygen electrode stability.

4. Conclusions

In this work, the effect of operating temperature on the cell durability of solid oxide electrolysis cells (SOEC) was studied. For this purpose, long-term tests of 2000 h were conducted at a current density of -1 $A \cdot cm^{-2}$ for three operating temperatures (750, 800 and 850 °C). The degradation rate deduced from the durability curves was found to increase with decreasing the temperature. However, using a same reference temperature before and after ageing (i.e. 750 °C) revealed a higher degradation rate with increasing the operating temperature. Therefore, a higher temperature induces a higher 'intrinsic' material degradation. The diagrams recorded at 750 °C also showed that the ohmic losses and the high-frequency contribution associated with the hydrogen electrode increased with the increase of the operating temperature, while the mid-frequency contribution associated with the oxygen electrode remained stable.

Advanced post-test characterizations were carried out before and after long-term operation. The microstructural evolution related to Ni migration and coarsening in the hydrogen electrode was found to be largely responsible for the performance loss observed in the EIS. Additionally, Ni migration increased with increasing temperature, in agreement with the evolution of the ohmic losses in the EIS diagrams. The chemical elemental characterizations confirmed the inter-diffusion between the layers already in the pristine cell. At the interface between electrolyte and BL, a Gd-rich IDL has been identified in the reference sample. No secondary phases such as $SrZrO_3$ were detected at the interface with the electrolyte. This result was explained by the presence of the IDL that could prevent an extensive cation diffusion from the electrolyte.

Regarding the oxygen electrode, an intermixing between LSCF and GDC phases with the diffusion of both Ce and Gd into LSCF was found in the reference. However, no significant change was observed after operation. Besides, no secondary phases were detected in all the samples by nanoXRD. Only a slight increase in Sr segregation with increasing ageing temperature was highlighted by XPS. All these characterizations showing a limited degradation of the oxygen electrode after long-term operation are perfectly consistent with the EIS diagrams. In order to discuss the stability of the oxygen electrode at such high temperature and polarization, several hypotheses have been proposed to explain this rather unexpected behaviour.

Acknowledgements

We acknowledge the European Synchrotron Radiation Facility (ESRF) for provision of synchrotron radiation facilities (experiment MA5526) to perform nano-scale XRF and XRD measurements at beamline ID16B. The work has also been supported by the project CELCER-EHT from the National Research Agency (grant agreement ANR-PEHY-008, France 2030). This work was also partially funded by Genvia company.

References

[1] Y. Leng, S.H. Chan, Q. Liu, Development of LSCF–GDC composite cathodes for low-temperature solid oxide fuel cells with thin film GDC electrolyte, International Journal of Hydrogen Energy 33 (2008) 3808–3817. https://doi.org/10.1016/j.ijhydene.2008.04.034.

[2] E. Effori, H. Moussaoui, F. Monaco, R.K. Sharma, J. Debayle, Y. Gavet, G. Delette, G.S. Larbi, E. Siebert, J. Vulliet, L. Dessemond, J. Laurencin, Reaction Mechanism and Impact of Microstructure on Performances for the LSCF-CGO Composite Electrode in Solid Oxide Cells, Fuel Cells 19 (2019) 429–444. https://doi.org/10.1002/fuce.201800185.

[3] V. Dusastre, J.A. Kilner, Optimisation of composite cathodes for intermediate temperature SOFC applications, Solid State Ionics 126 (1999) 163–174. https://doi.org/10.1016/S0167-2738(99)00108-3.

[4] C. Endler-Schuck, A. Leonide, A. Weber, S. Uhlenbruck, F. Tietz, E. Ivers-Tiffée, Performance analysis of mixed ionic–electronic conducting cathodes in anode supported cells, Journal of Power Sources 196 (2011) 7257–7262. https://doi.org/10.1016/j.jpowsour.2010.11.079.

[5] M.Z. Khan, R.-H. Song, A. Hussain, S.-B. Lee, T.-H. Lim, J.-E. Hong, Effect of applied current density on the degradation behavior of anode-supported flat-tubular solid oxide fuel cells, Journal of the European Ceramic Society 40 (2020) 1407–1417. https://doi.org/10.1016/j.jeurceramsoc.2019.11.017.

[6] J.A. Schuler, H. Yokokawa, C.F. Calderone, Q. Jeangros, Z. Wuillemin, A. Hessler-Wyser, J. Van herle, Combined Cr and S poisoning in solid oxide fuel cell cathodes, Journal of Power Sources 201 (2012) 112–120. https://doi.org/10.1016/j.jpowsour.2011.10.123.

[7] S.-D. Kim, D.-W. Seo, A.K. Dorai, S.-K. Woo, The effect of gas compositions on the performance and durability of solid oxide electrolysis cells, International Journal of Hydrogen Energy 38 (2013) 6569–6576. https://doi.org/10.1016/j.ijhydene.2013.03.115.

[8] M. Kim, H. Muroyama, T. Matsui, K. Eguchi, Influence of Water Vapor on Performance Degradation and Microstructural Change of (La,Sr)(Co,Fe)$O_{3-\delta}$ Cathode, J. Electrochem. Soc. 166 (2019) F1269. https://doi.org/10.1149/2.0641915jes.

[9] J. Laurencin, M. Hubert, D.F. Sanchez, S. Pylypko, M. Morales, A. Morata, B. Morel, D. Montinaro, F. Lefebvre-Joud, E. Siebert, Degradation mechanism of $La_{0.6}Sr_{0.4}Co_{0.2}Fe_{0.8}O_{3-\delta}/Gd_{0.1}Ce_{0.9}O_{2-\delta}$ composite electrode operated under solid oxide electrolysis and fuel cell conditions, Electrochimica Acta 241 (2017) 459–476. https://doi.org/10.1016/j.electacta.2017.05.011.

[10] C.E. Frey, Q. Fang, D. Sebold, L. Blum, N.H. Menzler, A Detailed Post Mortem Analysis of Solid Oxide Electrolyzer Cells after Long-Term Stack Operation, J. Electrochem. Soc. 165 (2018) F357. https://doi.org/10.1149/2.0961805jes.

[11] F. Monaco, M. Hubert, J. Vulliet, J.P. Ouweltjes, D. Montinaro, P. Cloetens, P. Piccardo, F. Lefebvre-Joud, J. Laurencin, Degradation of Ni-YSZ Electrodes in Solid Oxide Cells: Impact of Polarization and Initial Microstructure on the Ni Evolution, J. Electrochem. Soc. 166 (2019) F1229. https://doi.org/10.1149/2.1261915jes.

[12] M. Hubert, J. Laurencin, P. Cloetens, B. Morel, D. Montinaro, F. Lefebvre-Joud, Impact of Nickel agglomeration on Solid Oxide Cell operated in fuel cell and electrolysis modes, Journal of Power Sources 397 (2018) 240–251. https://doi.org/10.1016/j.jpowsour.2018.06.097.

[13] M.B. Mogensen, A. Hauch, X. Sun, M. Chen, Y. Tao, S.D. Ebbesen, K.V. Hansen, P.V. Hendriksen, Relation Between Ni Particle Shape Change and Ni Migration in Ni–YSZ Electrodes – a Hypothesis, Fuel Cells 17 (2017) 434–441. https://doi.org/10.1002/fuce.201600222.

[14] A. Sciazko, T. Shimura, Y. Komatsu, N. Shikazono, Ni-GDC and Ni-YSZ electrodes operated in solid oxide electrolysis and fuel cell modes, Journal of Thermal Science and Technology 16 (2021) JTST0013–JTST0013. https://doi.org/10.1299/jtst.2021jtst0013.

[15] M. Trini, A. Hauch, S. De Angelis, X. Tong, P.V. Hendriksen, M. Chen, Comparison of microstructural evolution of fuel electrodes in solid oxide fuel cells and electrolysis cells, Journal of Power Sources 450 (2020) 227599. https://doi.org/10.1016/j.jpowsour.2019.227599.

[16] N.H. Menzler, D. Sebold, Y.J. Sohn, S. Zischke, Post-test characterization of a solid oxide fuel cell after more than 10 years of stack testing, Journal of Power Sources 478 (2020) 228770. https://doi.org/10.1016/j.jpowsour.2020.228770.

[17] L. Rorato, Y. Shang, S. Yang, M. Hubert, K. Couturier, L. Zhang, J. Vulliet, M. Chen, J. Laurencin, Understanding the Ni Migration in Solid Oxide Cell: A Coupled Experimental and Modeling Approach, J. Electrochem. Soc. 170 (2023) 034504. https://doi.org/10.1149/1945-7111/acc1a3.

[18] Y. Shang, A. Lyck Smitshuysen, M. Yu, Y. Liu, X. Tong, P. Stanley Jørgensen, L. Rorato, J. Laurencin, M. Chen, 3D microstructural characterization of Ni/yttria-stabilized zirconia electrodes during long-term CO 2 electrolysis, Journal of Materials Chemistry A 11 (2023) 12245–12257. https://doi.org/10.1039/D3TA01503C.

[19] F. Monaco, D. Ferreira-Sanchez, M. Hubert, B. Morel, D. Montinaro, D. Grolimund, J. Laurencin, Oxygen electrode degradation in solid oxide cells operating in electrolysis and fuel cell modes: LSCF destabilization and interdiffusion at the electrode/electrolyte interface, International Journal of Hydrogen Energy (2021). https://doi.org/10.1016/j.ijhydene.2021.07.054.

[20] Z. Pan, Q. Liu, L. Zhang, X. Zhang, S.H. Chan, Effect of Sr Surface Segregation of $La_{0.6}Sr_{0.4}Co_{0.2}Fe_{0.8}O_{3-\delta}$ Electrode on Its Electrochemical Performance in SOC, J. Electrochem. Soc. 162 (2015) F1316. https://doi.org/10.1149/2.0371512jes.

[21] J. Szász, F. Wankmüller, V. Wilde, H. Störmer, D. Gerthsen, N.H. Menzler, E. Ivers-Tiffée, Nature and Functionality of $La_{0.58}Sr_{0.4}Co_{0.2}Fe_{0.8}O_{3-\delta}$ / $Gd_{0.2}Ce_{0.8}O_{2-\delta}$ / $Y_{0.16}Zr_{0.84}O_{2-\delta}$ Interfaces in SOFCs, J. Electrochem. Soc. 165 (2018) F898. https://doi.org/10.1149/2.0031811jes.

[22] D. Kim, J.W. Park, B.-H. Yun, J.H. Park, K.T. Lee, Correlation of Time-Dependent Oxygen Surface Exchange Kinetics with Surface Chemistry of $La_{0.6}Sr_{0.4}Co_{0.2}Fe_{0.8}O_{3-\delta}$ Catalysts, ACS Appl. Mater. Interfaces 11 (2019) 31786–31792. https://doi.org/10.1021/acsami.9b06569.

[23] H. Wang, S.A. Barnett, Degradation Mechanisms of Porous $La_{0.6}Sr_{0.4}Co_{0.2}Fe_{0.8}O_{3-\delta}$ Solid Oxide Fuel Cell Cathodes, J. Electrochem. Soc. 165 (2018) F564. https://doi.org/10.1149/2.1211807jes.

[24] W. Araki, T. Yamaguchi, Y. Arai, J. Malzbender, Strontium surface segregation in $La_{0.58}Sr_{0.4}Co_{0.2}Fe_{0.8}O_{3-\delta}$ annealed under compression, Solid State Ionics 268 (2014) 1–6. https://doi.org/10.1016/j.ssi.2014.09.019.

[25] J. Druce, H. Téllez, M. Burriel, M. D. Sharp, L. J. Fawcett, S. N. Cook, D. S. McPhail, T. Ishihara, H. H. Brongersma, J. A. Kilner, Surface termination and subsurface restructuring of perovskite-based solid oxide electrode materials, Energy & Environmental Science 7 (2014) 3593–3599. https://doi.org/10.1039/C4EE01497A.

[26] O. Celikbilek, M. Burriel, Recent advances in the understanding of the influence of surface chemistry and microstructure on the functional properties of solid oxide cell air electrodes, in: Nanoengineered Materials for Solid Oxide Cells, IOP Publishing, 2023. https://doi.org/10.1088/978-0-7503-4064-9ch2.

[27] Y. Wen, T. Yang, D. Lee, H. Nyung Lee, E. J. Crumlin, K. Huang, Temporal and thermal evolutions of surface Sr-segregation in pristine and atomic layer deposition modified $La_{0.6}Sr_{0.4}CoO_{3-\delta}$ epitaxial films, Journal of Materials Chemistry A 6 (2018) 24378–24388. https://doi.org/10.1039/C8TA08355J.

[28] A. Mahmood, S. Bano, J.H. Yu, K.-H. Lee, High-performance solid oxide electrolysis cell based on ScSZ/GDC (scandia-stabilized zirconia/gadolinium-doped ceria) bi-layered electrolyte and LSCF (lanthanum strontium cobalt ferrite) oxygen electrode, Energy 90 (2015) 344–350. https://doi.org/10.1016/j.energy.2015.06.109.

[29] J. Villanova, S. Schlabach, A. Brisse, A. Léon, X-ray fluorescence nano-imaging of long-term operated solid oxide electrolysis cells, Journal of Power Sources 421 (2019) 100–108. https://doi.org/10.1016/j.jpowsour.2019.02.084.

[30] X.C. Lu, J.H. Zhu, Effect of Sr and Mg Doping on the Property and Performance of the $La_{1-x}Sr_xGa_{1-y}Mg_yO_{3-\delta}$ Electrolyte, J. Electrochem. Soc. 155 (2008) B494. https://doi.org/10.1149/1.2895064.

[31] Y. Liu, K. Chen, L. Zhao, B. Chi, J. Pu, S.P. Jiang, L. Jian, Performance stability and degradation mechanism of $La_{0.6}Sr_{0.4}Co_{0.2}Fe_{0.8}O_{3-\delta}$ cathodes under solid oxide fuel cells operation conditions, International Journal of Hydrogen Energy 39 (2014) 15868–15876. https://doi.org/10.1016/j.ijhydene.2014.03.077.

[32] D. The, S. Grieshammer, M. Schroeder, M. Martin, M. Al Daroukh, F. Tietz, J. Schefold, A. Brisse, Microstructural comparison of solid oxide electrolyser cells operated for 6100 h and 9000 h, Journal of Power Sources 275 (2015) 901–911. https://doi.org/10.1016/j.jpowsour.2014.10.188.

[33] R. Knibbe, A. Hauch, J. Hjelm, S. Ebbesen, M. Mogensen, Durability of Solid Oxide Cells, Green 1 (2011) 141. https://doi.org/10.1515/green.2011.015.

[34] W.-H. Kim, H.-S. Song, J. Moon, H.-W. Lee, Intermediate temperature solid oxide fuel cell using (La,Sr)(Co,Fe)O_3-based cathodes, Solid State Ionics 177 (2006) 3211–3216. https://doi.org/10.1016/j.ssi.2006.07.049.

[35] A. Martínez-Amesti, A. Larrañaga, L.M. Rodríguez-Martínez, A.T. Aguayo, J.L. Pizarro, M.L. Nó, A. Laresgoiti, M.I. Arriortua, Reactivity between La(Sr)FeO_3 cathode, doped CeO_2 interlayer and yttria-stabilized zirconia electrolyte for solid oxide fuel cell applications, Journal of Power Sources 185 (2008) 401–410. https://doi.org/10.1016/j.jpowsour.2008.06.049.

[36] F. Tietz, Q. Fu, V.A.C. Haanappel, A. Mai, N.H. Menzler, S. Uhlenbruck, Materials Development for Advanced Planar Solid Oxide Fuel Cells, International Journal of Applied Ceramic Technology 4 (2007) 436–445. https://doi.org/10.1111/j.1744-7402.2007.02156.x.

[37] T. Shimura, A. He, N. Shikazono, Evaluation of $La_{0.57}Sr_{0.38}Co_{0.2}Fe_{0.8}O_{3-\delta}$ Electrode Performance Degradation Based on Three-Dimensional Microstructure Reconstruction and Electrochemical Simulation, J. Electrochem. Soc. 166 (2019) F821. https://doi.org/10.1149/2.1091912jes.

[38] S. Uhlenbruck, T. Moskalewicz, N. Jordan, H.-J. Penkalla, H.P. Buchkremer, Element interdiffusion at electrolyte–cathode interfaces in ceramic high-temperature fuel cells, Solid State Ionics 180 (2009) 418–423. https://doi.org/10.1016/j.ssi.2009.01.014.

[39] M. Morales, V. Miguel-Pérez, A. Tarancón, A. Slodczyk, M. Torrell, B. Ballesteros, J.P. Ouweltjes, J.M. Bassat, D. Montinaro, A. Morata, Multi-scale analysis of the diffusion barrier layer of gadolinia-doped ceria in a solid oxide fuel cell operated in a stack for 3000 h, Journal of Power Sources 344 (2017) 141–151. https://doi.org/10.1016/j.jpowsour.2017.01.109.

[40] H. Xu, K. Cheng, M. Chen, L. Zhang, K. Brodersen, Y. Du, Interdiffusion between gadolinia doped ceria and yttria stabilized zirconia in solid oxide fuel cells: Experimental investigation and kinetic modeling, Journal of Power Sources 441 (2019) 227152. https://doi.org/10.1016/j.jpowsour.2019.227152.

[41] F. Wankmüller, J. Szász, J. Joos, V. Wilde, H. Störmer, D. Gerthsen, E. Ivers-Tiffée, Correlative tomography at the cathode/electrolyte interfaces of solid oxide fuel cells, Journal of Power Sources 360 (2017) 399–408. https://doi.org/10.1016/j.jpowsour.2017.06.008.

[42] V. Wilde, H. Störmer, J. Szász, F. Wankmüller, E. Ivers-Tiffée, D. Gerthsen, $Gd_{0.2}Ce_{0.8}O_2$ Diffusion Barrier Layer between $(La_{0.58}Sr_{0.4})(Co_{0.2}Fe_{0.8})O_{3-\delta}$ Cathode and $Y_{0.16}Zr_{0.84}O_2$ Electrolyte for Solid Oxide Fuel Cells: Effect of Barrier Layer Sintering Temperature on Microstructure, ACS Appl. Energy Mater. 1 (2018) 6790–6800. https://doi.org/10.1021/acsaem.8b00847.

[43] L. Bernadet, J. Segura-Ruiz, L. Yedra, S. Estrade, F. Peiró, D. Montinaro, M. Torrell, A. Morata, A. Tarancón, Enhanced diffusion barrier layers for avoiding degradation in SOFCs aged for 14000 h during 2 years, Journal of Power Sources 555 (2023) 232400. https://doi.org/10.1016/j.jpowsour.2022.232400.

[44] T. Matsui, S. Li, Y. Inoue, N. Yoshida, H. Muroyama, K. Eguchi, Degradation Analysis of Solid Oxide Fuel Cells with (La,Sr)(Co,Fe)$O_{3-\delta}$ Cathode/Gd_2O_3–CeO_2 Interlayer/Y_2O_3–ZrO_2 Electrolyte System: The Influences of Microstructural Change and Solid Solution Formation, ECS Trans. 91 (2019) 1247. https://doi.org/10.1149/09101.1247ecst.

[45] J.C.D. Vero, K. Develos-Bagarinao, H. Kishimoto, T. Ishiyama, K. Yamaji, T. Horita, H. Yokokawa, Effect of Cathodic Polarization on the $La_{0.6}Sr_{0.4}Co_{0.2}Fe_{0.8}O_{3-\delta}$-Cathode/Gd-Doped Ceria-Interlayer/YSZ Electrolyte Interfaces of Solid Oxide Fuel Cells, J. Electrochem. Soc. 164 (2017) F259. https://doi.org/10.1149/2.0811704jes.

[46] Z.-P. Li, M. Toshiyuki, G.J. Auchterlonie, J. Zou, D. John, Mutual Diffusion Occurring at the Interface between $La_{0.6}Sr_{0.4}Co_{0.8}Fe_{0.2}O_3$ Cathode and Gd-doped Ceria Electrolyte during IT-SOFC Cell Preparation, ACS Appl. Mater. Interfaces 3 (2011) 2772–2778. https://doi.org/10.1021/am2005543.

[47] W. Zhang, H. Wang, K. Guan, Z. Wei, X. Zhang, J. Meng, X. Liu, J. Meng, $La_{0.6}Sr_{0.4}Co_{0.2}Fe_{0.8}O_{3-\delta}/CeO_2$ Heterostructured Composite Nanofibers as a Highly Active and Robust Cathode Catalyst for Solid Oxide Fuel Cells, ACS Appl. Mater. Interfaces 11 (2019) 26830–26841. https://doi.org/10.1021/acsami.9b06668.

[48] G. Sassone, O. Celikbilek, M. Hubert, K.D. Bagarinao, T. David, L. Guetaz, I. Martin, J. Villanova, L. Rorato, B. Morel, A. Léon, J. Laurencin, Advanced Nanoscale Characterizations of Solid Oxide Cell Electrodes, ECS Trans. 111 (2023) 885. https://doi.org/10.1149/11106.0885ecst.

[49] E. Da Rosa Silva, G. Sassone, M. Prioux, M. Hubert, B. Morel, J. Laurencin, A multiscale model validated on local current measurements for understanding the solid oxide cells performances, Journal of Power Sources 556 (2023) 232499. https://doi.org/10.1016/j.jpowsour.2022.232499.

[50] B. Wei, K. Chen, L. Zhao, Z. Lü, S.P. Jiang, Chromium deposition and poisoning at $La_{0.6}Sr_{0.4}Co_{0.2}Fe_{0.8}O_{3-\delta}$ oxygen electrodes of solid oxide electrolysis cells, Phys. Chem. Chem. Phys. 17 (2014) 1601–1609. https://doi.org/10.1039/C4CP05110F.

[51] C. Sommer, C. Straehle, U. Köthe, F.A. Hamprecht, Ilastik: Interactive learning and segmentation toolkit, in: 2011 IEEE International Symposium on Biomedical Imaging: From Nano to Macro, 2011: pp. 230–233. https://doi.org/10.1109/ISBI.2011.5872394.

[52] N. Fairley, V. Fernandez, M. Richard-Plouet, C. Guillot-Deudon, J. Walton, E. Smith, D. Flahaut, M. Greiner, M. Biesinger, S. Tougaard, D. Morgan, J. Baltrusaitis, Systematic and collaborative approach to problem solving using X-ray photoelectron spectroscopy, Applied Surface Science Advances 5 (2021) 100112. https://doi.org/10.1016/j.apsadv.2021.100112.

[53] N.I. Khamidy, J. Laurencin, D. Ferreira Sanchez, F. Monaco, F. Charlot, E. Djurado, Durability of nanostructured $LaPrNiO_{4+\delta}$ electrode for solid oxide cells: Electrochemical, microstructural, and structural investigation, Journal of Power Sources 450 (2020) 227724. https://doi.org/10.1016/j.jpowsour.2020.227724.

[54] G. Martinez-Criado, J. Villanova, R. Tucoulou, D. Salomon, J.-P. Suuronen, S. Laboure, C. Guilloud, V. Valls, R. Barrett, E. Gagliardini, Y. Dabin, R. Baker, S. Bohic, C. Cohen, J. Morse, ID16B: A hard X-ray nanoprobe beamline at the ESRF for nano-analysis, Journal of Synchrotron Radiation 23 (2016) 344–352. https://doi.org/10.1107/S1600577515019839.

[55] V.A. Solé, E. Papillon, M. Cotte, Ph. Walter, J. Susini, A multiplatform code for the analysis of energy-dispersive X-ray fluorescence spectra, Spectrochimica Acta Part B: Atomic Spectroscopy 62 (2007) 63–68. https://doi.org/10.1016/j.sab.2006.12.002.

[56] W. De Nolf, F. Vanmeert, K. Janssens, XRDUA: crystalline phase distribution maps by two-dimensional scanning and tomographic (micro) X-ray powder diffraction, J Appl Cryst 47 (2014) 1107–1117. https://doi.org/10.1107/S1600576714008218.

[57] A. Le Bail, H. Duroy, J.L. Fourquet, Ab-initio structure determination of LiSbWO6 by X-ray powder diffraction, Materials Research Bulletin 23 (1988) 447–452. https://doi.org/10.1016/0025-5408(88)90019-0.

[58] J.R. Carvajal, Commission on Powder Diffraction (IUCr), Newsletter 26 (2001) 12–19.

[59] K. Thompson, D. Lawrence, D.J. Larson, J.D. Olson, T.F. Kelly, B. Gorman, In situ site-specific specimen preparation for atom probe tomography, Ultramicroscopy 107 (2007) 131–139. https://doi.org/10.1016/j.ultramic.2006.06.008.

[60] X. Sun, P.V. Hendriksen, M.B. Mogensen, M. Chen, Degradation in Solid Oxide Electrolysis Cells During Long Term Testing, Fuel Cells 19 (2019) 740–747. https://doi.org/10.1002/fuce.201900081.

[61] J. Schefold, A. Brisse, F. Tietz, Nine Thousand Hours of Operation of a Solid Oxide Cell in Steam Electrolysis Mode, J. Electrochem. Soc. 159 (2011) A137. https://doi.org/10.1149/2.076202jes.

[62] A. Hauch, S.D. Ebbesen, S.H. Jensen, M. Mogensen, Solid Oxide Electrolysis Cells: Microstructure and Degradation of the Ni/Yttria-Stabilized Zirconia Electrode, J. Electrochem. Soc. 155 (2008) B1184. https://doi.org/10.1149/1.2967331.

[63] G. Schiller, A. Ansar, M. Lang, O. Patz, High temperature water electrolysis using metal supported solid oxide electrolyser cells (SOEC), J Appl Electrochem 39 (2009) 293–301. https://doi.org/10.1007/s10800-008-9672-6.

[64] G. Sassone, E.D.R. Silva, M. Prioux, M. Hubert, B. Morel, A. Léon, J. Laurencin, Multiscale Modelling of Solid Oxide Cells Validated on Electrochemical Impedance Spectra and Polarization Curves, ECS Trans. 111 (2023) 649. https://doi.org/10.1149/11106.0649ecst.

[65] Q. Fang, C.E. Frey, N.H. Menzler, L. Blum, Electrochemical Performance and Preliminary Post-Mortem Analysis of a Solid Oxide Cell Stack with 20,000 h of Operation, J. Electrochem. Soc. 165 (2018) F38–F45. https://doi.org/10.1149/2.0541802jes.

[66] Y. Wang, C. Wu, B. Zu, M. Han, Q. Du, M. Ni, K. Jiao, Ni migration of Ni-YSZ electrode in solid oxide electrolysis cell: An integrated model study, Journal of Power Sources 516 (2021) 230660. https://doi.org/10.1016/j.jpowsour.2021.230660.

[67] H. Moussaoui, J. Laurencin, Y. Gavet, G. Delette, M. Hubert, P. Cloetens, T. Le Bihan, J. Debayle, Stochastic geometrical modeling of solid oxide cells electrodes validated on 3D reconstructions, Computational Materials Science 143 (2018) 262–276. https://doi.org/10.1016/j.commatsci.2017.11.015.

[68] J. Sehested, J.A.P. Gelten, S. Helveg, Sintering of nickel catalysts: Effects of time, atmosphere, temperature, nickel-carrier interactions, and dopants, Applied Catalysis A: General 309 (2006) 237–246. https://doi.org/10.1016/j.apcata.2006.05.017.

[69] D. Kennouche, Y.K. Chen-Wiegart, C. Riscoe, J. Wang, S.A. Barnett, Combined electrochemical and X-ray tomography study of the high temperature evolution of Nickel – Yttria Stabilized Zirconia solid oxide fuel cell anodes, Journal of Power Sources 307 (2016) 604–612. https://doi.org/10.1016/j.jpowsour.2015.12.126.

[70] M.P. Hoerlein, M. Riegraf, R. Costa, G. Schiller, K.A. Friedrich, A parameter study of solid oxide electrolysis cell degradation: Microstructural changes of the fuel electrode, Electrochimica Acta 276 (2018) 162–175. https://doi.org/10.1016/j.electacta.2018.04.170.

[71] V. Bilalis, B. Li, H.L. Frandsen, M. Chen, The Effect of Operating Temperature on Galvanostatic Operation of Solid Oxide Electrolysis Cells, ECS Trans. 111 (2023) 429. https://doi.org/10.1149/11106.0429ecst.

[72] S. Gao, J. Li, Z. Lin, Theoretical model for surface diffusion driven Ni-particle agglomeration in anode of solid oxide fuel cell, Journal of Power Sources 255 (2014) 144–150. https://doi.org/10.1016/j.jpowsour.2014.01.033.

[73] J. Laurencin, D. Kane, G. Delette, J. Deseure, F. Lefebvre-Joud, Modelling of solid oxide steam electrolyser: Impact of the operating conditions on hydrogen production, Journal of Power Sources 196 (2011) 2080–2093. https://doi.org/10.1016/j.jpowsour.2010.09.054.

[74] S.H. Chan, K.A. Khor, Z.T. Xia, A complete polarization model of a solid oxide fuel cell and its sensitivity to the change of cell component thickness, Journal of Power Sources 93 (2001) 130–140. https://doi.org/10.1016/S0378-7753(00)00556-5.

[75] A.N. Tabish, H.C. Patel, P. Chundru, J.N. Stam, P.V. Aravind, An SOFC anode model using TPB-based kinetics, International Journal of Hydrogen Energy 45 (2020) 27563–27574. https://doi.org/10.1016/j.ijhydene.2020.07.037.

[76] K. Miyoshi, H. Iwai, M. Kishimoto, M. Saito, H. Yoshida, Chromium poisoning in (La,Sr)MnO_3 cathode: Three-dimensional simulation of a solid oxide fuel cell, Journal of Power Sources 326 (2016) 331–340. https://doi.org/10.1016/j.jpowsour.2016.06.110.

[77] Z. Duan, M. Yang, A. Yan, Z. Hou, Y. Dong, Y. Chong, M. Cheng, W. Yang, $Ba_{0.5}Sr_{0.5}Co_{0.8}Fe_{0.2}O_{3-\delta}$ as a cathode for IT-SOFCs with a GDC interlayer, Journal of Power Sources 160 (2006) 57–64. https://doi.org/10.1016/j.jpowsour.2006.01.092.

[78] S.J. Kim, K.J. Kim, G.M. Choi, Effect of $Ce_{0.43}Zr_{0.43}Gd_{0.1}Y_{0.04}O_{2-\delta}$ contact layer on stability of interface between GDC interlayer and YSZ electrolyte in solid oxide electrolysis cell, Journal of Power Sources 284 (2015) 617–622. https://doi.org/10.1016/j.jpowsour.2015.02.156.

[79] F. Wang, M. Nishi, M.E. Brito, H. Kishimoto, K. Yamaji, H. Yokokawa, T. Horita, Sr and Zr diffusion in LSCF/10GDC/8YSZ triplets for solid oxide fuel cells (SOFCs), Journal of Power Sources 258 (2014) 281–289. https://doi.org/10.1016/j.jpowsour.2014.02.046.

[80] E. Lay-Grindler, J. Laurencin, J. Villanova, I. Kieffer, F. Usseglio-Viretta, T.L. Bihan, P. Bleuet, A. Mansuy, G. Delette, Degradation Study of the $La_{0.6}Sr_{0.4}Co_{0.2}Fe_{0.8}O_3$ Solid Oxide Electrolysis Cell (SOEC) Anode after High Temperature Electrolysis Operation, ECS Trans. 57 (2013) 3177. https://doi.org/10.1149/05701.3177ecst.

[81] J.F. Moulder, W.F. Stickle, P.E. Sobol, K.D. Bomben, Handbook of X-ray Photoelectron Spectroscopy, Perkin-Elmer Corporation 40 (1992) 221.

[82] P.A.W. van der Heide, Photoelectron binding energy shifts observed during oxidation of group IIA, IIIA and IVA elemental surfaces, Journal of Electron Spectroscopy and Related Phenomena 151 (2006) 79–91. https://doi.org/10.1016/j.elspec.2005.11.001.

[83] J.-C. Dupin, D. Gonbeau, P. Vinatier, A. Levasseur, Systematic XPS studies of metal oxides , hydroxides and peroxides, Physical Chemistry Chemical Physics 2 (2000) 1319–1324. https://doi.org/10.1039/A908800H.

[84] E. Mutoro, E.J. Crumlin, H. Pöpke, B. Luerssen, M. Amati, M.K. Abyaneh, M.D. Biegalski, H.M. Christen, L. Gregoratti, J. Janek, Y. Shao-Horn, Reversible Compositional Control of Oxide Surfaces by Electrochemical Potentials, J. Phys. Chem. Lett. 3 (2012) 40–44. https://doi.org/10.1021/jz201523y.

[85] A.K. Opitz, C. Rameshan, M. Kubicek, G.M. Rupp, A. Nenning, T. Götsch, R. Blume, M. Hävecker, A. Knop-Gericke, G. Rupprechter, B. Klötzer, J. Fleig, The Chemical Evolution of the $La_{0.6}Sr_{0.4}CoO_{3-\delta}$ Surface Under SOFC Operating Conditions and Its Implications for Electrochemical Oxygen Exchange Activity, Top Catal 61 (2018) 2129–2141. https://doi.org/10.1007/s11244-018-1068-1.

[86] J.C. De Vero, K. Develos-Bagarinao, H. Kishimoto, T. Ishiyama, K. Yamaji, T. Horita, H. Yokokawa, Enhanced stability of solid oxide fuel cells by employing a modified cathode-interlayer interface with a dense $La_{0.6}Sr_{0.4}Co_{0.2}Fe_{0.8}O_{3-\delta}$ thin film, Journal of Power Sources 377 (2018) 128–135. https://doi.org/10.1016/j.jpowsour.2017.12.010.

[87] K. Develos-Bagarinao, R.A. Budiman, S.-S. Liu, T. Ishiyama, H. Kishimoto, K. Yamaji, Evolution of cathode-interlayer interfaces and its effect on long-term degradation, Journal of Power Sources 453 (2020) 227894. https://doi.org/10.1016/j.jpowsour.2020.227894.

[88] F. Wang, M.E. Brito, K. Yamaji, D.-H. Cho, M. Nishi, H. Kishimoto, T. Horita, H. Yokokawa, Effect of polarization on Sr and Zr diffusion behavior in LSCF/GDC/YSZ system, Solid State Ionics 262 (2014) 454–459. https://doi.org/10.1016/j.ssi.2014.04.002.

[89] M. Izuki, M.E. Brito, K. Yamaji, H. Kishimoto, D.-H. Cho, T. Shimonosono, T. Horita, H. Yokokawa, Interfacial stability and cation diffusion across the LSCF/GDC interface, Journal of Power Sources 196 (2011) 7232–7236. https://doi.org/10.1016/j.jpowsour.2010.11.013.

[90] A.L. Shaula, V.V. Kharton, F.M.B. Marques, A.V. Kovalevsky, A.P. Viskup, E.N. Naumovich, Oxygen permeability of mixed-conducting composite membranes: effects of phase interaction, J Solid State Electrochem 10 (2006) 28–40. https://doi.org/10.1007/s10008-005-0650-1.

[91] J.W. Druce, J. Kilner, Composite Ceramic Membranes for Oxygen Separation in Carbon Capture and Storage Systems, ECS Trans. 16 (2009) 327. https://doi.org/10.1149/1.3242247.

[92] H.Y. Tu, Y. Takeda, N. Imanishi, O. Yamamoto, $Ln_{0.4}Sr_{0.6}Co_{0.8}Fe_{0.2}O_{3-\delta}$ (Ln=La, Pr, Nd, Sm, Gd) for the electrode in solid oxide fuel cells, Solid State Ionics 117 (1999) 277–281. https://doi.org/10.1016/S0167-2738(98)00428-7.

[93] O. Celikbilek, G. Sassone, M. Prioux, D.F. Sanchez, A. Benayad, M. Hubert, B. Morel, J. Vulliet, A. Léon, J. Laurencin, Long-Term Tests and Advanced Post-Test Characterizations of the Oxygen Electrode in Solid Oxide Electrolysis Cells, ECS Trans. 111 (2023) 211. https://doi.org/10.1149/11106.0211ecst.

[94] T.L. Pham, J.H. Yu, J.-S. Lee, Conductivity Transitions of $La_{0.7}Sr_{0.3}MnO_{3\pm\delta}$ and $La_{0.6}Sr_{0.4}Co_{0.2}Fe_{0.8}O_{3-\delta}$ in $Ce_{0.9}Gd_{0.1}O_{2-\delta}$ Matrix for Dual-Phase Oxygen Transport Membranes, Crystals 11 (2021) 712. https://doi.org/10.3390/cryst11060712.

[95] J.H. Joo, G.S. Park, C.-Y. Yoo, J.H. Yu, Contribution of the surface exchange kinetics to the oxygen transport properties in $Gd_{0.1}Ce_{0.9}O_{2-\delta}$–$La_{0.6}Sr_{0.4}Co_{0.2}Fe_{0.8}O_{3-\delta}$ dual-phase membrane, Solid State Ionics 253 (2013) 64–69. https://doi.org/10.1016/j.ssi.2013.08.038.

[96] J.H. Joo, K.S. Yun, Y. Lee, J. Jung, C.-Y. Yoo, J.H. Yu, Dramatically Enhanced Oxygen Fluxes in Fluorite-Rich Dual-Phase Membrane by Surface Modification, Chem. Mater. 26 (2014) 4387–4394. https://doi.org/10.1021/cm501240f.

[97] F. Baiutti, F. Chiabrera, M. Acosta, D. Diercks, D. Parfitt, J. Santiso, X. Wang, A. Cavallaro, A. Morata, H. Wang, A. Chroneos, J. MacManus-Driscoll, A. Tarancon, A high-entropy manganite in an ordered nanocomposite for long-term application in solid oxide cells, Nat Commun 12 (2021) 2660. https://doi.org/10.1038/s41467-021-22916-4.

[98] W. Lee, B. Yildiz, Factors that Influence Cation Segregation at the Surfaces of Perovskite Oxides, ECS Trans. 57 (2013) 2115. https://doi.org/10.1149/05701.2115ecst.

[99] Z. Lu, S. Darvish, J. Hardy, J. Templeton, J. Stevenson, Y. Zhong, $SrZrO_3$ Formation at the Interlayer/Electrolyte Interface during $(La_{1-x}Sr_x)_{1-\delta}Co_{1-y}Fe_yO_3$ Cathode Sintering, J. Electrochem. Soc. 164 (2017) F3097. https://doi.org/10.1149/2.0141710jes.

[100] E. Ostrovskiy, Y.-L. Huang, E. D. Wachsman, Effects of surface chemical potentials on cation segregation, Journal of Materials Chemistry A 9 (2021) 1593–1602. https://doi.org/10.1039/D0TA08850A.

[101] E. Bucher, W. Sitte, Long-term stability of the oxygen exchange properties of $(La,Sr)_{1-z}(Co,Fe)O_{3-\delta}$ in dry and wet atmospheres, Solid State Ionics 192 (2011) 480–482. https://doi.org/10.1016/j.ssi.2010.01.006.

[102] R.R. Liu, S.H. Kim, S. Taniguchi, T. Oshima, Y. Shiratori, K. Ito, K. Sasaki, Influence of water vapor on long-term performance and accelerated degradation of solid oxide fuel cell cathodes, Journal of Power Sources 196 (2011) 7090–7096. https://doi.org/10.1016/j.jpowsour.2010.08.014.

[103] D. Zhang, M.L. Machala, D. Chen, Z. Guan, H. Li, S. Nemsak, E.J. Crumlin, H. Bluhm, W.C. Chueh, Hydroxylation and Cation Segregation in $(La_{0.5}Sr_{0.5})FeO_{3-\delta}$ Electrodes, Chem. Mater. 32 (2020) 2926–2934. https://doi.org/10.1021/acs.chemmater.9b05151.

Chapter conclusions

This chapter comprised the study of the cell degradation in SOEC mode under dry air, including the study of the effect of operating temperature on the cell degradation.

The evolution of the voltage in the durability curves was found to be more pronounced when decreasing the operating temperature. As discussed in the chapter, this refers as to the apparent degradation and it is due to the thermally activated behaviour of the electrodes activation overpotential. Therefore, a reference temperature was chosen to investigate the intrinsic degradation in the electrochemical response of the cell. The EIS diagrams put in evidence a clear evolution mainly in the HF arc and a limited change for the MF and LF arcs, also reported in the **Appendix A**. As an additional value, here it was shown that the intrinsic degradation was accelerated with increasing the operating temperature. More specifically, both the series resistance and the HF arc related resistance increased with the operating temperature. These changes in the EIS were attributed to the microstructural evolution of the hydrogen electrode. The post-test characterizations confirmed this finding and enabled estimating the ohmic losses attributed to the Ni migration, which was found to be promoted by the increased operating temperature. From the rough estimation, the Ni migration should explain most of the increase in the series resistance. In all the samples, no SZOs were detected possibly due to the operation under dry air or to the presence of the IDL. Regarding the oxygen electrode, no significant degradation was highlighted by the various post-test characterization techniques, aside from a slight Sr segregation that increased with increasing the operating temperature. In addition, it should be considered that already in the Reference sample, an inter-diffusion across all the cell layers was highlighted by the various post-test observations. For example, tt is worth noting that an intermixing between LSCF and GDC phases was evidenced by APT and STEM-EDS. More specifically, Ce and Gd were found inside the LSCF, already in the Reference sample. This feature could possibly have an impact on the cell durability, pointing out the relevance of the manufacturing conditions on the material stability.

To summarize, the cells degradation in SOEC mode under dry air was found to be dominated by the microstructural evolution of the hydrogen electrode, including Ni migration and Ni coarsening. A rather stable behaviour was found in the oxygen electrode with only slight Sr segregation. Furthermore, the studied cells undergone an evident elemental inter-diffusion across the various layers of the cell during the manufacturing. The operating temperature was found to promote the degradation in terms of microstructural evolution in the hydrogen electrode and, even if limited, in terms of Sr segregation in the oxygen electrode.

5. Long-term tests and post-test characterizations of SOCs aged in SOEC/SOFC mode under humid air

This chapter comprises the long-term tests and the post-test characterizations carried out on the cells aged under humid air in both SOEC and SOFC modes. The purposes of the chapter are the investigation of the effect of humid air and operating mode on the cell performance and material degradation.

Four long-term tests are performed at 800 °C for 1000 h: three tests in SOEC mode at -1 $A \cdot cm^{-2}$ and SC = 64%, under different air condition (dry, 3% and 8% humidity), and one test in SOFC mode at +1 $A \cdot cm^{-2}$ and FU = 64%, under 8% humid air. The evolution of the electrochemical response of the cell is evaluated in terms of durability curves and EIS. The cell degradation is investigated by various post-test characterization techniques, covering the microstructural, chemical and crystallographic aspects. The work done on this chapter has been submitted in the Journal of The Electrochemical Society (2024) (1).

References

1. G. Sassone, O. Celikbilek, M. Hubert, K. Develos-Bagarinao, A. Benayad, B. Morel, A. Léon, and J. Laurencin, Journal of The Electrochemical Society (2024).

Impact of Air Moisture and Operating Mode on the Degradation of Solid Oxide Cells

Giuseppe Sassone[a], Ozden Celikbilek[a], Maxime Hubert[a], Katherine Develos-Bagarinao[b], Anass Benayad[c], Bertrand Morel[a], Aline Léon[d], Jérôme Laurencin[a]

[a] Univ. Grenoble Alpes, CEA, Liten, DTCH, 38000 Grenoble, France
[b] Global Zero Emission Research Center, AIST, Tsukuba, Japan
[c] Univ. Grenoble Alpes, CEA, Liten, DTNM, 38000 Grenoble, France
[d] European Institute for Energy Research (EIFER), Emmy-Noether Strasse 11, 76131 Karlsruhe, Germany

Abstract

To study the impact of humid air on the solid oxide cell durability, long-term tests of 1000 h are performed in dry air condition and with a water content of 3% and 8% at 800°C and +/-1 A.cm^{-2}. The cell is made of a $La_{0.6}Sr_{0.4}Co_{0.2}Fe_{0.8}O_{3-\delta}$-$Ce_{0.8}Gd_{0.2}O_{2-\delta}$ (LSCF-GDC) oxygen electrode, a GDC diffusion barrier layer, an $Y_{0.16}Zr_{0.84}O_{1.92}$ (YSZ) electrolyte and a Ni-YSZ hydrogen electrode. In electrolysis mode, the degradation rate increases with increasing the water content in the air. Besides, the degradation rate is higher under electrolysis current than in fuel cell mode. At the highest level of humidity in electrolysis mode, the addition of water in the air affects the series and polarisation resistances in the impedance spectra. In this case, conversely to the dry condition, the post-test characterizations have revealed that the Ni migration is promoted at the cell outlet. Moreover, the LSCF decomposition is aggravated by the humid condition especially in electrolysis mode at the cell inlet. In this zone, it leads to the formation of a quasi-dense SrO phase at the top of the current collecting layer. Such insulating layer could induce a current redistribution in the cell explaining the higher Ni migration at the cell outlet.

1. Introduction

Solid oxide cells (SOCs) are high-temperature electrochemical devices. Among their several advantages, they can achieve high efficiencies without the use of expensive electro-catalysts. Thanks to their reversibility, the same system can be operated either in fuel cell mode (SOFC) for electricity production or in electrolysis mode (SOEC) for hydrogen production. This technology could therefore be used to balance the fluctuations between electricity production and consumption when using intermittent renewable energy sources. The SOCs could thus play a key role in the transition towards a fossil-free energy market.

A typical SOC consists of a dense electrolyte in yttria-stabilized zirconia (YSZ) sandwiched between two porous electrodes. The hydrogen electrode is usually a Ni-YSZ cermet, while the oxygen electrode is made of $La_{1-x}Sr_xCo_{1-y}Fe_yO_{3-\delta}$ (LSCF) material. A diffusion barrier layer of $Gd_xCe_{1-x}O_{2-\delta}$ (GDC) is generally added between the electrolyte and the oxygen electrode to limit the reactivity.

For large scale industrial application, the SOCs durability is still insufficient to maintain high efficiency over the requested lifetime of ca. 80 000 – 90 000 h [1,2]. Indeed, the SOCs suffer from several degradation phenomena that occur in the different cell layers. In the hydrogen electrode, a Ni particle coarsening is usually observed after ageing in both SOFC and SOEC modes [3]. Although the agglomeration tends to slow down after long-term operating time, it can explain a significant part of the performance degradation [3]. In addition, a substantial Ni migration away from the electrolyte interface occurs in SOEC mode [4–8]. It results in a Ni depletion in the active functional layer which induces an increase in the cell ohmic losses and polarisation resistance [9,10].

In the oxygen electrode, the LSCF decomposes upon operation with the release of cations from the perovskite structure [11–15]. More particularly, Sr segregates to the surface leading to the formation of an insulating layer made of strontium oxide-based compounds such as SrO [12,16]. This passivating film hinders the oxygen surface exchange between the gas phase and the material [14] and decreases the oxygen bulk diffusion coefficient [17]. Both phenomena are known to affect significantly the cell performances by increasing the electrode polarization resistance [18]. Additionally, LSCF can react with the electrolyte during the electrode sintering at high temperature to form $SrZrO_3$ (SZO), which can potentially evolve upon operation [19–24]. This insulating phase is reported to affect the cell performance when it forms a continuous layer [25,26]. Another phenomenon occurring near the GDC/YSZ interface is the formation of

an inter-diffusion layer (IDL) during the cell fabrication [27–31]. Despite the IDL is reported to cause additional ohmic losses in the cell [32], some authors reported that it could act as a protective layer against the formation of SZO during fabrication [31] and ageing [33].

The impact of the operating parameters, such as the temperature [15,34] and the operating mode [35–39], on the LSCF decomposition is still unclear. Regarding the role of polarization, some authors found a higher phase demixing for an operation in SOEC mode (i.e. anodic polarisation for the oxygen electrode) [35,36]. Conversely, other studies reported a mitigation (or even a suppression) of Sr segregation under anodic polarisation whereas an accelerated degradation was highlighted under cathodic polarization [37,40]. Air moisture can also have a significant impact on the oxygen electrode degradation [41]. Indeed, some authors have shown that a higher content of water molecules in the air leads to a stronger LSCF decomposition with formation of a SrO secondary phase that decreases the cell performances [41–45]. Moreover, the interaction of Sr surface-segregated species with water molecules from the air results in the formation of $Sr(OH)_2$ volatile species [46]. Such species can easily diffuse in the gas phase and reach other reaction sites where secondary phases can form, causing an additional loss in the cell performance [47,48]. Hence, the presence of water promotes both the LSCF decomposition and the reactivity among the cell layers. It is worth noting that only few studies have been dedicated to study the impact of humidity on the cell durability under current and all of them have been carried out in SOFC mode [41,42]. Therefore, the impact of the anodic polarisation under humidified condition still needs to be addressed.

This work aims to evaluate the effect of humid air and operating mode on the cell performance, focusing on the oxygen electrode degradation. To this end, four long-term tests were performed at 800 °C for 1000 h in different air conditions and in both SOEC and SOFC modes. Three tests were carried out in SOEC mode at -1 $A \cdot cm^{-2}$ and 64% steam conversion (SC) under dry air, 3% and 8% humid air (amount of water vapour defined as the ratio between the partial pressure of H_2O and the total pressure). Additionally, one test was conducted in SOFC mode at +1 $A \cdot cm^{-2}$ and 64% fuel utilisation (FU) under 8% humid air. The electrochemical response of the cells was evaluated by electrochemical impedance spectroscopy (EIS) performed in reference conditions. The material degradation was investigated using different post-test characterizations, which enable assessing the microstructural, chemical and crystallographic changes in the aged cells.

2. Materials and methods

Cell description. The hydrogen electrode supported cells used in the study have been already thoroughly described in [4,33]. The cells had a circular shape with an active surface area of 9.08 cm^2. The porous oxygen electrode consisted of a ca. 20 µm $La_{0.6}Sr_{0.4}Co_{0.2}Fe_{0.8}O_{3-\delta}$-$Ce_{0.8}Gd_{0.2}O_{2-\delta}$ (LSCF-GDC) functional layer (FL) on which a ca. 20 µm LSCF current collecting layer (CCL) was deposited. It can be noted that the LSCF powder used for the manufacturing exhibits a slight A-site deficiency of ca. 1% that was measured by inductively coupled plasma mass spectroscopy (ICP-MS) [33]. A thin GDC barrier layer (BL) of ca. 3 µm was added in between the oxygen electrode and a dense electrolyte made of $Y_{0.16}Zr_{0.84}O_{1.92}$ (8YSZ), which was ca. 8 µm thick. The porous hydrogen electrode was composed of a ca. 25 µm Ni-8YSZ functional layer and a thick ca. 280 µm Ni-3YSZ substrate.

2.1 Long-term tests and electrochemical characterizations

Experimental setup. The test rig used in this work has been already detailed in [33]. The main features of the setup are reported hereafter. The in-house test bench consists of a furnace, in which a metallic housing holds the cell to be tested. In order to avoid a gas leakage from the fuel compartment, a glass ceramic sealant is deposited on the cell periphery (Schott G018-311) [11,49]. The inlet gas flows are measured by flow meters (Brooks SLA5850S) for both fuel and air sides, before being fed to the centre of the cell. A radial co-flow configuration is used for the gas distribution along the cell radius. The steam is supplied by a steam generator. Dry compressed air (ISO 8573-1 class [1:1:1]) is fed into the air compartment. For this study, a bubbler was added at the air side and the air was moistened by controlling the bubbler temperature. Hence, a moisture content of 3% and 8% was reached by saturating the air inlet flow rate in the bubbler at respectively 24 °C and 41.5 °C. It can be noted that a membrane made of a metallic porous media is used to produce fine and homogeneous bubbles. Moreover, the bubbler dimensions have been designed to achieve saturation vapour pressure at the chosen temperature in the air stream. The pipe carrying the humid air was heated to avoid any condensation before entering the furnace. The current distribution at the collectors of the electrodes is ensured by a Ni grid (100 meshes·cm^{-2}) and two gold grids (100 meshes·cm^{-2}), for the hydrogen and oxygen electrodes, respectively. It can be noted that a ceramic holder in alumina is used at the oxygen electrode side to prevent the Cr-poisoning, which is commonly

observed when using metallic Cr-based interconnects [50]. In order to lower the contact resistance, a mechanical load of 600 $g \cdot cm^{-2}$ is applied on the cell. Finally, the water contained in the gas exhausts from the fuel compartment is condensed at the outlet of the setup. The verification of the correct steam flow is done by weighing the water collected downstream the condenser.

Experimental protocol. The cell was first mounted in its housing inside the furnace. In order to form the glass seal, the cell was heated up to 860 °C at a ramp of 1 $°C \cdot min^{-1}$ and maintained at this temperature for 90 minutes. During the heating up and the glass sealing, 0.5 $NL \cdot h^{-1}$ of N_2 and 0.5 $NL \cdot h^{-1}$ of compressed dry air were fed to the hydrogen and oxygen electrodes, respectively. Such gas flow rate were then increased to 4 $NL \cdot h^{-1}$ at both electrodes to perform the Ni-YSZ cermet reduction, which was done at 800 °C. During the cermet reduction process, H_2 gas flow was gradually increased to replace N_2. Once the gas was composed of pure H_2, the electrode was swept under a H_2 flow of 4 $NL \cdot h^{-1}$ for 16 h to ensure the complete cermet reduction into Ni-YSZ. After this step, the initial electrochemical characterizations were carried out and, subsequently, the ageing test was started at the chosen operating conditions (temperature, current density, gas flows, etc.). At the end of the durability test, the setup was cooled down to room temperature with a ramp of 1 $°C \cdot min^{-1}$, feeding a mixture of N_2 and H_2 to the hydrogen electrode to avoid the cermet re-oxidation.

Long-term tests. The durability experiments were carried out in SOEC mode at 800°C for 1000 h in dry air conditions and in accelerated ageing conditions with humid air. Two moisture content of 3% and 8% are investigated by controlling the bubbler temperature at 24 °C and 41.5 °C, respectively. To investigate the effect of polarisation, an additional test was performed in SOFC mode for 1000 h using 8% humid air. All the tests were performed in galvanostatic mode, applying a current density of -1 $A \cdot cm^{-2}$ with 64% steam conversion (SC) in SOEC mode and +1 $A \cdot cm^{-2}$ with 64% fuel utilisation (FU) in SOFC mode. The gas mixture fed to the hydrogen electrode had compositions of 10/90 and 90/10 vol.% H_2/H_2O for SOEC and SOFC operation, respectively. The total inlet gas fluxes at the oxygen and hydrogen electrodes were 36 $NmL \cdot min^{-1} \cdot cm^{-2}$ and 12 $NmL \cdot min^{-1} \cdot cm^{-2}$, respectively. In this work, the cell after Ni reduction is labelled “Reference”. The cell aged in dry air in electrolysis mode is referred to as “SOECdry”. The cells aged in humid air at 3% and 8% in SOEC mode, as well as the one aged for 1000 h in SOFC are named as “SOEC3%”, “SOEC8%” and “SOFC8%”, respectively.

Electrochemical characterizations. For all the experiments, the cell voltage evolution was monitored during the ageing tests. In addition, electrochemical impedance spectra (EIS) were acquired at the beginning and the end of each experiment, using a potentiostat/galvanostat (Autolab PGSTAT-302N), a frequency response analyser (FRA) module, and a 20 A current booster. The EIS were obtained in the frequency range from 10^{-2} – 10^{4} Hz by applying a sinusoidal AC perturbation on the current density with an amplitude of 11 $mA \cdot cm^{-2}$. For a sake of comparison, all the diagrams were measured in the same reference operating conditions at open circuit voltage (OCV), 800 °C with 10/90 vol.% H_2/H_2O gas composition at the hydrogen electrode and dry air at the oxygen electrode. The raw data collected on the NOVA ver. 1.11 software were post-treated to remove the inductive phenomena due to cabling and wiring. For this purpose, the experimental spectra were fitted using an electric equivalent circuit model (EECM) using the Zview ver. 2.70 software, as already shown in [33]. After the fitting procedure, the corrected spectra were simulated without the inductance by extending the frequency range to 10^{-3} – 10^{6} Hz.

2.2 Post-test characterizations

SEM microstructural observations. For the microstructural characterizations, the electrodes were embedded in a polymer resin (Epofix, Denmark) to fill the porosity. The impregnated samples were polished using a 0.25 µm diamond spray. Finally, a carbon coating was applied to the polished cross-sections to prevent charging effects during observations. The electrode microstructures were examined by field emission scanning electron microscopy (FEG-SEM Zeiss Merlin, Germany) in backscattered electron (BSE) mode using an accelerating voltage of 2 kV and a working distance of approximately 5-10 mm. In addition to the polished cross-sections, fractographies of the oxygen electrode were observed in secondary electron (SE) mode (with an accelerating voltage of 2 kV and a working distance of 7 mm). Finally, Energy-dispersive X-ray spectroscopy (EDS) was also performed on the SOEC8% sample. Cartographies of La, Sr, Co, Fe, Ce, Gd and O elements were acquired in order to get their distribution in the oxygen electrode microstructure.

XPS and SIMS surface chemical characterizations. X-ray photoelectron spectroscopy (XPS) was used to study the surface chemistry of both the LSCF current collecting layer and the LSCF-GDC functional layer. For the CCL, the top surface of the electrode was analysed without any specific preparation. To access the active layer, the CCL and a part of the FL were removed

using a cutter blade. In this case, the prepared samples were characterised by SEM. The images of the remaining electrode revealed a rather smooth surface, suitable for the XPS measurements. The analyses were performed using a VersaProbe-II instrument from ULVAC-Phi, which operates at room temperature, under ultra-high vacuum conditions ($p < 10^{-7}$ Pa). A focused monochromatic Al Kα radiation (1486.6 eV) was used to generate a 4 mA emission current and a 200 μm X-ray beam diameter. In order to minimize the charging effect at the surface, electron and argon charge neutralizer guns were employed. The spectrometer calibrations was done with the gold photo-emission lines ($Au4f_{7/2}$ emission at 83.9 eV, with respect to Fermi level). The acquisition of survey spectra and core-level peaks was carried out with two different constant pass energies of 117.9 eV and 23.3 eV, respectively. Spectra calibration was done using the carbon C 1s emission at 285.0 eV as reference. The CasaXPS software [51] was used to fit the XPS spectra and to carry out quantitative analyses**.** The fitting of the peaks was performed with a combination of Lorentzian (20%) and Gaussian (80%) distributions, considering a Shirley background. An energy separation of 1.8 eV and a branching ratio of 1.5 were imposed between the Sr $3d_{5/2}$ and $3d_{3/2}$ doublets to fit the Sr core-level spectra. In order to consider the transmission function of the spectrometer, the X-ray source relative sensitivity factors (RSF) were exported from the MultiPak library.

The elemental distribution across the cell layers was studied with high-resolution secondary ion mass spectrometry (SIMS, NanoSIMS 50L, Ametek CAMECA). For this analysis, the porous electrodes were filled with a high-vacuum-compatible resin and subsequently polished with a diamond slurry. A Cs^+ source, with a ≈ 23 nA current and a ≈ 100 nm diameter, was used as primary ion beam to scan the cross-sections. The region of interests (ROIs) with raster areas of around 20 μm × 20 μm were taken at different positions across the cell. The secondary ion mass species coming from the cell were collected simultaneously using a multi-collection system. The image processing was performed on the WinImage ver. 4.6 software (Ametek, Cameca).

XRD structural characterizations. X-ray diffraction (XRD) was performed on the Reference and SOEC8% samples on top of the oxygen electrode CCL. The diffractograms were fitted by Le Bail method using FullProf software [52,53].

3. Results and discussion

3.1 Long-term tests and electrochemical characterizations

The long-term tests were carried out considering different steam content in air, i.e. from dry air to moisture content of 3 % and 8 %, at a temperature of 800 °C in SOEC mode at -1 $A \cdot cm^{-2}$ with a steam conversion (SC) of 64%. In order to study the impact of operating mode, a complementary durability test was performed in SOFC mode at +1 $A \cdot cm^{-2}$ with a fuel utilization (FU) of 64%, and 8 % humid air. The cell voltage upon operation is plotted as a function of the elapsed time for all the experiments in Figure 4-2a.

Regarding the tests performed in electrolysis mode, it can be noted that the initial voltage at t=0 h for the SOEC3% cell is slightly higher than the other SOEC tests. This difference in the initial performance can be attributed either to a scattering in the cell microstructure or to a higher electrical contact resistance for this test. Moreover, as usually observed in other studies [54–57], the durability curves for the cells tested in SOEC mode present two regimes. During an initial period of a few hundreds of hours, a rather fast cell voltage degradation occurred, while, in a second period, it slowed down and stabilized towards a rather constant rate. For instance, this behaviour is obvious for the tested cell SOEC3%, for which the durability curve exhibits a sharp increase in cell voltage during the first 500 h, followed by a stable and low voltage degradation in the second part of the test.

The voltage degradation rates (DRs) for the SOECdry, SOEC3% and SOEC8% cells are 9.4 $\%\cdot kh^{-1}$, 10.5 $\%\cdot kh^{-1}$ and 33.6 $\%\cdot kh^{-1}$, respectively (see Table 5-1). These results point out that the degradation is significantly aggravated by the addition of steam in the air for the cell operated in SOEC mode. This statement is consistent with the ageing tests available in the literature, which were performed under humid air in fuel cell mode [41,58].

Regarding the test carried out in fuel cell mode, a much lower voltage degradation rate of 2.1 $\%\cdot kh^{-1}$ is found compared to SOEC experiments. Indeed, the degradation rate for SOEC8% is around 16 times higher than SOFC8%. This impact of the operating mode on the cell durability has been already reported in many studies under dry condition [7,35,36].

The EIS at OCV were acquired for each test in the reference conditions (i.e. 800°C, 10/90 vol.% H_2/H_2O) before and after ageing. All the Nyquist plots of the impedance spectra are shown in

Figure 4-2b-e, while the DRs computed on the polarization (R_{pol}) and series (R_s) resistances are listed in Table 5-1.

For the cell tested at 3% of steam in electrolysis mode, the degradation on the polarization resistance is roughly similar to the one obtained in dry air condition (see Table 5-1). This finding suggests that this intermediate rate of air humidification is not sufficient to induce an additional degradation on R_{pol} compared to the dry condition. However, at 8% of humid air in SOEC mode (SOEC8%), the DR on R_{pol} (DR_{Rpol}) is roughly 9 times higher than the one obtained under dry air condition. Thus, an evident material deterioration is expected for this condition. By contrast, the R_{pol} evolution related to the test in SOFC mode at 8% of humid air (SOFC8%) remains much lower than the one carried out in the same air condition under electrolysis mode (SOEC8%). This observation suggests a strong impact of the operating mode on the electrode degradation under humidified conditions. In addition, it can be noted the DR_{Rpol} for SOFC8% is in the same order than the SOECdry. When using same conditions of temperature and current, it has been shown that the degradation is higher in electrolysis mode than in fuel cell mode [35]. Therefore, in agreement with previous works [58], it appears in our case that the addition of steam should accelerate the degradation also in SOFC.

It can be observed in Figure 4-2b-e that the impedance spectra are composed of three main arcs at high frequency (HF), mid-frequency (MF) and low frequency (LF). A multiscale physics-based model was used in a previous study [59] to identify the limiting processes at the origin of these contributions. Specifically, it was shown that the HF contribution is mainly related to the kinetics in the hydrogen electrode while the arc at the MF is due to the electrochemical processes in the oxygen electrode along with the gas diffusion in the support layer. The third arc at LF is associated to the gas conversion losses. A visual inspection of the spectra reveals a rather limited evolution of the MF contribution for all the cells, except the SOEC8%. This result would indicate that 3% of humid air tested over 1000 h is not enough to induce a significant degradation in the active functional layer of the oxygen electrode. However, a large increase in the MF contribution can be observed for the cell SOEC8%. This increase is estimated to be around 92% using the EECM used for the inductance correction (cf. section 0). In this specific condition, it becomes obvious that the oxygen electrode material has been affected by the long-term operation.

For the cells tested in SOEC mode, both the HF contribution and the ohmic resistance increase during operation. This change in the EIS is usually attributed to the Ni migration and coarsening arising in the hydrogen electrode, as discussed in other articles [9,10]. It can be noted that the

R_s evolution deduced from the EIS of the SOEC3% cell is lower than that of the SOECdry cell. This unexpected result can be explained by the lower initial performance measured for the SOEC3% probably due to a higher contact resistance. Hence, it is not possible to directly compare the R_s evolution of the SOEC3% test with the other experiments. Nevertheless, it is worth noting that the increase in the ohmic losses for the SOEC8% cell is much more pronounced than the one obtained under dry condition. This statement means that another degradation phenomenon induced by the wet condition occurs at the oxygen electrode (in addition to the aforementioned microstructural evolution in the hydrogen electrode). This phenomenon could be related to a decrease in the CCL electronic conductivity and/or an increase in the contact resistance at the oxygen electrode side. Finally, it can be noted a substantial increase in the high frequency arc related to the hydrogen electrode of the SOEC8% cell. This remark would thus indicate that the strong degradation of the oxygen electrode could impact the hydrogen electrode response.

Regarding the SOFC8% test, a slight increase in the R_s is observed. This result is unexpected since no Ni migration should occur upon operation for 1000 h in the SOFC mode as pointed out in many articles [4–8]. Therefore, the slight R_s evolution in the cell could be associated to the additional phenomenon mentioned above, which is suspected to occur in the oxygen electrode in presence of humidified air. However, its impact is much lower in SOFC mode compared to the SOEC operation.

From these results, the exposure to a higher water content in the air was confirmed to accelerate the degradation in the cells upon operation, particularly in SOEC mode. More specifically, the oxygen electrode performance is strongly affected by an operation with 8% of humid air.

Table 5-1. Cell performance degradation related to voltage, R_s and R_{pol} for the different tests.

Cells	Cell voltage degradation ($\%\cdot kh^{-1}$)	R_s degradation ($\%\cdot kh^{-1}$)	R_{pol} degradation ($\%\cdot kh^{-1}$)
SOECdry	9.4	45.4	3.4
SOEC3%	10.5	35.7	3.3
SOEC8%	33.6	181.8	28.1
SOFC8%	2.1	16.7	3.3

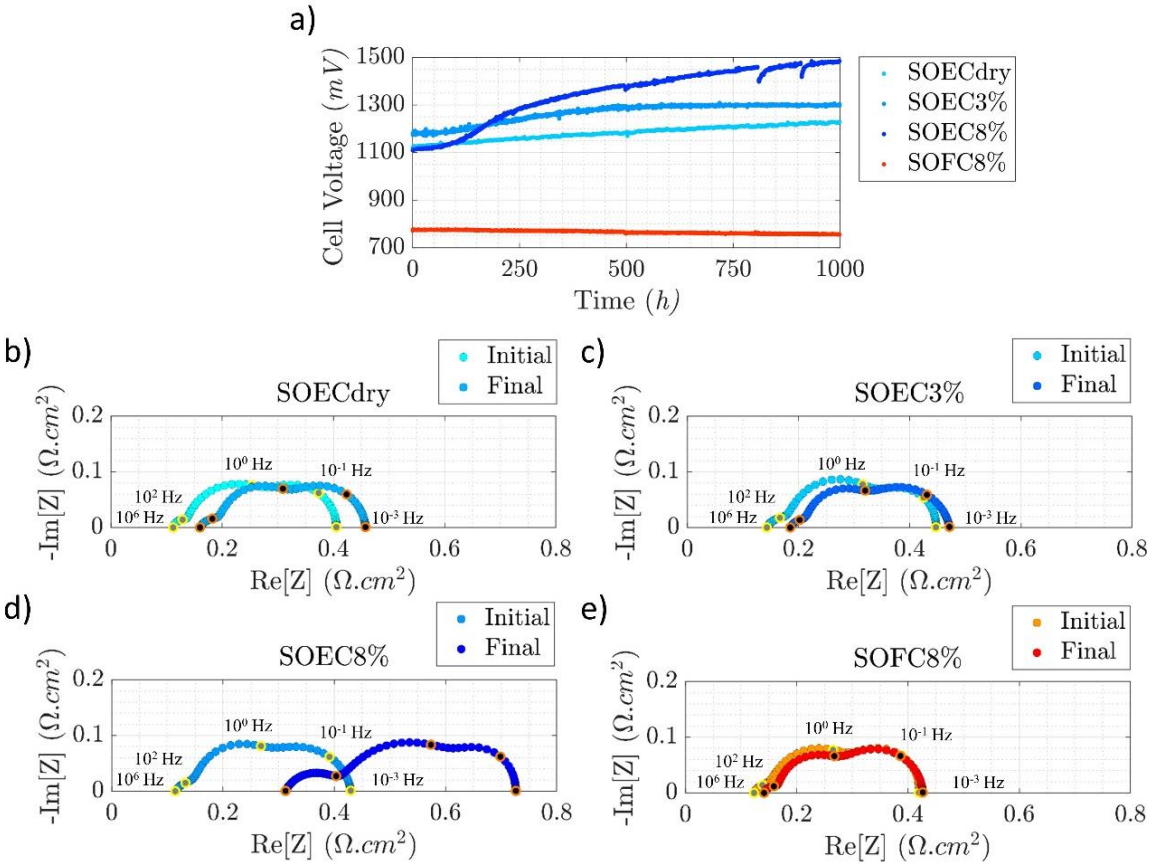

Figure 5-1. a) Durability curves showing the cell voltage evolution for the cells aged in SOEC mode at -1 A·cm^{-2}, 64% SC, 10/90 vol.% H_2/H_2O, 800 °C for 1000 h in dry air, 3% and 8% humid air. The cell aged in SOFC mode was operated at 1 A·cm^{-2}, 64% FU, 90/10 vol.% H_2/H_2O, 800 °C for 1000 h in 8% humid air. Nyquist plots b-e) show the impedance diagrams acquired at 800 °C before and after ageing under dry air, 3% and 8% humid air in SOEC, and under 8% humid air in SOFC, respectively.

3.2 Post-test characterizations

3.2.1 Hydrogen electrode

The SEM images taken at the hydrogen electrode/electrolyte interface are shown in Figure 5-2. For all the tested samples, the cermet microstructural evolution observed at cell inlet (i.e. cell centre) is compared to the cell outlet (i.e. cell periphery).

After ageing in SOEC mode under dry condition (Figure 5-2b), the Ni depletion is found to be much more pronounced at the cell inlet with respect to the Reference cell microstructure (Figure 5-2a). This result is in perfect agreement with a previous study performed on the same type of cell [33]. This behaviour was attributed to the higher current density at the cell inlet, where the gas are supplied [49]. Indeed, the Ni depletion is known to be driven by the electrode

overpotential, which depends on the local current distribution along the cell length [4,60]. Surprisingly, the opposite behaviour is observed for the cell aged in SOEC mode at 8% of humidity (SOEC8%). Indeed, a larger Ni depletion is detected at the cell outlet, whereas no significant Ni migration is found at the cell inlet (Figure 5-2d). For the SOEC3% sample, an intermediate microstructural evolution between the two previous cases is shown in Figure 5-2c, with a rather homogenous Ni depletion all along the cell radius (which seems to be slightly aggravated at the cell inlet). The unexpected distribution of Ni migration obtained for the samples aged in SOEC mode under humid air could be related to a change in the local current densities along the cell radius. Indeed, the higher Ni depletion at the cell outlet for SOEC8% would suggest a higher current density at the cell periphery. Hence, it can be suspected that the current is redistributed towards the cell outlet, leading to a stronger microstructural evolution in this region.

Concerning the SOFC8% sample, Figure 5-2e confirms that no Ni migration occurred during operation. As mentioned in section 0, it has been already reported that the Ni redistribution within the cermet is very limited during SOFC operation [4,7]. It can be noted that all these observations are coherent with the results from SIMS analyses reported in Figure S-C 1a.

The increase in the ohmic losses for the cell SOECdry (Figure 4-2b) is mainly explained by the Ni depletion observed within the cermet as discussed in [33]. For SOEC8%, the huge increase in the series resistance (which is 4 times the one under dry condition) cannot be explained by the cermet microstructure evolution alone. Indeed, the extent of the Ni depletion is roughly the same in the two samples except its repartition along the cell radius (which is reversed between the inlet and outlet). Therefore, the cermet microstructural observations suggest that another degradation phenomenon should occur at the oxygen electrode side for the SOEC8% sample. As no microstructural change is found for the cell SOFC8%, this additional degradation phenomenon in the oxygen electrode could be at the origin of the slight R_s increase for this sample.

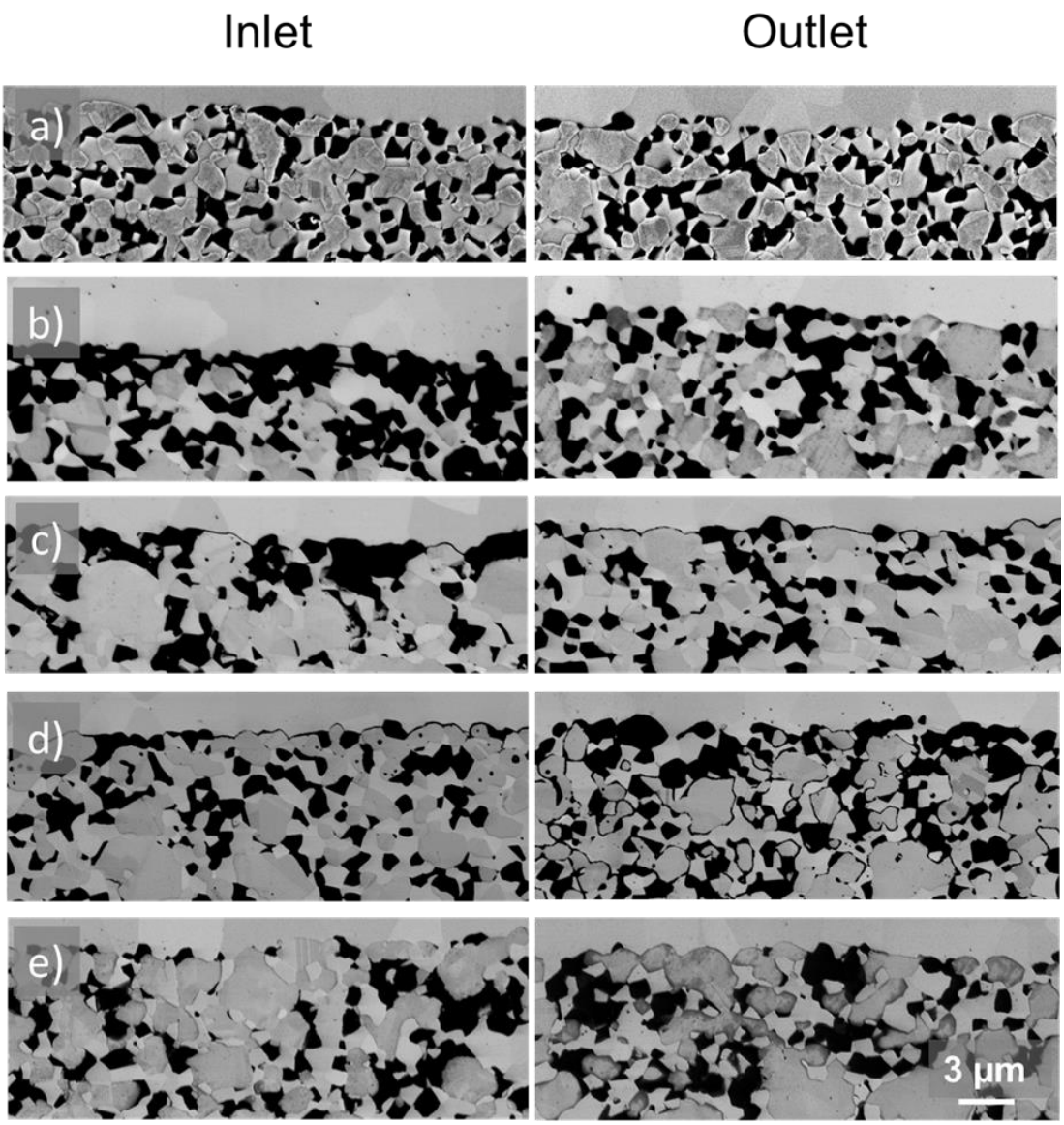

Figure 5-2. SEM observations of the hydrogen electrode at the interface with the electrolyte taken at the cell inlet and outlet for the a) Reference, b) SOECdry, c) SOEC3% and d) SOEC8%, e) SOFC8% samples.

3.2.2 Diffusion barrier layer and interfaces

The SEM images of the polished cross sections taken at the BL are shown in Figure 5-3 for all the samples. The elemental cartographies obtained by SIMS are reported in Figure S-C 1d-f for the same region of interest. It can be first noticed that Ni is observed inside the GDC BL after operation (Figure S-C 1a).

As already observed for this cell [33], the formation of an IDL is detected for all the tested samples. The IDL is related to an elemental inter-diffusion between GDC and YSZ as shown

in the SIMS analyses. It corresponds to a line of small grains at the interface between the electrolyte and the BL which are highlighted with red arrows in the SEM micrographs. It can be noted that the IDL was formed during the cell fabrication as it is already observed in the Reference cell. In this work, no significant evolution of the IDL is detected after ageing in good agreement with our previous study performed under dry condition [33].

SEM images of the Reference cell do not evidence any clear presence of dark grey contrast phases in the GDC BL, which are usually related to $SrZrO_3$ (Figure 5-3a) [35]. Besides, no supplementary secondary phases are detected after ageing even in humid air conditions (see Figure 5-3b-e). As reported previously, this behaviour can be attributed to the presence of the IDL that acts as a protective layer [31,33]. It should be considered that in our previous study on the same type of cells aged in dry air [33], the absence of SZO was possibly due either to the presence of the IDL or to the rather stable LSCF material under dry air. Thanks to this study on the effect of humid air on the cell degradation, the avoidance of such secondary phase formation can be attributed with greater confidence to the IDL.

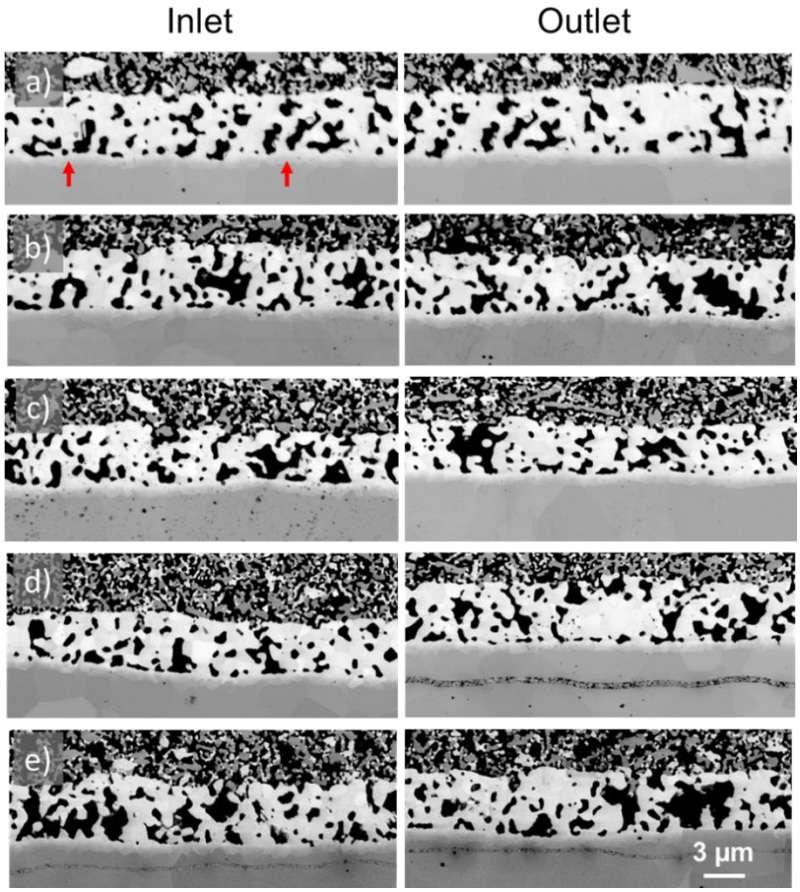

Figure 5-3. SEM observations of the BL for the a) Reference, b) SOECdry, c) SOEC3% and d) SOEC8%, e) SOFC8% samples.

3.2.3 Oxygen electrode

The SEM observations performed on the top of the LSCF CCL reveal the formation of a secondary phase in the samples aged under humid air conditions (highlighted by red arrows in Figure 5-4 and Figure 5-5). The evolution of this phase from the cell inlet up to the outlet is shown in Figure 5-4. Whatever the operating mode, it can be observed that the presence of this new phase is mostly detected at the cell centre where the air is introduced. This repartition of this new phase can be thus related to the high water content in air at the cell inlet. It would indicate a reactivity between LSCF and steam leading to strontium oxide based compounds at the cell inlet [41].

It is worth noting that the formation of this secondary phase results in a quasi-dense layer that spreads over a distance of 6-7 µm in the electrode depth for the SOEC8% sample (Figure 5-4d and Figure 5-5). For the SOEC3% sample, the quantity of this secondary phase appears to be much lower, although it is still clearly visible in the SEM image. For the SOFC8% cell, only a very small amount of this new phase is observed at the top of the CCL (cf. zoom in Figure S-C 3).

Additionally, it is possible to detect in Figure 5-4 some darker grey contrast particles distributed in the whole LSCF CCL for all the samples (they are highlighted by yellow arrows). However, the SEM characterizations have not revealed any evident evolution of these particles after operation. According to literature, this dark grey phase in the LSCF can be attributed to Co-Fe based oxides [41].

Finally, it is worth mentioning that no secondary phases have been detected in the FL even after operation with 8% of humid air.

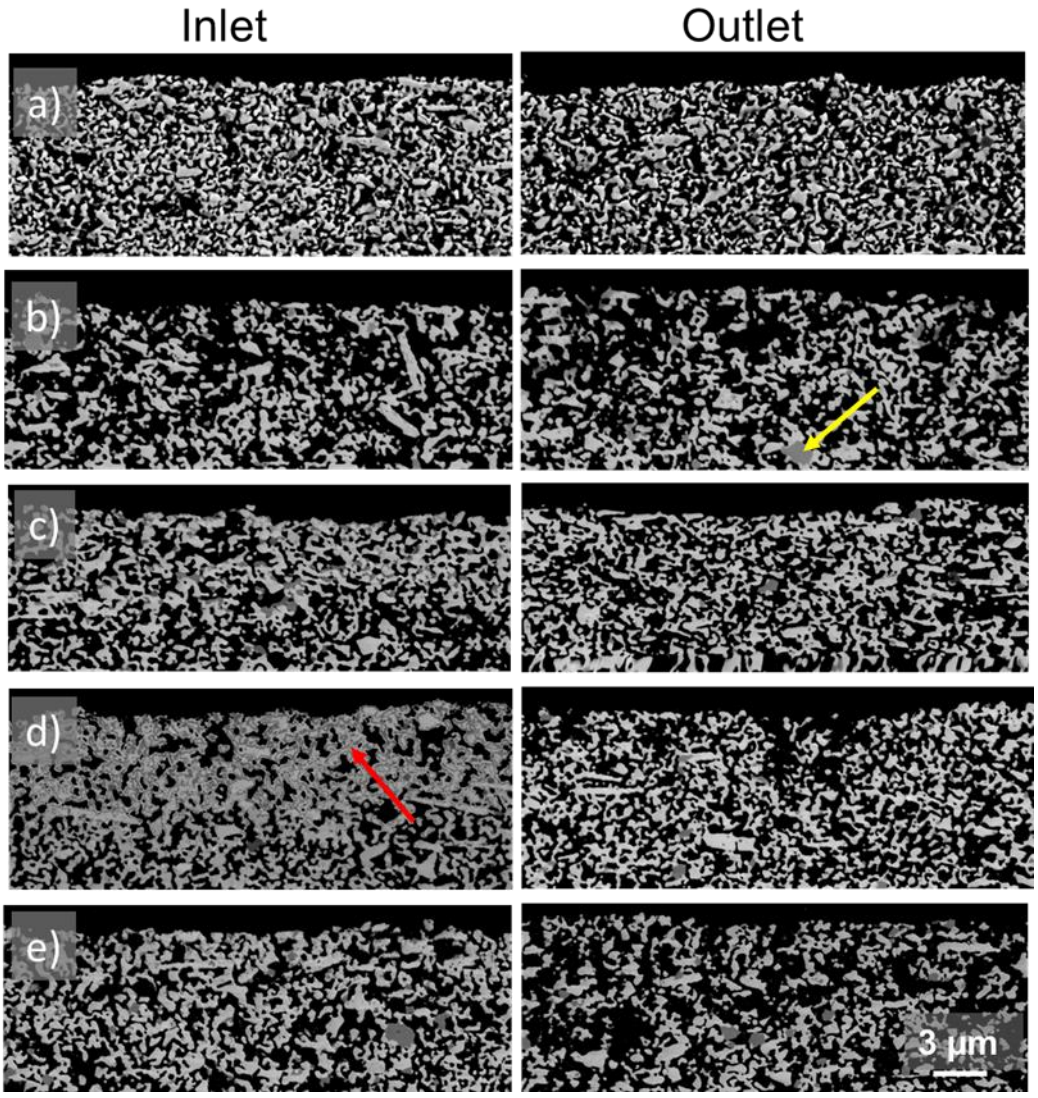

Figure 5-4. SEM observations of the oxygen electrode LSCF CCL for the a) Reference, b) SOECdry, c) SOEC3% and d) SOEC8%, e) SOFC8% samples.

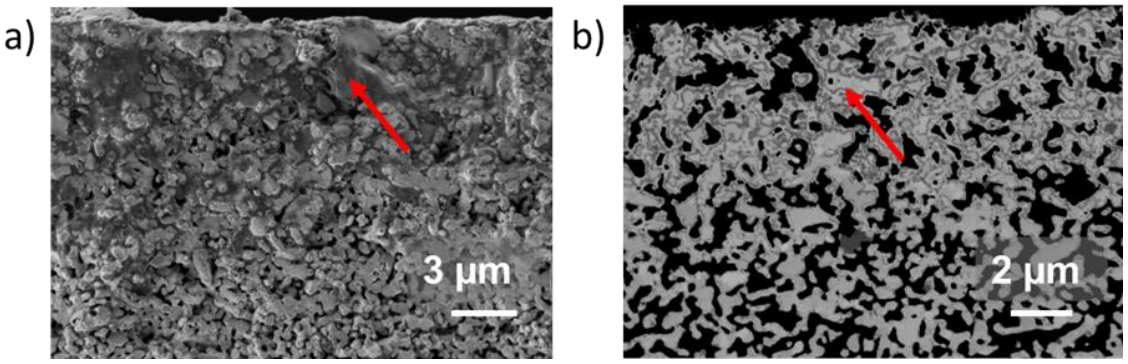

Figure 5-5. Magnified SEM a) fractographic and b) BSE observations on the SOEC8% sample.

In order to identify the secondary phase formed on top of the LSCF CCL, additional post-test characterizations are carried out on the Reference and SOEC8% samples. First, EDS analyses for the SOEC8% show that the top surface is enriched in Sr and O as shown by the black arrows in Figure 5-6. On the other hand, the maps for Co and Fe do not reveal any specific accumulation or change after operation. These results mean that the secondary phase formed on top of the CCL is probably made of strontium oxide (Figure 5-6). These results are coherent with the distribution of the chemical elements obtained by SIMS analysis (Figure S-C 2). As for the EDS maps, a high concentration of oxygen is observed in the layer. Moreover, some Co rich particles are clearly detected in the bulk of the CCL. Interestingly, Ni is also present in the CCL after ageing.

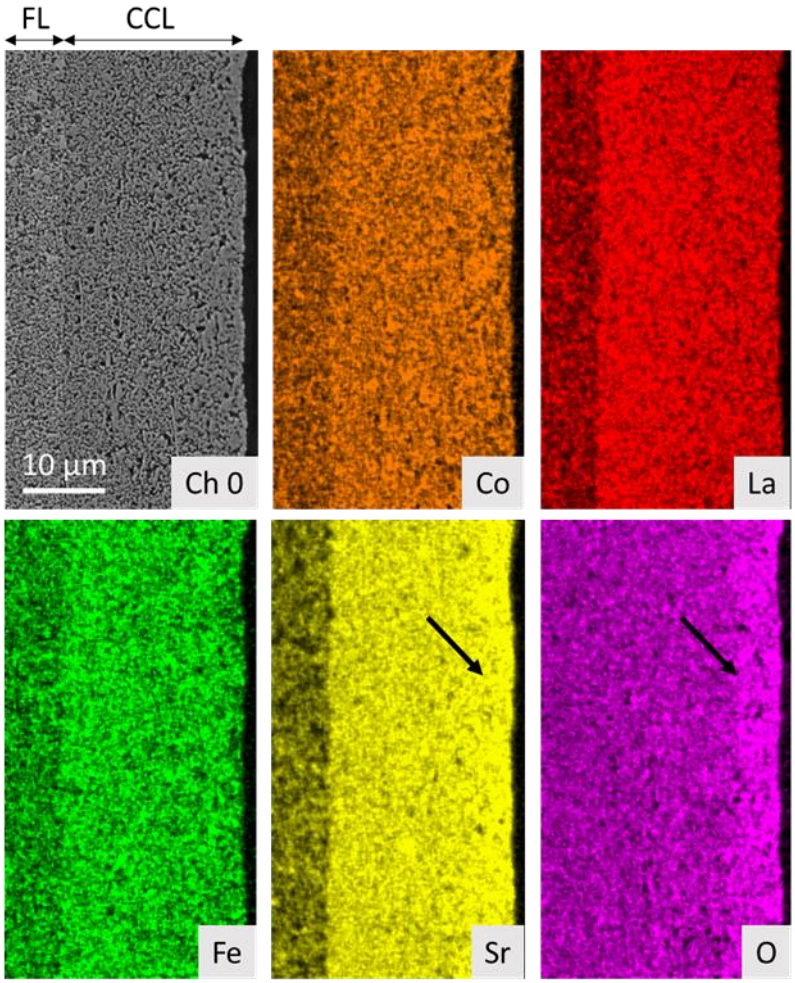

Figure 5-6. EDS analysis performed on the oxygen electrode LSCF CCL for the SOEC8% sample.

XRD analyses are performed on top of the LSCF CCL in order to assess the evolution in the crystallographic structure before and after ageing under wet condition (Figure 5-7). In the Reference sample, all the peaks are fitted by the LSCF phase. By contrast, the fitted XRD patterns related to the SOEC8% sample reveal the presence of SrO. For the same type of cell tested in dry condition up to 2000 h (at the same temperature and current density in SOEC mode) [33], it can be mentioned that no secondary phase is detected by XRD after ageing (Figure S-C 4). Therefore, the secondary phase observed in the SEM images after testing under wet condition can be mainly attributed to SrO. This statement is in good agreement with the results of Kim et al. [41], who observed stronger degradation under humid air (in SOFC mode) due to the promoted formation of SrO layer on the top of the LSCF. Besides, it is worth noting that the Sr release should also leads to the precipitation of some Co-rich particles as observed by SIMS in the bulk of the CCL.

Finally, in good agreement with the SIMS characterization, peaks attributed to the Ni phase appear on top of the LSCF CCL after ageing as shown in Figure 5-7b.

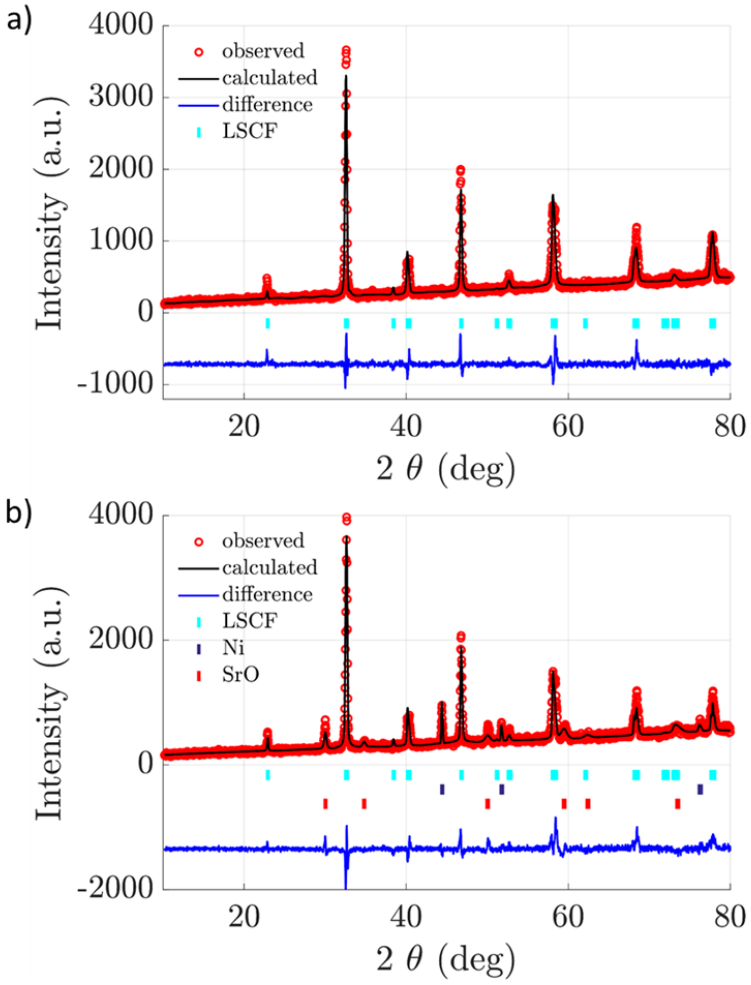

Figure 5-7. XRD pattern and fit obtained on the oxygen electrode LSCF CCL for the a) Reference and b) SOEC8% samples.

XPS is conducted on the outermost surface of the CCL and in the FL in complementarity with the EDS and XRD characterizations. Indeed, this technique allows the chemical environment analysis of surface species before and after ageing. Figure 5-8 displays the Sr 3d core-level spectra of the Reference, the SOEC8% and SOFC8% samples. The O 1s core-level spectra (Figure S-C 5) along with all the XPS fitting data (

Table S-C 1 – S-C 6) are reported in the Supporting information.

All spectra demonstrate a presence of lattice and surface components. In the Reference sample, the narrow peaks observed at the lower binding energy (BE) (O 1s: ~528.5-529.5 eV and Sr $3d_{5/2}$: ~131.8 eV) correspond to lattice components. The broader peaks observed at the higher BE (O 1s: ~531.4 eV and Sr $3d_{5/2}$: ~133.6 eV) correspond to surface components. The peak positions align with prior research identifying the surface layer as commonly consisting of SrO, $Sr(OH)_2$ and $SrCO_3$ [61].

In the aged samples, an additional surface oxygen peak is observed approximately at 530 eV in both the CCL and FL of the SOEC8% and CCL of the SOFC8% samples (Figure S-C 5). Since these cells are tested in humid air, it is reasonable to assume that this surface component can be attributed to hydroxyl bonds [62,63].

Unlike the other fits, the CCL of the SOEC8% displays a distinct third peak in the Sr 3d spectra, with the $3d_{5/2}$ component detected at around 134.0 eV. This has been seen simultaneously with a shift of the third O 1s component to a higher BE (532.3 eV). Taking into account the XRD and EDS findings and the very limited presence of carbonate peak in the C 1s core level spectra, the third surface-bound Sr peak could be attributed to strontium oxide related crystalline phase.

Figure 5-9 shows the ratio of surface-bound Sr to the sum of all Sr for all the samples collected on the CCL and the FL. As expected, it can be seen that the ratio remains almost unchanged in the two layers for the Reference cell. After ageing in SOFC and SOEC, the ratio becomes higher in the CCL compared to the FL, meaning that the Sr segregation is promoted at the top of the electrode. Besides, in the CCL, the ratio increases from ≈0.45 in the Reference sample to ≈0.72 and ≈0.98 in the SOFC8% and SOEC8% samples, respectively. In the FL, a similar increase can be observed, going from ≈0.47 to ≈0.58 and ≈0.84. These results indicate a substantial increase in the Sr segregation to the surface with ageing, SOEC8% sample being worse than SOFC8% sample. All these statements are in good agreement with SEM observations.

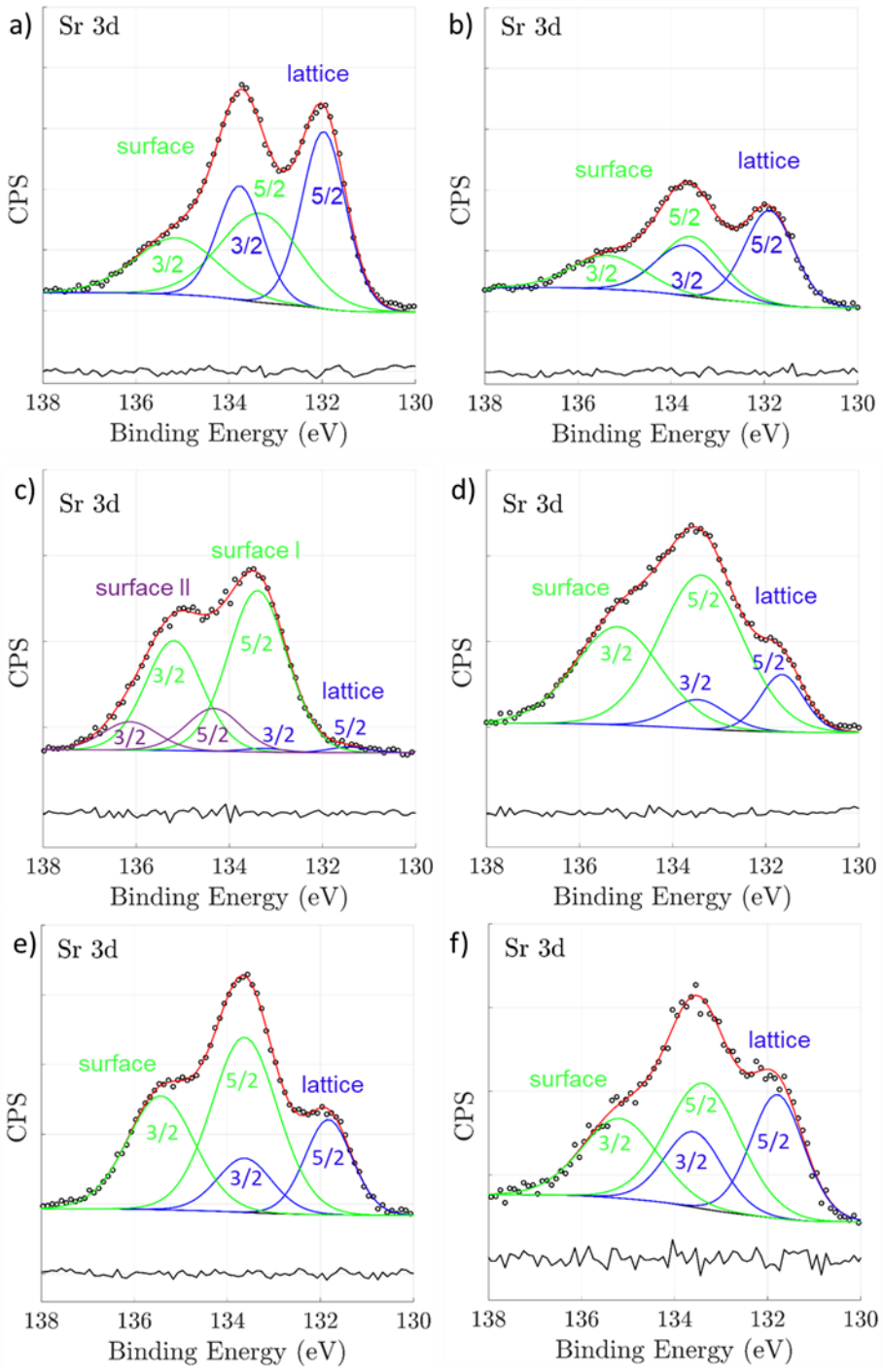

Figure 5-8. Sr 3d core-level spectra of a) Reference CCL, b) Reference FL, c) SOEC8% CCL, d) SOEC8% FL and e) SOFC8% CCL, f) SOFC8% FL.

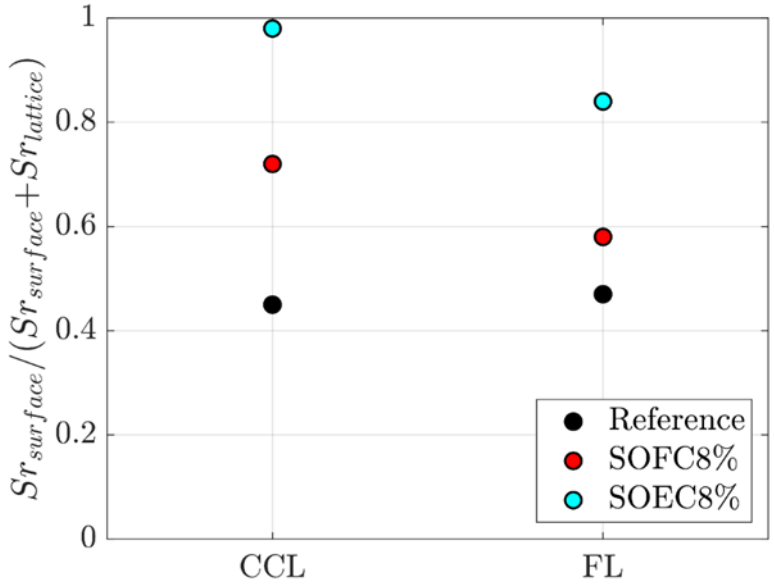

Figure 5-9. Ratio of surface-bound Sr to the sum of lattice-bound Sr and surface-bound Sr deduced from XPS analyses.

3.3 Discussion

The set of post-test characterizations performed on the oxygen electrode have shown a LSCF decomposition localised at the CCL, which is strongly aggravated in humid air condition. This decomposition is more pronounced at the cell inlet compared to the outlet. In addition, the decomposition is higher under electrolysis current with respect to the fuel cell mode. Thanks to XRD and XPS analyses, the secondary phase has been identified as a strontium oxide-based compound. As expected, Ni migration has been observed in the cell operated in electrolysis mode. However, a higher Ni depletion has been found at the cell outlet for the SOEC8%. This surprising result can be explained by the formation of a quasi-dense SrO layer on top of the oxygen electrode at the cell inlet. Indeed, considering the insulating nature of such phase ($3 \cdot 10^{-8}$ $\Omega \cdot cm^{-1}$ at 900 °C [64]), its presence is expected to affect the current distribution within the cell. Indeed, in normal condition for the pristine cell, the current density is higher at the cell inlet (centre), where the steam is supplied [49]. However, the formation of the insulating and almost dense layer on the top of the oxygen electrode is expected to hinder the current flow across the layers and the gas diffusion in the electrode. As a consequence, as depicted in Figure 5-10, the local current density is redistributed from the inlet to the outlet (knowing that the durability experiments are carried out in galvanostatic mode). Since the Ni migration should be driven by the activation overpotential, and hence by the local current density [4,65], the higher

current at the cell outlet should explain the higher Ni depletion in this zone, as illustrated in Figure 5-10b.

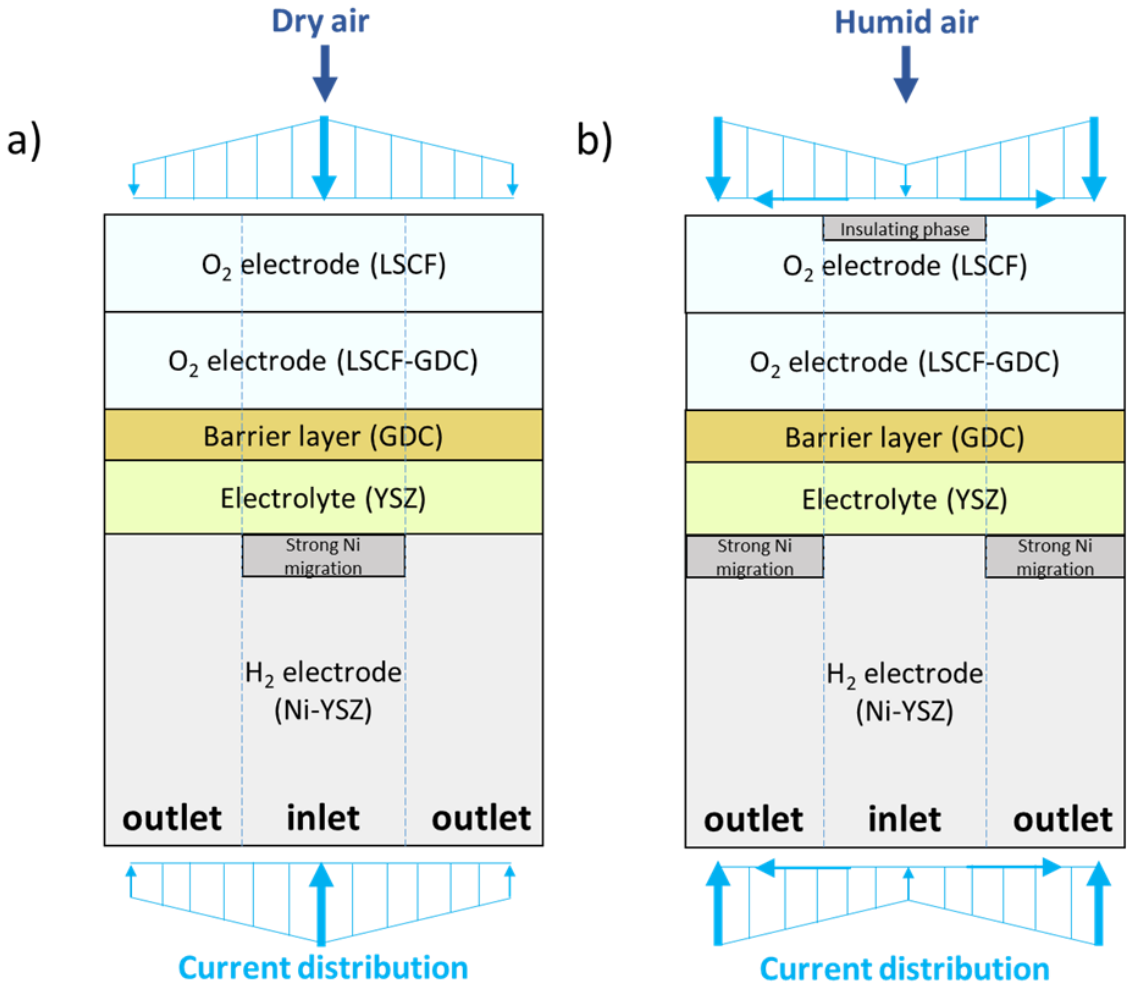

Figure 5-10. Schematics of the current distribution along the cell radius during SOEC operation under a) dry air and b) humid air.

It is worth noting that the results from post-test analyses are coherent with the electrochemical characterizations. First, the accelerated LSCF decomposition in humid air explains the higher degradation rate measured for the SOEC8% cell, as compared to the dry condition (SOECdry sample). Besides, the higher voltage degradation for the SOEC8% cell, with respect to the SOFC8% sample, is consistent with the higher demixing observed in electrolysis mode.

Regarding the impedance spectra for the SOEC8% sample, the increase in the MF contribution, which is related to the oxygen electrode, can be ascribed to the Sr segregation highlighted in both the CCL and FL after ageing (Figure 5-9). Additionally, in this operating condition, the promoted increase in the R_s can be attributed to both the Ni depletion at the hydrogen electrode,

but also to the SrO phase formed at top of the oxygen electrode. Indeed, this insulating layer would cause an additional electronic and contact resistance. Moreover, in this sample, the increase in the HF contribution associated to the hydrogen electrode is significantly higher than the dry condition. This result would not be explained by the Ni migration itself, as the depleted zone seems to be just reversed from the inlet to the outlet, when comparing the SOEC8% and SOECdry samples (see Figure 5-2). Therefore, it can be speculated that the SrO quasi-dense insulating phase would be sufficient to strongly hinder the current density at the cell inlet in such a way that the cell active surface area is lowered. According to this scenario, the series resistances along with the HF and MF contributions would be affected [66]. Finally, the slight increase in ohmic resistance detected for the SOFC8% should be related to the additional contact resistance induced by the formation of SrO, which is also observed for this cell (Figure 5-4). This statement is consistent with the study of Kim et al. [41], who tested cells in fuel cell mode under dry and wet conditions. Indeed, the authors have reported an evolution of both R_{pol} and R_s in the EIS, which was attributed to the accelerated oxygen electrode degradation under humidified air. More specifically, they proposed that the increase in R_s was related to the formation of secondary phases, such as SrO and Co-Fe-oxides, which have lower electronic conductivity as compared to the LSCF.

In this work, it has been shown that the addition of water molecules in the air accelerates the LSCF decomposition. However, the underlying mechanism that would explain the role of steam in the LSCF demixing is still unclear. It could be related to the formation of $Sr(OH)_2$ species adsorbed on the electrode surface under humid condition [35,41,46]. Besides, it has been found that this decomposition is aggravated under electrolysis mode. However, the effect of the operating mode on the LSCF demixing is not well understood.

During SOEC operation, the flow of supplied air is in the opposite direction to the produced oxygen. This could prevent the water molecules in the air to reach the functional layer close to the electrolyte. On the other hand, in SOFC mode, the gas flow should help the water molecule to penetrate in the depth of the electrode. Accordingly, we could expect a higher decomposition in SOFC mode, especially in the FL, which is contradictory with our experimental results.

It has been proposed in [35] that the LSCF decomposition could be enhanced by the accumulation of oxygen in the LSCF lattice under electrolysis mode. This accumulation takes place in the active FL where the decomposition should be accelerated. Even if this mechanism is consistent with the results found in the FL (Figure 5-9), it does not explain the higher

degradation in the CCL. From this point of view, additional studies are required to better understand the effect of operating mode on the LSCF decomposition under wet condition.

Finally, Ni is detected from the BL up to the CCL after operation. Its presence in the whole oxygen electrode thickness is clearly related to the use of humid air as it was not observed after ageing under dry condition [33]. The origin of Ni cannot come from the experimental setup made of alumina. However, as shown in [33], it is reminded that Ni is initially present in the electrolyte of the reference cell before operation. Indeed, the Ni dissolution into YSZ is known to occur during the cell sintering. It can be thus speculated that Ni would diffuse from the electrolyte towards the BL. Under the humid condition, it could form volatile molecules such as $Ni(OH)_2$ that could diffuse up to the CCL. Nevertheless, the presence of Ni metallic particles, which were detected by XRD at the top of the electrode, remains unexpected under oxidizing condition. It cannot come from artefacts due to the sample preparation as Ni was also observed in polished cross-sections by SIMS. Therefore, the unexpected presence of Ni in the oxygen electrode remains unclear and requires further investigations.

4. Conclusions

The effect of water vapour content in air on the cell degradation was studied in electrolysis and fuel cell mode. For this purpose, long-term tests were performed with dry air, 3% and 8% of humid air. The durability experiments were carried out for 1000 h at +/-1 $A.cm^{-2}$ and 800°C using typical solid oxide cells.

From the durability curves in SOEC mode, the degradation rates (DR) increased with increasing the water content in the air flow. In addition, the DR in SOEC mode was higher than the one in SOFC mode after operation in similar conditions. Regarding the electrochemical impedance spectra (EIS), the operation in electrolysis mode with 8% of humidity induced a strong evolution of the mid-frequency contribution related to the oxygen electrode. Moreover, the increase in the series resistance was found to be much higher than the one observed in dry condition.

Post-test characterizations by SEM, SIMS, XRD and XPS were conducted to analyse the degradation in the samples. In SOEC mode under dry air, a substantial Ni migration was detected at the cell inlet. By contrast, the Ni depletion was favoured at the cell outlet for the

SOEC samples aged in humid air. The characterizations of the oxygen electrode have revealed a strong decomposition of the LSCF material when increasing the water content in the supplied air. Under wet condition, this demixing was found to be strongly aggravated for an operation in electrolysis mode compared to the fuel cell mode. In addition, it was shown that the decomposition is much more pronounced in the current collecting layer at the cell inlet. It resulted in the formation of a strontium oxide layer that becomes quasi-dense for the sample aged in electrolysis mode at 8% of humidity. It has been proposed that such insulating layer can cause a local current redistribution in the cell that would induce a higher Ni migration at the cell outlet in the hydrogen electrode. Finally, Ni was also detected in the oxygen electrode after operation. It has been assumed that it could originate from the Ni dissolved in the electrolyte after the cell manufacturing.

All the post-test analyses have been found to be fully coherent with the electrochemical characterizations. Specifically, the high degradation rates and the evolution of the impedance spectra in electrolysis mode under wet condition can be explained by the accelerated LSCF decomposition in the electrode and the formation of a SrO layer in the current collecting layer.

Acknowledgments

The work has been supported by the project CELCER-EHT from the National Research Agency (grant agreement ANR-PEHY-008, France 2030). This work was also partially funded by Genvia company.

References

[1] D. Vladikova, B. Burdin, A. Sheikh, P. Piccardo, M. Krapchanska, D. Montinaro, R. Spotorno, Accelerated Stress Tests for Solid Oxide Cells via Artificial Aging of the Fuel Electrode, Energies 15 (2022) 3287. https://doi.org/10.3390/en15093287.

[2] A. Hagen, SOFCCell, Stack and System Level, in: Fuel Cells : Data, Facts and Figures, John Wiley & Sons, Ltd, 2016: pp. 304–320. https://doi.org/10.1002/9783527693924.ch31.

[3] F. Monaco, M. Hubert, J. Vulliet, J.P. Ouweltjes, D. Montinaro, P. Cloetens, P. Piccardo, F. Lefebvre-Joud, J. Laurencin, Degradation of Ni-YSZ Electrodes in Solid Oxide Cells: Impact of Polarization and Initial Microstructure on the Ni Evolution, J. Electrochem. Soc. 166 (2019) F1229. https://doi.org/10.1149/2.1261915jes.

[4] L. Rorato, Y. Shang, S. Yang, M. Hubert, K. Couturier, L. Zhang, J. Vulliet, M. Chen, J. Laurencin, Understanding the Ni Migration in Solid Oxide Cell: A Coupled Experimental and Modeling Approach, J. Electrochem. Soc. 170 (2023) 034504. https://doi.org/10.1149/1945-7111/acc1a3.

[5] M.B. Mogensen, A. Hauch, X. Sun, M. Chen, Y. Tao, S.D. Ebbesen, K.V. Hansen, P.V. Hendriksen, Relation Between Ni Particle Shape Change and Ni Migration in Ni–YSZ Electrodes – a Hypothesis, Fuel Cells 17 (2017) 434–441. https://doi.org/10.1002/fuce.201600222.

[6] A. Sciazko, T. Shimura, Y. Komatsu, N. Shikazono, Ni-GDC and Ni-YSZ electrodes operated in solid oxide electrolysis and fuel cell modes, Journal of Thermal Science and Technology 16 (2021) JTST0013–JTST0013. https://doi.org/10.1299/jtst.2021jtst0013.

[7] M. Trini, A. Hauch, S. De Angelis, X. Tong, P.V. Hendriksen, M. Chen, Comparison of microstructural evolution of fuel electrodes in solid oxide fuel cells and electrolysis cells, Journal of Power Sources 450 (2020) 227599. https://doi.org/10.1016/j.jpowsour.2019.227599.

[8] N.H. Menzler, D. Sebold, Y.J. Sohn, S. Zischke, Post-test characterization of a solid oxide fuel cell after more than 10 years of stack testing, Journal of Power Sources 478 (2020) 228770. https://doi.org/10.1016/j.jpowsour.2020.228770.

[9] Q. Fang, C.E. Frey, N.H. Menzler, L. Blum, Electrochemical Performance and Preliminary Post-Mortem Analysis of a Solid Oxide Cell Stack with 20,000 h of Operation, J. Electrochem. Soc. 165 (2018) F38–F45. https://doi.org/10.1149/2.0541802jes.

[10] Y. Wang, C. Wu, B. Zu, M. Han, Q. Du, M. Ni, K. Jiao, Ni migration of Ni-YSZ electrode in solid oxide electrolysis cell: An integrated model study, Journal of Power Sources 516 (2021) 230660. https://doi.org/10.1016/j.jpowsour.2021.230660.

[11] F. Monaco, D. Ferreira-Sanchez, M. Hubert, B. Morel, D. Montinaro, D. Grolimund, J. Laurencin, Oxygen electrode degradation in solid oxide cells operating in electrolysis and fuel cell modes: LSCF destabilization and interdiffusion at the electrode/electrolyte interface, International Journal of Hydrogen Energy (2021). https://doi.org/10.1016/j.ijhydene.2021.07.054.

[12] Z. Pan, Q. Liu, L. Zhang, X. Zhang, S.H. Chan, Effect of Sr Surface Segregation of La0.6Sr0.4Co0.2Fe0.8O3 − δ Electrode on Its Electrochemical Performance in SOC, J. Electrochem. Soc. 162 (2015) F1316. https://doi.org/10.1149/2.0371512jes.

[13] J. Szász, F. Wankmüller, V. Wilde, H. Störmer, D. Gerthsen, N.H. Menzler, E. Ivers-Tiffée, Nature and Functionality of La0.58Sr0.4Co0.2Fe0.8O3-δ / Gd0.2Ce0.8O2-δ / Y0.16Zr0.84O2-δ Interfaces in SOFCs, J. Electrochem. Soc. 165 (2018) F898. https://doi.org/10.1149/2.0031811jes.

[14] D. Kim, J.W. Park, B.-H. Yun, J.H. Park, K.T. Lee, Correlation of Time-Dependent Oxygen Surface Exchange Kinetics with Surface Chemistry of La0.6Sr0.4Co0.2Fe0.8O3−δ Catalysts, ACS Appl. Mater. Interfaces 11 (2019) 31786–31792. https://doi.org/10.1021/acsami.9b06569.

[15] H. Wang, S.A. Barnett, Degradation Mechanisms of Porous La0.6Sr0.4Co0.2Fe0.8O3-δ Solid Oxide Fuel Cell Cathodes, J. Electrochem. Soc. 165 (2018) F564. https://doi.org/10.1149/2.1211807jes.

[16] W. Araki, T. Yamaguchi, Y. Arai, J. Malzbender, Strontium surface segregation in La0.58Sr0.4Co0.2Fe0.8O3-δ annealed under compression, Solid State Ionics 268 (2014) 1–6. https://doi.org/10.1016/j.ssi.2014.09.019.

[17] J. Druce, H. Téllez, M. Burriel, M. D. Sharp, L. J. Fawcett, S. N. Cook, D. S. McPhail, T. Ishihara, H. H. Brongersma, J. A. Kilner, Surface termination and subsurface restructuring of perovskite-based solid oxide electrode materials, Energy & Environmental Science 7 (2014) 3593–3599. https://doi.org/10.1039/C4EE01497A.

[18] O. Celikbilek, M. Burriel, Recent advances in the understanding of the influence of surface chemistry and microstructure on the functional properties of solid oxide cell air electrodes, in: Nanoengineered Materials for Solid Oxide Cells, IOP Publishing, 2023. https://doi.org/10.1088/978-0-7503-4064-9ch2.

[19] D. The, S. Grieshammer, M. Schroeder, M. Martin, M. Al Daroukh, F. Tietz, J. Schefold, A. Brisse, Microstructural comparison of solid oxide electrolyser cells operated for 6100 h and 9000 h, Journal of Power Sources 275 (2015) 901–911. https://doi.org/10.1016/j.jpowsour.2014.10.188.

[20] R. Knibbe, A. Hauch, J. Hjelm, S. Ebbesen, M. Mogensen, Durability of Solid Oxide Cells, Green 1 (2011) 141. https://doi.org/10.1515/green.2011.015.

[21] W.-H. Kim, H.-S. Song, J. Moon, H.-W. Lee, Intermediate temperature solid oxide fuel cell using (La,Sr)(Co,Fe)O3-based cathodes, Solid State Ionics 177 (2006) 3211–3216. https://doi.org/10.1016/j.ssi.2006.07.049.

[22] A. Martínez-Amesti, A. Larrañaga, L.M. Rodríguez-Martínez, A.T. Aguayo, J.L. Pizarro, M.L. Nó, A. Laresgoiti, M.I. Arriortua, Reactivity between La(Sr)FeO3 cathode, doped CeO2 interlayer and yttria-stabilized zirconia electrolyte for solid oxide fuel cell applications, Journal of Power Sources 185 (2008) 401–410. https://doi.org/10.1016/j.jpowsour.2008.06.049.

[23] F. Tietz, Q. Fu, V.A.C. Haanappel, A. Mai, N.H. Menzler, S. Uhlenbruck, Materials Development for Advanced Planar Solid Oxide Fuel Cells, International Journal of Applied Ceramic Technology 4 (2007) 436–445. https://doi.org/10.1111/j.1744-7402.2007.02156.x.

[24] T. Shimura, A. He, N. Shikazono, Evaluation of La0.57Sr0.38Co0.2Fe0.8O3-δ Electrode Performance Degradation Based on Three-Dimensional Microstructure Reconstruction and Electrochemical Simulation, J. Electrochem. Soc. 166 (2019) F821. https://doi.org/10.1149/2.1091912jes.

[25] J.C. De Vero, K. Develos-Bagarinao, H. Kishimoto, T. Ishiyama, K. Yamaji, T. Horita, H. Yokokawa, Enhanced stability of solid oxide fuel cells by employing a modified cathode-interlayer interface with a dense La0.6Sr0.4Co0.2Fe0.8O3-δ thin film, Journal of Power Sources 377 (2018) 128–135. https://doi.org/10.1016/j.jpowsour.2017.12.010.

[26] V. Wilde, H. Störmer, J. Szász, F. Wankmüller, E. Ivers-Tiffée, D. Gerthsen, Gd0.2Ce0.8O2 Diffusion Barrier Layer between (La0.58Sr0.4)(Co0.2Fe0.8)O3−δ Cathode and Y0.16Zr0.84O2 Electrolyte for Solid Oxide Fuel Cells: Effect of Barrier Layer Sintering Temperature on Microstructure, ACS Appl. Energy Mater. 1 (2018) 6790–6800. https://doi.org/10.1021/acsaem.8b00847.

[27] J. Villanova, S. Schlabach, A. Brisse, A. Léon, X-ray fluorescence nano-imaging of long-term operated solid oxide electrolysis cells, Journal of Power Sources 421 (2019) 100–108. https://doi.org/10.1016/j.jpowsour.2019.02.084.

[28] S. Uhlenbruck, T. Moskalewicz, N. Jordan, H.-J. Penkalla, H.P. Buchkremer, Element interdiffusion at electrolyte–cathode interfaces in ceramic high-temperature fuel cells, Solid State Ionics 180 (2009) 418–423. https://doi.org/10.1016/j.ssi.2009.01.014.

[29] M. Morales, V. Miguel-Pérez, A. Tarancón, A. Slodczyk, M. Torrell, B. Ballesteros, J.P. Ouweltjes, J.M. Bassat, D. Montinaro, A. Morata, Multi-scale analysis of the diffusion barrier layer of gadolinia-doped ceria in a solid oxide fuel cell operated in a stack for 3000 h, Journal of Power Sources 344 (2017) 141–151. https://doi.org/10.1016/j.jpowsour.2017.01.109.

[30] H. Xu, K. Cheng, M. Chen, L. Zhang, K. Brodersen, Y. Du, Interdiffusion between gadolinia doped ceria and yttria stabilized zirconia in solid oxide fuel cells: Experimental investigation and kinetic modeling, Journal of Power Sources 441 (2019) 227152. https://doi.org/10.1016/j.jpowsour.2019.227152.

[31] F. Wankmüller, J. Szász, J. Joos, V. Wilde, H. Störmer, D. Gerthsen, E. Ivers-Tiffée, Correlative tomography at the cathode/electrolyte interfaces of solid oxide fuel cells, Journal of Power Sources 360 (2017) 399–408. https://doi.org/10.1016/j.jpowsour.2017.06.008.

[32] T. Matsui, S. Li, Y. Inoue, N. Yoshida, H. Muroyama, K. Eguchi, Degradation Analysis of Solid Oxide Fuel Cells with (La,Sr)(Co,Fe)O3-δ Cathode/Gd2O3–CeO2 Interlayer/Y2O3–ZrO2 Electrolyte System: The Influences of Microstructural Change and Solid Solution Formation, ECS Trans. 91 (2019) 1247. https://doi.org/10.1149/09101.1247ecst.

[33] G. Sassone, O. Celikbilek, M. Hubert, K. Develos-Bagarinao, T. David, L. Guetaz, I. Martin, J. Villanova, A. Benayad, L. Rorato, J. Vulliet, B. Morel, A. Léon, J. Laurencin, Effect of the operating temperature on the degradation of solid oxide electrolysis cells, Journal of Power Sources 605 (2024) 234541. https://doi.org/10.1016/j.jpowsour.2024.234541.

[34] Y. Wen, T. Yang, D. Lee, H. Nyung Lee, E. J. Crumlin, K. Huang, Temporal and thermal evolutions of surface Sr-segregation in pristine and atomic layer deposition modified La 0.6 Sr 0.4 CoO 3−δ epitaxial films, Journal of Materials Chemistry A 6 (2018) 24378–24388. https://doi.org/10.1039/C8TA08355J.

[35] J. Laurencin, M. Hubert, D.F. Sanchez, S. Pylypko, M. Morales, A. Morata, B. Morel, D. Montinaro, F. Lefebvre-Joud, E. Siebert, Degradation mechanism of La0.6Sr0.4Co0.2Fe0.8O3-δ/Gd0.1Ce0.9O2-δ composite electrode operated under solid oxide electrolysis and fuel cell conditions, Electrochimica Acta 241 (2017) 459–476. https://doi.org/10.1016/j.electacta.2017.05.011.

[36] C.E. Frey, Q. Fang, D. Sebold, L. Blum, N.H. Menzler, A Detailed Post Mortem Analysis of Solid Oxide Electrolyzer Cells after Long-Term Stack Operation, J. Electrochem. Soc. 165 (2018) F357. https://doi.org/10.1149/2.0961805jes.

[37] K. Chen, N. Li, N. Ai, Y. Cheng, W.D.A. Rickard, S.P. Jiang, Polarization-Induced Interface and Sr Segregation of in Situ Assembled La0.6Sr0.4Co0.2Fe0.8O3−δ Electrodes on Y2O3–ZrO2 Electrolyte of Solid Oxide Fuel Cells, ACS Appl. Mater. Interfaces 8 (2016) 31729–31737. https://doi.org/10.1021/acsami.6b11665.

[38] K. Chen, S.P. Jiang, Surface Segregation in Solid Oxide Cell Oxygen Electrodes: Phenomena, Mitigation Strategies and Electrochemical Properties, Electrochem. Energ. Rev. 3 (2020) 730–765. https://doi.org/10.1007/s41918-020-00078-z.

[39] Y. Li, W. Zhang, Y. Zheng, J. Chen, B. Yu, Y. Chen, M. Liu, Controlling cation segregation in perovskite-based electrodes for high electro-catalytic activity and durability, Chemical Society Reviews 46 (2017) 6345–6378. https://doi.org/10.1039/C7CS00120G.

[40] Z. He, L. Zhang, S. He, N. Ai, K. Chen, Y. Shao, S.P. Jiang, Cyclic polarization enhances the operating stability of La0.57Sr0.38Co0.18Fe0.72Nb0.1O3-δ oxygen electrode of reversible solid oxide cells, Journal of Power Sources 404 (2018) 73–80. https://doi.org/10.1016/j.jpowsour.2018.10.009.

[41] M. Kim, H. Muroyama, T. Matsui, K. Eguchi, Influence of Water Vapor on Performance Degradation and Microstructural Change of (La,Sr)(Co,Fe)O3−δ Cathode, J. Electrochem. Soc. 166 (2019) F1269. https://doi.org/10.1149/2.0641915jes.

[42] R.R. Liu, S.H. Kim, S. Taniguchi, T. Oshima, Y. Shiratori, K. Ito, K. Sasaki, Influence of water vapor on long-term performance and accelerated degradation of solid oxide fuel cell cathodes, Journal of Power Sources 196 (2011) 7090–7096. https://doi.org/10.1016/j.jpowsour.2010.08.014.

[43] E. Bucher, W. Sitte, Long-term stability of the oxygen exchange properties of (La,Sr)1−z(Co,Fe)O3−δ in dry and wet atmospheres, Solid State Ionics 192 (2011) 480–482. https://doi.org/10.1016/j.ssi.2010.01.006.

[44] P. Hjalmarsson, M. Søgaard, M. Mogensen, Electrochemical performance and degradation of (La0.6Sr0.4)0.99CoO3−δ as porous SOFC-cathode, Solid State Ionics 179 (2008) 1422–1426. https://doi.org/10.1016/j.ssi.2007.11.010.

[45] D. Zhang, M.L. Machala, D. Chen, Z. Guan, H. Li, S. Nemsak, E.J. Crumlin, H. Bluhm, W.C. Chueh, Hydroxylation and Cation Segregation in (La0.5Sr0.5)FeO3−δ Electrodes, Chem. Mater. 32 (2020) 2926–2934. https://doi.org/10.1021/acs.chemmater.9b05151.

[46] Z. Lu, S. Darvish, J. Hardy, J. Templeton, J. Stevenson, Y. Zhong, SrZrO3 Formation at the Interlayer/Electrolyte Interface during (La1-xSrx)1-δCo1-yFeyO3 Cathode Sintering, J. Electrochem. Soc. 164 (2017) F3097. https://doi.org/10.1149/2.0141710jes.

[47] F. Tietz, A. Mai, D. Stöver, From powder properties to fuel cell performance – A holistic approach for SOFC cathode development, Solid State Ionics 179 (2008) 1509–1515. https://doi.org/10.1016/j.ssi.2007.11.037.

[48] M.Z. Khan, R.-H. Song, M.T. Mehran, S.-B. Lee, T.-H. Lim, Controlling cation migration and inter-diffusion across cathode/interlayer/electrolyte interfaces of solid oxide fuel cells: A review, Ceramics International 47 (2021) 5839–5869. https://doi.org/10.1016/j.ceramint.2020.11.002.

[49] E. Da Rosa Silva, G. Sassone, M. Prioux, M. Hubert, B. Morel, J. Laurencin, A multiscale model validated on local current measurements for understanding the solid oxide cells performances, Journal of Power Sources 556 (2023) 232499. https://doi.org/10.1016/j.jpowsour.2022.232499.

[50] B. Wei, K. Chen, L. Zhao, Z. Lü, S.P. Jiang, Chromium deposition and poisoning at La0.6Sr0.4Co0.2Fe0.8O3−δ oxygen electrodes of solid oxide electrolysis cells, Phys. Chem. Chem. Phys. 17 (2014) 1601–1609. https://doi.org/10.1039/C4CP05110F.

[51] N. Fairley, V. Fernandez, M. Richard-Plouet, C. Guillot-Deudon, J. Walton, E. Smith, D. Flahaut, M. Greiner, M. Biesinger, S. Tougaard, D. Morgan, J. Baltrusaitis, Systematic and collaborative approach to problem solving using X-ray photoelectron spectroscopy, Applied Surface Science Advances 5 (2021) 100112. https://doi.org/10.1016/j.apsadv.2021.100112.

[52] A. Le Bail, H. Duroy, J.L. Fourquet, Ab-initio structure determination of LiSbWO6 by X-ray powder diffraction, Materials Research Bulletin 23 (1988) 447–452. https://doi.org/10.1016/0025-5408(88)90019-0.

[53] J.R. Carvajal, Commission on Powder Diffraction (IUCr), Newsletter 26 (2001) 12–19.

[54] A. Hauch, S.H. Jensen, S. Ramousse, M. Mogensen, Performance and Durability of Solid Oxide Electrolysis Cells, J. Electrochem. Soc. 153 (2006) A1741. https://doi.org/10.1149/1.2216562.

[55] S.-D. Kim, H. Moon, S.-H. Hyun, J. Moon, J. Kim, H.-W. Lee, Nano-composite materials for high-performance and durability of solid oxide fuel cells, Journal of Power Sources 163 (2006) 392–397. https://doi.org/10.1016/j.jpowsour.2006.09.015.

[56] A. Hauch, K. Brodersen, M. Chen, M.B. Mogensen, Ni/YSZ electrodes structures optimized for increased electrolysis performance and durability, Solid State Ionics 293 (2016) 27–36. https://doi.org/10.1016/j.ssi.2016.06.003.

[57] Q. Fang, L. Blum, D. Stolten, Electrochemical Performance and Degradation Analysis of an SOFC Short Stack Following Operation of More than 100,000 Hours, J. Electrochem. Soc. 166 (2019) F1320. https://doi.org/10.1149/2.0751916jes.

[58] J.S. Hardy, J.W. Stevenson, P. Singh, M.K. Mahapatra, E.D. Wachsman, M. Liu, K.R. Gerdes, Effects of Humidity on Solid Oxide Fuel Cell Cathodes, Pacific Northwest National Lab. (PNNL), Richland, WA (United States), 2015. https://doi.org/10.2172/1177304.

[59] G. Sassone, E.D.R. Silva, M. Prioux, M. Hubert, B. Morel, A. Léon, J. Laurencin, Multiscale Modelling of Solid Oxide Cells Validated on Electrochemical Impedance Spectra and Polarization Curves, ECS Trans. 111 (2023) 649. https://doi.org/10.1149/11106.0649ecst.

[60] Y. Shang, A. Lyck Smitshuysen, M. Yu, Y. Liu, X. Tong, P. Stanley Jørgensen, L. Rorato, J. Laurencin, M. Chen, 3D microstructural characterization of Ni/yttria-stabilized zirconia electrodes during long-term CO 2 electrolysis, Journal of Materials Chemistry A 11 (2023) 12245–12257. https://doi.org/10.1039/D3TA01503C.

[61] P.A.W. van der Heide, Photoelectron binding energy shifts observed during oxidation of group IIA, IIIA and IVA elemental surfaces, Journal of Electron Spectroscopy and Related Phenomena 151 (2006) 79–91. https://doi.org/10.1016/j.elspec.2005.11.001.

[62] Z. Sha, E. Cali, G. Kerherve, S. J. Skinner, Oxygen diffusion behaviour of A-site deficient (La 0.8 Sr 0.2) 0.95 Cr 0.5 Fe 0.5 O 3−δ perovskites in humid conditions, Journal of Materials Chemistry A 8 (2020) 21273–21288. https://doi.org/10.1039/D0TA08899D.

[63] K.A. Stoerzinger, W.T. Hong, E.J. Crumlin, H. Bluhm, M.D. Biegalski, Y. Shao-Horn, Water Reactivity on the LaCoO3 (001) Surface: An Ambient Pressure X-ray Photoelectron Spectroscopy Study, J. Phys. Chem. C 118 (2014) 19733–19741. https://doi.org/10.1021/jp502970r.

[64] N.A. Surplice, The electrical conductivity of calcium and strontium oxides, Br. J. Appl. Phys. 17 (1966) 175. https://doi.org/10.1088/0508-3443/17/2/303.

[65] M.P. Hoerlein, M. Riegraf, R. Costa, G. Schiller, K.A. Friedrich, A parameter study of solid oxide electrolysis cell degradation: Microstructural changes of the fuel electrode, Electrochimica Acta 276 (2018) 162–175. https://doi.org/10.1016/j.electacta.2018.04.170.

[66] J.I. Gazzarri, O. Kesler, Non-destructive delamination detection in solid oxide fuel cells, Journal of Power Sources 167 (2007) 430–441. https://doi.org/10.1016/j.jpowsour.2007.02.042.

Chapter conclusions

This chapter was dedicated to the study of the impact of humid air and operating mode on the cell degradation. Long-term tests, electrochemical characterizations and post-test analyses were carried out to advance the understanding of the effect these operating parameters on the degradation phenomena.

The durability cures showed a higher degradation rate (DR) on the cell voltage when progressively increasing the humidity level in the air. It was also evidenced an important role of the operating mode. Indeed, a rather low DR was observed for the test in SOFC mode, as compared to the SOEC.

The electrochemical characterizations were performed on each tested cell in the reference conditions, before and after ageing. The impedance spectra of the cell aged under dry air in SOEC mode highlighted an increase in the series and polarization resistances, as well as an increase in the high-frequency (HF) arc attributed to the hydrogen electrode kinetics. No clear evolution was found in the mid-frequency (MF) arc attributed to the oxygen electrode processes. When increasing the humidity in air to 8% in SOEC mode, a clear degradation was revealed in the MF arc. Additionally, higher ohmic losses were observed for this cell, as compared to the one aged under dry condition. Interestingly, a slight increase in the series resistance was found in the cell aged in SOFC mode as well. Nevertheless, the performance degradation on this sample were limited.

The post-test characterizations included various techniques to investigate the microstructural, chemical and structural evolution of the cell materials. In agreement with the electrochemical characterizations, a major microstructural evolution of the hydrogen electrode, including Ni coarsening and Ni migration, resulted from the SEM observations of the cell aged in SOEC under dry air. No signs of a clear degradation were found in the oxygen electrode, again confirming the EIS results. On the other hand, an evident oxygen electrode degradation was observed when increasing the water content in air. More specifically, the use of humid air accelerated the LSCF decomposition leading to the formation of a Sr-oxide based insulating phase on the oxygen electrode CCL. This insulating layer could cause a redistribution of the current towards the periphery of the cell. The higher current at the cell outlet promoted the Ni depletion in this region on the hydrogen electrode side. Considering the sample aged in SOFC mode, this degradation phenomena caused by the use of humid air were less prominent. Thus, the operating mode plays an important role on the cell degradation.

This study opened important open questions about the impact of air composition and operating mode, which will be addressed in future works.

6.Conclusions and perspectives

The purpose of this chapter is to highlight the key findings reported in the previous chapters of the manuscript. Specifically, the main outcomes of each chapter are listed and summarized in the following sections. General conclusions are drawn on the basis of the results and perspectives for future works are discussed as well.

6.1 Discussion of the advancement of knowledge

From the **Chapter III**, multiscale physics-based model capability in predicting the electrochemical response of the cell was evidenced. Both the stationary and dynamic models were validated. Specifically, the stationary model was able to predict both local (along the cell radius) and global electrochemical response of the cell in terms of i-V curves under various operating conditions. With the dynamic impedance model, it was possible to predict the experimental EIS at OCV under various gas compositions. Additionally, it was possible to identify the rate determining step (RDS) contributions in the EIS diagram. This model feature allowed to diagnose and monitor the state-of-health of the cell during the long-term operation.

The post-test characterizations focused on the oxygen electrode, presented in **Appendix A**, allowed assessing the stability after operation in SOEC mode at 750 °C, -1 $A \cdot cm^{-2}$. The study highlighted the rather stable behaviour of the LSCF in the oxygen electrode. This finding was in agreement with the resulting EIS that did not show any particular evolution of the mid-frequencies arc attributed to the oxygen electrode contribution with the multiscale physics-based model. No presence of $SrZrO_3$ was revealed by the different techniques. On the contrary, an inter-diffusion layer (IDL) was clearly identified, which was present already after cell manufacture and that slightly evolved after ageing according to microscale XRD results. Regarding the oxygen electrode, only a slight evolution of the LSCF lattice parameter was observed in the functional layer after ageing with microscale XRD. This was attributed to a slight LSCF decomposition. This was confirmed by the XPS analysis, which highlighted an evolution in the Sr surface-bound species after ageing.

The study of the effect of operating temperature was reported in the **Chapter IV** as well. The durability curves showed an apparent degradation that was the highest at the lowest temperature. This was attributed to the thermally activated behaviour of the electrodes activation overpotential. Hence, this study pointed out the need for performing electrochemical characterisations in the same reference conditions. The EIS revealed an increased intrinsic degradation with increasing the ageing temperature. More in detail, the change in the EIS after operation was noted mainly in the HF arc, while no evident change was observed at the MF and LF arcs. Thus, a stronger degradation was expected in the hydrogen electrode as compared to the oxygen electrode. The post-test characterizations confirmed this statement. More specifically, it was shown that the dominant degradation phenomena were the Ni migration and Ni coarsening at the hydrogen electrode. Furthermore, a promoted Ni migration was observed with increasing the operating temperature. This result brings some proof in a controversial

discussion in the literature on the effect of temperature on the cell degradation. On the other hand, no significant oxygen electrode degradation upon operation was deduced from the various techniques with high resolution down to the atomic scale. Only XPS analysis put in evidence an increase in the surface-bound Sr-based species after ageing. In addition, the atomic scale STEM-EDS and APT techniques revealed that Ce and Gd were present into the LSCF already before ageing. Overall, an inter-diffusion among all the cell layers was found for all the samples highlighting the fact that this process occurs during the cell fabrication, probably due to the high sintering temperatures. To summarize, it was shown that the ageing at different operating temperature under dry air affected mainly the degradation of the hydrogen electrode, with a lower impact on the IDL and the oxygen electrode.

The study of the effect of operating mode and the air water content was reported in the **Chapter V**. It was shown that both oxygen and hydrogen electrodes degradation was more pronounced in SOEC mode under humid air. More specifically, no Ni depletion and a lower LSCF decomposition were observed in SOFC mode. The introduction of water in the air flow caused an evident degradation of the oxygen electrode, which was pointed out also by the evolution of the MF arc in the EIS. In addition, a larger evolution in both polarization and series resistance was found under humid air, especially in SOEC mode. Considering the combination of the both the impact of humid air and operating mode, it was shown that the LSCF decomposition and the formation of SrO, along with the consequent oxygen electrode performance degradation (MF contribution in the EIS) were found to be more pronounced in SOEC under humid air, as compared to SOFC operation.

6.2 General conclusions

Within this thesis, the comprehension of degradation phenomena has been further advanced. Based on the aforementioned findings, possible solutions can be proposed concerning the impact of operating conditions (i.e. temperature, water content in air, operating mode). The multiscale physics-based model helped the interpretation of the experimental results and, thus, served as a tool to understand the cell response as a function of the operating parameter. Moreover, the work enabled drawing some hypotheses on the impact of manufacturing and operating conditions on the cell degradation phenomena.

It can be concluded that in the studied cell under the experimental setup and conditions described in the **Chapter II**, the dominant degradation phenomena occur in the hydrogen electrode upon SOEC operation. However, the degradation of the oxygen electrode appeared to be significantly more pronounced when introducing water in the air flow, especially in SOEC mode. Additionally, the operating mode plays an important role on the cell degradation. More specifically, the LSCF decomposition at the oxygen electrode resulted to be aggravated under humid air in SOEC mode as compared to the operation in SOFC mode. Nonetheless, it should be considered also the fact that the manufacturing of the cell can have a role on the cell durability. As discussed in this work, the IDL could actually act as an efficient dense diffusion BL to prevent the formation of the commonly observed SZOs. Indeed, the prominent presence of this inter-diffusion phase at the GDC/YSZ interface in all the samples could explain the absence of the SZO in this study, even after ageing under harsh conditions with humid air. Furthermore, the observed strong inter-diffusion among the various layers observed for all the samples highlight the important role of the manufacturing conditions in driving processes that can influence the cell performance and material stability.

6.3 Perspectives

These findings highlight the fact that a variety of factors affects the LSCF stability, which could explain the apparent conflicting results reported in the literature. It is needed to advance the knowledge, better understand the observed phenomena. More specifically, it is necessary to investigate the possible reasons behind the LSCF stability upon operation under dry air. As discussed in this work, this could be related either to the presence of Gd into the LSCF, to the LSCF A-site deficiency or to the use of dry air. Additionally, it is not clear the mechanism behind the aggravated LSCF decomposition in SOEC mode under humid air.

For these reasons, this section aims to anticipate the possible research direction to pursue in future works. Hence, the main perspectives based on the results collected using the three fold approach are further detailed in the following.

The multiscale physics-based model can be used to predict the electrochemical response at the complete cell level in various operating conditions. This feature enables investigating the optimal operating conditions at which the cell shows the best performance. Additionally, the model adapted and validated on the studied cell can be integrated by the electrochemical 3D model under development in the frame of Angel Trivino Pelaez postdoc research work. In this way, the model would be able to predict the performance degradation due to the Ni depletion in SOEC mode, which was identified as the dominant degradation phenomena. Hence, the multiscale physics-based model can be used as a tool for the diagnosis of the state of the health of the technology. Potentially, the model can be used for the prognosis if coupled with a degradation mechanism model in future works. In addition, atomic scale DFT calculations are undertaken in the frame of Karthikeyan Saravanabavan Ph.D. thesis, in order to unravel the LSCF degradation mechanism due to the presence of water molecules in air.

Regarding the long-term tests, in addition to the operating conditions already studied in this thesis, the impact of other operating parameters on the cell degradation could be investigated. As an example, long-term tests under ambient air conditions should be carried out in order to discriminate other factors contributing to the cell degradation in addition to the air humidity (e.g. air contaminants such as CO_2 or SO_2). Moreover, longer ageing time can be now achieved in the experimental setup. Indeed, longer operation can give more insight on the degradation processes along the lifetime of the cell, especially for those that are not visible for short ageing time.

In terms of post-test analyses, further investigations are foreseen to better understand the processes occurring in the oxygen electrode under different operating conditions, also exploring various ambient conditions (e.g. humidity, contaminants, etc.). In addition, the cells tested at the same conditions, only varying the ageing time, could be further characterized with post-test

techniques to study the effect of ageing time on the different layers of the cell. For instance, the cell aged for 5000 h within the thesis could provide interesting insights if studied with suitable post-test characterisations. To progress in this research direction the study of the impact of ageing time on the cell degradation should be addressed. Focusing on the oxygen electrode, the XPS resulted to be a promising technique to assess the degradation of this cell component, as compared to other technique. Indeed, the XPS was the only technique to clearly show a change after operation in the electrode, even in the cases where other techniques did not show any evidence of degradation.

Finally, the thesis enabled drawing hypotheses that can be verified in future works. As discussed in this thesis, the phenomena observed in the cells before ageing (i.e. LSCF A-site deficiency, presence of Gd into LSCF phase, presence of an IDL and absence of SZO at the GD/YSZ interface) could play an important role on the cell stability upon operation. Therefore, it is interesting to study the role of manufacturing conditions on the cell performance and durability. Another study could be addressed to evaluate the performance and stability upon operation of other materials. To conclude, based on the results obtained for the studied cell, one could suggest the following procedures to prevent or limit the observed degradation phenomena upon operation:

- Find the optimal operating conditions (e.g. current density, temperature) to mitigate the Ni migration in SOEC mode and ensure the cell performance stability over time;

- Operate in controlled environment (i.e. dry air) to slow down the LSCF decomposition.

Appendix A

Long-Term Tests and Advanced Post-Test Characterizations of the Oxygen Electrode in Solid Oxide Electrolysis Cells

Ozden Celikbilek[a], Giuseppe Sassone[a], Manon Prioux[a], Dario Ferreira Sanchez[b], Anass Benayad[c], Maxime Hubert[a], Bertrand Morel[a], Julien Vulliet[d], Aline Léon[e], Jérôme Laurencin[a]

[a] Univ. Grenoble Alpes, CEA-Liten, DTCH, 38000 Grenoble, France
[b] Paul Scherrer Institut, CH-5232 Villigen PSI, Switzerland
[c] Univ. Grenoble Alpes, CEA-Liten, DTNM, 38000 Grenoble, France
[d] CEA, DAM, Le Ripault, F-37260, Monts, France
[e] European Institute for Energy Research (EIFER), Emmy-Noether-Strasse 11, 76131 Karlsruhe/Deutschland

Solid oxide electrolysis cells (SOEC) are a promising energy conversion technology for the production of green hydrogen via steam electrolysis. However, performance loss remains a bottleneck for large-scale commercialization. Here, we investigate the different types of degradation occurring in a state-of-the-art cell composed of $La_{0.6}Sr_{0.4}Co_{0.2}Fe_{0.8}O_3$-$Ce_{0.8}Gd_{0.2}O_2$ (LSCF-GDC) composite for the oxygen electrode, GDC for the barrier layer, $Y_{0.16}Zr_{0.84}O_{1.92}$ (8YSZ) for the electrolyte and Ni-YSZ for the fuel electrode. Electrochemical impedance spectra measured before and after operation at 750 °C for 2000 hours at -1 A cm^{-2} in SOEC mode revealed no significant evolution for the oxygen electrode contribution. To investigate potential degradation of this electrode, we performed multi-modal chemical imaging based on synchrotron X-ray diffraction (μ-XRD) with a resolution at the micrometer-scale. In addition, we monitored the evolution of the chemical composition and chemical environment before and after ageing using laboratory X-ray photoelectron spectroscopy (XPS).

1. Introduction

With significant advantages over alternative power-to-gas technologies, solid oxide electrolysis cell (SOEC) technology has started to attract a lot of attention, particularly for its high efficiency in green hydrogen production. Over the years, significant improvements have been made in materials selection and cell manufacturing processes, both of which have a major impact on initial performance and durability. Despite the rapid development and improved performance of SOECs in recent years, their durability is still far from satisfactory. In most of the reported long-term tests, the fuel electrode is the primary source of degradation (1,2). Several articles reported that Ni particles migrates away from the electrolyte to the hydrogen electrode supporting layer during electrolysis operation (3,4). This leads to the disruption of the percolating Ni network and results in an irreversible electrochemical performance loss.

In addition to the hydrogen electrode, the oxygen electrode and the barrier layer are another source of degradation. They are also subject to complex set of phenomena, which, if left unaddressed, can also lead to rapid performance degradation. In this context, elemental intermixing between oxygen electrode (LSCF), barrier layer (GDC) and electrolyte (YSZ) is often observed (5,6). For instance, Sr segregation towards the LSCF surface is a commonly observed phenomenon that could be driven by electrostatic and strain energy minimization (7). It leads to the formation of a passivating layer (SrO, $SrCO_3$, $Sr(OH_2)$ etc.) which can hinder the oxygen exchange reactions on the surface and reduce the performance of the electrode (8). Interacting with the humidity in the air, the SrO can evaporate as $Sr(OH)_2$ molecules which can react with Zr of the YSZ electrolyte to form $SrZrO_3$ (SZO) in the porosity of the barrier layer (9). The solid state diffusion of Zr and Sr through the barrier layer can also lead to the formation of a dense and continuous SZO phase at the interfaces that can be detrimental to the performance, as its ionic conductivity is orders of magnitude lower than both GDC and YSZ at 800 °C ($\sigma_{\mathrm{SrZrO3}} = 1.87 \cdot 10^{-4}$ S/m, $\sigma_{\mathrm{YSZ}} = 5.4$ S/m , $\sigma_{\mathrm{GDC}} = 8.7$ S/m) (10,11).

Previous reports studied the influence of the sintering temperature of the GDC barrier layer, the operating temperature and the operating modes (electrolysis vs. fuel cell modes) on the SZO formation and its long-term behavior (12,13). They revealed that SZO readily forms during low-temperature GDC sintering and is exacerbated in electrolysis mode compared to fuel cell mode and at higher operating temperatures. A few other reports obtained dense GDC layers with low-temperature deposition techniques, such as pulsed laser deposition (14,15). SZO formation was still observed in both studies except when the post-deposition sintering was performed at high temperatures (15). Hence, microstructure alone cannot explain the inhibition of SZO formation.

Some studies reported that the chemical element interdiffusion between GDC and YSZ happens already during ceramic manufacture at high sintering temperatures (> 1000 °C) (13,16). The intermixing at the interface results in a dense inter-diffusion layer (IDL),

which is a solid solution between GDC and YSZ (17,18). A substantial reduction in the ionic conductivity of the IDL is reported, which results in an increase in its resistance and thus in the cell ohmic resistance (19). However, some studies suggested that IDL formation helps to lower or even to prevent SZO formation by inhibiting extensive Zr diffusion towards the LSCF/GDC interface (12,20,21).

In this work, we conducted a long-term ageing study at 750 °C for 2000 hours at -1 A cm^{-2} in SOEC mode. Then, we studied the local crystal lattice evolution due to inter-diffusion in different layers before and after operation using micrometer resolution synchrotron X-ray diffraction (µ-XRD) at the Paul Scherrer Institute (PSI, microXAS). In addition, we monitored the evolution of the chemical composition and chemical environment before and after ageing using laboratory X-ray photoelectron spectroscopy (XPS).

2. Experimental

Materials and methods

Cell description. The standard hydrogen electrode supported cells are composed of a $La_{0.6}Sr_{0.4}Co_{0.2}Fe_{0.8}O_{3-\delta}$ (LSCF) current collecting layer (CCL) and an LSCF-$Ce_{0.8}Gd_{0.2}O_{2-\delta}$ (LSCF-GDC) composite functional layer (FL) for the oxygen electrode, GDC for the barrier layer (BL), $Y_{0.16}Zr_{0.84}O_{1.92}$ for the electrolyte and Ni-YSZ for the hydrogen electrode. The cells have a circular shape and an active area of 9.08 cm^2. The CCL and FL are both ~20 µm, the BL is ~3 µm, the electrolyte is 8 µm and the fuel electrode is ~25 µm thick for the functional layer and ~280 µm for the support layer. In the following, the as-received sample is referred to as reference and the sample operated at high-temperature and under current for a long period of time is referred to as aged sample.

Electrochemical impedance spectroscopy. After the cell mounting in the experimental setup, the furnace is heated up to 860 °C with a heating rate of 1 °C·min^{-1} for 90 min to complete the glass sealing procedure. During this procedure, 0.5 Nl·h^{-1} of N_2 and 0.5 Nl·h^{-1} of dry compressed air (class [1:1:1] according to ISO 8573-1) are supplied at the hydrogen and oxygen electrodes, respectively. Subsequently, the temperature is decreased to 800 °C to reduce the NiO-YSZ cermet. The flows at the two electrodes are increased to 4 Nl·h^{-1}. The N_2 is progressively substituted with H_2 and maintained at the fuel electrode for a minimum of 16 h. Thereafter, initial electrochemical characterizations, i.e., impedance spectra at the open circuit voltage (OCV) and I-V curves, were carried out. Long-term tests were performed at 750 °C for 2000 h in the SOEC mode. The inlet flow at the hydrogen electrode was 12 NmL·min^{-1}·cm^{-2} with a composition of 10/90 H_2/H_2O whereas, 36 NmL·min^{-1}·cm^{-2} of dry compressed air was supplied to the air electrode. Finally, the operating current density was fixed at -1 A·cm^{-2}. The electrochemical impedance spectra

(EIS) were acquired at the OCV using a potentiostat/galvanostat (Autolab PGSTAT-302N) equipped with a Frequency Response Analyzer module (FRA) and a 20 A current booster. The spectra were acquired in Galvanostatic mode by imposing a sinusoidal current with an amplitude of 100 mA in the frequency range of 10^{-2} to 10^{4} Hz. The raw impedance spectra were collected using NOVA software (version 1.11).

Post-Test Characterizations

SEM. The microstructure of the films was studied by a field-emission gun scanning electron microscopy (FEG-SEM Zeiss Merlin, Germany) operating at an accelerating voltage of 3 kV and ~8-10 mm working distance. The samples were impregnated in polymer resin (Epofix, Denmark) to fill the pores and then polished using a diamond spray at 0.25 mm. A thin carbon coating was applied on the polished cross-section to avoid charging.

XPS. The surface chemistry was characterized using a PHI VersaProbe I XPS system operating under ultrahigh vacuum conditions ($p < 10^{-7}$ Pa) at ambient temperature. The system incorporates an Al Kα X-ray source (1486.6 eV) and generates a 4 mA emission current with an X-ray beam diameter of 200 µm. Pass energies of 200, and 20 eV were used for the survey and the core-level spectra. The quantitative analyses were performed using CasaXPS software (22). The relative sensitivity factors (RSF) were exported from the MultiPak library to take into account the transmission function of the spectrometer.

Synchrotron µXRD. The sample preparation and the setup of the microXAS beamline at the Swiss Light Source (SLS) was detailed in our previous work (13). The lamellae were extracted from the cells using plasma-focused ion beam (pFIB) Vion (FEI^{TM}) instrument coupled with a Xe^{+} ion source. The lamella was then fixed on a pin made of aluminum. The lamellae dimensions are ~80 µm in width, ~50 µm in height and ~20 µm in thickness. The experiment at the SLS was performed at 17.995 keV. A spot size of 1 µm was used along the horizontal scans, and 0.5 µm along the vertical scans. 2D powder diffraction rings were processed by azimuthal integration using pyFAI, a Python library, to obtain the 1D diffractograms (23). A total of ~60 and ~130 scans were taken along the horizontal and vertical axes, respectively. Then, all horizontal scans on the same axis were integrated to obtain a set of 1D diffractograms. Phase analysis was performed using Le Bail fitting method (24) in the FullProf software (25).

3. Results and Discussion

The electrochemical characterizations were carried out at 750 °C, in SOEC mode at -1 A·cm^{-2}, 64 % steam conversion (SC), 10/90 H_2/H_2O. The acquisitions for the EIS at the OCV (i.e. DC current equal to zero, with an amplitude for the imposed AC current equal to 100 mA) were taken at the beginning and at the end of the test (Figure S-A 1a). Three main arcs were discerned in the Nyquist plots, in the high-frequency (>1 kHz), mid-frequency (1 Hz – 1 kHz) and low-frequency (<1 Hz) ranges. These three arcs in the plots were ascribed to the fuel electrode, air electrode and gas conversion contributions respectively, using a physics-based multi-scale model (26). In particular, a significant evolution was observed in the high frequency region of the spectrum in the aged cell. However, the mid- and low-frequency regions did not show any particular evolution. Therefore, the majority of the degradation is expected to be hydrogen electrode related. It is worth noting that the increase of the polarization resistance at the high-frequency region was also concomitant with a shift in the ohmic resistance (Figure S-A 1a). The increase in both resistances is usually attributed to microstructural evolutions of the hydrogen electrode as a result of the Ni migration and Ni agglomeration (2,27). The cell voltage durability as a function of time in Figure S-A 1b shows that the degradation rate was higher and more variable in the first 800 h. It then stabilized at around 2.8%/kh until the end of the test.

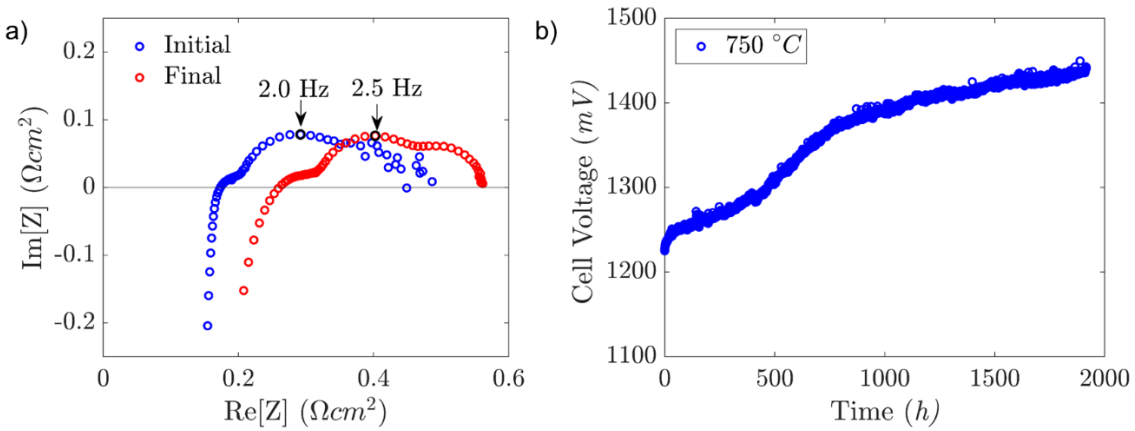

Figure S-A 1. a) Impedance spectra measured at OCV and 750 °C, before and after 2000 h of ageing in SOEC mode at -1 A·cm^{-2}, 64% SC, 10/90 H_2/H_2O, and b) the cell voltage durability.

Figure S-A 2 shows the cross-sectional SEM images of the reference and the aged cell. The images focus on the interface between the FL, BL and the electrolyte. The microstructure of the FL appears to remain fairly stable after ageing. Additionally, a dense layer of ~1 µm is visible in the GDC/YSZ interface for both samples, in agreement with

the previously-reported IDL observations (12,18). The thickness of the IDL does not seem to increase with ageing. However, some differences, such as higher pore formation is observed in YSZ, especially in the aged sample. Similar observations were made previously, which was attributed to higher oxygen equilibrium pressure inside the electrolyte, adjacent to the air electrode (28–30). On the other hand, others attributed these pores to elemental diffusion between adjacent layers and interpreted them as Kirkendall voids (31,32). Related to this, it is also possible to see that the grain boundaries in the electrolyte show a darker color contrast (see arrows in Figure S-A 2b), which is indicative of elemental diffusion. For instance, Mn was found in the grain boundaries of YSZ with lanthanum strontium manganite based air electrode (28,33).

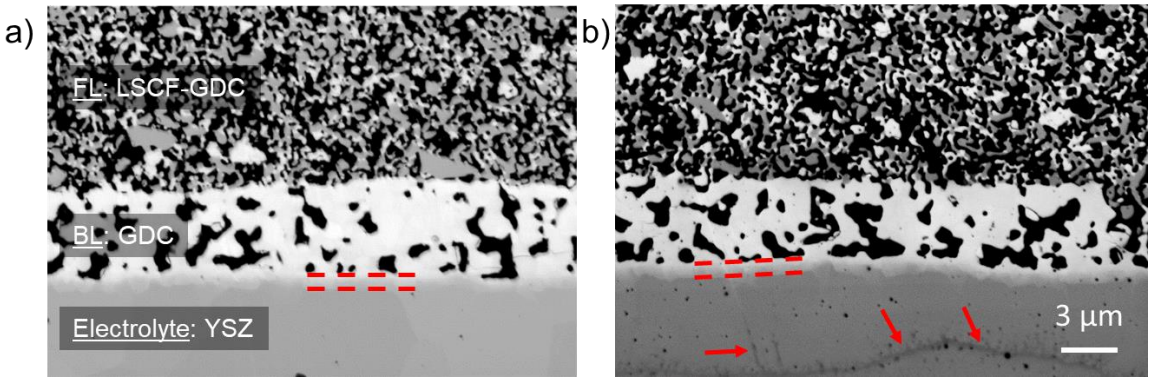

Figure S-A 2. Cross-section view SEM micrographs showing the LSCF-GDC/GDC/YSZ interface of a) reference and b) aged samples. The scale is the same for both samples. The inter-diffusion layer is shown with dashed lines at the interface of GDC/YSZ.

In the following, the chemical composition and the chemical environments (or oxidation states) of elements of interest in the reference and aged samples are compared. For this purpose, the top surface of the oxygen electrode was analyzed by XPS for both cells. Figure S-A 3 shows the Sr 3d, C 1s and O 1s core-level photoelectron spectra of the samples. The relative percentage of each elements are given in Table S-A 1 and Table S-A 2 for the reference and the aged cell, respectively.

The Sr 3d core-level spectra consist of a doublet with $3d_{5/2}$ at the lower BE (~131.9 eV) corresponding to the lattice-bound Sr and $3d_{3/2}$ at the higher BE (~133.3 eV) corresponding to the surface-bound Sr (34). It is highly likely that the surfaces contain a mixture of SrO, $Sr(OH)_2$ and $SrCO_3$ species (35,36). In terms of quantitative evolution, the ratio of surface-bound Sr to the total amount of Sr species has increased from 35% in the reference sample to 55% in the aged sample. In agreement with the previous reports, this observation indicates a significant Sr segregation towards the surface after ageing (7).

The C 1s core level spectra exhibit four components at approximately 285, 286.3, 288.4, 289.6 eV. The last one is related to the carboxyl and/or carbonate groups (O–C=O, CO_3^{2-}). The carbon contamination on the surface of both cells remain similar. Therefore, it can be assumed that the quantity of expected strontium carbonates ($SrCO_3$) remain constant before and after ageing.

The O 1s core-level spectra show more than one component; the sharp peak at the lower binding energy (BE) at ~528.5 eV (O–M1) is attributed to the lattice oxygen in the bulk of LSCF and the smaller peak at ~529.5 eV (O–M2) to the surface oxygen of LSCF (37). A rather dominant peak is observed at ~531.3 eV, which is usually attributed to the carbonates, hydroxides and oxides (37). This peak has significantly decreased from ~60% in the reference sample to 40% in the aged sample. This evolution could be ascribed to a decrease in $Sr(OH)_2$ concentration during operation. Indeed, strontium hydroxides might be evaporated in our experimental condition under sweeping dry air. Moreover, the formation of additional $Sr(OH)_2$ species in operation is expected to be limited. Therefore, the Sr segregation is highly likely to be related to an increase in SrO content. It is also consistent with the fact that SrO species contains two times lower oxygen content than $Sr(OH)_2$.

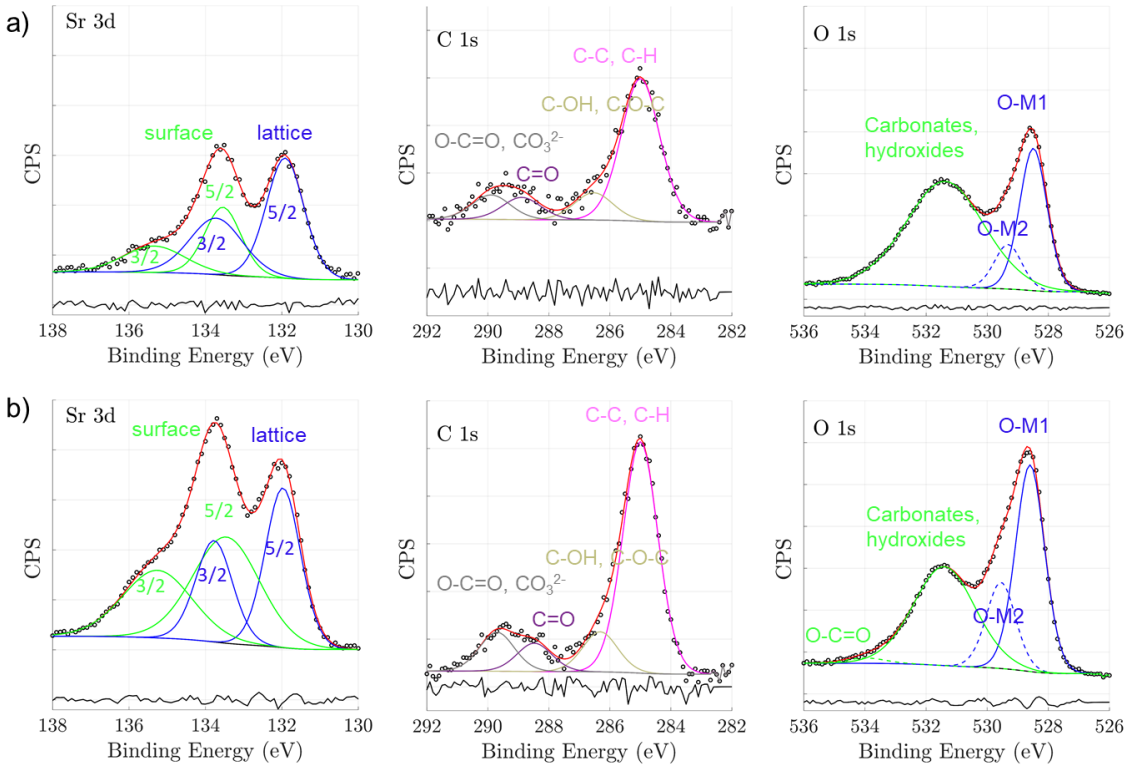

Figure S-A 3. Sr 3d, C 1s and O 1s core-level spectra of the top surface of the CCL in a) reference and b) sample aged at 750 °C for 2000 h in SOEC mode. The axes are set to same scale.

Table S-A 1: XPS fitting results of the reference sample including % concentration.

Name	BE (eV)	FWHM (eV)	Area	Conc (at.%)	Corrected RSF
O 1s – Lattice (O–M1)	528.49	1.06	176.56	16.05	16.223
O 1s – Surface (O–M2)	529.32	1.06	55.21	5.02	16.223
O 1s – Surface carbonates, hydroxides	531.37	2.98	367.43	33.41	16.223
O 1s – O–C=O, Organic species	-	-	-	-	16.223
Sr $3d_{5/2}$ – Lattice	131.92	1.16	72.36	2.23	47.847
Sr $3d_{3/2}$ – Lattice	133.72	1.63	47.75	1.47	47.847
Sr $3d_{5/2}$ – Surface	133.54	1.12	39.35	1.21	47.847
Sr $3d_{3/2}$ – Surface	135.34	1.90	25.96	0.80	47.847
C 1s – C–C,C–H	285.00	1.49	45.10	9.88	6.737
C 1s – C–O/OH	286.53	1.49	8.63	1.89	6.737
C 1s – C=O	288.89	1.49	7.03	1.54	6.737
C 1s – O–C=O, CO_3^{2-}	289.89	1.49	7.71	1.69	6.737
La $3d_{5/2}$	833.51	6.62	955.29	7.30	193.092
Co 2p	780.51	1.94	516.09	10.52	72.403
Fe 2p	709.91	3.59	413.92	6.99	87.349

Table S-A 2: XPS fitting results of the aged sample including % concentration.

Name	BE (eV)	FWHM (eV)	Area	Conc (at.%)	Corrected RSF
O 1s – Lattice (O–M1)	528.60	1.12	271.97	20.48	16.223
O 1s – Surface (O–M2)	529.55	1.12	113.45	8.54	16.223
O 1s – Surface carbonates, hydroxides	531.40	2.38	275.37	20.73	16.223
O 1s – O–C=O, Organic species	533.95	1.50	9.25	0.70	16.223
Sr $3d_{5/2}$ – Lattice	131.97	1.09	90.08	2.30	47.847
Sr $3d_{3/2}$ – Lattice	133.77	1.13	59.44	1.52	47.847
Sr $3d_{5/2}$ – Surface	133.69	2.07	113.55	2.90	47.847
Sr $3d_{3/2}$ – Surface	135.25	2.14	74.93	1.91	47.847
C 1s – C–C,C–H	285.00	1.35	66.30	12.00	6.737
C 1s – C–O/OH	286.32	1.35	11.48	2.08	6.737
C 1s – C=O	288.48	1.35	8.11	1.47	6.737
C 1s – O–C=O, CO_3^{2-}	289.70	1.35	11.15	2.02	6.737
La $3d_{5/2}$	833.40	6.76	1264.80	8.00	193.092
Co 2p	780.10	4.49	417.12	5.83	87.349
Fe 2p	710.30	3.35	563.78	9.51	72.403

The evolution of the phases observed along the sample thickness was investigated using a selected number of µ-XRD diffraction patterns. The data were selected from regions around the center of CCL, CCL/FL interface, FL, FL/BL interface, BL and BL/electrolyte interface (only BL/electrolyte interface are shown below). In general, the diffractograms contained only LSCF, GDC, YSZ, Al and NiO (only for the reference cell) phases. However, a small amount of an apparent cross-contamination between layers was observed; for example, GDC was detected along with LSCF in CCL, although the CCL should contain only LSCF. Nevertheless, this is probably due to experimental artifacts during the µXRD measurements which could be related to a slight tilting of the lamellae or a misalignment in the horizontal direction for the line scan. It is also likely that the pFIB milling for the lamellae preparation could introduce some element re-deposition along the cell layer, which could also explain the presence of NiO in the oxygen electrode.

LSCF detected in the diffractograms was fitted well with a cubic phase with $Pm\bar{3}m$ space group (no. 221). GDC and YSZ were fitted well with a cubic phase with $Fm\bar{3}m$ space group (no. 225). The XRD patterns and the structural refinement of the reference and the aged cell near the GDC/YSZ interface are shown in Figure S-A 4. The vertical lines under the diagram indicate the position of LSCF, GDC and YSZ. A shoulder peak and a long peak tailing with different intensities are visible between GDC and YSZ peaks. These peaks are related to solid-solution phases between GDC and YSZ, which are identified as IDL (16,38). It should be noted that the local spectra do not indicate the presence of $SrZrO_3$ phase formation even after ageing.

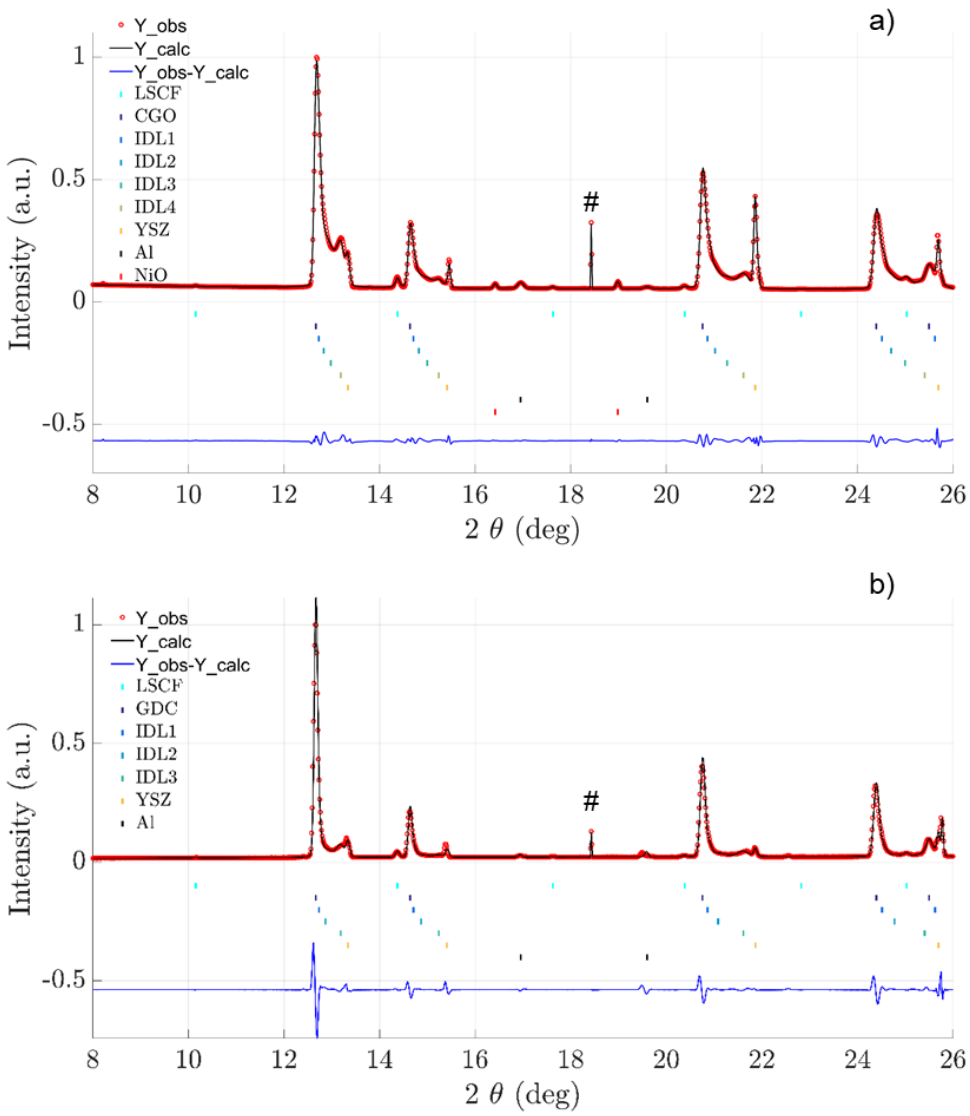

Figure S-A 4. X-ray diffractograms of a) reference cell, b) aged cell at 750 °C for 2000 h under electrolysis mode, near the GDC/YSZ interface focusing on the IDL. The color-coded phase identification is indicated with vertical lines. The peak indicated by # is related to the instrument.

It is important to remind that the cells are composed of 20% Gd-doped ceria in both the FL and the BL. The lattice parameter of GDC in the FL was refined to 5.425(0) Å, and that of YSZ was refined to 5.138(4) Å, both of which agree well with previously reported values (11). However, the lattice parameter of GDC was found to decrease to 5.407(9) Å near the GDC/YSZ interface, which is smaller than the expected value. It appears that a solid-state reaction and inter-diffusion phenomena occurred between GDC and YSZ already in the reference sample. The IDL was fitted well with four different cubic phases with lattice parameters of ~5.38, 5.34, 5.28 and 5.20 Å in the reference sample. However, only three cubic phases were fitted well with lattice parameters of ~5.38, 5.32, 5.20 Å in the aged

sample. Therefore, the inter-diffusion appears to continue during cell operation, as the IDL peaks designated as IDL2 and IDL3 (Figure S-A 4) with lattice parameters of 5.34, 5.28 Å in the reference sample merge into one peak with lattice parameter of ~5.32 Å (IDL2) in the aged sample. It is worth noting that an evolution in the IDL can contribute to the increase in the series resistance of the cell.

Figure S-A 5 demonstrates the evolution of LSCF lattice parameter as a function of the position in the electrode thickness for both the reference and the aged cells. A 0.32% decrease in the cell volume of LSCF was observed from the CCL to the FL in the reference sample. This is in accordance with previous reports that observed a lower lattice parameter for LSCF in the LSCF-GDC composite films (39). Similar to our work, Celikbilek et al. reported a 0.30% decrease in the cell volume of LSCF in the 60/40 vol.% LSCF-GDC composite film in comparison to reference LSCF (39). On the other hand, the lattice parameter of LSCF in the FL shows a slight increase in the aged cell compared to the reference one. In previous studies, Sr and Co loss from the LSCF lattice were attributed to the lattice expansion in the LSCF (40,41). Overall, µXRD results indicate that the aged cell shows a slight evolution due to intermixing of cations at the interfaces associated with the LSCF destabilization in the FL.

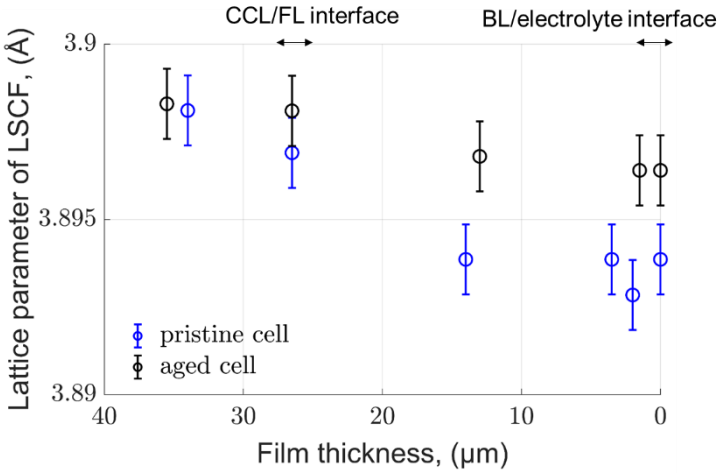

Figure S-A 5. Evolution of the lattice parameter of LSCF as a function of layer thickness for the reference and the aged cell. Vertical lines at 0 and 26.5 µm indicate the GDC/YSZ and CCL/FL interfaces respectively.

4. Conclusions

In this work, the degradation of SOECs was addressed performing long-term test and post-test characterizations. After assessing the global degradation in the performance with electrochemical characterizations, post-test analyses were carried out focusing on the oxygen electrode and the LSCF-GDC/GDC/YSZ interfaces. Post-test characterizations using synchrotron µ-XRD technique showed that an inter-diffusion layer formed between the GDC and YSZ layers already during cell fabrication. A slight evolution in the IDL from the µ-XRD patterns was detected after ageing, but $SrZrO_3$ formation was not found. In addition, a slight increase in the LSCF unit cell volume was observed after ageing that could be ascribed to the destabilization of LSCF. On the other hand, XPS results put in evidence that the aged cell surface was covered with a higher amount of surface-bound Sr species, probably related to SrO. Nevertheless, according to the impedance spectra and the post-test analyses, the ageing of the air electrode at 750 °C for 2000 h and under current (-1 $A.cm^{-2}$) seems to have a limited impact on the cell performance loss in these operating conditions. From this study, it appears that long-term tests under more aggravated conditions and/or longer duration are required to better observe and analyze the oxygen electrode degradation.

Acknowledgments

This project has received funding from the Fuel Cells and hydrogen 2 Joint Undertaking (JU) under grand agreement n°874577 (NewSOC project). The work has also been supported by Genvia, the projects CELCER-EHT from the National Research Agency (ANR) and CASSIOPEE from Carnot Energie du Futur. The µ-XRD experiments (proposal ID 20210398) were carried out at the micro-XAS beamline at the Swiss Light Source (SLS) Paul Scherrer Institut, Villigen, Switzerland.

References

1. X. Sun, P. V. Hendriksen, M. B. Mogensen, and M. Chen, *Fuel Cells*, **19**, 740–747 (2019).
2. Q. Fang, C. E. Frey, N. H. Menzler, and L. Blum, *J. Electrochem. Soc.*, **165**, F38–F45 (2018).
3. F. Monaco, M. Hubert, J. Vulliet, J. P. Ouweltjes, D. Montinaro, P. Cloetens, P. Piccardo, F. Lefebvre-Joud, and J. Laurencin, *J. Electrochem. Soc.*, **166**, F1229–F1242 (2019).
4. M. Trini, A. Hauch, S. De Angelis, X. Tong, P. V. Hendriksen, and M. Chen, *J. Power Sources*, **450**, 227599 (2020).
5. S. Uhlenbruck, T. Moskalewicz, N. Jordan, H. J. Penkalla, and H. P. Buchkremer, *Solid State Ionics*, **180**, 418–423 (2009).
6. F. Wang, M. Nishi, M. E. Brito, H. Kishimoto, K. Yamaji, H. Yokokawa, and T. Horita, *J. Power Sources*, **258**, 281–289 (2014).
7. B. Koo, K. Kim, J. K. Kim, H. Kwon, J. W. Han, and W. C. Jung, *Joule*, **2**, 1476–1499 (2018).
8. Y. Chen et al., *Energy Environ. Sci.*, **5**, 7979–7988 (2012).
9. J. Laurencin, M. Hubert, D. F. Sanchez, S. Pylypko, M. Morales, A. Morata, B. Morel, D. Montinaro, F. Lefebvre-Joud, and E. Siebert, *Electrochim. Acta*, **241**, 459–476 (2017).
10. F. Willy Poulsen and N. van der Puil, *Solid State Ionics*, **53**–**56**, 777–783 (1992).
11. A. Tsoga, A. Naoumidis, and D. Stöver, *Solid State Ionics*, **135**, 403–409 (2000).
12. V. Wilde, H. Störmer, J. Szász, F. Wankmüller, E. Ivers-Tiffée, and D. Gerthsen, *ACS Appl. Energy Mater.*, **1**, 6790–6800 (2018).
13. F. Monaco, D. Ferreira-Sanchez, M. Hubert, B. Morel, D. Montinaro, D. Grolimund, and J. Laurencin, *Int. J. Hydrogen Energy*, **46**, 31533–31549 (2021).
14. R. Knibbe, J. Hjelm, M. Menon, N. Pryds, M. Søgaard, H. J. Wang, and K. Neufeld, *J. Am. Ceram. Soc.*, **93**, 2877–2883 (2010).
15. M. Morales, A. Pesce, A. Slodczyk, M. Torrell, P. Piccardo, D. Montinaro, A. Tarancón, and A. Morata, *ACS Appl. Energy Mater.*, **1**, 1955–1964 (2018).
16. H. Xu, K. Cheng, M. Chen, L. Zhang, K. Brodersen, and Y. Du, *J. Power Sources*, **441**, 227152 (2019).
17. G. Rinaldi, S. Diethelm, E. Oveisi, P. Burdet, J. Van herle, D. Montinaro, Q. Fu, and A. Brisse, *Fuel Cells*, **17**, 541–549 (2017).
18. F. Tietz, D. Sebold, A. Brisse, and J. Schefold, *J. Power Sources*, **223**, 129–135 (2013).
19. T. Matsui, S. Li, Y. Inoue, N. Yoshida, H. Muroyama, and K. Eguchi, *J. Electrochem. Soc.*, **166**, F295–F300 (2019).
20. F. Wankmüller, J. Szász, J. Joos, V. Wilde, H. Störmer, D. Gerthsen, and E. Ivers-Tiffée, *J. Power Sources*, **360**, 399–408 (2017).
21. J. Szász, F. Wankmüller, V. Wilde, H. Störmer, D. Gerthsen, N. H. Menzler, and E. Ivers-Tiffée, *J. Electrochem. Soc.*, **165**, F898–F906 (2018).
22. N. Fairley et al., *Appl. Surf. Sci. Adv.*, **5**, 100112 (2021).
23. G. Ashiotis, A. Z. N. Deschildre, J. P. Wright, D. Karkoulis, F. E. Picca, and J. Kieffer, *J. Appl. Crystallogr.*, **48**, 510–519 (2015).
24. A. Le Bail, in *Proceedings of the International Conference,*, p. 846, NIST Special Publication (1992).
25. J. Rodríguez-Carvajal, *Comm. Powder Diffr. (IUCr). Newsl.*, **26**, 12–19 (2001).
26. G. Sassone, E. D. R. Silva, M. Prioux, M. Hubert, B. Morel, A. Léon, and J. Laurencin, *ECS Trans.*, **111**, accepted (2023).
27. Y. Wang, C. Wu, B. Zu, M. Han, Q. Du, M. Ni, and K. Jiao, *J. Power Sources*, **516**, 230660 (2021).
28. R. Knibbe, M. L. Traulsen, A. Hauch, S. D. Ebbesen, and M. Mogensen, *J. Electrochem. Soc.*, **157**, B1209 (2010).
29. M. A. Laguna-Bercero, R. Campana, A. Larrea, J. A. Kilner, and V. M. Orera, *J. Power Sources*, **196**, 8942–8947 (2011).
30. A. V. Virkar, *Int. J. Hydrogen Energy*, **35**, 9527–9543 (2010).

31. D. The, S. Grieshammer, M. Schroeder, M. Martin, M. Al Daroukh, F. Tietz, J. Schefold, and A. Brisse, *J. Power Sources*, **275**, 901–911 (2015).
32. H. Mitsuyasu, Y. Nonaka, and K. Eguchi, *Solid State Ionics*, **113**–**115**, 279–284 (1998).
33. Y. Chen, Y. Fan, S. Lee, G. Hackett, H. Abernathy, K. Gerdes, and X. Song, *J. Power Sources*, **438**, 227043 (2019).
34. E. Mutoro, E. J. Crumlin, H. Pöpke, B. Luerssen, M. Amati, M. K. Abyaneh, M. D. Biegalski, H. M. Christen, L. Gregoratti, J. Janek, and Y. Shao-Horn, *J. Phys. Chem. Lett.*, **3**, 40–44 (2012).
35. Z. Cai, M. Kubicek, J. Fleig, and B. Yildiz, *Chem. Mater.*, **24**, 1116–1127 (2012).
36. J. C. Dupin, D. Gonbeau, P. Vinatier, and A. Levasseur, *Phys. Chem. Chem. Phys.*, **2**, 1319–1324 (2000).
37. P. A. W. Van Der Heide, *J. Electron Spectros. Relat. Phenomena*, **151**, 79–91 (2006).
38. P. Hjalmarsson, X. Sun, Y. L. Liu, and M. Chen, *J. Power Sources*, **223**, 349–357 (2013).
39. O. Celikbilek, D. Jauffrès, E. Siebert, L. Dessemond, M. Burriel, C. L. Martin, and E. Djurado, *J. Power Sources*, **333**, 72–82 (2016).
40. J. S. Hardy, J. W. Templeton, D. J. Edwards, Z. Lu, and J. W. Stevenson, *J. Power Sources*, **198**, 76–82 (2012).
41. J. S. Hardy, C. A. Coyle, J. F. Bonnett, J. W. Templeton, N. L. Canfield, D. J. Edwards, S. M. Mahserejian, L. Ge, B. J. Ingram, and J. W. Stevenson, *J. Mater. Chem. A*, **6**, 1787–1801 (2018).

Appendix B

Chapter IV: Supporting information

Effect of the Operating Temperature on the Degradation of Solid Oxide Electrolysis Cells

Giuseppe Sassone[a], Ozden Celikbilek[a], Maxime Hubert[a], Katherine Develos-Bagarinao[b], Thomas David[c], Laure Guetaz[c], Isabelle Martin[d], Julie Villanova[e], Anass Benayad[c], Léa Rorato[a], Julien Vulliet[f], Bertrand Morel[a], Aline Léon[g], Jérôme Laurencin[a]

[a] Univ. Grenoble Alpes, CEA, Liten, DTCH, 38000 Grenoble, France
[b] Global Zero Emission Research Center, AIST, Tsukuba, Japan
[c] Univ. Grenoble Alpes, CEA, Liten, DTNM, 38000 Grenoble, France
[d] CAMECA Instruments Inc., 5470 Nobel Drive, Madison, Wisconsin 53711, United States
[e] ESRF the European Synchrotron, CS 40220, 38043, Grenoble Cedex 9, France
[f] CEA, DAM, Le Ripault, F-37260, Monts, France
[g] European Institute for Energy Research (EIFER), Emmy-Noether Strasse 11, 76131 Karlsruhe, Germany

Lamella sample for synchrotron characterization

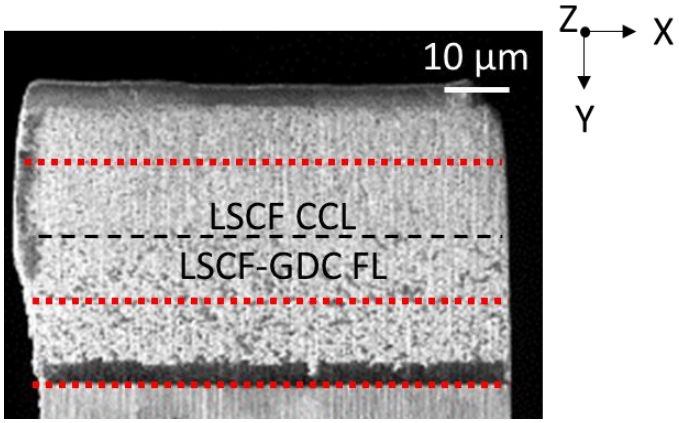

Figure S-B 1. Lamella sample used for the synchrotron analyses, with orange dashed lines indicating the XRD line scan positions.

EIS recorded during the durability experiments

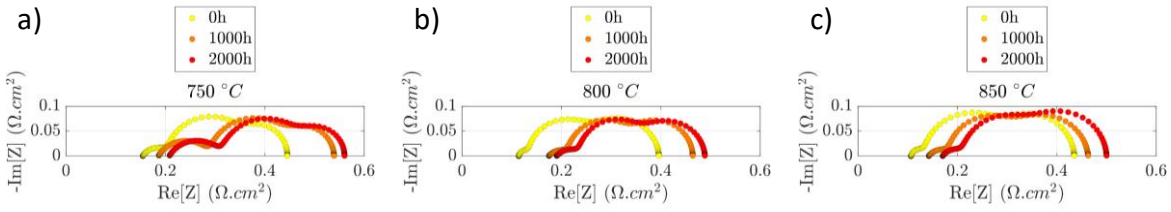

Figure S-B 2. Nyquist plots recorded at the operating temperature during the durability tests for the cells aged at a) 750 °C, b) 800 °C and c) 850 °C. (SOEC mode at -1 A·cm^{-2}, 64% SC, 10/90 vol.% H_2/H_2O).

XRD patterns at the barrier layer

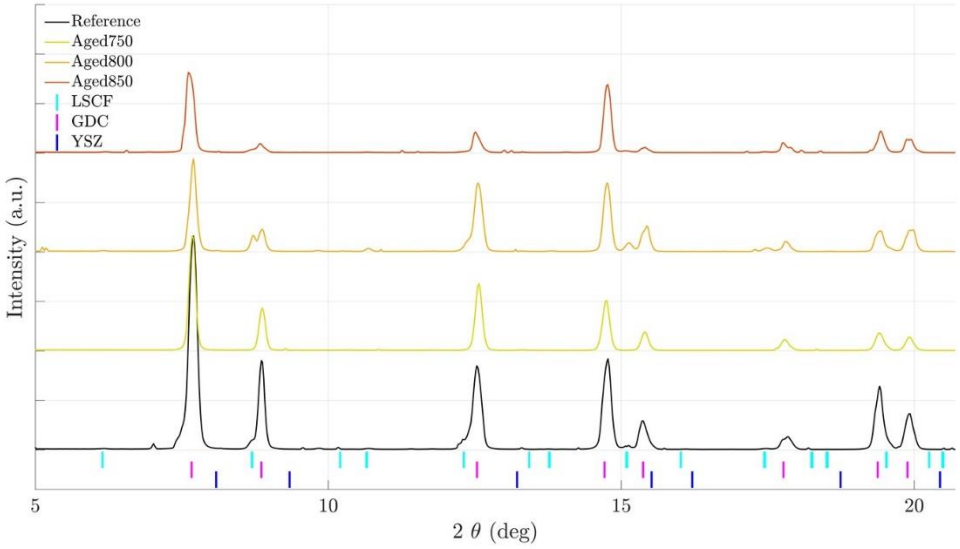

Figure S-B 3. XRD patterns at the barrier layer for the “Reference”, “Aged750”, “Aged800” and “Aged850” samples.

STEM analyses

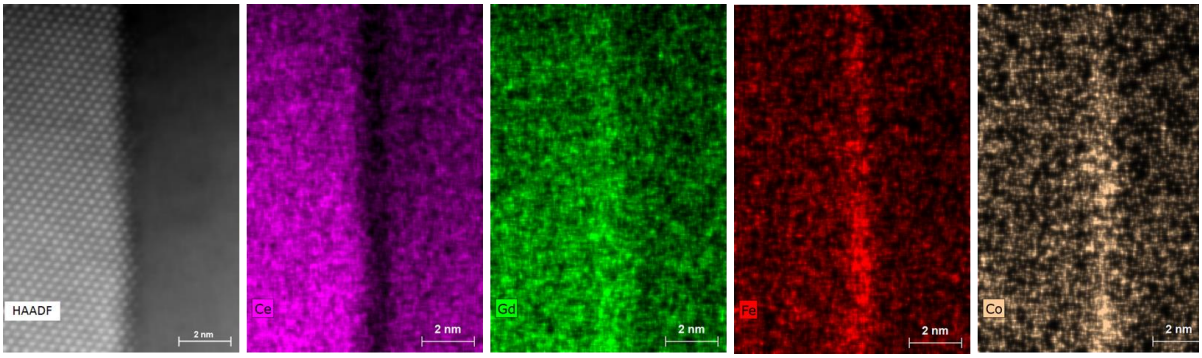

Figure S-B 4. HAADF/STEM image and the associated EDS elemental maps recorded in the area located along a grain boundary of two GDC grain in the “Reference” sample.

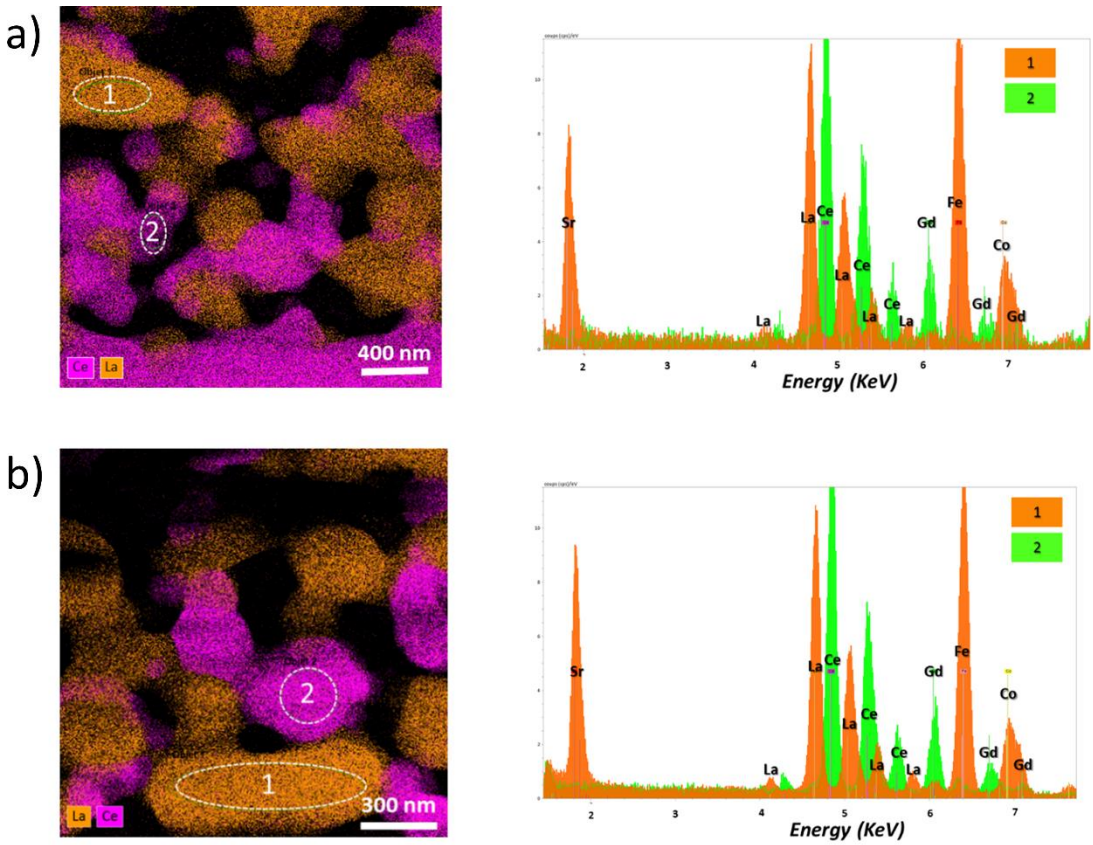

Figure S-B 5. STEM-EDS analyses performed on the oxygen electrode in LSCF-GDC layer: EDS elemental maps of La and Ce and spectra extracted respectively from LSCF and GDC grains, respectively marked 1 and 2 in maps. a) “Reference” and b) “Aged800” samples.

XRD patterns at the oxygen electrode

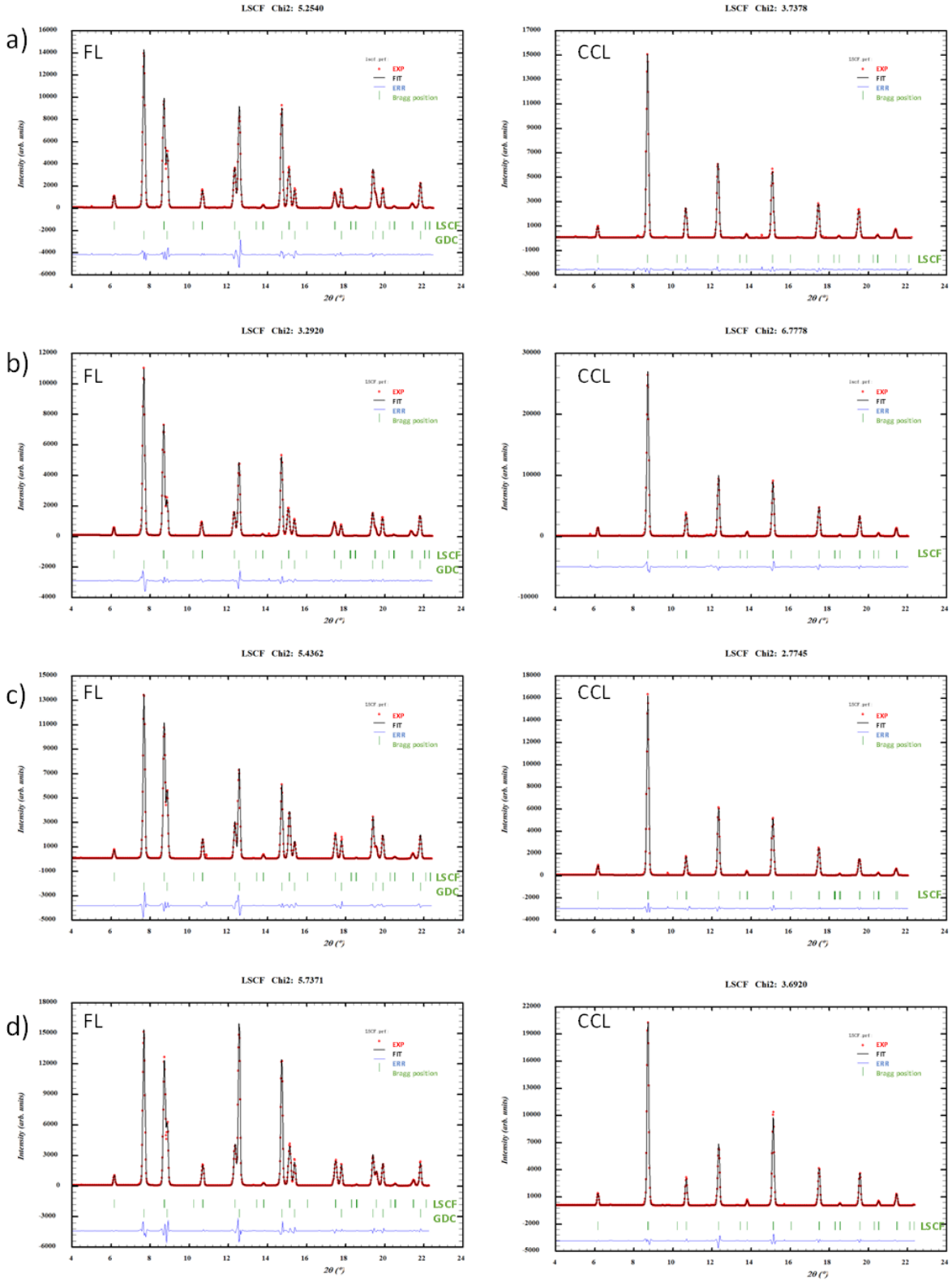

Figure S-B 6. XRD fits at the LSCF-GDC/GDC/YSZ interfaces performed on a) "Reference", b) "Aged750", c) "Aged800" and d) "Aged850" samples.

Surface analysis by XPS

The relative percentages of each contribution after peak fitting are given in Table S-B 1 (analyses of CCL) and Table S-B 2 (analyses of FL) for the Reference sample, and in Table S-B 3 (analyses of CCL) and Table S-B 4 (analyses of FL) for the Aged850 sample.

Table S-B 1. XPS fitting results of the CCL of the Reference sample including % atomic concentration. BE refers to binding energy and FWHM to full width at half maximum. –(O–M1 and O–M2) refer to the oxygen coordination in the bulk of the LSCF.

Name	BE (eV)	FWHM (eV)	Area	%Conc	Corrected RSF
O 1s – Lattice (O–M1)	528.6	1.1	252.2	25.6	16.223
O 1s – Lattice (O–M2)	529.5	1.1	107.5	10.9	16. 223
O 1s – Surface oxides, carbonates, hydroxides	531.3	2.4	269.8	27.4	16. 223
O 1s – O–C=O, Organic species	534.0	1.5	8.6	0.88	16.223
Sr $3d_{5/2}$ – Lattice	132.0	1.1	83.9	2.9	47.847
Sr $3d_{3/2}$ – Lattice	133.8	1.1	76.7	1.9	47.847
Sr $3d_{5/2}$ – Surface	133.3	2.0	55.4	2.6	47.847
Sr $3d_{3/2}$ – Surface	135.1	2.1	50.6	1.7	47.847
C 1s – C–C,C–H	285.0	1.4	78.5	19.2	6.737
C 1s – C–O/OH	286.4	1.4	10.6	2.6	6.737
C 1s – C=O	288.6	1.4	6.48	1.6	6.737
C 1s – O–C=O, CO_3^{2-}	290.4	1.4	11.32	2.8	6.737

Table S-B 2. XPS fitting results of the FL of the Reference sample including % atomic concentration. BE refers to binding energy and FWHM to full width at half maximum. –(O–M1 and O–M2) refer to the oxygen coordination in the bulk of the LSCF.

Name	BE (eV)	FWHM (eV)	Area	%Conc	Corrected RSF
O 1s – Lattice (O–M1)	528.7	1.2	243.6	26.9	16.223
O 1s – Lattice (O–M2)	529.4	1.2	139.4	15.4	16. 223
O 1s – Surface oxides, carbonates, hydroxides	531.3	2.6	239.1	26.4	16. 223
O 1s – O–C=O, Organic species					16.223
Sr $3d_{5/2}$ – Lattice	131.9	1.2	49.9	1.9	47.847
Sr $3d_{3/2}$ – Lattice	133.7	1.5	32.9	1.2	47.847
Sr $3d_{5/2}$ – Surface	133.6	1.6	40.1	1.5	47.847
Sr $3d_{3/2}$ – Surface	135.4	1.8	26.5	1.0	47.847
C 1s – C–C,C–H	285.0	1.4	68.7	18.3	6.737
C 1s – C–O/OH	286.4	1.4	8.6	2.3	6.737
C 1s – C=O	288.7	1.4	10.1	2.7	6.737
C 1s – O–C=O, CO_3^{2-}	289.8	1.4	9.5	2.5	6.737

Table S-B 3. XPS fitting results of the CCL of the Aged850 sample including % atomic concentration. BE refers to binding energy and FWHM to full width at half maximum. –(O–M1 and O–M2) refer to the oxygen coordination in the bulk of the LSCF.

Name	BE (eV)	FWHM (eV)	Area	%Conc	Corrected RSF
O 1s – Lattice (O–M1)	528.4	1.2	222.2	18.2	16.223
O 1s – Lattice (O–M2)	529.3	1.2	109.1	8.9	16. 223
O 1s – Surface oxides, carbonates, hydroxides	531.3	2.2	247.2	28.4	16. 223
O 1s – O–C=O, Organic species					16.223
Sr $3d_{5/2}$ – Lattice	131.9	1.2	92.9	2.6	47.847
Sr $3d_{3/2}$ – Lattice	133.7	1.3	61.3	1.7	47.847
Sr $3d_{5/2}$ – Surface	133.5	1.6	113.1	3.1	47.847
Sr $3d_{3/2}$ – Surface	135.3	1.7	74.6	2.1	47.847
C 1s – C–C,C–H	285.0	1.4	128.6	25.3	6.737
C 1s – C–O/OH	286.5	1.4	15.6	3.1	6.737
C 1s – C=O	288.45	1.4	13.8	2.7	6.737
C 1s – O–C=O, CO_3^{2-}	289.6	1.4	19.7	3.9	6.737

Table S-B 4. XPS fitting results of the FL of the Aged850 sample including % atomic concentration. BE refers to binding energy and FWHM to full width at half maximum. –(O–M1 and O–M2) refer to the oxygen coordination in the bulk of the LSCF.

Name	BE (eV)	FWHM (eV)	Area	%Conc	Corrected RSF
O 1s – Lattice (O–M1)	528.6	1.5	161.1	16.7	16.223
O 1s – Lattice (O–M2)	529.4	1.5	287.5	29.8	16. 223
O 1s – Surface oxides, carbonates, hydroxides	531.4	2.6	230.4	23.9	16. 223
O 1s – O–C=O, Organic species					16.223
Sr $3d_{5/2}$ – Lattice	131.5	1.3	12.2	0.4	47.847
Sr $3d_{3/2}$ – Lattice	133.3	1.1	8.1	0.3	47.847
Sr $3d_{5/2}$ – Surface	132.75	2.3	26.0	0.9	47.847
Sr $3d_{3/2}$ – Surface	134.55	2.1	17.1	0.6	47.847
C 1s – C–C,C–H	285.0	1.7	69.5	17.3	6.737
C 1s – C–O/OH	286.0	1.7	16.1	4.0	6.737
C 1s – C=O	288.9	1.7	17.7	4.4	6.737
C 1s – O–C=O, CO_3^{2-}	290.25	1.7	6.6	1.6	6.737

Appendix C

Chapter V: Supporting information

Impact of Air Moisture and Operating Mode on the Degradation of Solid Oxide Cells

Giuseppe Sassone[a], Ozden Celikbilek[a], Maxime Hubert[a], Katherine Develos-Bagarinao[b], Anass Benayad[c], Bertrand Morel[a], Aline Léon[d], Jérôme Laurencin[a]

[a] Univ. Grenoble Alpes, CEA, Liten, DTCH, 38000 Grenoble, France
[b] Global Zero Emission Research Center, AIST, Tsukuba, Japan
[c] Univ. Grenoble Alpes, CEA, Liten, DTNM, 38000 Grenoble, France
[d] European Institute for Energy Research (EIFER), Emmy-Noether Strasse 11, 76131 Karlsruhe, Germany

SIMS

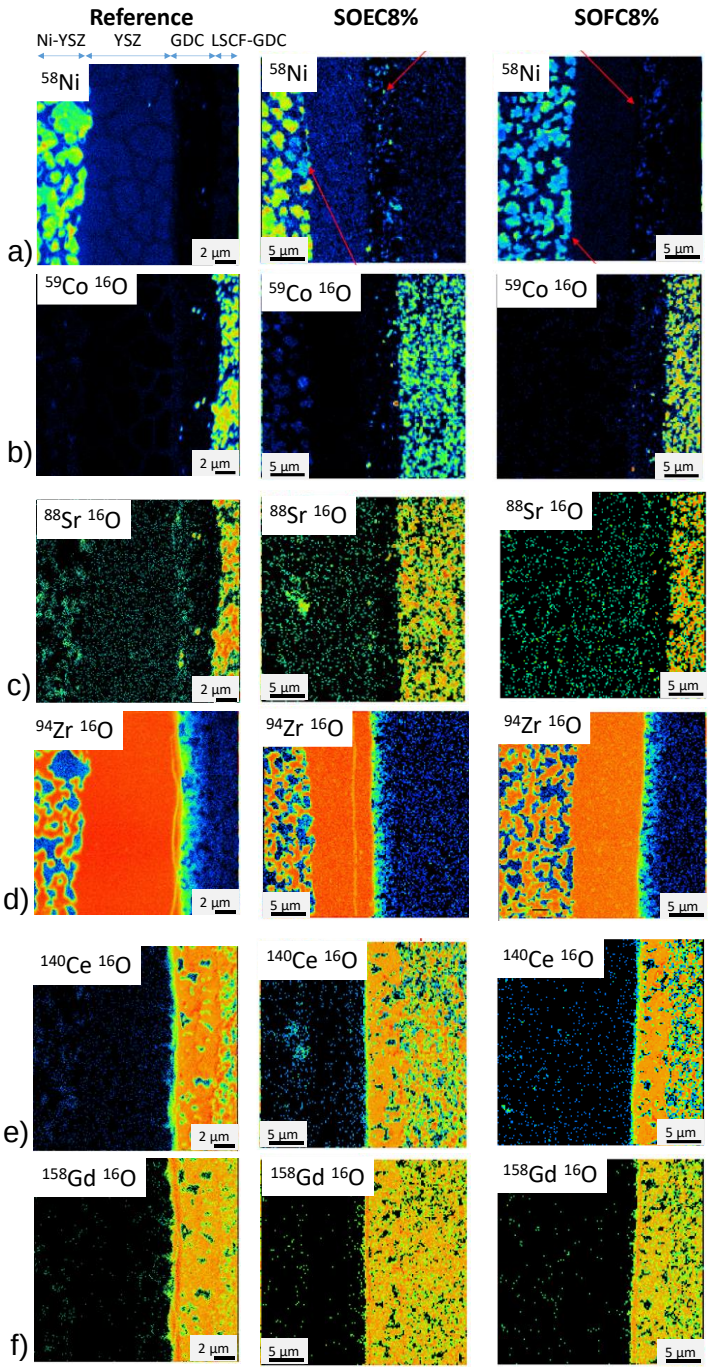

Figure S-C 1. SIMS elemental maps including the electrolyte, the barrier layer and a part of the hydrogen and oxygen electrodes for a) Ni, b) Co, c) Sr, d) Zr, e) Ce and f) Gd.

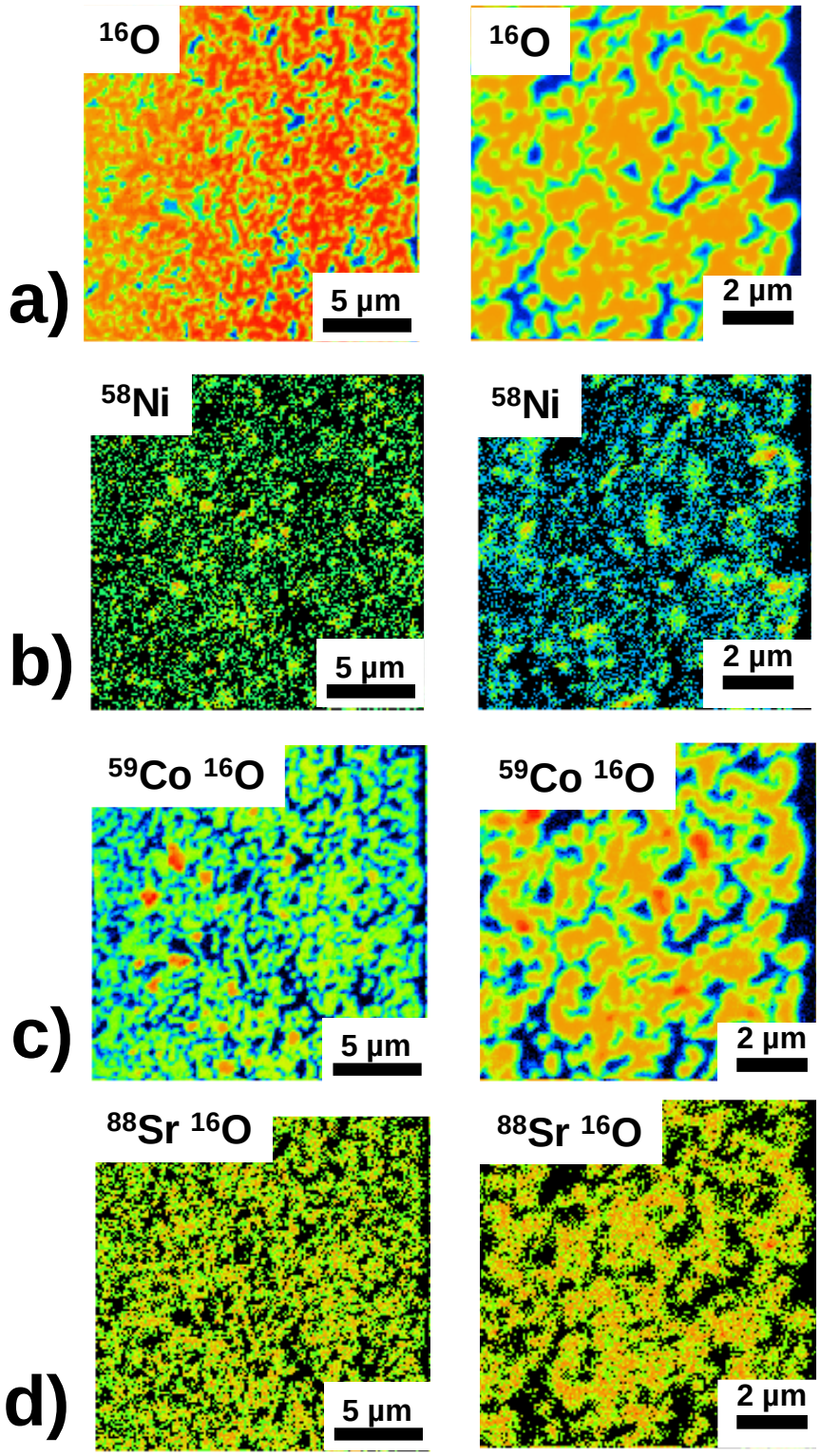

Figure S-C 2. SIMS elemental maps in the CCL of the oxygen electrode after operation under humid air (SOEC8% sample) for a) O, b) Ni, c) Co and d) Sr.

SEM

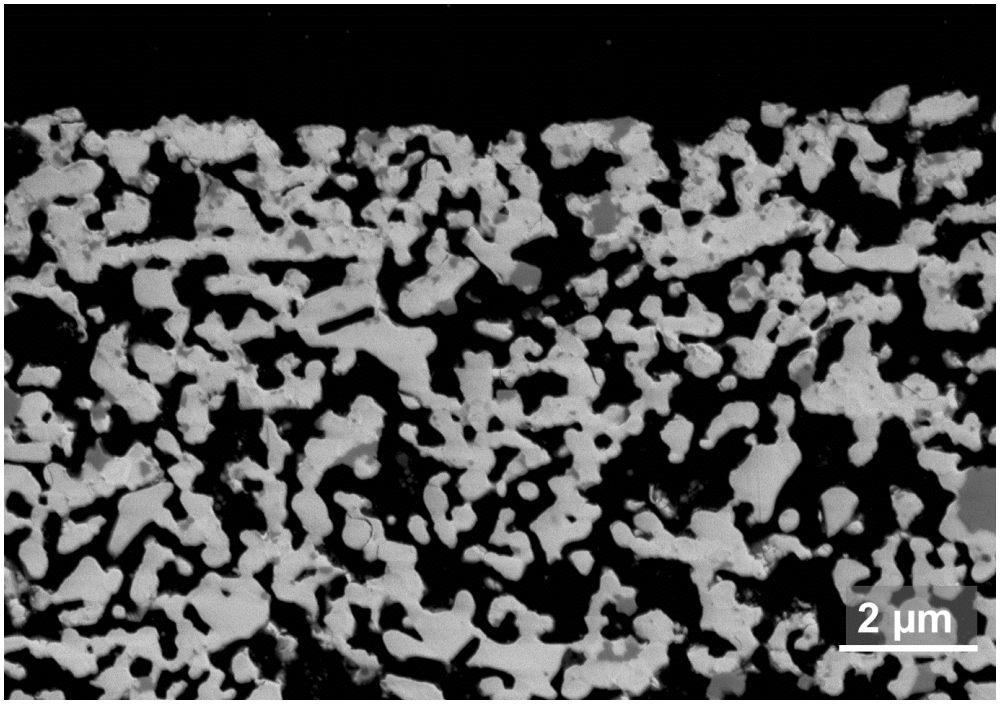

Figure S-C 3. SEM observations focused on top of the LSCF CCL of the SOFC8% sample.

XRD

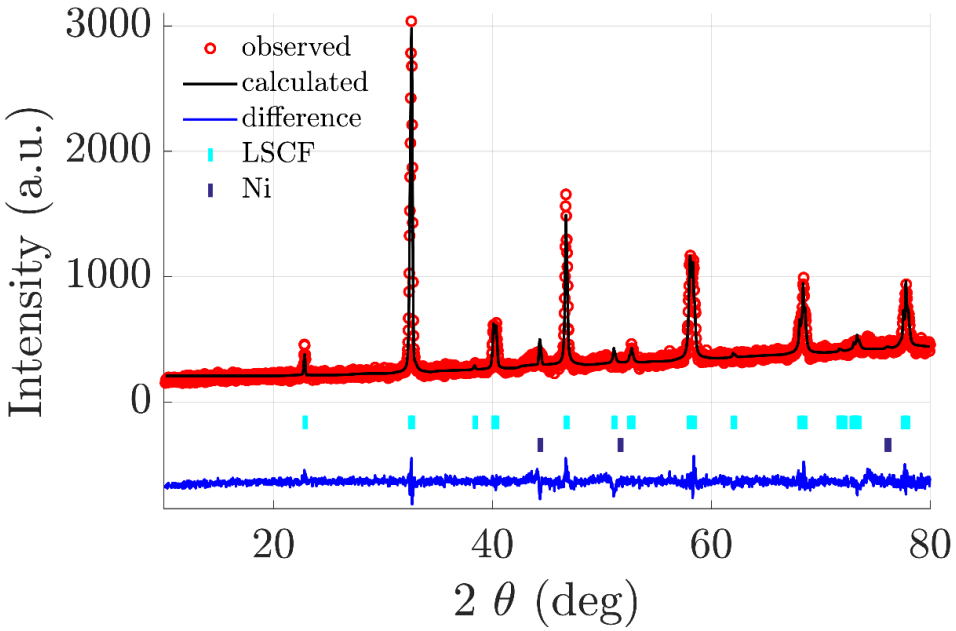

Figure S-C 4. XRD pattern and fit performed on the oxygen electrode LSCF CCL of a sample aged in the same conditions as the SOECdry for a longer ageing time of 2000 h.

XPS

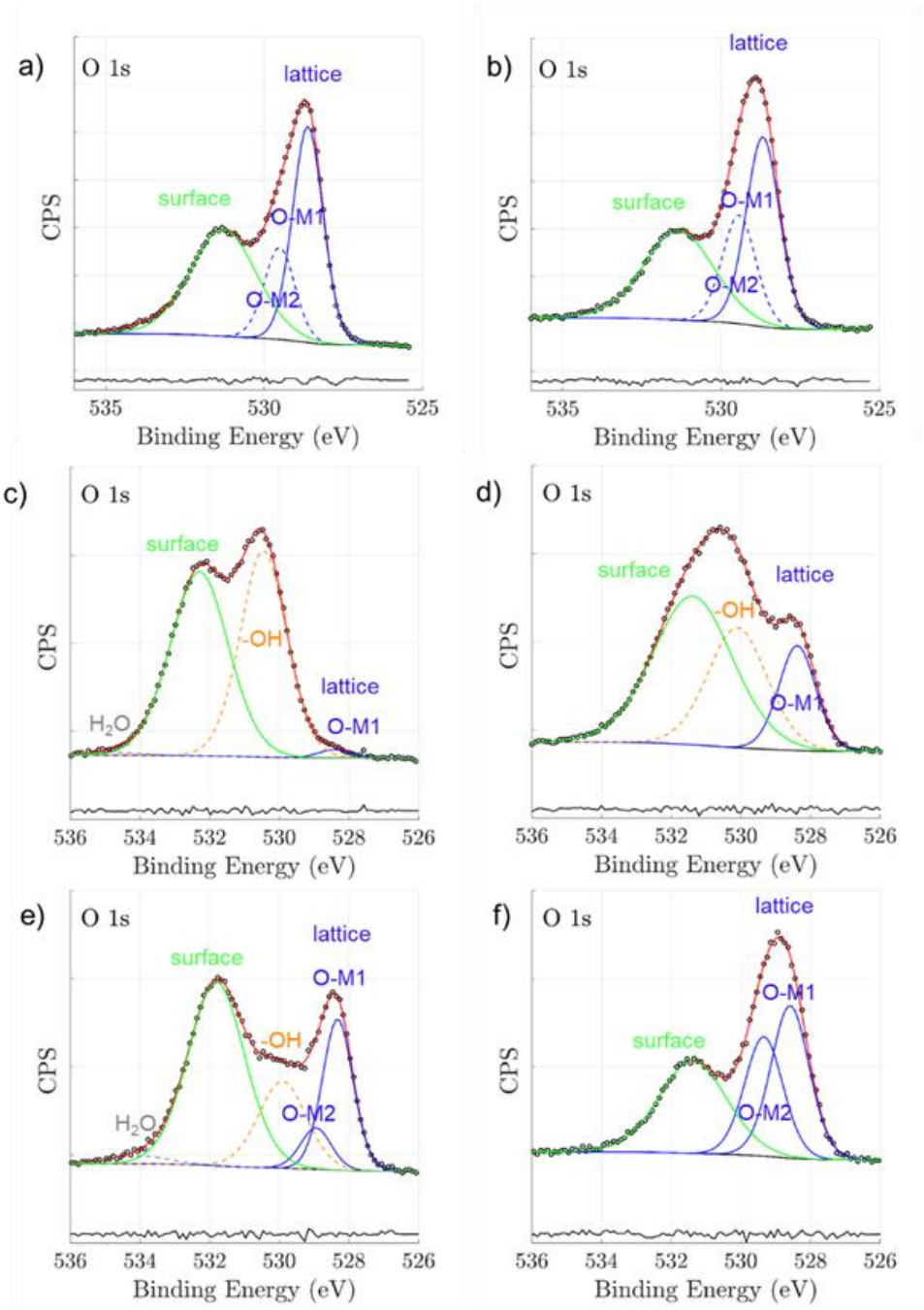

Figure S-C 5. O 1s core-level spectra of a) Reference CCL, b) Reference FL, c) SOEC8% CCL, d) SOEC8% FL and e) SOFC8% CCL, f) SOFC8% FL.

Table S-C 1. XPS fitting results of the **CCL of the Reference** sample including % atomic concentration. BE refers to binding energy and FWHM to full width at half maximum.

Name	BE (eV)	FWHM (eV)	Area	%Conc	Corrected RSF
O 1s – Lattice (O–M1)	528.6	1.1	252.2	25.6	16.223
O 1s – Lattice (O–M2)	529.5	1.1	107.5	10.9	16. 223
O 1s – Surface	531.3	2.4	269.8	27.4	16. 223
O 1s – O–C=O, Organic species	534.0	1.5	8.6	0.88	16.223
Sr $3d_{5/2}$ – Lattice	132.0	1.1	83.9	2.9	47.847
Sr $3d_{3/2}$ – Lattice	133.8	1.1	76.7	1.9	47.847
Sr $3d_{5/2}$ – Surface	133.3	2.0	55.4	2.6	47.847
Sr $3d_{3/2}$ – Surface	135.1	2.1	50.6	1.7	47.847
C 1s – C–C,C–H	285.0	1.4	78.5	19.2	6.737
C 1s – C–O/OH	286.4	1.4	10.6	2.6	6.737
C 1s – C=O	288.6	1.4	6.48	1.6	6.737
C 1s – O–C=O, CO_3^{2-}	290.4	1.4	11.32	2.8	6.737

Table S-C 2. XPS fitting results of the **FL of the Reference** sample including % atomic concentration. BE refers to binding energy and FWHM to full width at half maximum.

Name	BE (eV)	FWHM (eV)	Area	%Conc	Corrected RSF
O 1s – Lattice (O–M1)	528.7	1.2	243.6	26.9	16.223
O 1s – Lattice (O–M2)	529.4	1.2	139.4	15.4	16. 223
O 1s – Surface	531.3	2.6	239.1	26.4	16. 223
Sr $3d_{5/2}$ – Lattice	131.9	1.2	49.9	1.9	47.847
Sr $3d_{3/2}$ – Lattice	133.7	1.5	32.9	1.2	47.847
Sr $3d_{5/2}$ – Surface	133.6	1.6	40.1	1.5	47.847
Sr $3d_{3/2}$ – Surface	135.4	1.8	26.5	1.0	47.847
C 1s – C–C,C–H	285.0	1.4	68.7	18.3	6.737
C 1s – C–O/OH	286.4	1.4	8.6	2.3	6.737
C 1s – C=O	288.7	1.4	10.1	2.7	6.737
C 1s – O–C=O, CO_3^{2-}	289.8	1.4	9.5	2.5	6.737

Table S-C 3. XPS fitting results of the **CCL of the SOEC8%** sample including % atomic concentration. BE refers to binding energy and FWHM to full width at half maximum.

Name	BE (eV)	FWHM (eV)	Area	%Conc	Corrected RSF
O 1s – Lattice (O–M1)	528.4	1.1	4.8	0.8	16.223
O 1s – Surface (–OH)	530.5	1.6	179.7	28.6	16. 223
O 1s – Surface	532.3	2	200.9	32	16.223
O 1s – H_2O	534.8	1.6	2.9	0.5	16.223
Sr $3d_{5/2}$ – Lattice	131.4	1	1.7	0.1	47.847
Sr $3d_{3/2}$ – Lattice	133.2	1	1.1	0.1	47.847
Sr $3d_{5/2}$ – Surface I	133.4	1.5	72.1	3.9	47.847
Sr $3d_{3/2}$ – Surface I	135.2	1.4	47.6	2.6	47.847
Sr $3d_{5/2}$ – Surface II	134.3	1.4	17.7	1	47.847
Sr $3d_{3/2}$ – Surface II	136.1	1.4	11.7	0.6	47.847
C 1s – C–C,C–H	284.9	1.5	62.4	23.9	6.737
C 1s – C–O/OH	286.1	1.5	10.6	4.1	6.737
C 1s – C=O	288.3	1.5	3	1.1	6.737
C 1s – O–C=O, CO_3^{2-}	289.8	1.5	2.1	0.8	6.737

Table S-C 4. XPS fitting results of the **FL of the SOEC8%** sample including % atomic concentration. BE refers to binding energy and FWHM to full width at half maximum

Name	BE (eV)	FWHM (eV)	Area	%Conc	Corrected RSF
O 1s – Lattice (O–M1)	528.4	1.3	73.3	11.5	16.223
O 1s – Surface (–OH)	530.1	2	133.6	21	16. 223
O 1s – Surface	531.4	2.7	222.9	35	16. 223
Sr $3d_{5/2}$ – Lattice	131.7	1.1	18.9	1	47.847
Sr $3d_{3/2}$ – Lattice	133.5	1.4	12.5	0.7	47.847
Sr $3d_{5/2}$ – Surface	133.4	2.1	97.2	5.2	47.847
Sr $3d_{3/2}$ – Surface	135.2	2.2	64.1	3.4	47.847
C 1s – C–C,C–H	285	1.8	42.5	16.1	6.737
C 1s – C–O/OH	287.3	1.8	3.3	1.2	6.737
C 1s – C=O	289.3	1.8	10.2	3.9	6.737
C 1s – O–C=O, CO_3^{2-}	290.3	1.8	2.9	1.1	6.737

Table S-C 5. XPS fitting results of the **CCL of the SOFC8%** sample including % atomic concentration. BE refers to binding energy and FWHM to full width at half maximum.

Name	BE (eV)	FWHM (eV)	Area	%Conc	Corrected RSF
O 1s – Lattice (O–M1)	528.4	1.1	94.1	14.7	16.223
O 1s – Lattice (O–M2)	529.1	1.1	32.9	5.1	16. 223
O 1s – Surface (–OH)	530	1.2	47.6	7.5	16. 223
O 1s – Surface	531.8	2.1	215.4	33.7	16.223
Sr $3d_{5/2}$ – Lattice	131.8	1.2	41.9	2.2	47.847
Sr $3d_{3/2}$ – Lattice	133.6	1.4	27.7	1.5	47.847
Sr $3d_{5/2}$ – Surface	133.6	1.7	108.6	5.8	47.847
Sr $3d_{3/2}$ – Surface	135.4	1.7	71.7	3.8	47.847
C 1s – C–C,C–H	285	1.5	47.7	18	6.737
C 1s – C–O/OH	286.1	1.5	5.5	2.1	6.737
C 1s – C=O	288.5	1.5	2.8	1.1	6.737
C 1s – O–C=O, CO_3^{2-}	289.8	1.5	12.4	4.7	6.737

Table S-C 6. XPS fitting results of the **FL of the SOFC8%** sample including % atomic concentration. BE refers to binding energy and FWHM to full width at half maximum.

Name	BE (eV)	FWHM (eV)	Area	%Conc	Corrected RSF
O 1s – Lattice (O–M1)	528.6	1.3	110.1	24.4	16.223
O 1s – Lattice (O–M2)	529.3	1.3	86.2	19.1	16. 223
O 1s – Surface	531.4	2.3	117.7	26.1	16. 223
Sr $3d_{5/2}$ – Lattice	131.8	1.4	20.7	1.6	47.847
Sr $3d_{3/2}$ – Lattice	133.6	1.5	13.7	1	47.847
Sr $3d_{5/2}$ – Surface	133.4	1.8	28.7	2.2	47.847
Sr $3d_{3/2}$ – Surface	135.2	1.9	18.9	1.4	47.847
C 1s – C–C,C–H	285	1.5	29.7	15.9	6.737
C 1s – C–O/OH	286.5	1.5	4	2.2	6.737
C 1s – C=O	288.7	1.5	5.6	3	6.737
C 1s – O–C=O, CO_3^{2-}	289.9	1.5	5.8	3.1	6.737

Annex

This **Annex** is dedicated to the set of long-term tests and electrochemical characterizations performed in the frame of this thesis. Some of these are not presented and discussed in the main text of the thesis manuscript. Thus, a brief summary these results is reported hereafter.

Complete cells

In this section, the durability curves are shown for the complete cells in Figure A 1. In addition, the raw EIS related to each test were acquired to evaluate the effect on performance degradation of temperature (Figure A 2), humid air and operating mode under humid air (Figure A 3), as well as ageing time and operating mode under dry air (Figure A 4). The results related to the first two studies were already discussed in the main text of the manuscript, i.e. Chapter IV and Chapter V. Overall, it can be concluded that the performance degradation is promoted with increasing the temperature and the humidity level in air. Additionally, a more prominent degradation is observed in SOEC mode as compared to the SOFC mode. Finally, the degradation is faster for short ageing time while it tends to slow down. The degradation rates (DRs) measured in different time intervals of the durability curves are reported in Table A 1. All the tested cells show a durability curve that can be divided in two main regions: an in initial period with faster cell voltage degradation and a final period for which the cell voltage degradation is slower. The most evident example is the tested cell SOEC3%, for which the durability curve shows a very steep increase in the voltage during the first 500 h, and a quite stable voltage in the second half of the test.

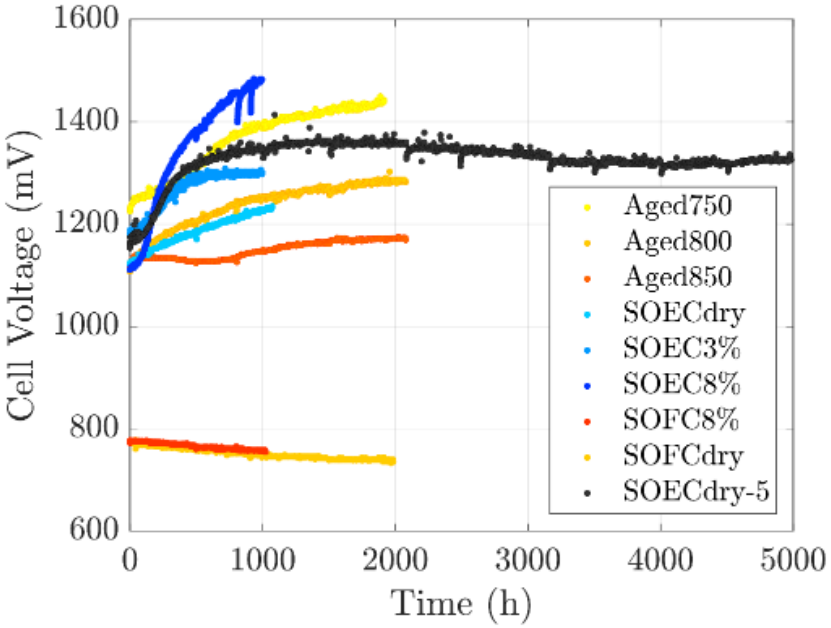

Figure A 1. Complete cells durability curves for all tests.

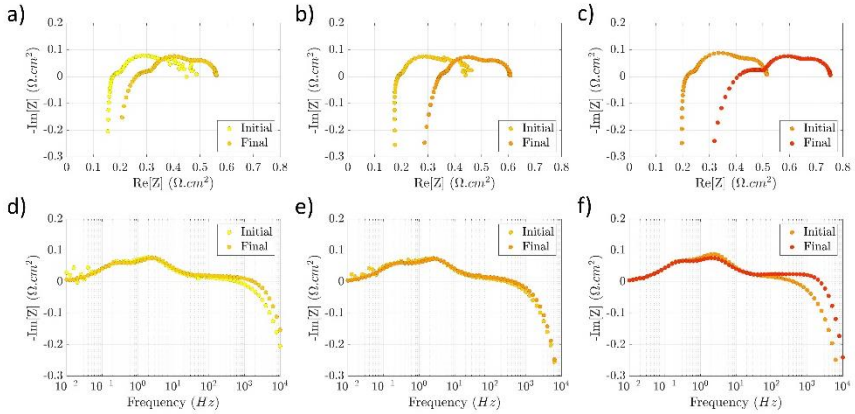

Figure A 2. Complete cells initial and final EIS at OCV, 750 °C, 10/90 vol.% H_2/H_2O for the tests related to the study of the effect of temperature under dry air conditions. Nyquist plots for a) Aged750, b) Aged800 and c) Aged850. Bode plots for d) Aged750, e) Aged800 and f) Aged850.

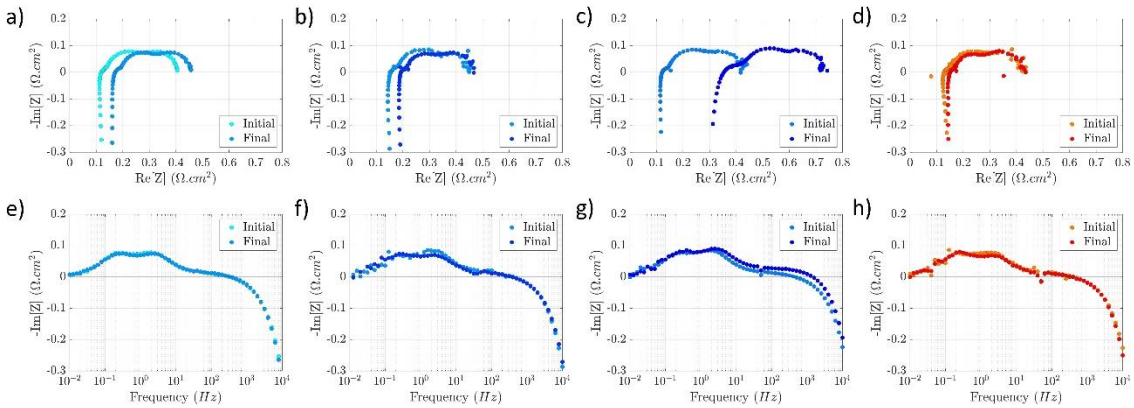

Figure A 3. Complete cells initial and final EIS at OCV, 800 °C, 10/90 vol.% H_2/H_2O for the tests related to the study of the effect of humid air conditions and operating mode. Nyquist plots for a) SOECdry, b) SOEC3%, c) SOEC8% and d) SOFC8%. Bode plots for e) SOECdry, f) SOEC3%, g) SOEC8% and h) SOFC8%.

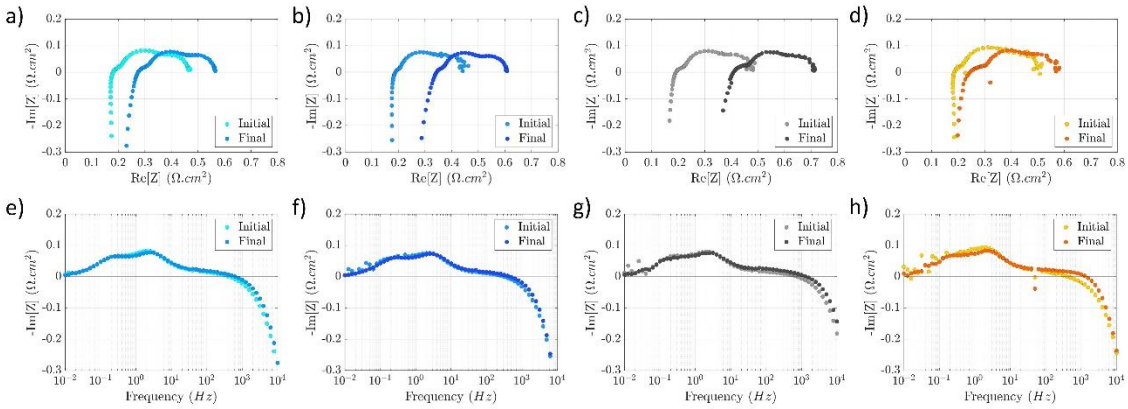

Figure A 4. Complete cells initial and final EIS at OCV, 750 °C, 10/90 vol.% H_2/H_2O for the tests related to the study of the effect of ageing time and operating mode under dry air conditions. Nyquist plots for a) SOECdry, b) Aged800, c) SOEC5k and d) SOFCdry. Bode plots for e) SOECdry, f) Aged800, g) SOEC5k and h) SOFCdry.

Table A 1. Degradation rates in %·kh^{-1} in different time intervals of the various tests.

Test	Interval (h)					
	0-500	500-1000	1500-2000	2000-4000	4000-5000	Total
Aged750	13.3	12.4	2.8	-	-	9.0
Aged800	18.0	8.2	2.0	-	-	7.8
Aged850	1.8	3.6	0.8	-	-	2.4
SOECdry	11.0	7.3	-	-	-	9.4
SOEC3%	19.0	1.5	-	-	-	10.5
SOEC8%	49.4	15.4	-	-	-	33.6
SOFC8%	2.2	2.2	-	-	-	2.1
SOFCdry	3.7	2.7	0.7	-	-	2.3
SOEC5k	28.4	3.9	<0.1	<0	0.8	2.9

Symmetrical cells

Durability tests were performed on symmetrical cell as well. Two types of symmetrical cells were tested. One composed of LSCF/GDC/YSZ/GDC/LSCF and one made of LSCF/LSCF-GDC/GDC/YSZ/GDC/LSCF-GDC/LSCF. In both cases, the GDC barrier layer was about 4

µm, and the YSZ electrolyte was 250 µm. On the other hand, the pure LSCF electrode thickness was around 25 µm, while the thickness of the LSCF CCL and the LSCF-GDC layer were approximatively 25 µm and 20 µm, respectively. In Figure A 5, a difference in the initial polarization resistance can be found for the test performed on the pure LSCF symmetrical cell for 2000 h (LSCF-2k). In addition, a decrease in the ohmic losses was found in the final EIS, which was attributed to an improvement of the contact resistance with ageing time (see Figure A 6a). This was the first test launched on symmetrical cells. After this test, the chamber of the cell was cleaned and the contact improved. Indeed, the two other tests performed for a longer ageing time of 4500 h on both the pure LSCF and the LSCF-GDC present the same initial polarization resistance. Nevertheless, a difference in the initial series resistance can be noted in Figure A 6b-c, which can be attributed to the larger thickness and the greater number of interfaces in the LSCF-GDC symmetrical cell. A greater evolution in the series resistance was observed in the LSCF test, while a greater evolutionin the polarization resistance was found in the LSCF-GDC test.

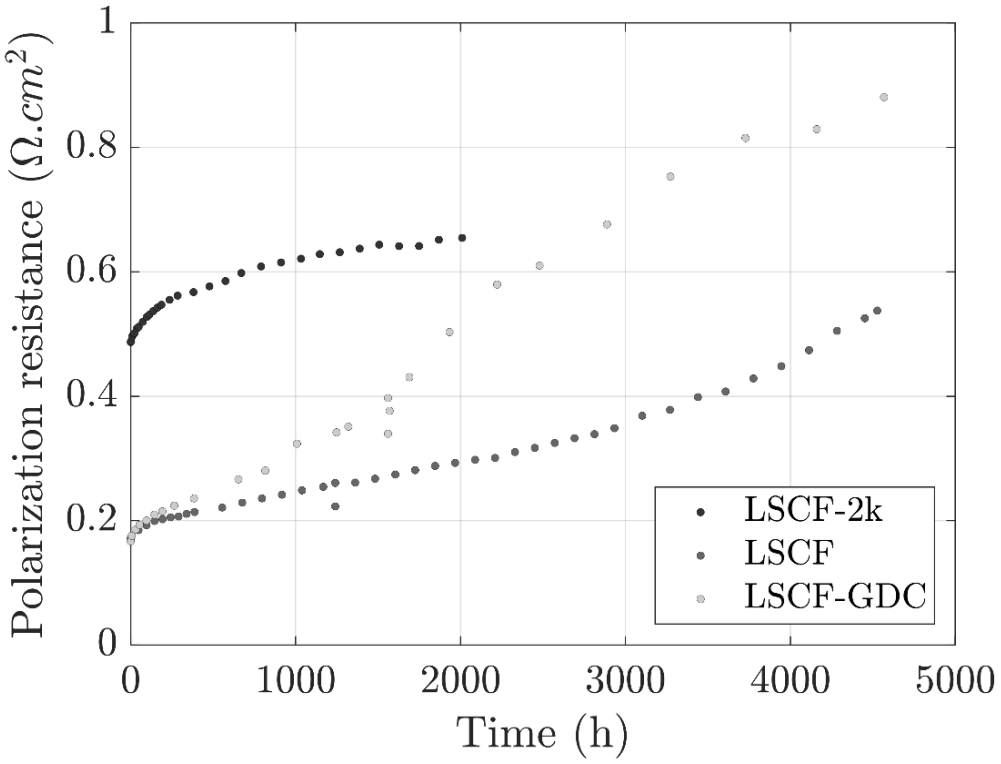

Figure A 5. Symmetrical cells durability curves for all tests.

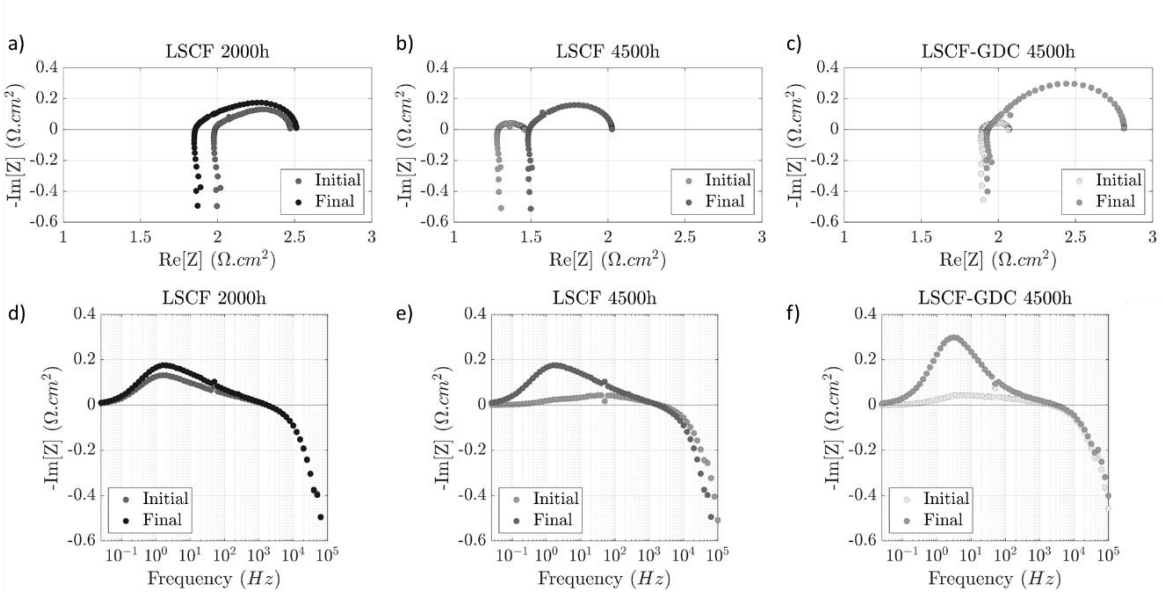

Figure A 6. Symmetrical cells initial and final EIS for all tests.